Stig-Kyrre Foss

DEPTH CONSISTENT PP AND PS SEISMIC ANGLE TOMOGRAPHY

Dr.ing.-thesis 2004:18

Faculty of Information Technology, Mathematics and Electrical Engineering
Department of Mathematical Sciences

NTNU

Stig-Kyrre Foss

DEPTH CONSISTENT PP AND PS SEISMIC ANGLE TOMOGRAPHY

Dr. Ing. Thesis

Department of Mathematical Sciences
Norwegian University of Science and Technology
2004

Summary

This thesis addresses the problem of finding background models yielding depth consistent migrated PP and PS images, i.e. geologically equivalent reflectors should be imaged at the same depth in the two images. The tomographic approach in search of a background medium, is performed as a combination of migration velocity analysis by differential semblance in angle and map migration. A practical strategy for obtaining estimates of all parameter values in a transversely isotropic medium with a known symmetry axis is presented. The approach combines the search of a background medium yielding optimum focusing ablility by differential semblance and the matching of PP and PS key reflectors in depth by means of map migration. This can also be used to match the imaged reflectors with known depths e.g. from well markers.

For the purpose of fast and computationally inexpensive imaging and tomography in angle, a complete review and analysis for the 2.5-D case is performed. The theory is also extended to anisotropic media under necessary and sufficient assumptions. An analysis is performed with regards to parameter issues in 2.5-D in anisotropic media. All inversion and migration results are derived in the natural coordinate system, namely scattering/reflection angle at the imaging point by means of the generalized Radon transform.

PREFACE

This thesis is submitted in partial fulfillment of the requirements for the degree "Doktor ingeniør" (Dr. Ing.) at the Norwegian University of Science and Technology (NTNU). I thank Gilles Lambaré, Bjørn N. Gjevik and Harald Krogstad for serving on my committee. The thesis work has been done over the past 3 years since January 2001 at the Department of Mathematical Sciences, NTNU, and has been financed by the URE-project (Uncertainty in Reservoir Estimation). The URE-project is a collaboration between the Department of Petroleum Engineering and Applied Geophysics and the Department of Mathematical Sciences.

I am forever grateful to my advisor Bjørn Ursin and co-advisor Martijn V. de Hoop for being my guides the last few years. Discussions with them and their continued support has been a great encouragement. I also thank Anders Sollid and Henning Omre for their help and encouragements. I thank Sverre Brandsberg-Dahl for sending me off on the right foot and talking me into spending one year during this work at Center for Wave Phenomena (CWP), Colorado School of Mines. I thank Ken Larner at CWP for all his help and hospitality, and Norman Bleistein for his comments and suggestions. I thank all my colleagues at the Department of Mathematical Sciences, the administrative staff and especially Anne Kajander, Per Kristian Hove and Erik Flå for all help.

This work would never have happened without the support and care of my family. I dedicate this work to them. I also would like to extend a warm thanks for the patience and encouragement of my friends at 'moldelista', in Denver, in Trondheim and other places. I thank Bjarte and Harald for keeping me sane all these years, and the other student at the URE-project; Store Jo, Lille Jo and Ole Petter.

I have had a fantastic and personally rewarding few years and thank all to blame.

Trondheim, February 2004

Stig-Kyrre Foss

Contents

Chapter 1

Thesis introduction

This introduction is intended for the reader unfamiliar with seismic problems and seismic jargon, but familiar with physics and mathematics. A brief review is given of the field of seismic processing while putting the current thesis in context of existing seismic methods. I suggest the reader familiar with seismics start reading from section 1.5. The thesis is a collection of papers either accepted or submitted for publication or in process to be submitted. Each paper is thus self contained with individual introductions describing its contribution in view of existing methods. Details pertaining to this are thus omitted in this thesis introduction.

1.1 A description of the problem

Seismic exploration is focused on studying the first few kilometers of the Earth's crust by means of indirect measurements. This is performed by a so-called *seismic experiment*. An artificial source creates a sound wave in the Earth which is subsequently recorded after passing through the crust. The recorded wavefield has the insignia of the medium through which it has travelled. Obtaining information of the medium from the recorded data has the form of a classical inverse problem (Tarantola, 1987). With this information structural images of the subsurface can be created and information on medium properties can be obtained. Creating such structural images is also called *migration*.

Migration is a process of moving or organizing the data to obtain structural information. E.g. depth migration sums or moves all the data back to the subsurface reflector in physical depth coordinates where the backscattered data originated. Migration requires knowledge of how the wavefield has travelled between the source and the receiver and is based upon

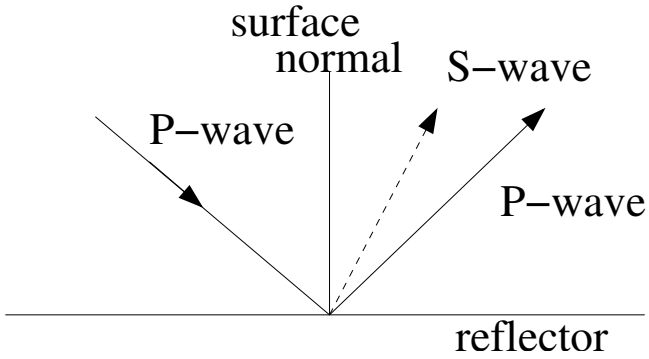

Figure 1.1: An incoming P-wave is reflected both as a P-wave and a S-wave in an isotropic medium.

some knowledge of the *background medium*. I.e. the medium in which the wavefield travels before and after reflection. The background medium can be a highly complex structure with large velocity differences. This is contrary to other indirect measurement situations such as medical imaging using e.g. ultra sound. In addition, the nature of the measurement forces us to illuminate by sound the medium and receive from mostly one direction, the surface. This limited acquisition aperture, band-limitations of the source amongst other reasons contributes to the so-called *velocity-depth ambiguity* (Stork & Clayton, 1986; Bube, 1995). This means that a whole range of different structural images, with different depths, can be created based upon different background models and independent information in our data.

In a seismic experiment the artificial source is usually a pressure source. The wavefield generated travels through the medium as a pressure wave, or P-wave. In an elastic medium, a reflection causes the wavefield to split into several wave modes such as shear wave, or S-wave, in addition to a reflected P-wave see Figure 1.1. The reflected P- and S-waves due to an incoming P-wave, so-called *PP* and *PS* reflection events, are recorded at the acquisition surface by directionally discriminating receivers forming a *multi component data set*. The Earth itself is a highly effective filter separating these events into distinct directional components before they arrive at the acquisition surface. From this data set we may create PP and PS migrated structural images of the subsurface based on the two different reflection events.

As they are based on two different physical wave phenomena the two different images contain different and complementary structural and medium parameter information. Traditionally the PP events were used in migration, but recently the ability to exploit the

migration of PS events have gained much attention. E.g. the S-waves are less sensitive to low velocity zones and attenuation in the medium compared to P-waves. Hence PS-events have been used to image beneath such regions (e.g. gas clouds), further the PS images in junction with PP images are used in fluid prediction. As indicated in Figure 1.1 the S-wave of a PS event has a different emergence angle from the reflecting surface than the P-wave from a PP event. As the P- and S-wave modes behave differently with respect to the medium properties, the aforementioned velocity-depth ambiguity applies separately to both the PP and PS migrated images. The purpose of this thesis is to limit this ambiguity by the additional demand of depth consistency between geologically equivalent key reflectors in PP and PS images. We consider elastic medium which is heterogeneous and anisotropic. This means that a wave is subjected to different medium properties both from point to point and with a directional dependence on how it passes through a point.

1.2 Migration: obtaining structural images

There exists a multitude of methods defined as migrations. Common to all is the creation of a structural image, also called *imaging*. The most obvious subdivisions of these methods are:

i. Depth migration: Structural image in physical coordinates.

ii. Time migration: Structural image where the 'depth'-coordinate is traveltime. This traveltime is usually the two-way traveltime of the imaged structure to the acquisition surface. Based upon idealized situations such as a locally layered 1-D Earth, but is used extensively in the industry.

Depth migration is the preferred migration technique in situations with a high degree of complexity in the subsurface. The literature usually further split migration in two categories namely; *wave equation* method and *Kirchhoff-based* methods. An instructive review and introduction is given by (Gazdag & Sguazzero, 1984). The categories are artificial as the Kirchhoff methods are also based on the wave equation. Similar to all wave equation methods (Claerbout, 1971) is the use of the full wavefield in the data which is propagated backwards in time to the reflecting surface. Finite difference is one such method by direct numerical computation solving the wave equation, while Fourier transform based methods or phase-shift methods uses a solution of the wave equation. This thesis considers Kirchhoff-type migration in depth only (Beylkin, 1984; Bleistein, 1987), we thus continue considering all references to 'Kirchhoff-type depth migration' as migration if not otherwise stated.

In the Kirchhoff-type methods, discussed in the following, we assume that the medium

through which the waves travel is elastic and can be split into a smooth term and a perturbation

$$\text{medium} = \text{smooth term} \; + \; \text{perturbation}. \tag{1.1}$$

The wavefield travels in the smooth part of the medium, the background medium. The reflections are generated at a perturbation in the medium only. The smooth part of the medium is the object of so-called *velocity analysis*, discussed in the next section. Under the above assumption a representation formulation can be deduced directly from the wave equation called the Lippmann-Schwinger (Wapenaar, 1996) equation, well known in physics. It models the observed wavefield at an acquisition surface surrounding the medium generated by a source and scattered at one or many locations within the enclosed region. This is also referred to as the forward modelling formula. The work presented is based on the so-called *Born approximation* which is a linearization of Lippmann-Schwinger, i.e. a single wave is reflected by a single perturbation. This means that only primaries considered in this approximation and not multiples. Multiples are events that have reflected more than once. We assume that the wavefield generated by the source travels in the background medium until it reaches a reflector, the perturbation. This reflector acts as a secondary source. The reflected wavefield travels to the acquisition surface and is recorded as data, see Figure 1.2. This happens for all subsurface points. The Green's function describing the movement of the wavefield uses an approximation assuming high frequency called the geometrical ray approximation (GRA) (Červený, 2001). However, the Born linearization is valid only if the characteristics strength of the reflector is smaller than the wavelenght (Beydoun & Mendes, 1989).

Information on subsurface reflectors is obtained by minimizing the difference between the observed data and the predicted data based on the forward modeling operator as a classical inverse problem formulation (Tarantola, 1987). The solution of this minimization problem yields estimates of the medium perturbations (1.1) is called *inversion*, while obtaining estimates of reflectivity we continue to call migration. Both inversion and migration, or structural reconstruction, at a single subsurface point is performed by stack/summing over traveltime curves in the data modelled by the forward modelling formula as the reflected contribution from the particular subsurface point.

1.3 Velocity analysis

The purpose of velocity analysis is to find the smooth background model equation (1.1); a prerequisite in both depth migration and inversion. All methods are based on the redundancy in the data. A typical seismic experiment is performed with multiple receivers and at least one source. Classical methods such as normal moveout (NMO) methods for

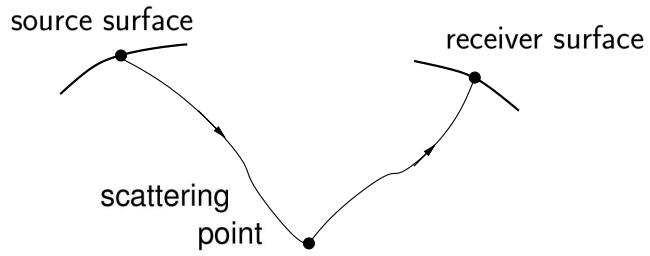

Figure 1.2: Born approximation, where the waves travel from the source to the subsurface points via the scattering point.

isotropic pure mode events uses traveltime curve fitting under simple assumptions such as a 1-D medium. The traveltime curves, shaped like hyperbolas, are fitted to the observed data in a common-shot gather, i.e. the collection of recorded results at multiple receiver location due to one shot. Each hyperbola represents an average velocity. The interval velocities of the 1-D model are found from these by the so-called *Dix equations*. This procedure can be extended to dipping plane layers and to anisotropic media (Alkhalifah & Tsvankin, 1995). Migration velocity analysis (Al-Yahya, 1989) uses the focusing ability in the migration procedure allowing for more complex traveltime curves. The quality of the focusing of the migration, and hence the sharpness of the structural image, is based on the stacking/summation curves in the data calculated by ray tracing in the background medium. The focusing ability can be measured by the moveout behavior of a so-called *common image-point gathers*. Other velocity analysis approaches exists such as stereotomography (Billette & Lambaré, 1998) which considers the traveltime and slope information of the reflection events directly in the data.

The problem of velocity analysis based on converted modes, such as PS events, has only recently been addressed. Due to the nature of the PS reflection, see Figure 1.1, the methods based on fitting hyperbolas do not work directly. Gretchka and Tsvankin (2002) suggested using PP and PS reflection data to obtain pure mode SS (Shear-Shear reflections) data before performing S-wave velocity analysis in such a way. Stereotomography has also recently been extended to PS events (Alerini *et al.*, 2002). Sollid (2000) used migration velocity analysis on PP and PS events. A similar approach is followed in this thesis.

1.4 A seismic survey; processing steps

As all field data examples in this thesis are based upon ocean bottom seismic (OBS) acquisition data, we give a brief review of this survey geometry. The first seismic survey

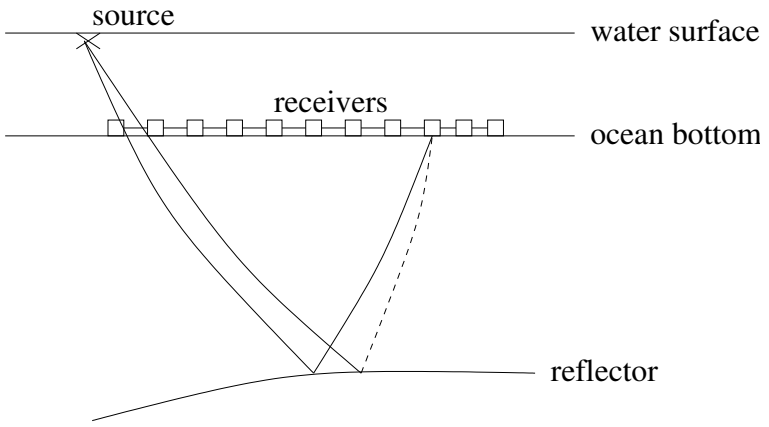

Figure 1.3: Acquisition setup of a OBS survey. Full drawn lines indicate the P-wave mode while the dotted lines indicate the S-wave mode.

with OBS acquisition geometry was performed by (Berg *et al.*, 1994). Usually with OBS, a source is towed by a boat while receivers are placed on the ocean bottom, see Figure 1.3. Indicated are both a PP and PS event with the same source and receiver. The full drawn lines indicate the P-wave mode, while the dotted line indicate the S-wave mode. This is a cost demanding and time consuming survey geometry, but it allows for very general acquisition geometry, high acquisition coverage and improved data quality compared to other marine acquisition geometries such as the use of towed streamers of receivers. Also, as S-waves do not travel in water, only P-waves, PS data need to be collected on the ocean bottom. The latest generation of ocean bottom receiver equipment constitutes a hydrophone, for recording the P-wave, and in addition a three-component geophone which is a directionally discriminating receiver.

The following steps are the main processing steps of the acquired seismic data:

i. **Preprocessing:** In order to obtain a sharper data wavelet the source signature is removed by deconvolution. As mentioned earlier, the usual migration/inversion schemes assume that there are no multiples in the data, only primaries. Several approaches for removal or attenuation of such events exists (Yilmaz, 1987; Dragoset & Jeričević, 1998; Amundsen, 1999). In order to remove unwanted signal and noise a band-pass filter is employed.

ii. **Velocity analysis**

iii. **Migration/inversion**

iv. **Interpretation:** After having obtained structural images, an interpretor can perform lithological analysis and so-called *amplitude-versus-angle* (AVA) analysis (Hilterman, 2001) to obtain information on medium properties or to perform fluid prediction. Usually the interpretor is involved in all of the above steps.

1.5 Outline of the thesis

The thesis is written as a collection of papers submitted to different scientific journals. Due to this the first uses one notation while the rest of the papers share one slightly different notation. However, lists of symbols have been included in the first and second paper.

The papers are grouped into two different parts. The first part is a theoretical part on 2.5-D migration which sets the stage for part two. 2.5-D is a simplification of studying only the waves having travelled in a plane yet exhibiting 3-D wave propagation effects. If the Earth varies in mostly two directions a representative slice through the Earth can be used to investigate the subsurface. We consider modelling and migration/inversion under this simplification. This allows for fast migration/inversion and velocity analysis. The second part of the thesis is devoted to velocity analysis. The field data example uses the 2.5-D framework of the first part, while the appendix contains supplementary information. All papers are referenced throughout the paper according to their status as submitted papers in the reference list in the back. The thesis consists of the following papers :

i) *Linearized 2.5-D parameter imaging-inversion in anisotropic elastic media* with M.V. de Hoop and B. Ursin. Submitted for publication in Geophysical Journal International 2003.

ii) *2.5-D modeling, inversion and angle migration in anisotropic elastic media* with B. Ursin. Accepted for publication in Geophysical Prospecting 2004.

iii) *Depth consistent PP and PS seismic angle tomography* with B. Ursin and M.V. de Hoop, in process 2004.

iv) Appendix: *A practical approach to PP angle tomography* with B. Ursin and A. Sollid. Submitted to Geophysical Prospecting 2004. Originally presented at the EAGE/SEG Summer Research Workshop in Trieste, Italy 2003.

'Linearized 2.5-D parameter imaging-inversion in anisotropic elastic media': This paper in chapter 2 is a fundamental paper on 2.5-D linearized migration in anisotropic media. The theory of 2.5-D migration, which is 3-D wave propagation in a plane was deduced by Bleistein (1986) for the acoustic wave equation case. Here, we introduce the 2.5-D framework

under necessary and sufficient conditions in an anisotropic medium. The paper presents a detailed derivation from Born modelling to least-squares inversion of medium parameters in 2.5-D. A restricted generalized Radon transform (GRT) is derived in order to compute common image-point gathers with a least-squares removal of the AVA-signature for the purpose of velocity analysis.

'2.5-D modeling, inversion and angle migration in anisotropic elastic media' is a complete review of modelling, migration and inversion in anisotropic elastic media for the case of 2.5-D. Also, we perform an analysis of parameter aspects under the 2.5-D assumption for the purpose of migration, inversion and velocity analysis.

'Depth consistent PP and PS angle tomography': This is the main paper of this thesis. It deals with the construction of background models yielding depth consistent PP and PS images. These background models are constructed by a combination of angle tomography to obtain uniform PP and PS common image-point gathers and map migration to match PP and PS key reflectors. Uniform gathers have a constant amplitude behavior at a given depth for all angles. The common image-point gathers, for the purpose of velocity analysis, are computed by the AVA-compensated migration formula derived in paper ii) for 2.5-D, the 3-D formulation is found in (Ursin, 2003). P-wave and S-wave normal incidence point (NIP) ray time information of key reflectors is obtained by a zero-reflection angle approximation of Gretchka and Tsvankin's (2002) 'PP+PS=SS'-approach. By map migration of the pure mode PP and SS time information in a given model the reflectors can be reconstructed in depth based solely on the P-wave and the S-wave velocity, respectively. The SS traveltime map migration reconstructs approximately the depth of the PS reflector based on the S-wave velocity. This enables a matching of the reflectors in depth without a costly retracing of the interfaces given a new background model. The matching of PP and PS images in depth usually requires anisotropy to be taken into account. A strategy is presented, similar to (Sollid & Ettrich, 1999), to obtain estimates of parameter values of a transversely isotropic medium using the aforementioned tools. The procedure is illustrated on an OBS data example from the North Sea using the 2.5-D formalism derived in papers i) and ii).

Appendix *'A practical approach to automated PP angle tomography'* presents all formulas for isotropic PP angle tomography under the 2.5-D formalism. The tomography procedure is regularized by a two-step optimization first optimizing for parameters of a layer based model with linear gradients and then optimizing for coefficients of a 2-D B-spline. The interfaces of the layerbased model are automatically updated in the optimization to always match the two-way traveltime of the reflectors, equivalent to the interfaces, observed in the data similar to (Gjøystdal & Ursin, 1981).

Part I

2.5-D modeling, inversion / migration

Chapter 2

Linearized 2.5-D parameter imaging-inversion in anisotropic elastic media

S.-K. Foss, M.V. de Hoop and B. Ursin
Submitted for publication to Geophysical Journal International

Summary

In this paper we derive 2.5-D high frequency modelling and imaging-inversion formulas of seismic reflection data in the Born approximation in anisotropic elastic media. The 2.5-D approach encompasses 3-D wave scattering measured in a common azimuth acquisition geometry subject to 2-D dimensional computations under appropriate assumptions. The lowest possible symmetry of the medium in this approach in principle, is monoclinic, while the medium must be translationally invariant in the normal direction to the associated symmetry plane. In the presence of caustics artifacts may be generated by the imaging-inversion procedures. We show that in the 2.5-D approach the analysis of artifacts in the 2-D symmetry plane implies the corresponding analysis in 3-D in the framework of the common azimuth acquisition geometry. An interesting aspect of our results is the occurrence of out-of-plane geometrical spreading in the least-squares removal of the contrast source radiation patterns on the data. We finally introduce the 2.5-D transform that gen-

erates common image-point gathers. This transform yields an efficient, though in general, approximate tool for migration velocity analysis in anisotropic media. A real ocean bottom seismic data example from the North Sea, using the derived formulas, is given.

Symbols and notation

Symbols	Description
t	time
ω	angular frequency
$\boldsymbol{x} = (x_1, x_3)(= (x_1, x_2, x_3))$	position vector (before redefinition in main text)
$G_{in}(\boldsymbol{x}^r, \omega, \boldsymbol{x}^s)$	Green's function in the frequency domain
$\boldsymbol{x}^s, \boldsymbol{x}^r$	source and receiver positions
$A(\boldsymbol{x}, \boldsymbol{x}^s)$	amplitude for a ray at $\boldsymbol{x}^s$ from $\boldsymbol{x}$
$\mathbf{h} = (h_1, h_2, h_3)$	polarization vector
$T(\boldsymbol{x}, \boldsymbol{x}^s)$	traveltime for a ray between $\boldsymbol{x}$ and $\boldsymbol{x}^s$
$\kappa(\boldsymbol{x}, \boldsymbol{x}^s)$	KMAH index for a ray between $\boldsymbol{x}$ and $\boldsymbol{x}^s$
$v(\boldsymbol{x})$	phase velocity
$\rho(\boldsymbol{x}) = \rho^{(0)}(\boldsymbol{x}) + \rho^{(1)}(\boldsymbol{x})$	density as a sum of a smoothly varying term and a perturbation
$c_{ijkl}(\boldsymbol{x}) = c^{(0)}_{ijkl}(\boldsymbol{x}) + c^{(1)}_{ijkl}(\boldsymbol{x})$	elastic stiffness tensor as a sum of smooth background parameters and a perturbation
det $\mathbf{Q}_2(\boldsymbol{x}, \boldsymbol{x}^s)$	relative geometrical spreading in local surface coordinates on the wavefront
$Q_2^{\parallel}(\boldsymbol{x}, \boldsymbol{x}^s)$	in-plane relative geometrical spreading
$Q_2^{\perp}(\boldsymbol{x}, \boldsymbol{x}^s)$	out-of-plane relative geometrical spreading
(q_1, q_2)	local wavefront coordinates
$\mathbf{p} = (p_1, p_2, p_3)$	slowness vector
$\boldsymbol{p}^s, \boldsymbol{p}^r$	slowness vector at at scattering point of the ray from the source and the receiver, respectively
$\mathbf{V} = (V_1, V_2, V_3)$	group velocity vector

$\hat{n}$	normal to slowness surface
$u_{mn}(\boldsymbol{x}^r, t, \boldsymbol{x}^s)$,	scattered field in time
$U_{mn}(\boldsymbol{x}^r, \omega, \boldsymbol{x}^s)$	scattered field in frequency
$\mathbf{L}$	modelling operator
$X \subset \mathbb{R}^2$	open subset in plane of consideration
$\Sigma \subset \partial X \times \partial X$	acquisition lines
$Y = \Sigma \times \mathbb{R}_{\geq 0}$	acquisition manifold
$D \subset \Sigma \times X$	open subset per branch in case of triclicated wavefields
$T(\boldsymbol{x}^r, \boldsymbol{x}, \boldsymbol{x}^s)$	two-way traveltime
$A^{\|\|}(\boldsymbol{x}, \boldsymbol{x}^s)$	GRA amplitude with only in-plane geometrical spreading
$\mathcal{L}_R^{\perp}(\boldsymbol{x}^r, \boldsymbol{x}, \boldsymbol{x}^s)$	total out-of-plane geometrical spreading
$\mathbf{w}(\boldsymbol{x}^r, \boldsymbol{x}, \boldsymbol{x}^s)$	radiation patterns 'vector'
$\mathbf{c}^{(1)}(\boldsymbol{x})$	medium parameter perturbation 'vector'
$v_\circ^s, v_\circ^r$	local average phase velocities
Λ_L^S	2.5-D canonical relation
$\boldsymbol{\alpha}^s, \boldsymbol{\alpha}^r$	take-off directions at scattering point
$\boldsymbol{k}$	wave vector
$\boldsymbol{k}^s, \boldsymbol{k}^r$	wave vector for source and receiver rays, respectively
Λ_L^{CA}	common azimuth (CA) canonical relation
$\mathbf{L}^\star$	imaging operator
ψ	pseudodifferential cutoff
$\mathbf{N}$	normal operator
$\mathcal{N}$	kernel of normal operator
$\mathcal{J}$	extended Jacobian
$\boldsymbol{\nu}^m$	migration dip covector
μ_{LS}	scaled extended Jacobian
θ	scattering angle
Γ	matrix used in inversion
δ_{BL}	band-limited delta function
$\mathbf{K}$	angle transform
$\mathcal{K}_{mn}$	kernel of angle transform
Φ	phase function
$\underline{\boldsymbol{m}} = \{\boldsymbol{m}_1, \ldots\}$	collection of parameterized slices of background medium
J	misfit functional
Ξ	matrix used in reflection tomography by differential semblance
$\mathbf{c}^{(0)}$	background medium parameters
λ	statistical regularization parameter

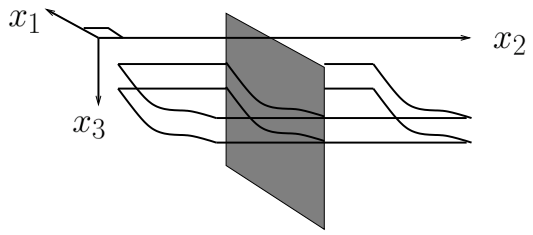

Figure 2.1: Cylindrical reflectors and the plane of consideration; (x_1, x_3)-plane.

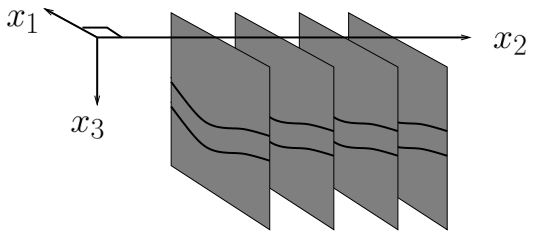

Figure 2.2: Parallell slices of the medium in the direction of the most dominant change.

Superscripts s and r indicate source and receiver respectively.

2.1 Introduction

In this paper we derive general single scattering 2.5-D modelling and imaging-inversion formulas in anisotropic elastic media under precise assumptions. The lowest possible symmetry of the medium in this approach, in principle, is monoclinic, while the medium must be translationally invariant in the direction normal to the associated symmetry plane. All results are put in the context of common azimuth (CA) migration as discussed, for example, by de Hoop *et al* (2003a). If the Earth varies in mostly two directions, a representative plane containing these directions will suffice in describing the subsurface; the 2.5-D framework applies approximately (it is exact if there are only two directions of change). This enables a fast computational way, through a slicewise approach, to reflection tomography. Further, it simplifies the ability to monitor the regularization of this kind of tomography. Figure 2.1 shows a representative slice in the direction of the dominant change while Figure 2.2 shows several parallel such slices in a medium with a smooth out-of-plane behavior.

Goldin (1986) and Červený (1981) considered the notion of 3-D wave propagation in 2-D

media, the 2-D medium being contained in the mentioned plane. Bleistein (1986) introduced the notion of 2.5-D in seismic applications when restricting the attention to waves that travel and scatter in this plane alone consistent with the CA acquisition geometry if such geometry is aligned with the plane, but exhibit 3-D geometrical spreading. He considered the acoustic wave equation and derived modelling and Kirchoff migration formulas for this case. Several authors have since considered 2.5-D Kirchhoff migration in isotropic elastic media (Tygel *et al.*, 1998; Dellinger *et al.*, 2000). Geoltrain (1989) extended the approach to Kirchhoff migration in transversely isotropic media with a vertical symmetry axis.

The imaging-inversion results in this paper are derived using the inverse generalized Radon transform (GRT) (Miller *et al.*, 1987) using natural coordinates at each subsurface point to be imaged, namely scattering angle and migration dip. Sollid and Ursin (2003) derived a 2.5-D migration formula, using the GRT, in transversely isotropic media. A review of 2-D and 2.5-D inversion and migration is found in (Foss & Ursin, 2004). Using the aforementioned choice of coordinates removes the use of a Beylkin determinant (de Hoop *et al.*, 1999). Additionally, this choice unravels caustics that may occur in an inhomogeneous medium giving rise to multivalued travel time functions. In the presence of caustics, strictly speaking, the GRT should be developed with Maslov Green's functions. However, de Hoop and Brandsberg-Dahl (2000) carried out an analysis that showed that as long as there are no caustics occurring at the source or receiver positions, through a stationary phase argument, the Maslov formulation reduces to a GRT based upon the geometrical ray approximation (GRA) for the Green's functions. Following this observation, we employ the GRA Green's function in our development. The formulas derived in this paper are applicable in the presence of multipathing and caustics under assumptions that will be clarified.

The high frequency linearized inversion, given a smooth background medium, yields the most singular part of the unknown medium contrast and is developed in the framework of pseudodifferential and Fourier integral operators (FIOs), see e.g. Duistermaat (1996). This was done in the acoustic case by Rakesh (1988), Hansen (1991) and in the anisotropic elastic case by Stolk and de Hoop (2002). We derive a new 2.5-D linearized inversion formula, using the GRT, for anisotropic media under appropriate assumptions. These assumptions are extensions of those by Bleistein (1986) necessitated by the introduction of anisotropy and give rise to certain restrictions on the types of media possible in the 2.5-D framework. The inversion procedure, based upon the 2.5-D Born modelling integral, is an analogue to the one based on least squares. The 2.5-D Born modelling integral is obtained by recognizing the out-of-plane variable as a phase variable. Following Bleistein (1986) the out-of-plane integral in the 3-D Born modelling integral is approximated using the method of stationary phase. This is not defined in the presence of out-of-plane caustics

(however, the 3-D integral is still defined (de Hoop & Brandsberg-Dahl, 2000)). Using the inversion result we derive a new least-squares AVA-compensated (amplitude-vs-angle) formula for the creation of common-image point gathers used in reflection tomography (Brandsberg-Dahl *et al.*, 2003b). Implicitly our formulas yield FIOs in 3-D subject to a 2-D computation. The application and development of the 2-D approximation in global seismology can be found in Bostock *et al.* (2001).

In the presence of caustics, in the CA geometry, imaging artifacts may occur; for the acoustic case, see Nolan and Symes (1997). An artifact is defined as a false event in the image that is not contained in the medium contrast, i.e. an image reflector that is not there. The inversion is artifact-free under the so-called *Bolker condition* (Guillemin, 1985). When this condition is violated, the image resulting from the inversion procedure will contain artifacts we have coined *artifacts of type 1*. The transformation of seismic data into common-image point gathers, based upon the GRT, can be viewed as introducing a restriction to a fixed scattering angle in the inversion formula (Brandsberg-Dahl *et al.*, 2003a). This restriction will in the presence of caustics give rise to *artifacts of type 2* (for an exhaustive analysis of these, see Stolk (2002)). Brandsberg-Dahl *et al* (2003a) suppressed such artifacts by a procedure called focusing in dip by selecting contributions to the imaging-inversion integral from isochrones by an isochrone filter.

The outline of the paper is as follows. In section 2.2, we introduce the notation and the fundamental assumptions pertaining to 2.5-D. We also show by an example that, due to the anisotropy, an additional assumption is required to restrict the rays to travel in-plane, compared to Bleistein (1986). A detailed description of all aspects of the 2.5-D Born single scattering modelling formula is given. The derivation of this formula can be found in the Appendix 2.A; it is based on approximating the out-of-plane integral of the 3-D Born modelling formula by the method of stationary phase (Bleistein, 1986) given that there are no out-of-plane caustics. We give a description of which elastic parameters can be determined in the 2.5-D framework of CA data. A more detailed description of the parametrization and resolution of the smooth and perturbed parts of the medium in this context is given by Foss and Ursin (2004). Additionally, we give the precise assumptions subject to which our 2.5-D modelling is well defined and show how it pertains to the CA acquisition geometry. Section 2.3 contains the detailed guide through our inversion procedure which is an analogue to least squares inversion. The inversion follows closely that of de Hoop and Brandsberg-Dahl (2000). We show that the 2-D Bolker condition pertaining to the symmetry plane implies the likewise condition in 3-D subject to the restriction to CA. First, we construct the adjoint (imaging) operator of the 2.5-D modelling operator. Second, we evaluate the normal operator and identify its 'inverse' up to leading order.

Third, we compose this 'inverse' with mentioned adjoint to find the 2.5-D inversion operator. (For 'inverse', one should read parametrix which is the inverse modulo smoothing operators.) The actual inversion result, for the most singular part of the medium contrast, is given in subsection 2.3.2 as an inverse by GRT in natural coordinates. In section 2.4 we present the 2.5-D transformation of the data to common-image point gathers. Section 2.5 shows results using the formulas derived in this paper applied to real ocean bottom cable (OBC) seismic data from the North Sea. We conclude with a discussion on future applications.

2.2 Modelling

2.2.1 Green's functions in a smoothly varying medium

The geometrical ray approximation (GRA) to the Green's functions is a causal, short period approximate solution to the elastic wave equation, in the frequency domain given by

$$\rho(\boldsymbol{x})\omega^2 G_{in} + \partial_j(c_{ijkl}(\boldsymbol{x})\partial_l G_{kn}) = -\delta_{in}\delta(\boldsymbol{x}-\boldsymbol{x}^s) \quad i,j,k,l,n = 1,2,3, \tag{2.1}$$

where ω is angular frequency and the position vector is denoted by $\boldsymbol{x} = (x_1, x_2, x_3)$, $\rho(\boldsymbol{x})$ and $c_{ijkl}(\boldsymbol{x})$ are density and the stiffness tensor, respectively. The Kronecker delta, δ_{in}, gives the source term on the right-hand side in the canonical directions, operative at the source point, $\boldsymbol{x}^s$, through the delta function δ. The summation convention applies here and in the following. The Green's function is a sum over the different wave modes, where each term is of the form

$$G_{ip}(\boldsymbol{x},\omega,\boldsymbol{x}^s) = A(\boldsymbol{x},\boldsymbol{x}^s)h_i^s(\boldsymbol{x})h_p(\boldsymbol{x}^s)e^{\mathrm{i}\omega T(\boldsymbol{x},\boldsymbol{x}^s)}, \tag{2.2}$$

in which $T(\boldsymbol{x},\boldsymbol{x}^s)$ is the travel time along the ray connecting $\boldsymbol{x}$ with $\boldsymbol{x}^s$. (We do not explicitly indicate the mode of propagation; we treat the modes of propagation separately.) h_i^s and h_p are components of the unit polarization vectors at the endpoints of the ray, where the superscript s indicates that this polarization vector is associated with the ray originating at $\boldsymbol{x}^s$. This convention will be used in the following; superscripts s and r indicate the association of a variable with either a source or a receiver point, $\boldsymbol{x}^s$ and $\boldsymbol{x}^r$, respectively. $A(\boldsymbol{x},\boldsymbol{x}^s)$ is the amplitude, which becomes complex in the presence of caustics, and can be written in the form (Červený, 2001)

$$A(\boldsymbol{x},\boldsymbol{x}^s) = \frac{e^{-\mathrm{i}\frac{\pi}{2}\kappa(\boldsymbol{x},\boldsymbol{x}^s)}}{4\pi[\rho(\boldsymbol{x})v^s(\boldsymbol{x})\rho(\boldsymbol{x}^s)v(\boldsymbol{x}^s)]^{1/2}|\det\,\mathbf{Q}_2(\boldsymbol{x},\boldsymbol{x}^s)|^{1/2}}. \tag{2.3}$$

Here, v^s and v are the phase velocities at $\boldsymbol{x}$ and $\boldsymbol{x}^s$, respectively, in the direction of the ray connecting these points. $|\det \mathbf{Q}_2(\boldsymbol{x}, \boldsymbol{x}^s)|^{1/2}$ is the relative geometrical spreading factor given by

$$[Q_2]_{ij}^{-1}(\boldsymbol{x}, \boldsymbol{x}^s) = -\frac{\partial^2 T(\boldsymbol{x}, \boldsymbol{x}^s)}{\partial q_i^s \partial q_j}, \quad i, j = 1, 2, \tag{2.4}$$

where q_j and q_i^s are local surface coordinates on the wave front at the points $\boldsymbol{x}$ and $\boldsymbol{x}^s$, respectively. $\kappa(\boldsymbol{x}, \boldsymbol{x}^s)$ is the KMAH index and counts the caustics that the ray encounters between $\boldsymbol{x}^s$ and $\boldsymbol{x}$; it accounts for the phase shifts this causes. The subtleties concerning the computation of this index in the presence of anisotropy for the quasi shear waves are elucidated in (Klimeš, 1997).

We are concerned with 2.5-D modelling, and imaging-inversion of elastic waves in anisotropic media in the Born approximation. To justify the 2.5-D approach we need to invoke appropriate assumptions. Two of the assumptions pertains to restricting the ray geometry to the (x_1, x_3)-plane in the modelling, the first being:

Assumption 1 (Symmetries)

a) The medium is invariant in the out-of-plane direction (x_2).

b) The (x_1, x_3)-plane of propagation is a plane of mirror symmetry.

The translational invariance of assumption 1 a) guarantees that the out-of-plane wave slowness is constant. Assumption 1 b) ensures that the wave front is symmetric about the symmetry plane. The lowest possible anisotropic symmetry is then monoclinic which has only one plane of mirror symmetry.

Due to the symmetry we may choose one of the wave front coordinates to coincide with the out-of-plane direction, say $q_2 = x_2$. The first wave front coordinate, say q_1, is chosen in-plane. Thus, in the 2.5-D approach (due to assumption 1 b)), $\frac{\partial T(\boldsymbol{x}, \boldsymbol{x}^s)}{\partial q_1^s}$ and $\frac{\partial^2 T(\boldsymbol{x}, \boldsymbol{x}^s)}{\partial q_1}$ are equal functions in x_2 and hence $\frac{\partial^2 T(\boldsymbol{x}, \boldsymbol{x}^s)}{\partial q_1^s \partial x_2} = \frac{\partial^2 T(\boldsymbol{x}, \boldsymbol{x}^s)}{\partial x_2^s \partial q_1} = 0$. In those wave front coordinates, the relative geometrical spreading matrix in equation (2.4) becomes a diagonal matrix,

$$\mathbf{Q}_2(\boldsymbol{x}, \boldsymbol{x}^s) = -\begin{bmatrix} \dfrac{1}{\dfrac{\partial^2 T(\boldsymbol{x}, \boldsymbol{x}^s)}{\partial q_1^s \partial q_1}} & 0 \\ 0 & \dfrac{1}{\dfrac{\partial p_2}{\partial x_2}} \end{bmatrix} = \begin{bmatrix} Q_2^{\parallel}(\boldsymbol{x}, \boldsymbol{x}^s) & 0 \\ 0 & Q_2^{\perp}(\boldsymbol{x}, \boldsymbol{x}^s) \end{bmatrix}, \tag{2.5}$$

where $Q_2^{\|}(\boldsymbol{x}, \boldsymbol{x}^s)$ and $Q_2^{\perp}(\boldsymbol{x}, \boldsymbol{x}^s)$ are the in-plane and out-of-plane relative geometrical spreading factors, respectively. This structure implies that the relative geometrical spreading in equation (2.3) factors into an in-plane and an out-of-plane component,

$$|\det \mathbf{Q}_2(\boldsymbol{x}, \boldsymbol{x}^s)|^{1/2} = |Q_2^{\|}(\boldsymbol{x}, \boldsymbol{x}^s) Q_2^{\perp}(\boldsymbol{x}, \boldsymbol{x}^s)|^{1/2}. \tag{2.6}$$

Note that the argument in equation (2.5) for the splitting of the in-plane and out-of-plane spreading is not dependent on the actual constant value of p_2.

2.2.2 Scattering in the Born approximation

The 2.5-D Born modelling formula is derived from the 3-D Born modelling formula by a stationary phase argument integrating out the out-of-plane coordinate, following Bleistein (1986). The domain in the symmetry plane in which the 2-D scattering takes place is denoted by $X \subset \mathbb{R}^2$. From now on, let $\boldsymbol{x} = (x_1, x_3) \in X$.

The stationary phase argument involves the stationarity condition (Appendix 2.A, equation (2.A-3))

$$\partial_{x_2}(T(\boldsymbol{x}^s, \boldsymbol{x}) + T(\boldsymbol{x}, \boldsymbol{x}^r)) = p_2^s + p_2^r = 0, \tag{2.7}$$

where $\boldsymbol{p}^2 = (p_1^s, p_2^s, p_3^s)$ and $\boldsymbol{p}^r = (p_1^r, p_2^r, p_3^r)$ are the slowness vectors associated with the source ray and the receiver ray, respectively. We wish to restrict our attention to rays that only travel in-plane. However, the stationary phase argument in equation (2.7) admits out-of-plane contributions. A simple example that satisfies equation (2.7), using p_2^s equal a constant, for qSV-qSV scattering ('q' stands for 'quasi' in the following) is illustrated in Figure 2.3. The medium is transversely isotropic with a vertical symmetry axis (x_3-axis). By controlling the Thomsen parameters, ϵ and δ (Thomsen, 1986), we may change the shape of the slowness surface smoothly as shown on the right of the figure for three different depths in the model used in the ray tracing on the left. All axes are given in meters. The group velocity vector, $\mathbf{V}$, is perpendicular to the slowness surface and governs the direction of the ray. This is indicated with the surface normal to the slowness surface, $\hat{n}$. As suggested in the figure, we may change smoothly the direction of the energy velocity, sending the rays out of the plane and back again while keeping p_2 fixed (implication of assumption 1 a)). Two rays are shot at a small positive and negative angle with the x_3-axis in the out-of-plane direction ($p_1^s = p_1^r = 0$) from $(x_1, x_2, x_3) = (0, 0, 200)$. They travel in the (x_2, x_3)-plane and intersect at the point $(0, 0, 2800)$ with incoming angles following Snell's law and satisfying equation (2.7). We note that the anisotropy in this example allows triplications on the symmetry axis, which is unusual in a sedimentary sequence setting.

We admit in-plane scattering events only, by imposing:

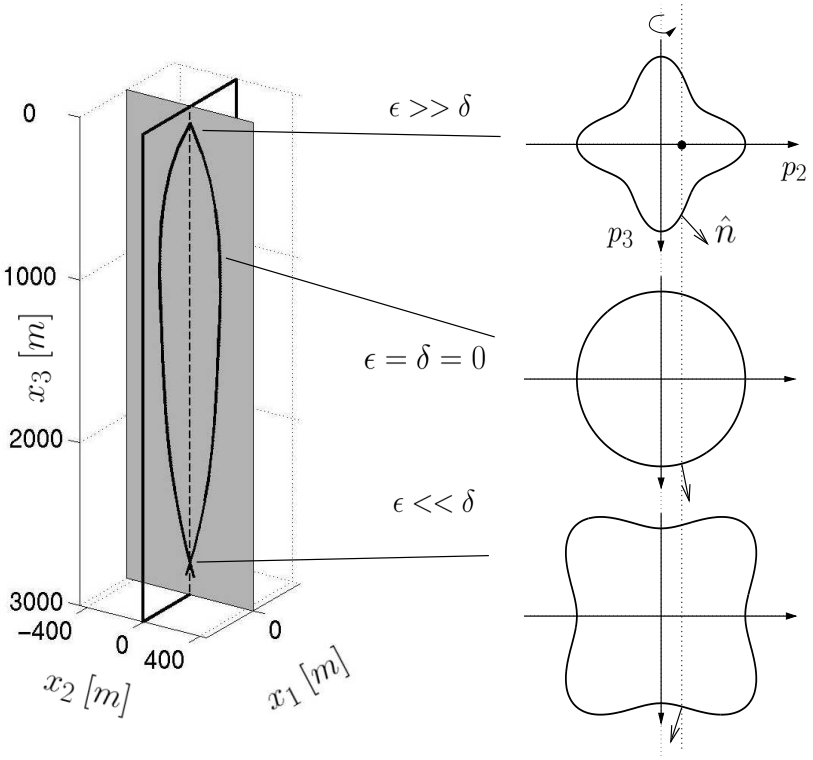

Figure 2.3: Example of rays travelling out-of-plane that are in the stationary point set equation (2.7)

Assumption 2 (Seismic phase restriction) *Only seismic events with at least one ray, or leg, associated with a wave type that pertains to a convex slowness surface are considered.*

If one of the ray legs is associated with a convex slowness surface, the only solution to equation (2.7) is $p_2^r = p_2^s = 0$. Due to the symmetry in assumption 1 b) this also means that $V_2^s = V_2^r = 0$. This follows because $p_2^r = -p_2^s \neq 0$ on a convex slowness surface will induce group velocity vectors pointing out of the plane (the middle slowness surface on the right of Figure 2.3 illustrates this). The group vectors send seismic energy away from the plane never to return. In particular, P waves always have a convex slowness surface (Musgrave, 1970); hence, qP-qP and qP-qSV scattering events always satisfy assumption 2.

The medium parameters are represented by a sum of a smooth part, $\rho^{(0)}$ and $c_{ijkl}^{(0)}$, and a singular perturbation, $\rho^{(1)}$ and $c_{ijkl}^{(1)}$:

$$\rho(\boldsymbol{x}) = \rho^{(0)}(\boldsymbol{x}) + \rho^{(1)}(\boldsymbol{x}), \quad c_{ijkl}(\boldsymbol{x}) = c_{ijkl}^{(0)}(\boldsymbol{x}) + c_{ijkl}^{(1)}(\boldsymbol{x}). \tag{2.8}$$

Note that both the smooth part and the perturbation are restricted in accordance with assumption 1a) and b) making the reflectors parts of the cylindrical surfaces (see Figure 2.1). In the Born approximation, the waves travel in the smooth part of the medium and are scattered off the perturbation once. In the imaging-inversion problem the smooth medium is assumed to be known. It is the medium perturbation we will invert for. The multicomponent data collected in a seismic experiment, u_{mn}, will, under the condition of a smooth background, in this approximation be the asymptotic part of the modelling formula. The subscripts indicate that u_{mn} is the m-component of the recorded wave field due to a body force in the n-direction. The data (scattered wave field) can be modelled by an operator $\mathbf{L}$ acting on the medium perturbation (see Appendix 2.A for a detailed derivation, where U_{mn} is the time-Fourier transform of the data u_{mn})

$$\begin{aligned} u_{mn}(\boldsymbol{x}^s, \boldsymbol{x}^r, t) &= \mathbf{L}\mathbf{c}^{(1)}(\boldsymbol{x}^s, \boldsymbol{x}^r, t) \\ &\approx \sum_{i\in I} \sqrt{\frac{\mathrm{i}}{2\pi}} \int_X \int_{\mathbb{R}} h_m(\boldsymbol{x}^r)\omega^{3/2}\rho^{(0)}(\boldsymbol{x}) \frac{A^{||}(\boldsymbol{x}^s, \boldsymbol{x})A^{||}(\boldsymbol{x}, \boldsymbol{x}^r)}{\mathcal{L}^{\perp}(\boldsymbol{x}^r, \boldsymbol{x}, \boldsymbol{x}^s)} \\ &\qquad \cdot \mathbf{w}^T(\boldsymbol{x}^r, \boldsymbol{x}, \boldsymbol{x}^s)\mathbf{c}^{(1)}(\boldsymbol{x}) e^{\mathrm{i}\omega(T^{(i)}(\boldsymbol{x}^r, \boldsymbol{x}, \boldsymbol{x}^s)-t)} h_n(\boldsymbol{x}^s)\mathrm{d}\omega\mathrm{d}\boldsymbol{x}. \end{aligned} \tag{2.9}$$

Here, $T^{(i)}$ is the two-way travel time given by

$$T^{(i)}(\boldsymbol{x}^r, \boldsymbol{x}, \boldsymbol{x}^s) = T(\boldsymbol{x}^s, \boldsymbol{x}) + T(\boldsymbol{x}, \boldsymbol{x}^r). \tag{2.10}$$

(Note that the modelling equation is valid up to leading order since we inserted the GRA

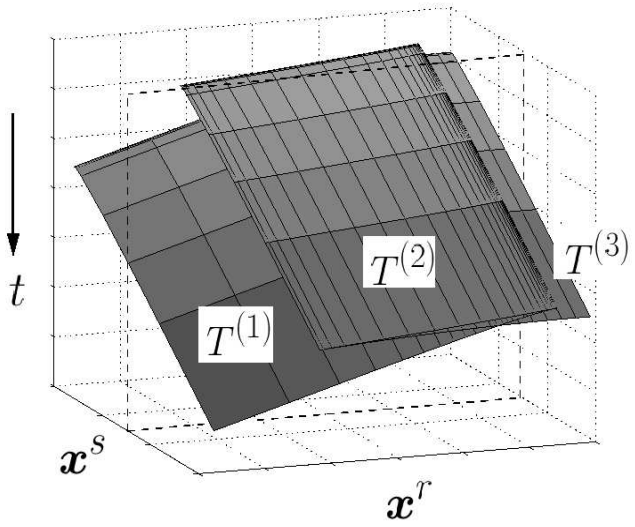

Figure 2.4: Triplications of the recorded wave field with travel time functions per branch denoted $T^{(1)}$, $T^{(2)}$ and $T^{(3)}$. Dotted plane indicates a common shot gather.

amplitudes in the oscillatory integral representations for the Green's functions.) We consider $\boldsymbol{x}^s, \boldsymbol{x}^r \in X$. Restricting $\boldsymbol{x}^s, \boldsymbol{x}^r$ further to smooth source and receiver lines forming the manifold $\Sigma \subset \partial X \times \partial X$, we introduce the 2-D acquisition manifold $Y = \Sigma \times \mathbb{R}_{\geq 0} \ni (\boldsymbol{x}^s, \boldsymbol{x}^r, t)$, where t is time. The significance of the superscript (i) on $T^{(i)}$ is in the case of multivaluedness of two-way travel time in the presence of caustics. In that case $i \in I$ labels the branches of the two-way travel time and I is the collection of them. The set $\{T^{(i)}\}_{i \in I}$ describes the two-way travel times for all branches. Each $T^{(i)}$ is defined on a subset $D^{(i)}$ of $\Sigma \times X$, i.e. a particular subset of acquisition and scattering points $(\boldsymbol{x}^s, \boldsymbol{x}^r, \boldsymbol{x})$. In a generic inhomogeneous medium, caustics will form. Figure 2.4 shows an example of multivaluedness: a triplication in the recorded wave field, the dotted plane indicating how this is recorded for a single source. The branches are assigned a number to separate them indicated on the travel time functions $T^{(1)}$, $T^{(2)}$, $T^{(3)}$. We will omit this indexing of the branches for clarity of notation until the distinction becomes important again (see the discussion on artifacts). The sum over the different travel time branches in equation (2.9) will thus be suppressed and assumed implicit in the following.

The amplitudes, $A^{\|}(\boldsymbol{x}^s, \boldsymbol{x})$ and $A^{\|}(\boldsymbol{x}, \boldsymbol{x}^r)$, are the GRA amplitudes (see equation (2.5)) with only the in-plane geometrical spreading factor $Q_2^{\|}$, for example

$$A^{\|}(\boldsymbol{x}, \boldsymbol{x}^s) = \frac{e^{-\mathrm{i}\frac{\pi}{2}\kappa(\boldsymbol{x}\ ,\boldsymbol{x}^{\ s})\operatorname{sgn}\omega}}{4\pi[\rho(\boldsymbol{x})v^s(\boldsymbol{x})\rho(\boldsymbol{x}^s)v(\boldsymbol{x}^s)]^{1/2}|Q_2^{\|}(\boldsymbol{x}, \boldsymbol{x}^s)|^{1/2}}. \tag{2.11}$$

The two-way out-of-plane geometrical spreading is given by

$$\mathcal{L}^{\perp}(\boldsymbol{x}^r, \boldsymbol{x}, \boldsymbol{x}^s) = |Q_2^{\perp}(\boldsymbol{x}^s, \boldsymbol{x}) + Q_2^{\perp}(\boldsymbol{x}, \boldsymbol{x}^r)|^{1/2}. \tag{2.12}$$

The out-of-plane geometrical spreading $Q_2^{\perp}$ for the source ray, for example, can be expressed as

$$Q_2^{\perp}(\boldsymbol{x}^s, \boldsymbol{x}) = \int_{ray} \frac{V_2}{p_2} \mathrm{d}t, \tag{2.13}$$

where the integral is along the ray parametrized by travel time t connecting $\boldsymbol{x}^s$ with $\boldsymbol{x}$. The integrand V_2/p_2 tends to a value as both V_2, p_2 tend to zero (in accordance with the 2.5-D approach, where $p_2 = 0$, $V_2 = 0$). Closed form expressions for the integrand for isotropic, transversely isotropic and orthorhombic media can be found in Ettrich *et al.* (2002), equations (15), (19) and (22), respectively. The medium perturbations are collected in the matrix $\mathbf{c}^{(1)}(\boldsymbol{x})$ and the radiation patterns equivalently in $\mathbf{w}(\boldsymbol{x}^r, \boldsymbol{x}, \boldsymbol{x}^s)$. They will be defined in the next subsection.

Remark 1 *We restrict our analysis to the part of phase space where out-of-plane caustics do not occur. Thus we mute events associated with rays forming out-of-plane caustics (see Remark 4 in the appendix).*

2.2.2.1 Medium perturbations and radiation patterns

Since by assumption 1, the medium is restricted to monoclinic or higher symmetry, there are at most 13 stiffness parameters plus density as independent unknown distributions. The stiffness tensor is given by (if the (x_1, x_3)-plane is the symmetry plane):

$$[c_{ijkl}] = \begin{bmatrix} c_{1111} & c_{1122} & c_{1133} & 0 & c_{1113} & 0 \\ c_{1122} & c_{2222} & c_{2233} & 0 & c_{2213} & 0 \\ c_{1133} & c_{2233} & c_{3333} & 0 & c_{3313} & 0 \\ 0 & 0 & 0 & c_{2323} & 0 & c_{2312} \\ c_{1113} & c_{2213} & c_{3313} & 0 & c_{1313} & 0 \\ 0 & 0 & 0 & c_{1223} & 0 & c_{1212} \end{bmatrix}. \tag{2.14}$$

The medium perturbations are collected in the 14×1 matrix for monoclinic anisotropy (Burridge *et al.*, 1998)

$$\mathbf{c}^{(1)}(\boldsymbol{x}) = \left\{ \frac{\rho^{(1)}(\boldsymbol{x})}{\rho^{(0)}(\boldsymbol{x})}, \frac{c_{ijkl}^{(1)}(\boldsymbol{x})}{\rho^{(0)}(\boldsymbol{x}) v_\circ^s(\boldsymbol{x}) v_\circ^r(\boldsymbol{x})} \right\}, \tag{2.15}$$

where $v_\circ^s$ and $v_\circ^r$ are local phase velocities averaged over all phase angles. These are introduced for computational purposes so that the matrix has components of similar magnitude

(Burridge *et al.*, 1998). We restrict the indices of $c^{(1)}_{ijkl}$ to the 13 independent components of the stiffness tensor (cf. (12)). With higher symmetry, such as isotropy, the matrix reduces accordingly (Beylkin & Burridge, 1990). The radiation pattern matrix is defined similarly as the 14×1 matrix (Burridge *et al.*, 1998)

$$\mathbf{w}(\boldsymbol{x}^r, \boldsymbol{x}, \boldsymbol{x}^s) = \left\{h^s_m(\boldsymbol{x})h^r_m(\boldsymbol{x}), [h^s_i(\boldsymbol{x})p^s_j(\boldsymbol{x})h^r_k(\boldsymbol{x})p^r_l(\boldsymbol{x})]v^s_\circ(\boldsymbol{x})v^r_\circ(\boldsymbol{x})\right\}, \tag{2.16}$$

where the indices follow those of the stiffness matrix in the ordering defined by the matrix or inner product $\mathbf{w}^T(\boldsymbol{x}^r, \boldsymbol{x}, \boldsymbol{x}^s)\mathbf{c}^{(1)}(\boldsymbol{x})$ in the modelling equation (2.9). Since the out-of-plane slowness will be zero, $p^s_2 = p^r_2 = 0$, we see from equation (2.16) that the contribution vanishes if $j, l = 2$ in $c^{(1)}_{ijkl}$. In view of assumptions 1 and 2, having $p^s_2 = p^r_2 = 0$, the polarizations of qP and qSV waves satisfy $h_2 = 0$. Thus the parameters we can invert for from qP-qP and qP-qSV scattering are the 7 parameters out of the 14 independent ones in a monoclinic medium, $c^{(1)}_{1111}, c^{(1)}_{1133}, c^{(1)}_{3333}, c^{(1)}_{1113}, c^{(1)}_{3313}, c^{(1)}_{1313}$ and density $\rho^{(1)}$ ($h_2 = 0$, and hence the contributions for $i, k = 2$ in $c^{(1)}_{ijkl}$ are zero). The kinematic aspects for a monoclinic background medium are governed by the same partitioning of parameters (Chapman & Pratt, 1992; Foss & Ursin, 2004).

Remark 2 *In imaging, the smooth background medium is given, and hence the relevant amplitudes can be computed in the lowest possible symmetry admitted by the 2.5-D framework: monoclinic. However, for inversion and reflection tomography, having observations restricted to the plane under consideration, only parameters associated with this plane can be estimated. Hence the lowest possible symmetry is transversely isotropic with a symmetry axis in the plane. Due to the rotational symmetry of the medium, parameters needed in out-of-plane amplitude calculations are found from in-plane propagation (Ettrich* et al.*, 2002, ; equation (19)).*

2.2.3 The modelling operator in common azimuth

The 3-D Born modelling operator has been shown to be a Fourier integral operator (FIO) under the mild conditions that there are no direct rays between the source and the receiver reaching the medium perturbation (i.e. rays that have scattered off a subsurface point over an angle π) and no grazing rays (i.e. rays that reach the acquisition surface tangentially to the surface) (Rakesh, 1988; Hansen, 1991). The 3-D modelling operator with common azimuth (CA) acquisition geometry (Biondi & Palacharla, 1996) is also an FIO under similar conditions (Nolan & Symes, 1997; de Hoop *et al.*, 2003b). 2.5-D implies CA (but

not the other way) aligning our symmetry plane with the acquisition geometry, i.e. $x_2^s = x_2^r$. We conclude that the 2.5-D modelling operator (2.9) has the properties of a FIO, and has the following canonical relation (superscript S indicates that this is a canonical relation in two space dimensions coinciding with the symmetry plane)

$$\Lambda_L^S = \{(\boldsymbol{x}^s(\boldsymbol{x},\boldsymbol{\alpha}^s), \boldsymbol{x}^r(\boldsymbol{x},\boldsymbol{\alpha}^r), T(\boldsymbol{x}^s(\boldsymbol{x},\boldsymbol{\alpha}^s), \boldsymbol{x}, \boldsymbol{x}^r(\boldsymbol{x},\boldsymbol{\alpha}^r)), \boldsymbol{k}^s(\boldsymbol{x},\boldsymbol{\alpha}^s,\omega), \boldsymbol{k}^r(\boldsymbol{x},\boldsymbol{\alpha}^r,\omega), \omega; \\ \boldsymbol{x}, -\boldsymbol{k}(\boldsymbol{x}^s(\boldsymbol{x},\boldsymbol{\alpha}^s), \boldsymbol{x}, \boldsymbol{x}^r(\boldsymbol{x},\boldsymbol{\alpha}^r),\omega)) | (\boldsymbol{x},\boldsymbol{\alpha}^s,\boldsymbol{\alpha}^r) \in K, \omega \in \mathbb{R} \setminus 0\}\,. \quad (2.17)$$

The canonical relation is a table that describes how reflectors induce reflections geometrically. The canonical relation is intimately connected to ray tracing in phase space (Billette & Lambaré, 1998). $\boldsymbol{\alpha}^s(\boldsymbol{x})$ and $\boldsymbol{\alpha}^r(\boldsymbol{x})$ are the take-off directions of the rays originating at the scattering point $\boldsymbol{x} \in X$ and are given by the unit phase vectors $\boldsymbol{\alpha}^s(\boldsymbol{x}) = \boldsymbol{p}^s(\boldsymbol{x})/|\boldsymbol{p}^s(\boldsymbol{x})|$ and $\boldsymbol{\alpha}^r(\boldsymbol{x}) = \boldsymbol{p}^r(\boldsymbol{x})/|\boldsymbol{p}^r(\boldsymbol{x})|$ (see Figure 2.5). K is an appropriately chosen subset of $X \times S^1 \times S^1$ (S^1 is the unit circle). On the canonical relation (2.17) $\boldsymbol{k}(\boldsymbol{x}^s(\boldsymbol{x},\boldsymbol{\alpha}^s), \boldsymbol{x}, \boldsymbol{x}^r(\boldsymbol{x},\boldsymbol{\alpha}^r),\omega) = \omega\nabla_{\boldsymbol{x}}\, T(\boldsymbol{x}^s(\boldsymbol{x},\boldsymbol{\alpha}^s), \boldsymbol{x}, \boldsymbol{x}^r(\boldsymbol{x},\boldsymbol{\alpha}^r))$ has the interpretation of wave vector (the Fourier dual of $\boldsymbol{x}$). Given a take-off direction ($\boldsymbol{\alpha}^s$ or $\boldsymbol{\alpha}^r$) at a scattering point $\boldsymbol{x}$, rays are traced to an acquisition line giving unique intersection points ($\boldsymbol{x}^s = \boldsymbol{x}^s(\boldsymbol{x},\boldsymbol{\alpha}^s)$ or $\boldsymbol{x}^r = \boldsymbol{x}^r(\boldsymbol{x},\boldsymbol{\alpha}^r)$) as well as slowness vectors; these slowness vectors are projected onto the aforementioned acquisition line resulting into $\boldsymbol{k}^s/\omega$, $\boldsymbol{k}^r/\omega$, from which $\boldsymbol{k}^s(\boldsymbol{x},\boldsymbol{\alpha}^s,\omega)$, $\boldsymbol{k}^r(\boldsymbol{x},\boldsymbol{\alpha}^r,\omega)$ are derived.

Remark 3 *The 3-D CA Born scattering operator yields the following canonical relation (compare with the 2.5-D Born modelling operator above in equation (2.17))*

$$\Lambda_L^{CA} = \{(x_1^s, x_2^s, x_1^r, t, k_1^s, k_2^s + k_2^r, k_1^r, \omega; x_1, x_2, x_3, -k_1, -k_2, -k_3)\}\,, \quad (2.18)$$

where $(x_1^s, x_2^s, x_1^r, x_2^s, t, k_1^s, k_2^s, k_1^r, k_2^r, \omega; x_1, x_2, x_3, -k_1, -k_2, -k_3)$ *are contained in the Born modelling 3-D canonical relation* Λ_L^{3D} *which is the counterpart of* Λ_L^S *in three space dimensions (e.g. Stolk and de Hoop (2002)). Note that* t *is here a general two-way travel time function in order to separate it from the one in equation (2.10) which is limited to a plane. Due to the translational invariance of the medium, assumption 1a), the individual* k_2^s *and* k_2^r *are preserved. Hence at the scattering point* $k_2 = k_2^s + k_2^r$*, in which* k_2^s *and* k_2^r *attain their values at the source and the receiver, respectively. This equality can also be written as* $k_2 = \omega(p_2^s + p_2^r)$*. In view, again, of the invariance in the out-of-plane direction the 2-component of any reflector dips must vanish. Hence, given a source and a receiver ray such that* $k_2^s + k_2^r \neq 0$*, no specular reflection will return to the acquisition manifold.*

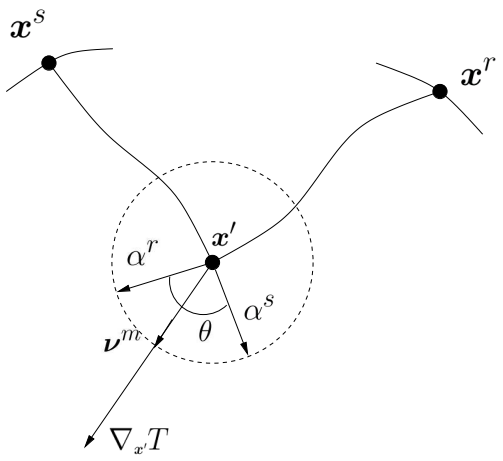

Figure 2.5: Coordinate systems.

This is also confirmed by the stationary phase argument underlying the 2.5-D analysis, see equation (2.7).

The modelling operator maps the medium perturbation to the data

$$\mathbf{L} : \mathbf{c}^{(1)} \rightarrow u_{mn}. \tag{2.19}$$

2.3 2.5-D imaging - inversion

In this section, we develop the inversion for the medium parameters collected in the matrix $\mathbf{c}^{(1)}$ in equation (2.15). The inversion can be viewed as an analogue to matrix least-squares inversion. In this context, we introduce the adjoint, $\mathbf{L}^\star$, of the forward operator the so-called *imaging operator*, and apply it to equation (2.9),

$$\mathbf{L}^\star(\psi \mathbf{L}\mathbf{c}^{(1)}) = \mathbf{L}^\star u, \tag{2.20}$$

where u is shorthand for the data (indices are suppressed, see the discussion below). The composition of the imaging with the forward operator gives us the *normal operator*, $\mathbf{N} = \mathbf{L}^\star\psi\mathbf{L}$. The operator $\mathbf{L}^\star$ images reflectors properly if $\mathbf{L}^\star\psi\mathbf{L}$ is a pseudodifferential operator (Stolk & de Hoop, 2002). Here ψ is a pseudodifferential cutoff ('tapered mute') to ensure that the mild conditions of subsection 2.2.3, making the modelling operator an FIO, are satisfied. In the following we will refer to $\mathbf{L}^\star\psi\mathbf{L}$ as the normal operator $\mathbf{N}$ where ψ is assumed implicitly.

Assumption 3 *The projection of the canonical relation Λ_L^S of the 2.5-D modelling operator on the acquisition variables $(\boldsymbol{x}^s, \boldsymbol{x}^r, t, \boldsymbol{k}^s, \boldsymbol{k}^r, \omega)$ is one-to-one.*

This assumption is consistent with a 2-D Bolker condition (Guillemin, 1985), for the acoustic case see Ten Kroode *et al.* (1998). It means that $(\boldsymbol{x}^s, \boldsymbol{x}^r, t, \boldsymbol{k}^s, \boldsymbol{k}^r, \omega)$ determine a scattering point $\boldsymbol{x} \in X$ and associated wave vector $\boldsymbol{k}$, uniquely and smoothly. This condition ensures that the normal operator is an elliptic pseudodifferential operator. Hence the procedure of imaging the modelled data, equation (2.20), does not generate reflectors that were not there to begin with, i.e. that are not present in $\mathbf{c}^{(1)}$.

Since $\mathbf{N}$ is elliptic and pseudodifferential we can construct its parametrix, denoted by $\langle \mathbf{N}^{-1} \rangle$. The brackets indicate that this is a pseudo inverse. Following the analogue of least-squares inversion, an estimate of the medium perturbation in equation (2.15) can be recovered from the composition

$$\hat{\mathbf{c}}^{(1)} \approx \langle \mathbf{N}^{-1} \rangle \mathbf{L}^{\star} u, \tag{2.21}$$

where u is the data. If assumption 3 is violated we generate artifacts (discussed in the introduction). A less restrictive condition and a discussion of the implied artifacts can be found in de Hoop and Brandsberg-Dahl (2000) and Stolk (2000).

In view of Remark 3, assumption 3 (or the 2-D Bolker condition) in the symmetry plane implies the 3-D CA Bolker condition. This condition encompasses that for any point in Λ_L^{CA}, i.e., for an intersecting pair of source and receiver rays, given $(x_1^s, x_2^s, x_1^r, x_2^s, t, k_1^s, k_2^s + k_2^r, k_1^r, \omega)$, there is only one (t, k_2^s) that explains the reflection.

2.3.1 The adjoint scattering (imaging) and the normal operators

In this subsection, we evaluate the adjoint $\mathbf{L}^{\star}$ of the modelling operator $\mathbf{L}$ and deduce the leading order contribution to the normal operator $\mathbf{N}$ for which we can derive a parametrix. We will write the action of the normal operator as a pseudodifferential operator, i.e. as integrals over $\boldsymbol{x}$ and its Fourier dual $\boldsymbol{k}$, the wave vector. The inverse of the integrand thus obtained (the integrand yields the so-called *symbol* of the normal operator) generates the 'inverse' of the normal operator up to leading order.

We let the acquisition coordinates be defined on the two acquisition lines in the symmetry plane, ∂S and ∂R for sources and receivers, respectively. By the reciprocity theorem of the time-correlation type found in de Hoop and de Hoop (1997) the adjoint or imaging

operator $\mathbf{L}^\star$ can be written

$$\mathbf{L}^\star u(\boldsymbol{x}') \approx \frac{1}{\sqrt{2\pi\mathrm{i}}} \int_{\partial S\times\partial R}\int_{\mathbb{R}}\int_{\mathbb{R}\geq 0} \omega'^{3/2}\rho^{(0)}(\boldsymbol{x}')\frac{(A^{\shortparallel}(\boldsymbol{x}^s,\boldsymbol{x}')A^{\shortparallel}(\boldsymbol{x}',\boldsymbol{x}^r))^\star}{\mathcal{L}^\perp(\boldsymbol{x}^r,\boldsymbol{x}',\boldsymbol{x}^s)^\star}$$
$$\cdot\,\mathbf{w}(\boldsymbol{x}^r,\boldsymbol{x}',\boldsymbol{x}^s)h_m(\boldsymbol{x}^r;\boldsymbol{x}')u_{mn}(\boldsymbol{x}^s,\boldsymbol{x}^r,t)h_n(\boldsymbol{x}^s;\boldsymbol{x}')e^{-\mathrm{i}\omega'(T(\boldsymbol{x}^r,\boldsymbol{x}',\boldsymbol{x}^s)-t)}\mathrm{d}t\mathrm{d}\omega'\mathrm{d}\boldsymbol{x}^s\mathrm{d}\boldsymbol{x}^r, \quad (2.22)$$

where ω' is the frequency and * indicates the adjoint as well as complex conjugation. The polarization vectors associated with the scattering off the point $\boldsymbol{x}'$ are denoted by $h_m(\boldsymbol{x}^r;\boldsymbol{x}')$ and $h_n(\boldsymbol{x}^s;\boldsymbol{x}')$ to distinguish them from the polarization vectors due to the scattering off $\boldsymbol{x}$ as in equation (2.9). Note that there is a summation over the different indices of the data u_{mn} in the integrand of the adjoint, following the summation convention. Hence the notation of $\mathbf{L}^\star$ acting on all the data denoted by u. Note also that $\mathbf{w} = (\mathbf{w}^T)^\star$.

Composing the imaging operator with the modelling operator (having used a pseudodifferential cutoff for when it fails to satisfy assumption 3) gives us the normal operator. The u_{mn} from the modelling equation (2.9) is inserted into the above expression to yield

$$\mathbf{L}^\star\psi\mathbf{L}\mathbf{c}^{(1)}(\boldsymbol{x}') \approx$$
$$\frac{1}{2\pi}\int_{\partial S\times\partial R}\int_X\int_{\mathbb{R}}\int_{\mathbb{R}}\int_{\mathbb{R}\geq 0}\omega'^{3/2}\omega^{3/2}\rho^{(0)}(\boldsymbol{x}')\rho^{(0)}(\boldsymbol{x})\frac{(A^{\shortparallel}(\boldsymbol{x}^s,\boldsymbol{x}')A^{\shortparallel}(\boldsymbol{x}',\boldsymbol{x}^r))^\star}{\mathcal{L}^\perp(\boldsymbol{x}^r,\boldsymbol{x}',\boldsymbol{x}^s)^\star}\frac{A^{\shortparallel}(\boldsymbol{x}^s,\boldsymbol{x})A^{\shortparallel}(\boldsymbol{x},\boldsymbol{x}^r)}{\mathcal{L}^\perp(\boldsymbol{x}^r,\boldsymbol{x}',\boldsymbol{x}^s)}$$
$$\cdot\, e^{\mathrm{i}\omega(T(\boldsymbol{x}^r,\boldsymbol{x},\boldsymbol{x}^s)-t)-\mathrm{i}\omega'(T(\boldsymbol{x}^r,\boldsymbol{x}',\boldsymbol{x}^s)-t)}\mathrm{d}t\mathrm{d}\omega\mathrm{d}\omega'\mathrm{d}\boldsymbol{x}\mathrm{d}\boldsymbol{x}^s\mathrm{d}\boldsymbol{x}^r. \quad (2.23)$$

If assumption 3 is satisfied it is indeed an elliptic pseudodifferential operator. The integral over t yields a delta function $\delta(\omega-\omega')$ so we can collapse the integral over ω' and set $\omega = \omega'$. Invoking a Taylor expansion about $\boldsymbol{x}'$ for the two-way travel time $T(\boldsymbol{x}^r,\boldsymbol{x},\boldsymbol{x}^s)$ yields, due to the fact that higher order derivatives give smoother contributions to the amplitude (Hörmander, 1983) through expansion of the exponential,

$$\omega[T(\boldsymbol{x}^r,\boldsymbol{x},\boldsymbol{x}^s) - T(\boldsymbol{x}^r,\boldsymbol{x}',\boldsymbol{x}^s)] = \omega[(\nabla_{\boldsymbol{x}'}T)(\boldsymbol{x}^r,\boldsymbol{x}',\boldsymbol{x}^s)\cdot(\boldsymbol{x}-\boldsymbol{x}')] + \ldots. \quad (2.24)$$

Inserting (2.24) in the phase function of the normal operator yields

$$\mathbf{N}\mathbf{c}^{(1)}(\boldsymbol{x}') \approx \int_{\partial S\times\partial R}\int_X\int_{\mathbb{R}}\omega^3\rho^{(0)}(\boldsymbol{x}')\rho^{(0)}(\boldsymbol{x})\frac{(A^{\shortparallel}(\boldsymbol{x}^s,\boldsymbol{x}')A^{\shortparallel}(\boldsymbol{x}',\boldsymbol{x}^r))^\star}{\mathcal{L}^\perp(\boldsymbol{x}^r,\boldsymbol{x}',\boldsymbol{x}^s)^\star}\frac{A^{\shortparallel}(\boldsymbol{x}^s,\boldsymbol{x})A^{\shortparallel}(\boldsymbol{x},\boldsymbol{x}^r)}{\mathcal{L}^\perp(\boldsymbol{x}^r,\boldsymbol{x}',\boldsymbol{x}^s)}$$
$$\cdot\,\mathbf{w}(\boldsymbol{x}^r,\boldsymbol{x}',\boldsymbol{x}^s)\mathbf{w}^T(\boldsymbol{x}^r,\boldsymbol{x},\boldsymbol{x}^s)\mathbf{c}^{(1)}(\boldsymbol{x})h_m(\boldsymbol{x}^r)h_m(\boldsymbol{x}^r;\boldsymbol{x}')h_n(\boldsymbol{x}^s)h_n(\boldsymbol{x}^s;\boldsymbol{x}')$$
$$\cdot\, e^{\mathrm{i}\omega\nabla_{\boldsymbol{x}'}T(\boldsymbol{x}^r,\boldsymbol{x}',\boldsymbol{x}^s)\cdot(\boldsymbol{x}-\boldsymbol{x}')}\mathrm{d}\omega\mathrm{d}\boldsymbol{x}\mathrm{d}\boldsymbol{x}^s\mathrm{d}\boldsymbol{x}^r. \quad (2.25)$$

The most dominant contribution to the oscillatory integral (2.25) occurs when $\boldsymbol{x}$ and $\boldsymbol{x}'$ are near one another making up a small neighbourhood of support (Beylkin, 1985). Additionally, the amplitudes, polarization vectors and the radiation patterns vary slowly

compared to any other part of the integrand. We may then assume that they are constant in a small neighbourhood of $\boldsymbol{x}'$. Since the polarization vectors are normalized we obtain

$$\mathbf{Nc}^{(1)}(\boldsymbol{x}') \approx \int_{\partial S\times\partial R}\int_X\int_{\mathbb{R}} \omega^3\rho^{(0)}(\boldsymbol{x}')^2\frac{|A^{||}(\boldsymbol{x}^s,\boldsymbol{x}')A^{||}(\boldsymbol{x}',\boldsymbol{x}^r))|^2}{|\mathcal{L}^\perp(\boldsymbol{x}^r,\boldsymbol{x}',\boldsymbol{x}^s)|^2} \cdot \mathbf{w}(\boldsymbol{x}^r,\boldsymbol{x}',\boldsymbol{x}^s)\mathbf{w}^T(\boldsymbol{x}^r,\boldsymbol{x}',\boldsymbol{x}^s)\mathbf{c}^{(1)}(\boldsymbol{x})e^{\mathrm{i}\omega\nabla_{\boldsymbol{x}'}T(\boldsymbol{x}^r,\boldsymbol{x}',\boldsymbol{x}^s)\cdot(\boldsymbol{x}-\boldsymbol{x}')}\mathrm{d}\omega\mathrm{d}\boldsymbol{x}\mathrm{d}\boldsymbol{x}^s\mathrm{d}\boldsymbol{x}^r. \quad (2.26)$$

2.3.1.1 Subsurface coordinates

We choose to work with coordinates directly at the imaging point $\boldsymbol{x}'$ and introduce the change of variables

$$(\boldsymbol{x}',\boldsymbol{x}^s,\boldsymbol{x}^r) \leftarrow (\boldsymbol{x}',\boldsymbol{\alpha}^s,\boldsymbol{\alpha}^r), \quad (2.27)$$

where $\boldsymbol{\alpha}^s$ and $\boldsymbol{\alpha}^r$ are the phase directions associated with the rays connecting the image point and the source and receiver, respectively (see Figure 2.5). The right implication is also true, but in the case of multipathing per branch only (see subsection 2.2.2). This transformation removes the use of the Beylkin determinant (de Hoop *et al.*, 1999). It also unfolds caustics (de Hoop & Brandsberg-Dahl, 2000) through well-defined mappings from the scattering point to the acquisition manifold. The domains of integration then become

$$\partial S\times\partial R \longleftarrow\!\!\shortmid\; S^s\times S^r \text{ for given } \boldsymbol{x}'. \quad (2.28)$$

Here S^s and S^r are two unit circles in the symmetry plane for the sources and receivers, respectively. We introduce the extended Jacobian

$$\mathcal{J}(\boldsymbol{\alpha}^r,\boldsymbol{x}',\boldsymbol{\alpha}^s) = |\rho^{(0)}(\boldsymbol{x}')A^{||}(\boldsymbol{x}^s,\boldsymbol{x}')A^{||}(\boldsymbol{x}',\boldsymbol{x}^r)|^2\frac{\partial(\boldsymbol{x}^s,\boldsymbol{x}^r)}{\partial(\boldsymbol{\alpha}^s,\boldsymbol{\alpha}^r)}, \quad (2.29)$$

and change the coordinates through the mapping in equation (2.27) in all relevant places in the following. The in-plane geometrical spreading of $A^{||}$ and the Jacobian cancel each other up to projection factors. Using the expression for the extended Jacobian in equation (2.26) yields

$$\mathbf{Nc}^{(1)}(\boldsymbol{x}') \approx \int_{S^s\times S^r}\int_X\int_{\mathbb{R}} \frac{\omega^3}{|\mathcal{L}^\perp(\boldsymbol{\alpha}^r,\boldsymbol{x}',\boldsymbol{\alpha}^s)|^2}\mathbf{w}(\boldsymbol{\alpha}^r,\boldsymbol{x}',\boldsymbol{\alpha}^s)\mathbf{w}^T(\boldsymbol{\alpha}^r,\boldsymbol{x}',\boldsymbol{\alpha}^s) \cdot \mathbf{c}^{(1)}(\boldsymbol{x})e^{\mathrm{i}\omega\nabla_{\boldsymbol{x}'}T(\boldsymbol{\alpha}^r,\boldsymbol{x}',\boldsymbol{\alpha}^s)\cdot(\boldsymbol{x}-\boldsymbol{x}')}\mathcal{J}(\boldsymbol{\alpha}^r,\boldsymbol{x}',\boldsymbol{\alpha}^s)\mathrm{d}\omega\mathrm{d}\boldsymbol{x}\mathrm{d}\boldsymbol{\alpha}^s\mathrm{d}\boldsymbol{\alpha}^r. \quad (2.30)$$

In accordance with the reasoning in subsection 2.3.1 we write equation (2.30) as an integral over $\boldsymbol{x}$ and its Fourier dual $\boldsymbol{k} = \omega\nabla_{\boldsymbol{x}'}T$, i.e. in the form of a pseudodifferential operator. We introduce a new frequency $\bar{\omega} = \omega|\nabla_{\boldsymbol{x}'}T|$. Then $\omega\nabla_{\boldsymbol{x}'}T = \bar{\omega}\boldsymbol{\nu}^m$, where

$\boldsymbol{\nu}^m = \nabla_{\boldsymbol{x}'} T/|\nabla_{\boldsymbol{x}'} T|$ is the migration dip and is a function of $\boldsymbol{\alpha}^r, \boldsymbol{x}', \boldsymbol{\alpha}^s$. With the appropriate substitution this yields

$$\mathbf{Nc}^{(1)}(\boldsymbol{x}') \approx \int_{S^s\times S^r}\int_X\int_{\mathbb{R}} \frac{|\nabla_{\boldsymbol{x}'} T(\boldsymbol{\alpha}^r, \boldsymbol{x}', \boldsymbol{\alpha}^s)|^{-4}\bar{\omega}^3}{|\mathcal{L}^\perp(\boldsymbol{\alpha}^r, \boldsymbol{x}', \boldsymbol{\alpha}^s)|^2}\mathbf{w}(\boldsymbol{\alpha}^r, \boldsymbol{x}', \boldsymbol{\alpha}^s)\mathbf{w}^T(\boldsymbol{\alpha}^r, \boldsymbol{x}', \boldsymbol{\alpha}^s) \cdot \mathbf{c}^{(1)}(\boldsymbol{x})e^{\mathrm{i}\bar{\omega}\boldsymbol{\nu}^a\,(\boldsymbol{\alpha}^r,\boldsymbol{x}',\boldsymbol{\alpha}^s)\cdot(\boldsymbol{x}-\boldsymbol{x}')}\mathcal{J}(\boldsymbol{\alpha}^r, \boldsymbol{x}', \boldsymbol{\alpha}^s)\mathrm{d}\bar{\omega}\mathrm{d}\boldsymbol{x}\mathrm{d}\boldsymbol{\alpha}^s\mathrm{d}\boldsymbol{\alpha}^r. \quad (2.31)$$

Defining

$$\mu_{LS}(\boldsymbol{\alpha}^r, \boldsymbol{x}', \boldsymbol{\alpha}^s) = \frac{\mathcal{J}(\boldsymbol{\alpha}^r, \boldsymbol{x}', \boldsymbol{\alpha}^s)}{|\nabla_{\boldsymbol{x}'} T(\boldsymbol{\alpha}^r, \boldsymbol{x}', \boldsymbol{\alpha}^s)|^4}, \quad (2.32)$$

results in the simplified expression

$$\mathbf{Nc}^{(1)}(\boldsymbol{x}') \approx \int_{S^s\times S^r}\int_X\int_{\mathbb{R}} \bar{\omega}^3\frac{\mu_{LS}(\boldsymbol{\alpha}^r, \boldsymbol{x}', \boldsymbol{\alpha}^s)}{|\mathcal{L}^\perp(\boldsymbol{\alpha}^r, \boldsymbol{x}', \boldsymbol{\alpha}^s)|^2}\mathbf{w}(\boldsymbol{\alpha}^r, \boldsymbol{x}', \boldsymbol{\alpha}^s)\mathbf{w}^T(\boldsymbol{\alpha}^r, \boldsymbol{x}', \boldsymbol{\alpha}^s) \cdot \mathbf{c}^{(1)}(\boldsymbol{x})e^{\mathrm{i}\bar{\omega}\boldsymbol{\nu}^a\,(\boldsymbol{\alpha}^r,\boldsymbol{x}',\boldsymbol{\alpha}^s)\cdot(\boldsymbol{x}-\boldsymbol{x}')}\mathrm{d}\bar{\omega}\mathrm{d}\boldsymbol{x}\mathrm{d}\boldsymbol{\alpha}^s\mathrm{d}\boldsymbol{\alpha}^r. \quad (2.33)$$

2.3.1.2 Migration dip, scattering angle and the leading order contribution

We change variables again, from the phase angles to scattering angle θ, which is the angle between $\boldsymbol{\alpha}^s$ and $\boldsymbol{\alpha}^r$, and the migration dip $\boldsymbol{\nu}^m$ (see Figure 2.5). The scattering angle follows to be

$$\theta = \theta(\boldsymbol{\alpha}^r, \boldsymbol{x}', \boldsymbol{\alpha}^s) = \arccos(\boldsymbol{\alpha}^s \cdot \boldsymbol{\alpha}^r). \quad (2.34)$$

To be able to integrate over the migration dip, there is assumed to be no scattering over $\theta = \pi$ so that $\nabla_{\boldsymbol{x}'} T \neq 0$ and $\boldsymbol{\nu}^m$ is defined. We have

$$(\boldsymbol{x}', \boldsymbol{\alpha}^s, \boldsymbol{\alpha}^r) \leftrightarrows (\boldsymbol{x}', \boldsymbol{\nu}^m, \theta). \quad (2.35)$$

In 2.5-D this mapping exists both ways; there is no integration over the azimuth (de Hoop & Brandsberg-Dahl, 2000). The domains of integration can now be written as

$$S^s \times S^r \longrightarrow E_{\boldsymbol{\nu}^a} \times E_\theta \text{ for given } \boldsymbol{x}'. \quad (2.36)$$

Changing all relevant coordinates under the mapping in equation (2.35) and collecting the integration over the scattering angle θ yields

$$\mathbf{Nc}^{(1)}(\boldsymbol{x}') \approx \int_{E_{\boldsymbol{\nu}^a}}\int_{\mathbb{R}}\int_X \bar{\omega}^3\left\{\int_{E_\theta}\frac{\mu_{LS}(\boldsymbol{x}', \boldsymbol{\nu}^m, \theta)}{|\mathcal{L}^\perp(\boldsymbol{x}', \boldsymbol{\nu}^m, \theta)|^2} \cdot \mathbf{w}(\boldsymbol{x}', \boldsymbol{\nu}^m, \theta)\mathbf{w}^T(\boldsymbol{x}', \boldsymbol{\nu}^m, \theta)\frac{\partial(\boldsymbol{\alpha}^s, \boldsymbol{\alpha}^r)}{\partial(\boldsymbol{\nu}^m, \theta)}\mathrm{d}\theta\right\}\mathbf{c}^{(1)}(\boldsymbol{x})e^{\mathrm{i}\bar{\omega}\boldsymbol{\nu}^a\cdot(\boldsymbol{x}-\boldsymbol{x}')}\mathrm{d}\boldsymbol{x}\mathrm{d}\bar{\omega}\mathrm{d}\boldsymbol{\nu}^m. \quad (2.37)$$

We introduce the square matrix (of the dimensionality of $\mathbf{w}$)

$$\Gamma(\boldsymbol{x}', \boldsymbol{\nu}^m) = \frac{1}{2}\int_{E_\theta} \frac{\mu_{LS}(\boldsymbol{x}', \boldsymbol{\nu}^m, \theta)}{|\mathcal{L}^\perp(\boldsymbol{x}', \boldsymbol{\nu}^m, \theta)|^2}\mathbf{w}(\boldsymbol{x}', \boldsymbol{\nu}^m, \theta)\mathbf{w}^T(\boldsymbol{x}', \boldsymbol{\nu}^m, \theta)\frac{\partial(\boldsymbol{\alpha}^s, \boldsymbol{\alpha}^r)}{\partial(\boldsymbol{\nu}^m, \theta)}\mathrm{d}\theta + (\ldots)(\boldsymbol{x}', -\boldsymbol{\nu}^m), \quad (2.38)$$

where the second term is the same as the first but with $\boldsymbol{\nu}^m$ replaced by $-\boldsymbol{\nu}^m$. This enables us to rewrite equation (2.37) with positive $\bar{\omega}$ only as

$$\mathbf{N}\mathbf{c}^{(1)}(\boldsymbol{x}') \approx \frac{1}{(2\pi)^2}\int_{E_{\boldsymbol{\nu}^a}}\int_{\mathbb{R}\geq 0}\int_X \bar{\omega}^2 8\pi^2\Gamma(\boldsymbol{x}', \boldsymbol{\nu}^m)\mathbf{c}^{(1)}(\boldsymbol{x})e^{\mathrm{i}\bar{\omega}\boldsymbol{\nu}^a\cdot(\boldsymbol{x}-\boldsymbol{x}')}\bar{\omega}\mathrm{d}\boldsymbol{x}\mathrm{d}\bar{\omega}\mathrm{d}\boldsymbol{\nu}^m. \quad (2.39)$$

This has now explicitly the form of a pseudodifferential operator with integration over $\boldsymbol{x}$ and its dual $\boldsymbol{k}$ through the identification $\boldsymbol{k} = \bar{\omega}\boldsymbol{\nu}^m$. We recognize here the leading order symbol, $\bar{\omega}^2 8\pi^2\Gamma(\boldsymbol{x}', \boldsymbol{\nu}^m)$, of $\mathbf{N}$. Note the differences when compared with the 3-D case found in de Hoop and Brandsberg-Dahl (2000): the out-of-plane geometrical spreading $\mathcal{L}^\perp$ naturally appears in the leading order symbol of the normal operator in equation (2.38) combined with the radiation patterns. Also the power of (2π) has been modified in accordance with the stationary phase calculation in 2.5-D.

2.3.2 Least-squares inversion

To leading order, the inverse normal operator composed with the normal operator from the last subsection should yield the identity. The departure from the identitity is due to taking the generalized inverse of and smoother contributions to the normal operator. We denote the generalized inverse of $\mathbf{N}$ by $\langle\mathbf{N}^{-1}\rangle$. The resolution is controlled by $\langle\mathbf{N}^{-1}\rangle\mathbf{N}$. General analysis of the resolution is given by de Hoop *et al* (1999) and for the 2.5-D case by Foss and Ursin (2004).

Note that

$$\frac{1}{(2\pi)^2}\int_{\mathbb{R}\geq 0}\int_{S^1} e^{\mathrm{i}\bar{\omega}\boldsymbol{\nu}^a\cdot(\boldsymbol{x}-\boldsymbol{x}')}\bar{\omega}\mathrm{d}\boldsymbol{\nu}^m\mathrm{d}\bar{\omega} = \delta(\boldsymbol{x}-\boldsymbol{x}'). \quad (2.40)$$

In view of limited illuminations, the support of $\bar{\omega}$ will be bounded while $\boldsymbol{\nu}^m \in E_{\boldsymbol{\nu}^a} \subset S^1$. Equation (2.40) becomes a band-limited delta function, $\delta_{BL}(\boldsymbol{x})$ (Bleistein, 1984). The kernel of the parametrix of $\mathbf{N}$ (we denote the kernel of $\mathbf{N}$ as $\mathcal{N}$) is found to be

$$\langle\mathcal{N}^{-1}\rangle(\boldsymbol{x}', \boldsymbol{x}) = \frac{1}{(2\pi)^2}\int_{\mathbb{R}\geq 0}\int_{E_{\boldsymbol{\nu}^a}} \bar{\omega}^{-2}\langle 8\pi^2\Gamma(\boldsymbol{x}', \boldsymbol{\nu}^m)\rangle^{-1}e^{\mathrm{i}\bar{\omega}\boldsymbol{\nu}^a\cdot(\boldsymbol{x}-\boldsymbol{x}')}\bar{\omega}\mathrm{d}\boldsymbol{\nu}^m\mathrm{d}\bar{\omega}. \quad (2.41)$$

Note that one of the $\bar{\omega}$ variables is placed with the integration variables since $(\bar{\omega}, \boldsymbol{\nu}^m)$ yield polar coordinates in $\boldsymbol{k}$-space. The composition of this kernel and the kernel of the normal

operator then becomes

$$\int \langle \mathcal{N}^{-1} \rangle(\boldsymbol{x}', \boldsymbol{y}) \mathcal{N}(\boldsymbol{y}, \boldsymbol{x}) \mathrm{d}\boldsymbol{y} \sim \delta_{BL}(\boldsymbol{x}' - \boldsymbol{x}) + \text{lower order terms.} \tag{2.42}$$

We replace $\boldsymbol{x}'$ with $\boldsymbol{x}$ in the imaging operator (2.22). The real part of the composition is symmetric in ω' while the imaginary part is odd and disappears. The integration over ω' then becomes one-sided by taking the real part and multiplying by 2 (de Hoop & Brandsberg-Dahl, 2000). Using equation (2.21) the least-squares estimate of the medium perturbation becomes

$$\begin{aligned}
&\hat{\mathbf{c}}^{(1)}(\boldsymbol{x}') = \langle \mathbf{N}^{-1} \rangle \mathbf{L}^{\star} u(\boldsymbol{x}') \\
&\approx \frac{-1}{(2\pi)^2} \frac{1}{\pi} \mathrm{Re} \Big\{ \int_X d\boldsymbol{x} \int_{\mathbb{R}\geq 0} \bar{\omega}^{-1} \mathrm{d}\bar{\omega} \int_{E_{\boldsymbol{\nu}^a}} \mathrm{d}\boldsymbol{\nu}^m \int_{\partial S \times \partial R} \mathrm{d}\boldsymbol{x}^s \mathrm{d}\boldsymbol{x}^r \int_{\mathbb{R}\geq 0} \mathrm{d}\omega' \langle 8\pi^2 \Gamma(\boldsymbol{x}', \boldsymbol{\nu}^m) \rangle^{-1} \\
&\cdot \sqrt{2\pi} (\mathrm{i}\omega')^{3/2} \rho^{(0)}(\boldsymbol{x}') \frac{(A^{||}(\boldsymbol{x}^s, \boldsymbol{x}') A^{||}(\boldsymbol{x}', \boldsymbol{x}^r))^{\star}}{\mathcal{L}^{\perp}(\boldsymbol{x}^r, \boldsymbol{x}', \boldsymbol{x}^s)^{\star}} \mathbf{w}(\boldsymbol{x}^r, \boldsymbol{x}, \boldsymbol{x}^s) h_m(\boldsymbol{x}^r; \boldsymbol{x}') U_{mn}(\boldsymbol{x}^s, \boldsymbol{x}^r, \omega') h_n(\boldsymbol{x}^s; \boldsymbol{x}') \\
&\qquad \cdot e^{\mathrm{i}\bar{\omega}\boldsymbol{\nu}^a \cdot (\boldsymbol{x} - \boldsymbol{x}') - \mathrm{i}\omega' T(\boldsymbol{x}^r, \boldsymbol{x}, \boldsymbol{x}^s)} \Big\}.
\end{aligned} \tag{2.43}$$

We have introduced the time-Fourier transform $U_{mn}(\boldsymbol{x}^s, \boldsymbol{x}^r, \omega')$ of the data, $u_{mn}(\boldsymbol{x}^s, \boldsymbol{x}^r, t')$. We proceed by Taylor expanding $T(\boldsymbol{x}^s, \boldsymbol{x}, \boldsymbol{x}^r)$ about $\boldsymbol{x}'$ as in equation (2.24). By the same argument as around equation (2.26), $\boldsymbol{x}'$ is assumed to be close to $\boldsymbol{x}$ as this yields the largest contribution to the oscillatory integral. The amplitude factors and the radiation patterns are slowly varying and can be considered constant in a small neighbourhood of $\boldsymbol{x}'$. This means that we may substitute $\boldsymbol{x}'$ for $\boldsymbol{x}$ for slowly varying components,

$$\begin{aligned}
&\hat{\mathbf{c}}^{(1)}(\boldsymbol{x}') \approx \\
&\frac{-1}{(2\pi)^{3/2}\pi} \mathrm{Re} \Big\{ \int_X \mathrm{d}\boldsymbol{x} \int_{\mathbb{R}\geq 0} \bar{\omega}^{-1} \mathrm{d}\bar{\omega} \int_{E_{\boldsymbol{\nu}^a}} \mathrm{d}\boldsymbol{\nu}^m \int_{\partial S \times \partial R} \mathrm{d}\boldsymbol{x}^s \mathrm{d}\boldsymbol{x}^r \int_{\mathbb{R}\geq 0} \mathrm{d}\omega' \langle 8\pi^2 \Gamma(\boldsymbol{x}', \boldsymbol{\nu}^m) \rangle^{-1} (\mathrm{i}\omega')^{3/2} \\
&\quad \cdot \rho^{(0)}(\boldsymbol{x}') \frac{(A^{||}(\boldsymbol{x}^s, \boldsymbol{x}') A^{||}(\boldsymbol{x}', \boldsymbol{x}^r))^{\star}}{\mathcal{L}^{\perp}(\boldsymbol{x}^r, \boldsymbol{x}', \boldsymbol{x}^s)^{\star}} \mathbf{w}(\boldsymbol{x}^r, \boldsymbol{x}', \boldsymbol{x}^s) h_m(\boldsymbol{x}^r; \boldsymbol{x}') U_{mn}(\boldsymbol{x}^s, \boldsymbol{x}^r, \omega') h_n(\boldsymbol{x}^s; \boldsymbol{x}') \\
&\qquad \cdot e^{-\mathrm{i}\omega' T(\boldsymbol{x}^r, \boldsymbol{x}', \boldsymbol{x}^s)} e^{\mathrm{i}(\bar{\omega}\boldsymbol{\nu}^a - \omega' \nabla_{\boldsymbol{x}'} T(\boldsymbol{x}^r, \boldsymbol{x}', \boldsymbol{x}^s)) \cdot (\boldsymbol{x} - \boldsymbol{x}')} \Big\}.
\end{aligned} \tag{2.44}$$

We observe that the integration over $\boldsymbol{x}$ now becomes a delta function,

$$\begin{aligned}
&\int_X \mathrm{d}\boldsymbol{x} e^{\mathrm{i}(\bar{\omega}\boldsymbol{\nu}^a - \omega' \nabla_{\boldsymbol{x}'} T(\boldsymbol{x}^r, \boldsymbol{x}', \boldsymbol{x}^s)) \cdot (\boldsymbol{x} - \boldsymbol{x}')} \\
&\quad = 4\pi^2 \delta(\bar{\omega}\boldsymbol{\nu}^m - \omega' \nabla_{\boldsymbol{x}'} T(\boldsymbol{x}^r, \boldsymbol{x}', \boldsymbol{x}^s)) = 4\pi^2 \delta(\bar{\omega}\boldsymbol{\nu}^m - \omega' \boldsymbol{\nu}^m |\nabla_{\boldsymbol{x}'} T(\boldsymbol{x}^r, \boldsymbol{x}', \boldsymbol{x}^s)|),
\end{aligned} \tag{2.45}$$

since $\boldsymbol{\nu}^m = \nabla_{\boldsymbol{x}'} T/|\nabla_{\boldsymbol{x}'} T|$. Using that $\bar{\omega} = \omega|\nabla_{\boldsymbol{x}'} T|$ and the result in equation (2.44), the integration over $\bar{\omega}$ and $\boldsymbol{\nu}^m$ collapses to

$$\hat{\mathbf{c}}^{(1)}(\boldsymbol{x}') \approx \frac{-\sqrt{2\pi}}{\pi}\mathrm{Re}\Big\{ \int_{\partial S\times\partial R} \mathrm{d}\boldsymbol{x}^s\mathrm{d}\boldsymbol{x}^r \int_{\mathbb{R}\geq 0} \frac{\mathrm{d}\omega'}{(\omega'|\nabla_{\boldsymbol{x}'} T(\boldsymbol{x}^r,\boldsymbol{x}',\boldsymbol{x}^s)|)^2}\langle 8\pi^2\Gamma(\boldsymbol{x}',\boldsymbol{\nu}^m)\rangle^{-1}(\mathrm{i}\omega')^{3/2}$$
$$\cdot\,\rho^{(0)}(\boldsymbol{x}')\frac{(A^{\shortparallel}(\boldsymbol{x}^s,\boldsymbol{x}')A^{\shortparallel}(\boldsymbol{x}',\boldsymbol{x}^r))^\star}{\mathcal{L}^{\perp}(\boldsymbol{x}^r,\boldsymbol{x}',\boldsymbol{x}^s)^\star}\mathbf{w}(\boldsymbol{x}^s,\boldsymbol{x}',\boldsymbol{x}^r)h_m(\boldsymbol{x}^r;\boldsymbol{x}')U_{mn}(\boldsymbol{x}^s,\boldsymbol{x}^r,\omega')h_n(\boldsymbol{x}^s;\boldsymbol{x}')$$
$$\cdot\, e^{-\mathrm{i}\omega' T(\boldsymbol{x}^r,\boldsymbol{x}',\boldsymbol{x}^s)}\Big\}. \quad (2.46)$$

Taking 8π out of the generalized inverse and making the appropriate changes yields

$$\hat{\mathbf{c}}^{(1)}(\boldsymbol{x}') \approx \frac{1}{(2\pi)^{5/2}}\mathrm{Re}\Big\{ \int_{\partial S\times\partial R} \mathrm{d}\boldsymbol{x}^s\mathrm{d}\boldsymbol{x}^r \int_{\mathbb{R}\geq 0} \frac{\mathrm{d}\omega'}{(\omega'\mathrm{i})^{1/2}|\nabla_{\boldsymbol{x}'} T(\boldsymbol{x}^r,\boldsymbol{x}',\boldsymbol{x}^s)|^2}\langle\Gamma(\boldsymbol{x}',\boldsymbol{\nu}^m)\rangle^{-1}$$
$$\cdot\,\rho^{(0)}(\boldsymbol{x}')\frac{(A^{\shortparallel}(\boldsymbol{x}^s,\boldsymbol{x}')A^{\shortparallel}(\boldsymbol{x}',\boldsymbol{x}^r))^\star}{\mathcal{L}^{\perp}(\boldsymbol{x}^r,\boldsymbol{x}',\boldsymbol{x}^s)^\star}\mathbf{w}(\boldsymbol{x}^r,\boldsymbol{x}',\boldsymbol{x}^s)h_m(\boldsymbol{x}^r;\boldsymbol{x}')U_{mn}(\boldsymbol{x}^s,\boldsymbol{x}^r,\omega')h_n(\boldsymbol{x}^s;\boldsymbol{x}')$$
$$\cdot\, e^{-\mathrm{i}\omega' T(\boldsymbol{x}^r,\boldsymbol{x}',\boldsymbol{x}^s)}\Big\}. \quad (2.47)$$

(Equation (2.47) is in fact a direct manifestation of the composition of a pseudodifferential operator with a FIO (Treves, 1980, , Section 6.1. Chapter VIII)). The surface coordinates $\boldsymbol{x}^r$ and $\boldsymbol{x}^s$ are changed to the phase directions at the scattering point as in relation (2.27). Using equation (2.29) and (2.32), the appropriate Jacobian can be expressed as

$$\frac{\partial(\boldsymbol{x}^s,\boldsymbol{x}^r)}{\partial(\boldsymbol{\alpha}^s,\boldsymbol{\alpha}^r)} = \frac{\mu_{LS}(\boldsymbol{\alpha}^r,\boldsymbol{x}',\boldsymbol{\alpha}^s)|\nabla_{\boldsymbol{x}'} T(\boldsymbol{x}^r,\boldsymbol{x}',\boldsymbol{x}^s)|^4}{|\rho^{(0)}(\boldsymbol{x}')A^{\shortparallel}(\boldsymbol{x}^s,\boldsymbol{x}')A^{\shortparallel}(\boldsymbol{x}',\boldsymbol{x}^r)|^2}. \quad (2.48)$$

Inserting the result in equation (2.47) yields the estimate of the medium perturbation

$$\hat{\mathbf{c}}^{(1)}(\boldsymbol{x}') \approx \frac{1}{(2\pi)^{5/2}}\mathrm{Re}\Big\{ \int_{S^s\times S^r} \mathrm{d}\boldsymbol{\alpha}^s\mathrm{d}\boldsymbol{\alpha}^r \int_{\mathbb{R}\geq 0} \frac{\mathrm{d}\omega'}{(\omega'\mathrm{i})^{1/2}}\mu_{LS}(\boldsymbol{\alpha}^r,\boldsymbol{x}',\boldsymbol{\alpha}^s)\langle\Gamma(\boldsymbol{x}',\boldsymbol{\nu}^m)\rangle^{-1}$$
$$\cdot\frac{|\nabla_{\boldsymbol{x}'} T(\boldsymbol{\alpha}^r,\boldsymbol{x}',\boldsymbol{\alpha}^s)|^2\mathbf{w}(\boldsymbol{\alpha}^r,\boldsymbol{x}',\boldsymbol{\alpha}^s)h_m(\boldsymbol{x}^r;\boldsymbol{x}')U_{mn}(\boldsymbol{x}^s,\boldsymbol{x}^r,\omega')h_n(\boldsymbol{x}^s;\boldsymbol{x}')}{\rho^{(0)}(\boldsymbol{x}')A^{\shortparallel}(\boldsymbol{\alpha}^s,\boldsymbol{x}')A^{\shortparallel}(\boldsymbol{x}',\boldsymbol{\alpha}^r)\mathcal{L}^{\perp}(\boldsymbol{\alpha}^r,\boldsymbol{x}',\boldsymbol{\alpha}^s)^\star}e^{-\mathrm{i}\omega' T(\boldsymbol{\alpha}^r,\boldsymbol{x}',\boldsymbol{\alpha}^s)}\Big\}. \quad (2.49)$$

We observe in the denominator the out-of-plane geometrical spreading, which also exists in the expression for Γ (equation (2.38)). Changing the variables from phase angles to scattering angle θ and migration dip $\boldsymbol{\nu}^m$ as in (2.35) yields

$$\hat{\mathbf{c}}^{(1)}(\boldsymbol{x}') \approx \frac{1}{(2\pi)^{5/2}}\mathrm{Re}\Big\{ \int_{E_{\boldsymbol{\nu}^a}\times E_\theta} \mathrm{d}\theta\mathrm{d}\boldsymbol{\nu}^m\frac{\partial(\boldsymbol{\alpha}^s,\boldsymbol{\alpha}^r)}{\partial(\boldsymbol{\nu}^m,\theta)} \int_{\mathbb{R}\geq 0} \frac{\mathrm{d}\omega'}{(\omega'\mathrm{i})^{1/2}}\mu_{LS}(\boldsymbol{x}',\boldsymbol{\nu}^m,\theta)\langle\Gamma(\boldsymbol{x}',\boldsymbol{\nu}^m)\rangle^{-1}$$
$$\cdot\frac{|\nabla_{\boldsymbol{x}'} T(\boldsymbol{x}',\boldsymbol{\nu}^m,\theta)|^2\mathbf{w}(\boldsymbol{x}',\boldsymbol{\nu}^m,\theta)h_m(\boldsymbol{x}^r;\boldsymbol{x}')U_{mn}(\boldsymbol{x}^s,\boldsymbol{x}^r,\omega')h_n(\boldsymbol{x}^s;\boldsymbol{x}')}{\rho^{(0)}(\boldsymbol{x}')A^{\shortparallel}(\boldsymbol{\alpha}^s,\boldsymbol{x}')A^{\shortparallel}(\boldsymbol{x}',\boldsymbol{\alpha}^r)\mathcal{L}^{\perp}(\boldsymbol{x}',\boldsymbol{\nu}^m,\theta)^\star}e^{-\mathrm{i}\omega' T(\boldsymbol{x}',\boldsymbol{\nu}^m,\theta)}\Big\}, \quad (2.50)$$

where we have left the phase directions in the argument of the in-plane amplitudes to distinguish them. The Jacobian inside the integral can be found in (Burridge *et al.*, 1998). The integral over migration dip makes this an inverse by generalized Radon transform (GRT).

2.4 Transformation into angle gathers

When constructing angle gathers we fix the scattering angle, θ, and integrate over the migration dip, $\boldsymbol{\nu}^m$. The restriction can introduce artifacts in the angle gathers when the medium is inhomogeneous (i.e. in the presence of caustics) due to multipathing in the recorded wave-field. These artifacts are different from the artifacts due to the failure of assumption 3. These artifacts are not present in the inversion by equation (2.50) since they stack destructively (Stolk & de Hoop, 2002).

Since the restriction to a fixed scattering angle means that we no longer stack over all the data, but rather over subsets of the data that change with image point and scattering angle, we reintroduce $\boldsymbol{x}^s$ and $\boldsymbol{x}^r$ as the variables of integration. This requires the notion of branches of the two-way travel time (see equation (2.10)). We define $\theta^{(i)}$ as $\theta(\boldsymbol{\alpha}^r, \boldsymbol{x}', \boldsymbol{\alpha}^s)$ (cf. (2.34)-(2.35)) composed with the inverse of map (2.27), associating the scattering angle with the acquisition coordinates $\boldsymbol{x}^s, \boldsymbol{x}^r$. We define the 'angle' transform $\mathbf{K}$ (the GRT) via a restriction of the imaging operator $\mathbf{L}^\star$ in equation (2.22) to fixed angle $\theta^{(i)} = \theta'$, where $i \in I$ indexes the travel time branch. We reintroduce the sum over the different travel time branches suppressed since equation (2.9). Thus we multiply the kernel of $\mathbf{L}^\star$ in equation (2.22) by a delta function, $\delta(\theta^{(i)} - \theta')$. The kernel of $\mathbf{K}$, denoted by $\mathcal{K}_{mn}$, can be written as an oscillatory integral (after a change of $\boldsymbol{x}'$ to $\boldsymbol{x}$)

$$\mathcal{K}_{mn}(\boldsymbol{x}, \theta', \boldsymbol{x}^s, \boldsymbol{x}^r, t) = \sum_{i\in I}(2\pi\sqrt{\mathrm{i}})^{-1} \int \omega'^{3/2}\rho^{(0)}(\boldsymbol{x}) \cdot \frac{(A^{||}(\boldsymbol{x}^s, \boldsymbol{x})A^{||}(\boldsymbol{x}, \boldsymbol{x}^r))^\star}{\mathcal{L}^\perp(\boldsymbol{x}^r, \boldsymbol{x}, \boldsymbol{x}^s)^\star}\mathbf{w}(\boldsymbol{x}^r, \boldsymbol{x}, \boldsymbol{x}^s)h_m(\boldsymbol{x}^r; \boldsymbol{x})h_n(\boldsymbol{x}^s; \boldsymbol{x})e^{-\mathrm{i}\Phi^{(i)}(\boldsymbol{x}, \boldsymbol{x}^r, \boldsymbol{x}^s, t, \theta', \omega', \varepsilon)}\mathrm{d}\omega'\mathrm{d}\varepsilon. \tag{2.51}$$

Here ε is the Fourier dual of the scattering angle θ (Stolk & de Hoop, 2002) and

$$\Phi^{(i)}(\boldsymbol{x}, \boldsymbol{x}^r, \boldsymbol{x}^s, t, \theta', \omega', \varepsilon) = \omega'[T^{(i)}(\boldsymbol{x}^r, \boldsymbol{x}, \boldsymbol{x}^s) - t] + \varepsilon[\theta' - \theta^{(i)}(\boldsymbol{x}^r, \boldsymbol{x}, \boldsymbol{x}^s)]. \tag{2.52}$$

The artifacts of the restriction can be evaluated by considering the composition $\mathbf{KL}$, a θ'-family of operators each member of which resembles the normal operator. The artifacts in the angle gathers can be recognized by their 'move-out' in angle. A multi-dimensional filter in the Fourier domain (see equation (2.51)) can be applied to remove the artifacts

associated with $|\varepsilon| \geq \varepsilon_0 > 0$. Brandsberg-Dahl *et al.* (2003a) suppressed the artifacts by so-called *focusing in dip*.

By proceeding as suggested above using the appropriate changes of variables leading up to equation (2.50), the angle dependent parameter estimates (used to construct common-image point gathers) are given by

$$\hat{\mathbf{c}}^{(1)}(\boldsymbol{x}';\theta') \approx \frac{1}{(2\pi)^{5/2}}\mathrm{Re}\left\{\int_{E_{\boldsymbol{\nu}^m}} \mathrm{d}\boldsymbol{\nu}^m \frac{\partial(\boldsymbol{\alpha}^s,\boldsymbol{\alpha}^r)}{\partial(\boldsymbol{\nu}^m,\theta')}\int_{\mathbb{R}\geq 0}\frac{\mathrm{d}\omega'}{(\omega'\mathrm{i})^{1/2}}\mu_{LS}(\boldsymbol{x}',\boldsymbol{\nu}^m,\theta')\langle\Gamma(\boldsymbol{x}',\boldsymbol{\nu}^m)\rangle^{-1}\right.$$
$$\left.\cdot\frac{|\nabla_{\boldsymbol{x}'}\,T(\boldsymbol{x}',\boldsymbol{\nu}^m,\theta')|^2\mathbf{w}(\boldsymbol{x}',\boldsymbol{\nu}^m,\theta')h_m(\boldsymbol{x}^r;\boldsymbol{x}')U_{mn}(\boldsymbol{x}^s,\boldsymbol{x}^r,\omega')h_n(\boldsymbol{x}^s;\boldsymbol{x}')}{\rho^{(0)}(\boldsymbol{x}')A^{||}(\boldsymbol{\alpha}^s,\boldsymbol{x}')A^{||}(\boldsymbol{x}',\boldsymbol{\alpha}^r)\mathcal{L}^{\perp}(\boldsymbol{x}',\boldsymbol{\nu}^m,\theta')^\star}e^{-\mathrm{i}\omega' T(\boldsymbol{x}',\boldsymbol{\nu}^m,\theta')}\right\}. \tag{2.53}$$

Note that we again have suppressed the summation of the travel time branches. The factor $\Gamma(\boldsymbol{x}',\boldsymbol{\nu}^m)$ is an average in θ of the radiation patterns. $\langle\Gamma(\boldsymbol{x}',\boldsymbol{\nu}^m)\rangle^{-1}$ then acts as a least-squares (LS) removal of the radiation patterns. This is hence a LS-AVA-compensated parameter estimate. Since, upon filtering, $\hat{\mathbf{c}}^{(1)}(\boldsymbol{x}';\theta')$ should only depend smoothly on θ' if the correct background medium is used, the detection of smoothness can be used as a criterion for velocity analysis. Brandsberg-Dahl *et al.* (2003b) followed such an angle tomographic approach to determine the background medium.

2.5 Example

Here we give an example using real data from the North Sea. The data set is acquired using ocean bottom cable (OBC) acquisition. We use data from a single ocean bottom cable making the intersection of a presumed symmetry plane and the ocean bottom.

Using equation (2.50) we perform an isotropic inversion considering PP-scattering events and an isotropic background medium. This yields information on the three independent parameter perturbations $\rho^{(1)}$, $c^{(1)}_{1111}$ and $c^{(1)}_{1133}$ in equation (2.15). An image is created as a linear combination of these parameters given in Figure 2.6. The geology varies mostly in the imaging plane making this an accurate 2.5-D problem under our assumptions 1 and 2. However, at depths greater than 3000 meters, the 2.5-D framework deteriorates. By this we mean that the geology also varies significantly in the out-of-plane direction sending energy out of the computational plane. Hence, sufficient information on the reflectors here is simply not contained in our data (the single acquisition cable data set). Top part of Figure 2.7 is a high resolution detail from Figure 2.6, with surface position from 3000 to $4000\,m$ and depth from 1850 to $2150\,m$. The V-shape in lower part of the image is a distinct geological feature believed to be either a slump fault or an erosive channel deposit.

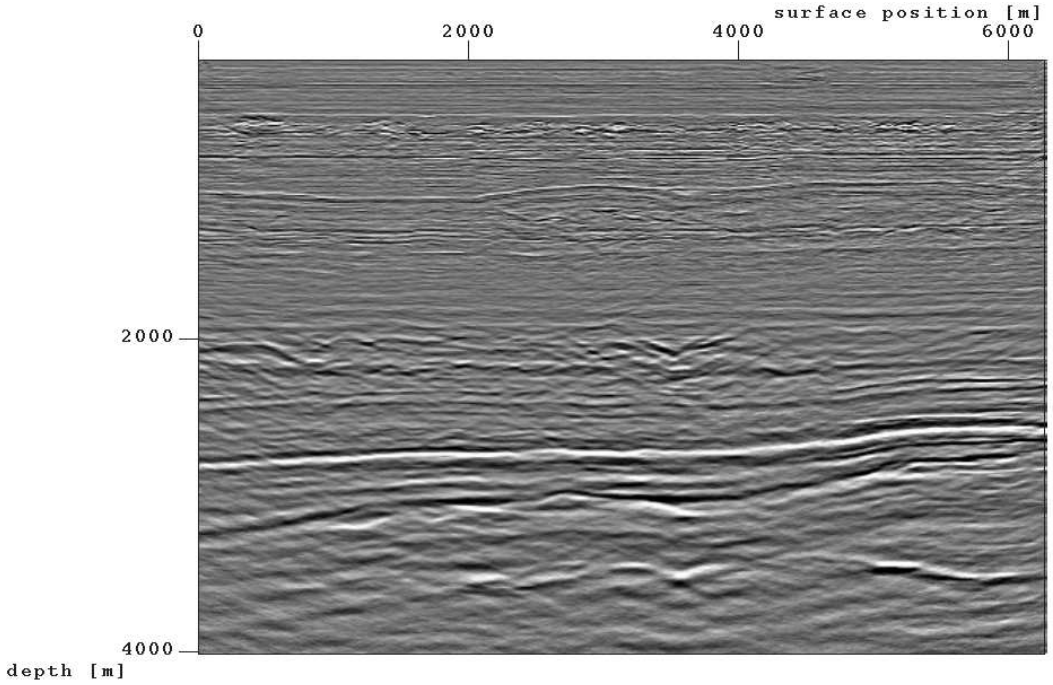

Figure 2.6: Image created as a linear combination of inverted parameters from equation (2.50) using PP-scattering event of the North Sea (OBC) data set.

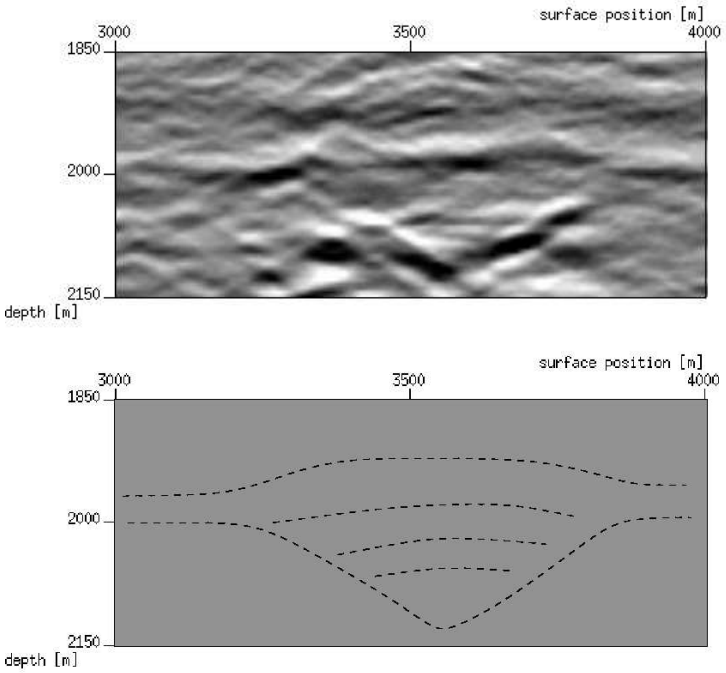

Figure 2.7: Top figure is a high resolution image of detail from Figure 2.6. The image shows a possible slump fault or erosive channel deposit. Their dominant features are captured in this 2-D slice. The bottom figure is a schematic drawing of the image as an erosive channel deposit.

As a slump fault the left part of the V-shape has dropped and new layers have deposited on the slope created. Lower part of the figure is a schematic drawing of the feature as an erosive channel, where water has dug into the horizontal layer and new material has deposited later leaving a slight curve in the layer, the V-shape. Both of these geological features have a slowly varying behavior in one direction. Given that our computational plane is intersecting at the right angle, the main features are described by this slice and the smoothly varying behavior are in the out-of-plane direction. Hence the 2.5-D framework applies with decent accuracy.

Figure 2.8 shows LS-AVA-compensated common-image point gathers for PP- and PS-scattering events, respectively, created as a combination of the parameters from equation (2.53) at surface position $x_1 = 1500\,m$. The combinations are chosen as the appropriate acoustic impedances; i.e. P-wave impedance for the PP-gather and S-wave impedance for the PS-gather. The vertical scale is from $800\,m$ to $3200\,m$ in depth. Following convention,

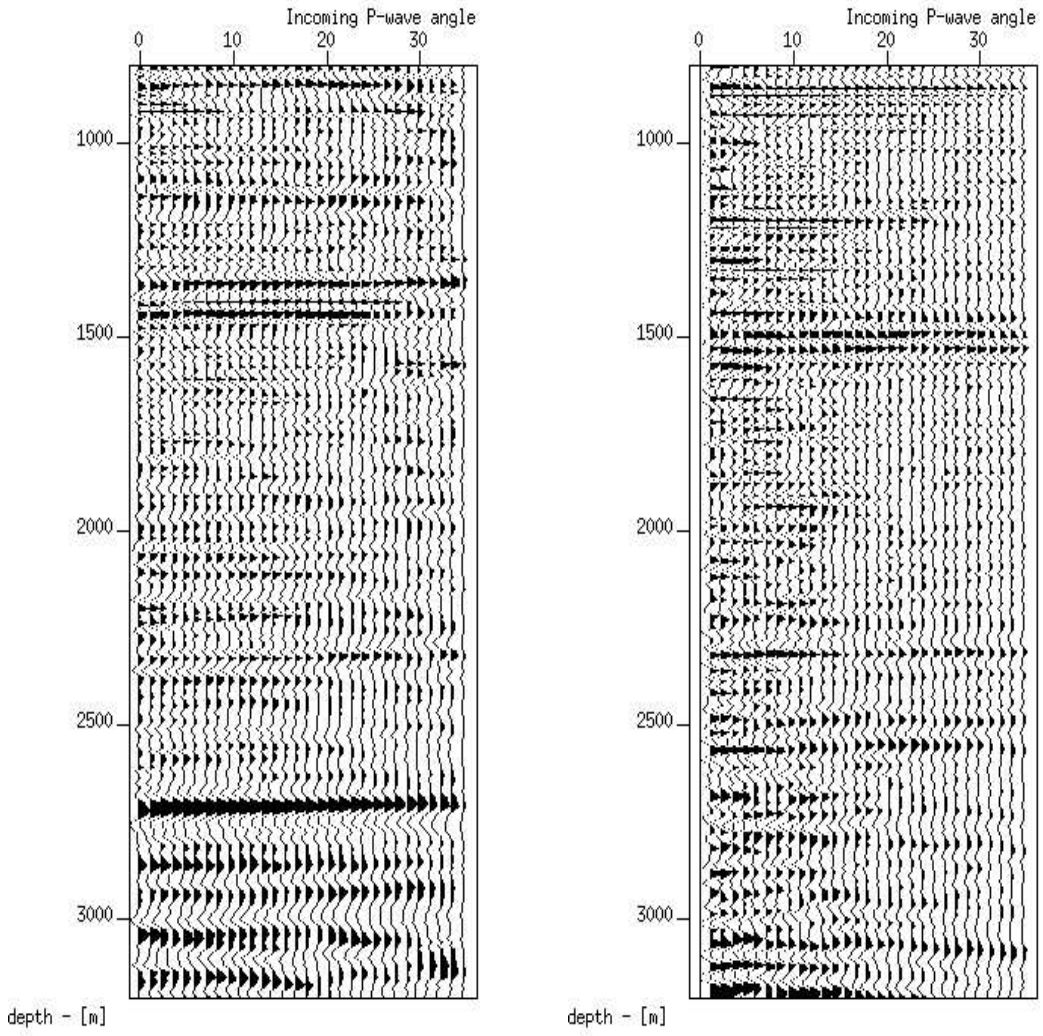

Figure 2.8: LS-AVA-compensated common-image point gathers for PP- and PSV-scattering, respectively at surface position $1500\,m$ in Figure 2.6 created using equation (2.53). The depth range is from 800 to $3200\,m$. Both common-image point gathers are plotted as functions of incoming P-wave angle, from 0 to 35 degrees.

both common-image point gathers are plotted as functions of incoming P-wave angle, ranging from 0 to 35 degrees. Note that the zero angle contribution of the PS-gather is set to zero as this is not defined. Only a subset of the reflectors are comparable in depth between PP and PS gathers, yet with very different strength in amplitudes. As mentioned, the imaging is done in an isotropic smooth background medium, yet the medium is anisotropic. The anisotropy has a strong effect on the travel times and thus the depths. This can explain why certain reflectors, when comparing the two common-image point gathers, seem to be at different depths. Note that the amplitude behavior is close to constant with angle. Hence, for this range of scattering angles, the LS-AVA-compensation in equation (2.53) suppresses the amplitude behavior. This is important in angle tomography through the use of 'differential semblance' (Brandsberg-Dahl *et al.*, 2003b). It is clear from this example, that a joint treatment of (q)P and (q)S velocities becomes necessary in reflection tomography.

2.6 Discussion

This paper presents the general form of 2.5-D modeling, imaging-inversion and AVA-compensated angle transform formulas in anisotropic elastic media under necessary and sufficient assumptions. The results extend those of Bleistein (1986) to the cases of multipathing and anisotropic elasticity. Assumption 1 restricts us to a monoclinic medium as the lowest possible symmetry. However, under the addition of assumption 2, the wave propagation is restricted to the plane. Any symmetries lower than a transversely isotropic medium with the symmetry axis contained in the plane of consideration have to be excluded for the purpose of inversion and reflection tomography.

In the presence of caustics, artifacts may be generated by the imaging-inversion procedures. Subject to the Bolker condition such artifacts are avoided. We have made the observation that the 2-D Bolker condition in the symmetry plane implies the Bolker condition in three dimensions in the framework of the common azimuth acquisition geometry. Artifacts in the common image-point gathers are also controlled by the ray geometry in the symmetry plane only and can thus be filtered out by 2-D considerations. An interesting aspect of our results is the appearance of out-of-plane contributions, by the geometrical spreading, contained naturally in the least-squares removal of the radiation patterns. Intuitively this can be understood as the removal of the stationary contribution to the radiation patterns from the out-of-plane geometrical spreading.

The primary applications of our 2.5-D formulation are a slicewise approach to (i) time-lapse seismics, and (ii) reflection tomography. We elaborate on the second application. The new least-squares AVA-compensated transform of seismic data into common-image point

gathers in anisotropic media enables a slicewise approach to migration velocity analysis. This is a better compensation of the AVA-effects than by a pointwise removal as found in (Brandsberg-Dahl *et al.*, 2003b). Given a medium that has its dominant change in two directions we may invoke the 2.5-D assumptions approximatively to slices in the smoothly varying direction as done in the example, section 2.5. We parametrize the medium in a finite dimensional subspace of possible smooth background models by a collection of slices $\underline{\mathbf{m}} = \{\mathbf{m}(x_2)\}$, for all values of x_2 under consideration, where each $\mathbf{m}(x_2)$ is the 2-D parametrization of a slice at x_2. Angle tomography (Brandsberg-Dahl *et al.*, 2003b) can be done per slice by differential semblance (Symes & Carazzone, 1991) on AVA-compensated common-image point gathers generated by equation (2.53). We extend this by applying the appropriate out-of-plane 'annihilator' as a Tikhonov regularizer to the misfit functional

$$J[\underline{\mathbf{m}}] = \frac{1}{2}\int \Big\{ \int\int \left| \left[\partial_\theta - (\partial_\theta \Xi(\boldsymbol{x},\theta,x_2))\Xi(\boldsymbol{x},\theta,x_2)^{-1}\right] \hat{\mathbf{c}}^{(1)}[\underline{\mathbf{m}}](\boldsymbol{x};\theta,x_2)\right|^2 \mathrm{d}\boldsymbol{x}\mathrm{d}\theta \\ + \lambda \int \left|\partial_{x_2}^2 \mathbf{c}^{(0)}[\underline{\mathbf{m}}](\boldsymbol{x},x_2)\right|^2 \mathrm{d}\boldsymbol{x} \Big\} \mathrm{d}x_2, \quad (2.54)$$

where (cf. equation (2.38))

$$\Xi(\boldsymbol{x},\theta,x_2) = \frac{\mu_{LS}(\boldsymbol{x},\boldsymbol{\nu}^m,\theta)}{|\mathcal{L}^\perp(\boldsymbol{x},\boldsymbol{\nu}^m,\theta)|^2} \frac{\partial(\boldsymbol{\alpha}^s,\boldsymbol{\alpha}^r)}{\partial(\boldsymbol{\nu}^m,\theta)} \langle \Gamma(\boldsymbol{x},\boldsymbol{\nu}^m)\rangle^{-1} \mathbf{w}(\boldsymbol{x},\boldsymbol{\nu}^m,\theta)\mathbf{w}^T(\boldsymbol{x},\boldsymbol{\nu}^m,\theta). \quad (2.55)$$

All relevant parameters of equation (2.55) are calculated for $\boldsymbol{\nu}^m$ in the wavefront set of $\mathbf{c}^{(1)}$. $\mathbf{c}^{(0)}[\underline{\mathbf{m}}](\boldsymbol{x},x_2)$ is a vector of the parameters of the background medium given the current parametrization $\underline{\mathbf{m}}$. λ in equation (2.54) is a statistical quantity controlling the trade-off between in-plane and out-of-plane fit (Tenorio, 2001) and $\boldsymbol{x} = (x_1, x_3)$. ∂_θ and ∂_{x_2} are the partial derivatives with respect to the scattering angle and out-of-plane coordinate, respectively. The LS-AVA-compensated inversion result from equation (2.53) is denoted $\hat{\mathbf{c}}^{(1)}[\underline{\mathbf{m}}](\boldsymbol{x};\theta,x_2)$ to emphasize that it is generated using the current parametrization of the smooth background model, $\underline{\mathbf{m}}$, for the slice at out-of-plane coordinate x_2. The minimum of this function indicates a smooth background model such that the data are in the range of the 2.5-D modelling operator. In this way the 2.5-D framework provides a fast computational tool for 3-D tomography and an increased ability to monitor the regularization of the search for a fitting model.

Acknowledgement

Stig-Kyrre Foss would like to thank the Center for Wave Phenomena, Colorado School of Mines for the opportunity to stay as a guest from Fall 2001 to Summer 2002. He would also like to thank the URE-project, NTNU, Trondheim, Norway for financial support, and

Sverre Brandsberg-Dahl for the use of Figure 2.4. The authors thank Statoil for the use of the North Sea data, Børge Arntsen for data handling and Barbara McLenon for her help preparing the manuscript.

Appendix 2.A. The 2.5-D Born modelling formula

The 3-D Born formula is a high frequency approximation to the field scattered off the medium perturbation at $\boldsymbol{x} \in \mathbb{R}^3$, collected at the receiver position $\boldsymbol{x}^r$ generated by a source at $\boldsymbol{x}^s$. This field is calculated by substituting the appropriate GRA Green's functions (2.2) in the Born approximation. It gives that, under assumption 1 on the medium, the m-direction of the scattered field at the receiver position $\boldsymbol{x}^r$ due to a n-component source at $\boldsymbol{x}^s$ written as a Fourier integral operator is

$$U_{mn}(\boldsymbol{x}^r, \boldsymbol{x}^s, \omega) \approx \int_X \left\{ \int_{\mathbb{R}} \omega^2 h_m(\boldsymbol{x}^r) \rho^{(0)}(\boldsymbol{x}) A(\boldsymbol{x}^s, \boldsymbol{x}) A(\boldsymbol{x}, \boldsymbol{x}^r) \mathbf{w}^T(\boldsymbol{x}^r, \boldsymbol{x}, \boldsymbol{x}^s) e^{\mathrm{i}\omega T(\boldsymbol{x}^r, \boldsymbol{x}, \boldsymbol{x}^s)} h_n(\boldsymbol{x}^s) \mathrm{d}x_2 \right\} \cdot \mathbf{c}^{(1)}(x_1, x_3) \mathrm{d}x_1 \mathrm{d}x_3. \quad (2.\text{A-}1)$$

The medium perturbation $\mathbf{c}^{(1)}$ and the radiation patterns $\mathbf{w}$ are, for the lowest possible symmetry (triclinic), 22×1-matrices of the form as in equations (2.15) and (2.16), respectively. The domain of integration of the (x_1, x_3)-coordinates, X, is defined in subsection 2.2.2

Upon scaling, $x_2 = \tilde{x}_2/|\omega|$, we recognize the phase variables $(\tilde{x}_2, \omega)$. We proceed as in Bleistein (1986) and use the method of stationary phase to integrate out the out-of-plane variable x_2 in (2.A-1). The one-dimensional stationary phase formula approximates integrals of the type

$$\int f(\sigma) e^{\mathrm{i}\omega T(\sigma)} \mathrm{d}\sigma \approx \sqrt{\frac{2\pi}{|\omega||\partial_\sigma^2 T(\sigma_0)|}} f(\sigma_0) e^{\mathrm{i}\omega T(\sigma_0) + \mathrm{i}(\pi/4)\mathrm{sgn}(\omega)\mathrm{sgn}(\partial_\sigma^2 \mathrm{T}(\sigma_0))}, \quad (2.\text{A-}2)$$

for sufficiently large $|\omega|$ and $\partial_\sigma^2 T(\sigma_0) \neq 0$, where σ_0 is the stationary point, such that $\partial_\sigma T(\sigma)|_{\sigma=\sigma_0} = 0$. In the mentioned integral, the stationary point is given by

$$\partial_{x_2} T(\boldsymbol{x}^r, \boldsymbol{x}, \boldsymbol{x}^s) = p_2^s + p_2^r = 0. \quad (2.\text{A-}3)$$

Due to assumptions 1 and 2, the only solution to (2.A-3) is $p_2^s = p_2^r = 0$ which implies that the stationary point is $x_2 = 0$. A discussion on this is given in the main text. Observe that the sum of the slownesses in equation (2.A-3) also occurs in the common azimuth case, equation (2.18). The second derivative of the phase function at the stationary point is

$$\partial_{x_2}^2 T(\boldsymbol{x}^r, \boldsymbol{x}, \boldsymbol{x}^s)\big|_{x_2=0, p_2=0} = (\partial_{x_2} p_2^s + \partial_{x_2} p_2^r)|_{x_2=0, p_2=0} = \frac{1}{Q_2^\perp(\boldsymbol{x}, \boldsymbol{x}^s)} + \frac{1}{Q_2^\perp(\boldsymbol{x}, \boldsymbol{x}^r)}, \quad (2.\text{A-}4)$$

where $Q_2^\perp(\boldsymbol{x}, \boldsymbol{x}^s)$ and $Q_2^\perp(\boldsymbol{x}, \boldsymbol{x}^r)$ are the out-of-plane geometrical spreading factors defined in equation (2.5) for the rays connecting the imaging point $\boldsymbol{x}$ with the source $\boldsymbol{x}^s$ and receiver $\boldsymbol{x}^r$, respectively.

Remark 4

In points, in phase space, where either $Q_2^{\perp}(\boldsymbol{x},\boldsymbol{x}^s)$ or $Q_2^{\perp}(\boldsymbol{x},\boldsymbol{x}^r)$ tends to zero the travel time function is not smooth. We observe this in equation (2.A-4) where the Hessian of the travel time function will tend towards infinity and will not be defined. This essentially means that the stationary phase argument does not hold. The integral over x_2 in equation (2.A-1) remains. Out-of-plane caustics are thus not allowed for the stationary phase formula to be applicable. We restrict the analysis in the following to rays with no out-of-plane caustics.

From this it follows that $\mathrm{sgn}(\partial_{x_2}^2 T(\boldsymbol{x}^r,\boldsymbol{x},\boldsymbol{x}^s)|_{x_2=0}) = 1$ since the out-of-plane geometrical spreading is positive. The stationary phase formula (2.A-2) then yields for the x_2 integral (in view of Remark 4)

$$\begin{aligned}\int_X \left[\omega^2 \int_{\mathbb{R}} h_m(\boldsymbol{x}^r)\rho^{(0)}(\boldsymbol{x})A(\boldsymbol{x}^s,\boldsymbol{x})A(\boldsymbol{x},\boldsymbol{x}^r)\mathbf{w}^T(\boldsymbol{x}^r,\boldsymbol{x},\boldsymbol{x}^s)\mathbf{c}^{(1)}(\boldsymbol{x})e^{\mathrm{i}\omega T(\boldsymbol{x}^r,\boldsymbol{x},\boldsymbol{x}^s)}h_n(\boldsymbol{x}^s)\mathrm{d}x_2\right]\mathrm{d}x_1\mathrm{d}x_3 \\ \approx \sqrt{2\pi\mathrm{i}}\omega^{3/2}\int_X h_m(\boldsymbol{x}^r)\frac{(Q_2^{\perp}(\boldsymbol{x},\boldsymbol{x}^s)Q_2^{\perp}(\boldsymbol{x},\boldsymbol{x}^r))^{1/2}}{(Q_2^{\perp}(\boldsymbol{x},\boldsymbol{x}^s)+Q_2^{\perp}(\boldsymbol{x},\boldsymbol{x}^r))^{1/2}}\rho^{(0)}(\boldsymbol{x})A(\boldsymbol{x}^s,\boldsymbol{x})A(\boldsymbol{x},\boldsymbol{x}^r) \\ \cdot\, \mathbf{w}^T(\boldsymbol{x}^r,\boldsymbol{x},\boldsymbol{x}^s)\mathbf{c}^{(1)}(\boldsymbol{x})e^{\mathrm{i}\omega T(\boldsymbol{x}^r,\boldsymbol{x},\boldsymbol{x}^s)}h_n(\boldsymbol{x}^s)\Big|_{x_2=0,p_2=0}\mathrm{d}x_1\mathrm{d}x_3. \quad \text{(2.A-5)}\end{aligned}$$

Using equation (2.6) this equation reduces to the 2.5-D modelling formula (2.9) in the main text (here in the frequency domain),

$$\begin{aligned}&U_{mn}(\boldsymbol{x}^s,\boldsymbol{x}^r,\omega) \\ &= \sqrt{2\pi\mathrm{i}}\omega^{3/2}\int_X h_m(\boldsymbol{x}^r)\rho^{(0)}(\boldsymbol{x})\frac{A^{||}(\boldsymbol{x}^s,\boldsymbol{x})A^{||}(\boldsymbol{x},\boldsymbol{x}^r)}{\mathcal{L}^{\perp}(\boldsymbol{x}^r,\boldsymbol{x},\boldsymbol{x}^s)}\mathbf{w}^T(\boldsymbol{x}^r,\boldsymbol{x},\boldsymbol{x}^s)\mathbf{c}^{(1)}(\boldsymbol{x})e^{\mathrm{i}\omega T(\boldsymbol{x}^r,\boldsymbol{x},\boldsymbol{x}^s)}h_n(\boldsymbol{x}^s)\mathrm{d}\boldsymbol{x}.\end{aligned} \quad \text{(2.A-6)}$$

Chapter 3

2.5-D modeling, inversion and angle migration in anisotropic elastic media

S.-K. Foss and B. Ursin
Accepted for publication in Geophysical Prospecting 2004

Summary

2.5-D modeling approximates 3-D wave propagation in the dip-direction of a 2-D geological model. Attention is restricted to ray paths for waves propagating in a plane. In this way fast inversion or migration can be performed. For velocity analysis this reduction of the problem is particularly useful.

We review 2.5-D modeling for Born volume scattering and Born-Helmholtz surface scattering. The amplitudes are corrected for 3-D wave propagation, taking into account both in-plane and out-of-plane geometrical spreading. We also derive some new inversion / migration results. An AVA-compensated migration routine is presented that is simplified compared to earlier results. This formula can be used to create common-image gathers for use in velocity analysis by studying the residual moveout. We also give a migration formula for the energy-flux-normalized plane-wave reflection coefficient that models large contrast in the medium parameters not treated by the Born and the Born-Helmholtz equation results. All results are derived using the generalized Radon transform (GRT) directly in the natural coordinate system characterized by scattering angle and migration dip. Con-

sequently, no Jacobians are needed in their calculation.

Inversion and migration in an orthorhombic medium or a transversely isotropic (TI) medium with tilted symmetry axis are the lowest symmetries for practical purposes (symmetry axis is in the plane). We give an analysis by the derived methods of the parameters for these two types of media used in velocity analysis, inversion and migration. The kinematics of the two media involve the same parameters, hence there is no distinction when doing velocity analysis. The in-plane scattering coefficient, used in the inversion and migration, also depends on the same parameters for both media. The out-of-plane geometrical spreading, necessary for amplitude-preserving computations, for the TI medium is dependent on the same parameters that govern in-plane kinematics. For orthorhombic media information on additional parameters is required that is not needed for in-plane kinematics and the scattering coefficients.

Resolution analysis of the scattering coefficient suggests that direct inversion by GRT yields unreliable parameter estimates. A more practical approach to inversion is amplitude-preserving migration followed by AVA-analysis.

Symbols and notation

Symbols	Description
t	time
ω	frequency
$\mathbf{x} = (x_1, x_2, x_3)$	position vector
$\mathbf{y} = (y_1, y_2, y_3)$	image point
$G_{in}(\mathbf{x}^r, \omega, \mathbf{x}^s)$	Green's function in the frequency domain
$\mathbf{x}^s, \mathbf{x}^r$	source and receiver positions
$v(\mathbf{x})$	phase velocity
$V(\mathbf{x})$	group velocity
$\det\ \mathbf{Q}_2(\mathbf{x}, \mathbf{x}^s)$	relative geometrical spreading in local surface coordinates on the wavefront
$T(\mathbf{x}, \mathbf{x}^s)$	traveltime for a ray between $\mathbf{x}$ and $\mathbf{x}^s$
(q_1, q_2)	local wavefront coordinates
$\mathbf{p} = (p_1, p_2, p_3)$	slowness vector
$\mathbf{p}^s, \mathbf{p}^r$	slowness vector at at scattering point of the ray from the source and the receiver, respectively
$\mathbf{h} = (h_1, h_2, h_3)$	polarization vector
$A(\mathbf{x}, \mathbf{x}^s)$	amplitude for a ray at $\mathbf{x}^s$ from $\mathbf{x}$
$\kappa(\mathbf{x}, \mathbf{x}^s)$	KMAH index for a ray between $\mathbf{x}$ and $\mathbf{x}^s$
$Q_2^{\parallel}(\mathbf{x}, \mathbf{x}^s)$	in-plane relative geometrical spreading
$Q_2^{\perp}(\mathbf{x}, \mathbf{x}^s)$	out-of-plane relative geometrical spreading
$c_{ijkl}(\mathbf{x}) = c^{(0)}_{ijkl}(\mathbf{x}) + c^{(1)}_{ijkl}(\mathbf{x})$	elastic stiffness tensor as a sum of smooth background parameters and a perturbation
$\rho(\mathbf{x}) = \rho^{(0)}(\mathbf{x}) + \rho^{(1)}(\mathbf{x})$	density as a sum of a smoothly varying term and

	a perturbation
$U^{(1)}_{mn}(\mathbf{x}^r, \omega, \mathbf{x}^s)$	scattered field
$T(\mathbf{x}^r, \mathbf{x}, \mathbf{x}^s)$	two-way traveltime
$S(\mathbf{x})$	scattering coefficient
$A^{\|\|}(\mathbf{x}, \mathbf{x}^s)$	GRA amplitude with only
	in-plane geometrical spreading
$\mathcal{L}^{\perp}_R(\mathbf{x}^r, \mathbf{x}, \mathbf{x}^s)$	total out-of-plane
	geometrical spreading
$\mathbf{r}(\mathbf{x}^r, \mathbf{x}, \mathbf{x}^s)$	$M \times 1$ radiation patterns vector
$\mathbf{c}^{(1)}(\mathbf{x})$	$M \times 1$ medium parameter perturbation vector
$\boldsymbol{\sigma} = (\sigma_1, \sigma_2)$	surface coordinates
$\mathbf{p}^m$	migration slowness
$\boldsymbol{\nu}^m = \mathbf{p}^m / \|\mathbf{p}^m\|$	migration dip vector
ν	migration dip angle
$\boldsymbol{\nu}^\phi$	geological dip vector
θ	scattering angle
$\boldsymbol{\Lambda}(\boldsymbol{\nu}^m; \mathbf{y})$	$M \times M$ matrix used in inversion
E_ν, E_θ	domain of migration dip and
	scattering angle, respectively
$\tilde{U}(\mathbf{x}^r, \omega, \mathbf{x}^s; \mathbf{y})$,	preconditioned data in frequency and
$\tilde{u}(\mathbf{x}^r, T(\mathbf{x}^r, \mathbf{y}, \mathbf{x}^s), \mathbf{x}^s; \mathbf{y})$	time domain
$\tilde{u}^{(1)}_{mn}(\mathbf{x}^r, T(\mathbf{x}^r, \mathbf{y}, \mathbf{x}^s), \mathbf{x}^s)$	phase-corrected data
$\mathbf{p}^h$	horizontal slowness vector
α^r, α^s	angles of group velocities
	from the surface normal
$R(p^h \boldsymbol{\nu}^h(\mathbf{y}))$	reflection coefficient
$\boldsymbol{\nu}^h = \mathbf{p}^h / p^h$	horizontal unit slowness
$p^h = \|\mathbf{p}^h\|$	magnitude of horizontal slowness
$w(t)$	wavelet
$\|\mathbf{p}^\phi\|$	stretch factor

Superscripts s and r indicate source and receiver respectively.

3.1 Introduction

2.5-D modeling and inversion/migration considers 3-D wave propagation with source and receivers in a vertical plane or along a single line and a subsurface that is constant in the horizontal direction perpendicular to that plane. This allows one to work with data from a reduced data set in a computationally efficient way. This is especially important in velocity analysis, which gives initial estimates of the subsurface medium. As the problems often become too large to handle effectively in the full 3-D case, one often considers slices in the Earth using the 2.5-D framework. Velocity analysis and amplitude-versus-angle analysis can be done by studying common-image gathers created with formulas derived by Brandsberg-Dahl, De Hoop and Ursin (1999; 2003a) and Brandsberg-Dahl, Ursin and De Hoop (2003b).

The notion of 2.5-D modeling was introduced in seismic applications by Bleistein (1986) who considered modeling and Kirchhoff migration for the scalar wave equation. Several authors had earlier addressed the problem as 3-D wave propagation in a 2-D medium (Červený, 1981; Goldin, 1986). The technique considers 3-D data generated and collected for source and receivers in a vertical plane or along a line that is the intersection with the plane in a seismic experiment. It is assumed that the parameters of the subsurface medium vary only in this plane, and for anisotropic medium this is additionally a symmetry plane. For example it can be chosen to be one of the symmetry planes of an orthorhombic medium (Schoenberg & Helbig, 1997). The medium is assumed unchanging in the orthogonal out-of-plane direction. We therefore confine our attention to wave propagation for which slowness and hence group velocity (due to the symmetry) are considered to be zero in this direction. This restricts the rays to remain in this plane. The kinematics of the wave propagation is therefore 2-D (Ettrich *et al.*, 2002). The waves still travel in a 3-D medium and exhibit in-plane and out-of-plane geometrical spreading (Wang & Houseman, 1994; Wang, 2003).

We review 2.5-D modeling in a compact way and derive some new linearized 2.5-D inversion/migration formulas in elastic anisotropic media. The subsurface medium parameters are divided into known background parameters, such as density and stiffness parameters (from velocity analysis) and the unknown medium perturbations. Linearized inversion inverts for the most singular part of the unknown medium perturbations. This was done by Beylkin and Burridge (1990) for isotropic media using the generalized Radon transform (GRT). De Hoop *et al.* (1994) expanded this to the anisotropic case. De Hoop and Bleistein (1997) considered the inversion of surface reflection data. A review of 3-D parameter inversion and angle migration is given by Ursin (2003). Most 2.5-D formulas published are valid for fluids and isotropic solids; see Stockwell (1995) for references and Dellinger

et al. (2000) and Tygel *et al.* (1998). Geoltrain (1989) did 2.5-D Kirchhoff migration in transversely isotropic media (TI) with a vertical symmetry axis, and Sollid (2000) did 2.5-D angle migration for TI media. We use inverse GRT here to derive all results in general anisotropic media under the restrictions mentioned above. Introducing a 2-D inverse GRT, we derive inversion formulas for the medium perturbations and migration formulas for both 2.5-D Born and Born-Helmholtz scattering, i.e., line scattering and cylindrical surface reflection, respectively. These are valid for only small contrasts in the medium perturbations. We give equivalent results for 2-D problems, found in Appendix 3.C, for comparison with the 2.5-D results. 2-D versions of formulas are also needed when testing the formulas on synthetic data generated with a finite-difference modeling code, which is usually 2-D. We also introduce an inversion formula for the reflection coefficient, where parameter contrasts are large (Ursin, 2003).

The first section of the paper starts by introducing the notation used in the rest of the paper. There, we also show that, for 2.5-D, the geometrical spreading of the wave propagation factors into an in-plane and an out-of-plane part, as shown by Ettrich *et al.* (2002). Starting with the single-scattering 3-D Born modeling formula (Ursin & Tygel, 1997), we proceed as in Bleistein (1986) to approximate the integral in the out-of-plane direction by the method of stationary phase. This reduces to the 2.5-D Born modeling equation, which models field data collected by receivers in a vertical plane. The wavefield is generated by a point source; and receivers in the same plane observe the back-scattered waves generated by perturbations in the subsurface. The derived inversion and migration formulas benefit from a preconditioning of the data and the use of the 2-D inverse GRT (Appendix 3.A). The entire inversion procedure is done in detail in Appendix 3.B for this case. In the text, we also present a migration procedure (Sollid & Ursin, 2003) that can be used for amplitude-versus-angle (AVA) analysis and an AVA-compensated migration formula (the so-called *restricted* GRT result) for the purpose of velocity analysis (Brandsberg-Dahl *et al.*, 1999; Brandsberg-Dahl *et al.*, 2003a).

We proceed by considering Born-Helmholtz modeling and inversion formulas. The Born-Helmholtz modeling equation is a surface-scattering equation that models the reflected wavefield from a surface reflection (de Hoop & Bleistein, 1997; Ursin & Tygel, 1997). A geological interface can be seen as a localized unknown medium perturbation along that interface superimposed on the smooth background. By applying this in the 2.5-D Born modeling formula, we get the 2.5-D Born-Helmholtz modeling equation. The inversion result is the medium perturbation restricted to the geological interface (Stolk & de Hoop, 2002). All inversion results are done assuming a delta-function-like source wavelet. Seismic field data are generated by a band-limited wavelet. When using such data in our formulas the inversion/migration results become blurred (de Hoop *et al.*, 1999) resulting in erroneous

amplitude behavior. For surface-reflected data with a band-limited wavelet the inversion result is scaled and convolved with a stretched version of the wavelet (Tygel *et al.*, 1994). We correct for the scaling factor (Jaramillo & Bleistein, 1999; Sollid & Ursin, 2003; Ursin, 2003) to derive inversion, migration and AVA-compensated migration formulas where this has been taken into account. Additionally, we introduce a new reciprocal surface scattering modeling equation and migration formula, which yields the reflection result for large contrast of the medium at the interface (Ursin, 2003).

The final section discusses the estimation of the stiffness and density parameters in 2.5-D for velocity analysis and inversion/migration. The discussion is limited to orthorhombic media and TI media with vertical symmetry axis because these are the lowest symmetries for practical purposes. The analysis extends to TI and orthorhombic media with a known dipping symmetry axis within the plane of consideration, which is equivalent through the Bond transformation (Carcione, 2001). Under the assumptions of 2.5-D, all kinematic aspects of wave propagation and the inversion of parameters will be the same for both media. For amplitude computations, however, while the parameters that govern the out-of-plane geometrical spreading are the same as those that govern the in-plane kinematics for transversely isotropic media, for orthorhombic media all independent stiffness parameters are required some of which cannot be obtained from 2.5-D inversion. We show by resolution analysis (de Hoop *et al.*, 1999) the inability for direct inversion of all parameters in an orthorombic medium.

3.2 2.5-D geometrical ray approximation

In the frequency domain, the Green's function G_{in} for 3-D wave propagation in an anisotropic elastic inhomogenous medium satisfies

$$\rho(\mathbf{x})\omega^2 G_{in} + \partial_j(c_{ijkl}(\mathbf{x})\partial_l G_{kn}) = -\delta_{in}\delta(\mathbf{x}-\mathbf{x}^s), \quad i,j,k,l,n = 1,2,3, \tag{3.1}$$

where ρ is density and c_{ijkl} is the stiffness tensor. The function δ_{in} is the Kronecker delta, which gives the source term in the canonical directions, ω is frequency, $\mathbf{x} = (x_1, x_2, x_3)$ is the position vector, and $\mathbf{x}^s$ is the position of the source. We use ∂_j to indicate the derivative $\partial/\partial x_j$, and the summation convention is assumed if not otherwise is stated. The Green's function is defined in some domain $\mathcal{D}$ with homogeneous boundary conditions and thus satisfies the reciprocity relation (Aki & Richards, 1980)

$$G_{in}(\mathbf{x},\omega,\mathbf{x}^s) = G_{ni}(\mathbf{x}^s,\omega,\mathbf{x}). \tag{3.2}$$

In anisotropic elastic media there can exist three wave modes qP, qS1 and qS2. The geometrical ray approximation (GRA) is a high-frequency, leading-order approximation of

the Green's function in equation (3.1). Higher-order terms are smoother. The GRA gives a sum over these wave modes for rays between $\mathbf{x}^s$ and $\mathbf{x}$, where each term is of the form (Červený, 2001)

$$G_{ip}(\mathbf{x},\omega,\mathbf{x}^s) = h_i^s(\mathbf{x})A(\mathbf{x},\mathbf{x}^s)e^{i\omega T(\mathbf{x},\mathbf{x}^s)}h_p(\mathbf{x}^s), \tag{3.3}$$

where $T(\mathbf{x},\mathbf{x}^s)$ is the traveltime along the ray between $\mathbf{x}^s$ and $\mathbf{x}$. $h_i^s(\mathbf{x})$ and $h_p(\mathbf{x}^s)$ are components of the unit polarization vectors at each end of the ray connecting $\mathbf{x}$ and $\mathbf{x}^s$. The superscript s is to associate the polarization vector with this ray. $A(\mathbf{x},\mathbf{x}^s)$ is a complex amplitude function for the different wave modes at $\mathbf{x}$ after having traveled from $\mathbf{x}^s$. The amplitude, which becomes complex in the presence of caustics, is given by

$$A(\mathbf{x},\mathbf{x}^s) = \frac{e^{-i(\pi/2)\kappa(\mathbf{x},\mathbf{x}^s)\operatorname{sgn}\omega}}{4\pi[\rho(\mathbf{x})v^s(\mathbf{x})\rho(\mathbf{x}^s)v(\mathbf{x}^s)]^{1/2}|\det\mathbf{Q}_2(\mathbf{x},\mathbf{x}^s)|^{1/2}}, \tag{3.4}$$

where v^s and v are the phase velocities at $\mathbf{x}$ and $\mathbf{x}^s$, respectively. The KMAH-index, $\kappa(\mathbf{x},\mathbf{x}^s)$, takes into account the phase shifts due to caustics the ray passes through from $\mathbf{x}^s$ to $\mathbf{x}$ (Červený, 2001; Klimeš, 1997). $|\det\mathbf{Q}_2(\mathbf{x},\mathbf{x}^s)|^{1/2}$ is the relative geometrical spreading factor determined from

$$[Q_2]_{ij}^{-1}(\mathbf{x},\mathbf{x}^s) = -\frac{\partial^2 T(\mathbf{x},\mathbf{x}^s)}{\partial q_i^s \partial q_j}, \quad i,j=1,2, \tag{3.5}$$

where q_j and q_i^s are local surface coordinates on the wavefront at the points $\mathbf{x}$ and $\mathbf{x}^s$ respectively.

All factors of the GRA Green's function are calculated by ray tracing. The kinematic ray tracing system can be written (Červený, 1972)

$$V_i = \frac{dx_i}{dT} = a_{ijkl}p_l h_j h_k, \tag{3.6}$$

$$\frac{dp_i}{dT} = -\frac{1}{2}\partial_{x_i}(a_{mjkl})p_m p_l h_j h_k, \quad i,j,k,l,m=1,2,3, \tag{3.7}$$

where $\mathbf{V} = (V_1,V_2,V_3)$ is the group velocity, $\mathbf{p} = (p_1,p_2,p_3)$ is the slowness and $a_{ijkl} = c_{ijkl}/\rho$ are the density normalized stiffnesses. The polarization vectors are associated with the wave mode considered. In 2.5-D (Ettrich *et al.*, 2002), we wish to restrict the wave propagation to a plane, here the (x_1,x_3)-plane. Under the assumption of no change in the medium in the x_2-direction, i.e. out-of-plane, $\partial p_2/\partial T = 0$, which yields $p_2 = \textit{constant}$. The rays in the plane will stay in the (x_1,x_3)-plane, which happens for rays that have slowness constant equal to zero in the out-of-plane direction; $p_2 = 0$. The group velocity then is also zero in the out-of-plane direction as long as the (x_1,x_3)-plane is an anisotropic symmetry plane. This yields the solution $x_2 = \textit{constant}$ in equation (3.6). We shall consider the plane with $x_2 = 0$ in particular.

Considering equation (3.5) for 2.5-D modeling, we choose q_1 to be in the (x_1, x_3)-plane and q_2 to be in the x_2-direction, normal to the plane. From the discussion above, $p_2 = \partial T(\mathbf{x}, \mathbf{x}^s)/\partial x_2$ is constant along a given ray, since the medium parameters do not depend on x_2. In particular, $p_2 = 0$ in the (x_1, x_3)-plane. From this it follows that

$$\frac{\partial^2 T(\mathbf{x}, \mathbf{x}^s)}{\partial q_1^s \partial q_2} = \frac{\partial p_2^s(\mathbf{x})}{\partial q_1^s} = 0, \tag{3.8}$$

and

$$\frac{\partial^2 T(\mathbf{x}, \mathbf{x}^s)}{\partial q_2^s \partial q_1} = \frac{\partial p_2(\mathbf{x}^s)}{\partial q_1} = 0. \tag{3.9}$$

$\mathbf{p}^s = (p_1^s, p_2^s, p_3^s)$ and $\mathbf{p}^r = (p_1^r, p_2^r, p_3^r)$ denote the slowness vectors at the point $\mathbf{x}$ for the rays from the source $\mathbf{x}^s$ and receiver $\mathbf{x}^r$, respectively. The matrix in equation (3.5) thus becomes diagonal. The resulting relative geometrical spreading is

$$\mathbf{Q}_2(\mathbf{x}, \mathbf{x}^s) = - \begin{bmatrix} \dfrac{1}{\dfrac{\partial^2 T(\mathbf{x}, \mathbf{x}^s)}{\partial q_1^s \partial q_1}} & 0 \\ 0 & \dfrac{1}{\dfrac{\partial p_2}{\partial x_2}} \end{bmatrix} = \begin{bmatrix} Q_2^{\parallel}(\mathbf{x}, \mathbf{x}^s) & 0 \\ 0 & Q_2^{\perp}(\mathbf{x}, \mathbf{x}^s) \end{bmatrix}, \tag{3.10}$$

where $Q_2^{\parallel}(\mathbf{x}, \mathbf{x}^s)$ and $Q_2^{\perp}(\mathbf{x}, \mathbf{x}^s)$ are defined as the in-plane and out-of-plane relative geometrical spreading factors, respectively. This means that the relative geometrical spreading factor of the GRA amplitudes (3.4) splits into an out-of-plane and an in-plane factor

$$|\det \mathbf{Q}_2(\mathbf{x}, \mathbf{x}^s)|^{1/2} = |\mathrm{Q}_2^{\parallel}(\mathbf{x}, \mathbf{x}^s) \mathrm{Q}_2^{\perp}(\mathbf{x}, \mathbf{x}^s)|^{1/2}. \tag{3.11}$$

The inverse of the out-of-plane factor is

$$\frac{\partial p_2(\mathbf{x}^s)}{\partial x_2} = \frac{\partial p_2^s(\mathbf{x})}{\partial x_2}, \tag{3.12}$$

since p_2 is constant for a given ray. Note that derivatives of the slowness, polarization vector, or amplitude give higher-order, thus smoother, terms (de Hoop & Brandsberg-Dahl, 2000). This will become important in the derivations of high-frequency formulas in the following.

3.3 2.5-D Born modeling integral

The medium parameters can be described as a sum of a smooth part, $\rho^{(0)}$ and $c_{ijkl}^{(0)}$, and a perturbation, $\rho^{(1)}$ and $c_{ijkl}^{(1)}$:

$$\rho(\mathbf{x}) = \rho^{(0)}(\mathbf{x}) + \rho^{(1)}(\mathbf{x}), \quad c_{ijkl}(\mathbf{x}) = c_{ijkl}^{(0)}(\mathbf{x}) + c_{ijkl}^{(1)}(\mathbf{x}). \tag{3.13}$$

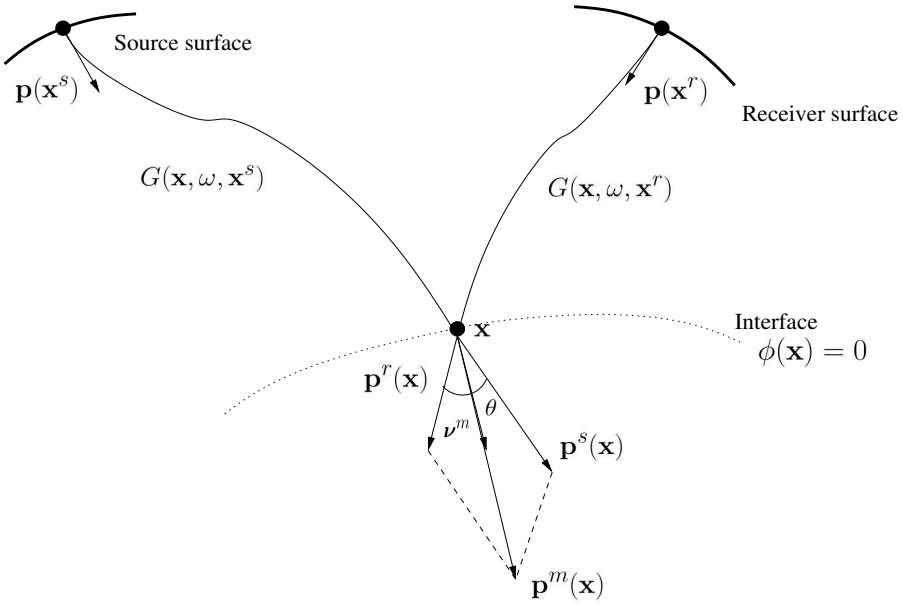

Figure 3.1: Single scattering with Green's functions connecting the scattering point $\mathbf{x}$ with the source and the receiver, $\mathbf{x}^s$ and $\mathbf{x}^r$, respectively. Scattering point on the interface $\phi(\mathbf{x}) = 0$.

The 3-D Born modeling formula is a single-scattering approximation to a seismic experiment wherein a source at $\mathbf{x}^s$ generates a wavefield that travels through the smooth part of the medium until it is scattered off a contrast in the medium (the perturbation) and again travels in the smooth medium to the receiver at $\mathbf{x}^r$. The wavefield is assumed not to scatter at any part of the medium apart from the scattering point. We let the GRA Green's functions in equation (3.3) describe the wave propagation in the smoothly varying part of the medium in equation (3.13) (see Figure 3.1). The 3-D Born formula gives the scattered field u_{mn} observed at $\mathbf{x}^r$. This would be the equivalent to data collected in a seismic field experiment. We assume that we know the smoothly varying part of the medium and wish to find the medium perturbations. In the frequency domain this becomes the m-direction of the scattered field at receiver position $\mathbf{x}^r$ due to a n-directional source at $\mathbf{x}^s$ is (see Ursin & Tygel (1997) for a detailed derivation)

$$u_{mn}(\mathbf{x}^r,\omega,\mathbf{x}^s) \;\approx\; \omega^2 \int_{\mathcal{D}} h_m(\mathbf{x}^r)\rho^{(0)}(\mathbf{x})A(\mathbf{x}^s,\mathbf{x})A(\mathbf{x},\mathbf{x}^r)S(\mathbf{x})e^{i\omega T(\mathbf{x}^r,\mathbf{x},\mathbf{x}^s)}h_n(\mathbf{x}^s)d\mathbf{x}, \quad (3.14)$$

where the two-way traveltime is

$$T(\mathbf{x}^r,\mathbf{x},\mathbf{x}^s) = T(\mathbf{x}^s,\mathbf{x}) + T(\mathbf{x},\mathbf{x}^r), \quad (3.15)$$

and the scattering coefficient is

$$S(\mathbf{x}) = \mathbf{r}^T(\mathbf{x}^r, \mathbf{x}, \mathbf{x}^s)\mathbf{c}^{(1)}(\mathbf{x}). \tag{3.16}$$

We define the medium perturbations by the M-component column vector (Burridge *et al.*, 1998)

$$\mathbf{c}^{(1)}(\mathbf{x}) = \left\{ \frac{\rho^{(1)}(\mathbf{x})}{\rho^{(0)}(\mathbf{x})}, \frac{c^{(1)}_{ijkl}(\mathbf{x})}{\rho^{(0)}(\mathbf{x})v^s_\circ(\mathbf{x})v^r_\circ(\mathbf{x})} \right\}, \tag{3.17}$$

where $v^s_\circ$ and $v^r_\circ$ are local phase velocities averaged over all phase angles (Burridge *et al.*, 1998). These are introduced for numerical purposes so that the matrix has components of similar size (see discussion around equation (3.51) in a later section). The indices of $c^{(1)}_{ijkl}$ cover all the 21 independent indices of the stiffness tensor in general anisotropic media (Tsvankin, 2001), i.e. $M = 22$. With higher symmetry, such as isotropy, the size of the matrix reduces accordingly. For example for isotropy $M = 3$ for PP scattering events, and $M = 2$ for PS scattering events (Beylkin & Burridge, 1990). The radiation patterns are defined similarly as a M-component column vector by

$$\mathbf{r}(\mathbf{x}^r, \mathbf{x}, \mathbf{x}^s) = \left\{ h^s_m(\mathbf{x})h^r_m(\mathbf{x}), [h^s_i(\mathbf{x})p^s_j(\mathbf{x})h^r_k(\mathbf{x})p^r_l(\mathbf{x})]v^s_\circ(\mathbf{x})v^r_\circ(\mathbf{x}) \right\}. \tag{3.18}$$

The indices correspond to those of the stiffness tensor in the medium perturbation $\mathbf{c}^{(1)}$. All parts of the Born integral except the unknown medium perturbations are obtained from the respective GRA Green's functions and are thus calculated in the background medium. The angle between the rays from the source and the receiver (given by the slowness vectors) is called the scattering angle, $\theta \in [0, \pi\rangle$, defined by

$$\cos\theta = \frac{\mathbf{p}^s \cdot \mathbf{p}^r}{|\mathbf{p}^s||\mathbf{p}^r|}. \tag{3.19}$$

The domain of the scattering angle is denoted E_θ. We also define the migration slowness as the sum of the two slowness vectors at the scattering point; $\mathbf{p}^m = \mathbf{p}^s + \mathbf{p}^r$. The unit vector $\boldsymbol{\nu}^m = \mathbf{p}^m/|\mathbf{p}^m|$ is called the migration dip. We can parametrize this unit vector by the migration dip angle, ν, since $\boldsymbol{\nu}^m = (\cos\nu, \sin\nu)$, where $\nu \in E_\nu$ (see Figure 3.1), the domain of the migration dip angle.

We reduce the 3-D Born modeling formula to 2.5-D by restricting the rays to the vertical (x_1, x_3)-plane, with $x_2 = 0$ and $p_2 = 0$, as explained in the previous section. The waves still travel in a 3-D medium so the ray amplitudes exhibit 3-D geometrical spreading. We proceed as in Bleistein (1986) to use the method of stationary phase to approximate the integral in the out-of-plane variable x_2. The 1-D stationary phase formula approximates, for some function $f(\sigma)$, the integral

$$\int f(\sigma)e^{i\omega T(\sigma)}d\sigma \approx \sqrt{\frac{2\pi}{|\omega||\partial^2_\sigma T(\sigma_0)|}} f(\sigma_0)e^{i\omega T(\sigma_0)+i(\pi/4)\mathrm{sgn}(\omega)\mathrm{sgn}(\partial^2_\sigma \mathrm{T}(\sigma_0))}, \tag{3.20}$$

for sufficiently large $|\omega|$ and $\partial_\sigma^2 T(\sigma_0) \neq 0$, where σ_0 is the stationary point, such that $\partial_\sigma T(\sigma)|_{\sigma=\sigma_0} = 0$ (Bleistein, 1984).

We apply the stationary phase formula to the Born integral in equation (3.14) and integrate with respect to x_2. The stationary point is at

$$\partial_{x_2} T(\mathbf{x}^r, \mathbf{x}, \mathbf{x}^s) = p_2^s(\mathbf{x}) + p_2^r(\mathbf{x}) = 0, \tag{3.21}$$

which gives $p_2^s = p_2^r = 0$ for $x_2 = 0$. From equation (3.10) and (3.12) it follows that

$$\partial_{x_2}^2 T(\mathbf{x}^r, \mathbf{x}, \mathbf{x}^s)\big|_{x_2=0, p_2=0} = (\partial_{x_2} p_2^s + \partial_{x_2} p_2^r)|_{x_2=0, p_2=0} = \frac{1}{Q_2^\perp(\mathbf{x}, \mathbf{x}^s)} + \frac{1}{Q_2^\perp(\mathbf{x}, \mathbf{x}^r)}, \tag{3.22}$$

where $Q_2^\perp(\mathbf{x}, \mathbf{x}^s)$ and $Q_2^{r\perp}(\mathbf{x}, \mathbf{x}^r)$ are the out-of-plane relative geometrical spreading factors for the rays from the source $\mathbf{x}^s$ and receiver $\mathbf{x}^r$, respectively, to the scattering point $\mathbf{x}$. Furthermore, $\mathrm{sgn}(\partial_{x_2}^2 T(\mathbf{x}^r, \mathbf{x}, \mathbf{x}^s)\big|_{x_2=0}) = 1$, since the out-of-plane relative geometrical spreading is positive from (3.22). Inside the Born integral will be a division by

$$\left[Q_2^\perp(\mathbf{x}^r, \mathbf{x}) Q_2^\perp(\mathbf{x}, \mathbf{x}^s) \partial_{x_2}^2 T(\mathbf{x}^r, \mathbf{x}, \mathbf{x}^s)\right]^{1/2} = \left[Q_2^\perp(\mathbf{x}^r, \mathbf{x}) + Q_2^\perp(\mathbf{x}, \mathbf{x}^s)\right]^{1/2} = \mathcal{L}_R^\perp(\mathbf{x}^r, \mathbf{x}, \mathbf{x}^s), \tag{3.23}$$

which is the total out-of-plane relative geometrical spreading factor given by the integral along the ray (Ettrich *et al.*, 2002),

$$\mathcal{L}_R^\perp(\mathbf{x}^r, \mathbf{x}, \mathbf{x}^s) = \left[\int_{ray} \frac{V_2}{p_2} d\tau\right]^{1/2}, \tag{3.24}$$

where V_2 is the x_2-component of the group velocity and τ denotes traveltime.

Defining an in-plane amplitude factor

$$A^{||}(\mathbf{x}, \mathbf{x}^s) = \frac{e^{-i(\pi/2)\kappa(\mathbf{x}, \mathbf{x}^s)\mathrm{sgn}\,\omega}}{4\pi[\rho(\mathbf{x}) v^s(\mathbf{x}) \rho(\mathbf{x}^s) v(\mathbf{x}^s)]^{1/2} |Q_2^{||}(\mathbf{x}, \mathbf{x}^s)|^{1/2}}, \tag{3.25}$$

we obtain the 2.5-D Born integral for line scattering

$$\begin{aligned} u_{mn}(\mathbf{x}^r, \omega, \mathbf{x}^s) = \sqrt{2\pi}|\omega|^{3/2} e^{i(\pi/4)\mathrm{sgn}\,\omega} \\ \cdot \int_{\mathcal{D}(x_2=0)} h_m(\mathbf{x}^r) \frac{\rho^{(0)}(\mathbf{x}) A^{||}(\mathbf{x}^r, \mathbf{x}) A^{||}(\mathbf{x}, \mathbf{x}^s)}{\mathcal{L}_R^\perp(\mathbf{x}^r, \mathbf{x}, \mathbf{x}^s)} \\ \cdot S(\mathbf{x}) e^{i\omega T(\mathbf{x}^r, \mathbf{x}, \mathbf{x}^s)} h_n(\mathbf{x}^s) dx_1 dx_3. \end{aligned} \tag{3.26}$$

The 2.5-D Born integral corresponds to the response of line scatterers a point source and measured at a point receiver. The point source will induce a wavefield that has 3-D geometrical spreading accounted for by out-of-plane and in-plane geometrical spreading computed

along the rays from the source and the receivers to the scattering line. In addition, the integral has been multiplied by a factor $\sqrt{2\pi i/\omega}$ (a half-integration in the time-domain), attributable to scattering from the line. All kinematic aspects of the ray tracing are restricted to the plane.

The 3-D wave propagation with a point source, line scatterer, and point receiver can be reduced to the 2.5-D case, as we have seen, by approximating the out-of-plane integral by the method of stationary phase, equation (3.26). Going from the 2.5-D formulas for 2-D propagation, however, is not possible in a similar manner (see Appendix 3.C). *Ad hoc* methods have been suggested such as multiplying by the appropriate phase factor $\sqrt{2\pi i/\omega}$ and setting the out-of-plane geometrical spreading, $\mathcal{L}_R^{\perp}$, to 1, see Stockwell (1995). Physically, the inability to deduce 2-D behavior from 2.5-D in any rigoreous mathematical way is because the 2-D problem has a line source and line receivers, as opposed to a point source and point receivers.

3.4 Line-scattering inversion/migration

Data collected in a seismic experiment with a point source, under the approximations in the Born modeling integral (3.26), carry contributions from two-way travel (such as amplitude change, traveltime and phase-shifts), the radiation patterns due to the scattering and the medium perturbations. Intuitively, inversion would then remove all effects of the wave propagation on the data apart from the change in the wavefield due to the medium perturbation. The inversion formula is given in Appendix 3.A as an inverse GRT derived from a Fourier transform identity. An estimate of the medium perturbation at the imaging point, $\mathbf{y}$, then becomes (a detailed derivation is given in Appendix 3.B)

$$\hat{\mathbf{c}}^{(1)}(\mathbf{y}) \;=\; \int_{E_\nu} \langle \mathbf{\Lambda}(\boldsymbol{\nu}^m;\mathbf{y})\rangle^{-1} \int_{E_\theta} \mathbf{r}(\mathbf{x}^r,\mathbf{y},\mathbf{x}^s)\tilde{u}(\mathbf{x}^r,T(\mathbf{x}^r,\mathbf{y},\mathbf{x}^s),\mathbf{x}^s;\mathbf{y})|\mathbf{p}^m(\mathbf{y})|^2 d\theta d\nu, \quad (3.27)$$

where the $M \times M$-matrix $\mathbf{\Lambda}$ is given by

$$\mathbf{\Lambda}(\boldsymbol{\nu}^m;\mathbf{y}) = \int_{E_\theta} \mathbf{r}(\boldsymbol{\nu}^m,\theta;\mathbf{y})\mathbf{r}^T(\boldsymbol{\nu}^m,\theta;\mathbf{y})d\theta, \quad (3.28)$$

and $\langle \mathbf{\Lambda}(\boldsymbol{\nu}^m;\mathbf{y})\rangle^{-1}$ indicates a pseudo-inverse. This factor removes the amplitude variations attributable to the radiation patterns. A discussion on practical issues in an implementation, concerning the choice of the domains E_θ and E_ν, can be found in De Hoop *et al.* (1999). The data corrected, for amplitude, phase and traveltime, are (see Appendix 3.B)

$$\begin{aligned}\tilde{u}(\mathbf{x}^r,T(\mathbf{x}^r,\mathbf{y},\mathbf{x}^s),\mathbf{x}^s;\mathbf{y}) = \\ h_m(\mathbf{x}^r;\mathbf{y})\,\tilde{u}^{(1)}_{mn}(\mathbf{x}^r,T(\mathbf{x}^r,\mathbf{y},\mathbf{x}^s),\mathbf{x}^s)\,h_n(\mathbf{x}^s;\mathbf{y})\,2\sqrt{2\pi}\,\mathcal{L}_R^{\perp}(\mathbf{x}^r,\mathbf{y},\mathbf{x}^s) \\ \cdot\,[\rho^{(0)}(\mathbf{x}^r)v(\mathbf{x}^r)v^r(\mathbf{y})v^s(\mathbf{y})\rho^{(0)}(\mathbf{x}^s)v(\mathbf{x}^s)]^{1/2}\,|Q_2^{\parallel}(\mathbf{x}^r,\mathbf{y})Q_2^{\parallel}(\mathbf{y},\mathbf{x}^s)|^{1/2}. \quad (3.29)\end{aligned}$$

The different terms in the correction of the data in equation (3.29) are found by the GRA Green's function of the source and receiver rays, equation (3.3). To account for possible caustics in the wave field, the phase-corrected data $\tilde{u}^{(1)}_{mn}(\mathbf{x}^r, T(\mathbf{x}^r, \mathbf{y}, \mathbf{x}^s), \mathbf{x}^s)$ can have a sign change, a Hilbert transform, or both depending on the KMAH-index $\kappa(\mathbf{x}^r, \mathbf{y}) + \kappa(\mathbf{y}, \mathbf{x}^s)$. Additionally, a multiplication with $(-i\omega)^{-1/2}$ is done when taking the inverse Fourier transform. This works as a half integration and is a result of the stationary phase approximation in the derivation of the 2.5-D modeling formula (3.26). $\tilde{u}^{(1)}_{mn}$ is given explicitly in Appendix 3.B, equation (3.B-11).

2.5-D amplitude-preserving migration may be defined as a process that produces reflectivity as a function of scattering angle. These angle gathers may be analyzed directly, used as input to angle stacks, or as input to an inversion algorithm, (amplitude-versus-angle (AVA) analysis). Sollid and Ursin (2003) derived the following simple migration algorithm which gives an estimate of the scattering coefficient

$$\hat{S}(\theta; \mathbf{y}) = \int_{E_\nu} \tilde{u}(\mathbf{x}^r, T(\mathbf{x}^r, \mathbf{y}, \mathbf{x}^s), \mathbf{x}^s; \mathbf{y}) |\mathbf{p}^m(\mathbf{y})|^2 d\nu. \tag{3.30}$$

3.5 2.5-D Born-Helmholtz modeling integral

A geological interface defines a surface across which there exists a jump in the medium parameters. The medium parameters vary smoothly above and beneath such an interface defined by the function $\phi(\mathbf{x}) = 0$. The medium perturbation can then be expressed by

$$\mathbf{c}^{(1)}(\mathbf{x}) = \mathbf{c}^{(1)}(\mathbf{x})\big|_{\phi(\mathbf{x})=0} H(\phi(\mathbf{x})), \tag{3.31}$$

where $H(\phi(\mathbf{x}))$ is a unit step function at the interface:

$$H(\phi(\mathbf{x})) = \begin{cases} 1 & \mathbf{x} \text{ is below the interface} \\ 0 & \mathbf{x} \text{ is above the interface,} \end{cases} \tag{3.32}$$

and $\mathbf{c}^{(1)}(\mathbf{x})\big|_{\phi(\mathbf{x})=0}$ now is the jump in the medium parameters across the interface. Applying the divergence theorem to the 2.5-D Born line-scattering integral in equation (3.26) and neglecting a smoothly varying part, gives (Ursin & Tygel, 1997; de Hoop & Bleistein, 1997)

$$\begin{aligned} u_{mn}(\mathbf{x}^r, \omega, \mathbf{x}^s) = \sqrt{2\pi}|\omega|^{1/2} e^{i(3\pi/4)\operatorname{sgn}\omega} \\ \cdot \int_{\mathcal{D}(x_2=0)} h_m(\mathbf{x}^r) \frac{\rho^{(0)}(\mathbf{x}) A^{||}(\mathbf{x}^r, \mathbf{x}) A^{||}(\mathbf{x}, \mathbf{x}^s)}{\mathcal{L}^{\perp}(\mathbf{x}^r, \mathbf{x}, \mathbf{x}^s)} \\ \cdot \mathbf{r}^T(\mathbf{x}^r, \mathbf{x}, \mathbf{x}^s) \frac{\nabla_{\mathbf{x}} \mathbf{c}^{(1)}(\mathbf{x}) \cdot \nabla_{\mathbf{x}} T(\mathbf{x}^r, \mathbf{x}, \mathbf{x}^s)}{|\nabla_{\mathbf{x}} T(\mathbf{x}^r, \mathbf{x}, \mathbf{x}^s)|^2} \\ \cdot e^{i\omega T(\mathbf{x}^r, \mathbf{x}, \mathbf{x}^s)} h_n(\mathbf{x}^s) d\mathbf{x}. \end{aligned} \tag{3.33}$$

The gradient of $\mathbf{c}^{(1)}(\mathbf{x})$ is given by

$$\nabla_{\mathbf{x}}\mathbf{c}^{(1)}(\mathbf{x}) = \mathbf{c}^{(1)}(\mathbf{x})\big|_{\phi(\mathbf{x})=0}\,\delta(\phi(\mathbf{x}))\nabla_{\mathbf{x}}\phi(\mathbf{x}), \tag{3.34}$$

where $\delta(\phi(\mathbf{x}))$ is a spatial delta function at the reflecting surface. The surface is cylindrical under assumptions of 2.5-D, i.e., no variations in the out-of-plane direction. Equation (3.34) can be written

$$\nabla_{\mathbf{x}}\mathbf{c}^{(1)}(\mathbf{x}) = \mathbf{c}^{(1)}(\mathbf{x})\big|_{\phi(\mathbf{x})=0}\,\gamma(\mathbf{x})\boldsymbol{\nu}^{\phi}, \tag{3.35}$$

where $\gamma(\mathbf{x}) = \delta(\phi(\mathbf{x}))|\nabla_{\mathbf{x}}\phi(\mathbf{x})|$ is the so-called *singular function* (Bleistein, 1984), and $\boldsymbol{\nu}^{\phi}$ is the unit normal to the interface pointing downwards, corresponding to the local geological dip

$$\boldsymbol{\nu}^{\phi} = |\nabla_{\mathbf{x}}\phi|^{-1}\nabla_{\mathbf{x}}\phi. \tag{3.36}$$

We insert equation (3.35) in equation (3.33) and get the 2.5-D Born-Helmholtz modeling integral (see Figure 3.1)

$$\begin{aligned} u_{mn}(\mathbf{x}^r,\omega,\mathbf{x}^s) = \sqrt{2\pi}|\omega|^{1/2}e^{i(3\pi/4)\mathrm{sgn}\,\omega} \\ \cdot\int_{\mathcal{D}(x_2=0)} h_m(\mathbf{x}^r)\frac{\rho^{(0)}(\mathbf{x})A^{||}(\mathbf{x}^r,\mathbf{x})A^{||}(\mathbf{x},\mathbf{x}^s)}{\mathcal{L}^{\perp}(\mathbf{x}^r,\mathbf{x},\mathbf{x}^s)} \\ \cdot\,\mathbf{r}^T(\mathbf{x}^r,\mathbf{x},\mathbf{x}^s)\;\mathbf{c}^{(1)}(\mathbf{x})\big|_{\phi(\mathbf{x})=0}\,\gamma(\mathbf{x}) \\ \cdot\frac{\boldsymbol{\nu}^{\phi}(\mathbf{x})\cdot\boldsymbol{\nu}^{m}(\mathbf{x})}{|\mathbf{p}^m(\mathbf{x})|}e^{i\omega T(\mathbf{x}^r,\mathbf{x},\mathbf{x}^s)}h_n(\mathbf{x}^s)d\mathbf{x}. \end{aligned} \tag{3.37}$$

The delta function $\delta(\phi(\mathbf{x}))$, in the singular function $\gamma(\mathbf{x})$, can be viewed as making this integral over $\mathcal{D}(x_2 = 0)$ into an integral over the scattering surface. The factor $|\nabla_{\mathbf{x}}\phi(\mathbf{x})|$ in $\gamma(\mathbf{x})$ is a Jacobian between $\mathbf{x}$ and the line coordinate σ along the scattering surface. Note that we now have new factors of ω in front of the integrals relative to those for the Born modeling expression in equation (3.26). The Born-Helmholtz modeling integral then is

$$\begin{aligned} u_{mn}(\mathbf{x}^r,\omega,\mathbf{x}^s) = \sqrt{2\pi}|\omega|^{1/2}e^{i(3\pi/4)\mathrm{sgn}\,\omega} \\ \cdot\int_{\Sigma} h_m(\mathbf{x}^r)\frac{\rho^{(0)}(\mathbf{x})A^{||}(\mathbf{x}^r,\mathbf{x})A^{||}(\mathbf{x},\mathbf{x}^s)}{\mathcal{L}^{\perp}(\mathbf{x}^r,\mathbf{x},\mathbf{x}^s)} \\ \cdot\,S(\mathbf{x})\frac{\boldsymbol{\nu}^{\phi}(\mathbf{x})\cdot\boldsymbol{\nu}^{m}(\mathbf{x})}{|\mathbf{p}^m(\mathbf{x})|}e^{i\omega T(\mathbf{x}^r,\mathbf{x},\mathbf{x}^s)}h_n(\mathbf{x}^s)d\sigma, \end{aligned} \tag{3.38}$$

which is a line integral in the (x_1, x_3)-plane along the reflecting cylindrical surface denoted Σ. Note that $\mathbf{c}^{(1)}(\mathbf{x})\big|_{\phi(\mathbf{x})=0}$ is used in formula (3.16) for the scattering coefficient.

3.6 Cylindrical surface-scattering inversion/migration

For the Born-Helmholtz surface-scattering modeling formula (3.37), the medium perturbation is restricted to that surface. We solve for the medium perturbation localized by the delta function in the singular function making up the surface (Bleistein, 1984; Stolk, 2000). By comparing the Born-Helmholtz integral (3.38) with the Born integral (3.26) we observe that in order to invert in the same way, the corrected data should be multiplied by a factor $|\mathbf{p}^m(\mathbf{y})|/\boldsymbol{\nu}^\phi(\mathbf{y})\cdot\boldsymbol{\nu}^m(\mathbf{y})$, and, in the Fourier domain, by $-i\omega$, which serves as a differentiation in the time domain. Inversion at the imaging point for the perturbation multiplied by the singular function, using the inversion formula in Appendix 3.A, then yields

$$\hat{\mathbf{c}}^{(1)}(\mathbf{y})\big|_{\phi(\mathbf{y})=0}\,\gamma(\mathbf{y}) = \int_{E_\nu}\langle\boldsymbol{\Lambda}(\boldsymbol{\nu}^m;\mathbf{y})\rangle^{-1} \cdot \int_{E_\theta}\mathbf{r}(\mathbf{x}^r,\mathbf{y},\mathbf{x}^s)\partial_t\tilde{u}(\mathbf{x}^r,T(\mathbf{x}^r,\mathbf{y},\mathbf{x}^s),\mathbf{x}^s;\mathbf{y})\frac{|\mathbf{p}^m(\mathbf{y})|^3}{\boldsymbol{\nu}^\phi(\mathbf{y})\cdot\boldsymbol{\nu}^m(\mathbf{y})}d\theta d\nu, \quad (3.39)$$

where $\boldsymbol{\Lambda}$ is defined in equation (3.28). The corrected data are the time derivative of that used for the line-scattering inversion in equation (3.29). The time derivative makes the half integration of the data in equation (3.29) (see Appendix 3.B) into a half derivative. Note that we use equation (3.29), but the only time dependency is given by the data $\tilde{u}^{(1)}_{mn}$. The derivative hence works on this function only given explicitly in Appendix 3.B, equation (3.B-12). The dominant contributions to the integral above come from specular reflections. For specular reflection, the migration dip and the surface normal coincide. One therefore usually uses only the stationary value and sets $\boldsymbol{\nu}^\phi(\mathbf{y})\cdot\boldsymbol{\nu}^m(\mathbf{y}) = 1$ (de Hoop & Bleistein, 1997).

The results derived so far in this paper assume the source to be a delta function. In seismic field data, the source is a band-limited wavelet $w(t)$, which blurs the inversion/migration (de Hoop *et al.*, 1999). The smearing of the inversion/migration result in space can be accounted for in the surface scattering results in this paper (Jaramillo & Bleistein, 1999; Sollid & Ursin, 2003; Ursin, 2003). The singular function $\gamma(\mathbf{x})$ in equation (3.39) is replaced by

$$|\mathbf{p}^\phi(\mathbf{x}^\phi)|w(|\mathbf{p}^\phi(\mathbf{x}^\phi)|\boldsymbol{\nu}^\phi\cdot(\mathbf{y}-\mathbf{x}^\phi)), \quad (3.40)$$

with $\mathbf{x}^\phi$ defined from $\phi(\mathbf{x}^\phi)=0$. Performing the suggested substitution of (3.40) in (3.39) compensates for the blurring and yields the correct amplitude behavior. Using $|\mathbf{p}^m(\mathbf{y})| \approx |\mathbf{p}^\phi|$ and $\boldsymbol{\nu}^\phi(\mathbf{y})\cdot\boldsymbol{\nu}^m(\mathbf{y}) = 1$ at a specular reflection, yields (see Ursin (2003) for a detailed

derivation)

$$\hat{\mathbf{c}}^{(1)}(\mathbf{y})\big|_{\phi(\mathbf{y})=0}\, w(|\mathbf{p}^{\phi}(\mathbf{x}^{\phi})|\boldsymbol{\nu}^{\phi}\cdot(\mathbf{y}-\mathbf{x}^{\phi})) = \int_{E_\nu}\langle\boldsymbol{\Lambda}(\boldsymbol{\nu}^m;\mathbf{y})\rangle^{-1} \cdot \int_{E_\theta}\mathbf{r}(\mathbf{x}^r,\mathbf{y},\mathbf{x}^s)\partial_t\tilde{u}(\mathbf{x}^r,T(\mathbf{x}^r,\mathbf{y},\mathbf{x}^s),\mathbf{x}^s;\mathbf{y})|\mathbf{p}^m(\mathbf{y})|^2 d\theta d\nu. \quad (3.41)$$

Note that the order of $|\mathbf{p}^m(\mathbf{y})|$ has now changed in the integrand. Using phase velocities normal to the surface, the so-called *stretch factor* (Tygel *et al.*, 1994) is given by

$$|\mathbf{p}^{\phi}| = \frac{1}{v^s}+\frac{1}{v^r}, \quad (3.42)$$

where v^s and v^r are the phase velocities of the rays from the source and receiver in the direction of the interface normal, $\boldsymbol{\nu}^{\phi}$. We proceed similarily for migration and get

$$\hat{S}(\theta;\mathbf{y})\Big|_{\phi(\mathbf{y})=0}\, w(|\mathbf{p}^{\phi}(\mathbf{x}^{\phi})|\boldsymbol{\nu}^{\phi}\cdot(\mathbf{y}-\mathbf{x}^{\phi})) = \int_{E_\nu}\partial_t\tilde{u}(\mathbf{x}^r,T(\mathbf{x}^r,\mathbf{y},\mathbf{x}^s),\mathbf{x}^s;\mathbf{y})|\mathbf{p}^m(\mathbf{y})|^2 d\nu. \quad (3.43)$$

Here, the factor $|\mathbf{p}^{\phi}|$ evaluated at the stationary point is

$$|\mathbf{p}^{\phi}| = \left[\frac{1}{(v^s)^2}+\frac{1}{(v^r)^2}+\frac{2\cos\theta}{v^s v^r}\right]^{1/2}, \quad (3.44)$$

where the phase velocities v^s and v^r are in the directions calculated from Snell's law using that $\boldsymbol{\nu}^m = \boldsymbol{\nu}^{\phi}$.

For velocity estimation and estimation of the geological dip, a pointwise correction for the radiation patterns (for each scattering angle) can be applied in this migration procedure. This AVA-compensated migration was introduced by Brandberg-Dahl *et al* (1999; 2003b) under the name *restricted inverse GRT*. The result is an estimate of the perturbations in model parameters, which are functions of scattering angle (Ursin, 2003):

$$\hat{\mathbf{c}}^{(1)}(\theta;\mathbf{y})\big|_{\phi(\mathbf{y})=0}\, w(|\mathbf{p}^{\phi}(\mathbf{x}^{\phi})|\boldsymbol{\nu}^{\phi}\cdot(\mathbf{y}-\mathbf{x}^{\phi})) = \int_{E_\nu}\frac{\mathbf{r}(\mathbf{x}^r,\mathbf{y},\mathbf{x}^s)}{|\mathbf{r}(\mathbf{x}^r,\mathbf{y},\mathbf{x}^s)|^2}\partial_t\tilde{u}(\mathbf{x}^r,T(\mathbf{x}^r,\mathbf{y},\mathbf{x}^s),\mathbf{x}^s;\mathbf{y})|\mathbf{p}^m(\mathbf{y})|^2 d\nu, \quad (3.45)$$

assuming $|\mathbf{r}(\mathbf{x}^r,\mathbf{y},\mathbf{x}^s)| \neq 0$. The factor $\mathbf{r}(\mathbf{x}^r,\mathbf{y},\mathbf{x}^s)/|\mathbf{r}(\mathbf{x}^r,\mathbf{y},\mathbf{x}^s)|^2$ is a simplified pseudo-inverse of the radiation patterns for each scattering angle compared to the one by Brandsberg-Dahl *et al* (2003a). Velocity analysis can be performed by studying the residual moveout of the common-image gathers created as a linear combination of the inversion results in

equation (3.45). We use the linear combination corresponding to the normalized radiation patterns $\mathbf{e}(\mathbf{x}^r, \mathbf{x}, \mathbf{x}^s) = \mathbf{r}(\mathbf{x}^r, \mathbf{x}, \mathbf{x}^s)/|\mathbf{r}(\mathbf{x}^r, \mathbf{x}, \mathbf{x}^s)|$ evaluated for specular reflection and simply denoted $\mathbf{e}(\theta; \mathbf{y})$. This yields the image

$$\mathcal{I}(\theta; \mathbf{y}) = \mathbf{e}(\theta; \mathbf{y}) \cdot \hat{\mathbf{c}}^{(1)}(\theta; \mathbf{y})\big|_{\phi(\mathbf{y})} w(|\mathbf{p}^\phi(\mathbf{x}^\phi)|\boldsymbol{\nu}^\phi \cdot (\mathbf{y} - \mathbf{x}^\phi)). \tag{3.46}$$

For a heterogeneous isotropic background medium, the radiation patterns $\mathbf{r}(\mathbf{x}^r, \mathbf{y}, \mathbf{x}^s)$ do not depend on the migration dip. Then

$$\mathcal{I}(\theta; \mathbf{y}) = \frac{1}{|\mathbf{r}(\theta; \mathbf{y})|} \hat{S}(\theta; \mathbf{y})\Big|_{\phi(\mathbf{y})=0} w(|\mathbf{p}^\phi(\mathbf{x}^\phi)|\boldsymbol{\nu}^\phi \cdot (\mathbf{y} - \mathbf{x}^\phi)), \tag{3.47}$$

where $|\mathbf{r}(\theta; \mathbf{y})|$ is the norm of the radiation patterns for scattering angle θ evaluated at the image point $\mathbf{y}$.

3.7 Large parameter-contrast modeling and migration

The cylindrical surface-scattering inversion/migration formula derived in the previous section corresponds to using a linearized plane-wave reflection coefficient. This is valid only for small contrasts in the medium perturbations and for pre-critical reflection angles at the reflecting surface. Ursin (2003) extended this to large angles and large parameter contrasts by introducing the horizontal slowness component $\mathbf{p}^h = p^h \boldsymbol{\nu}^h$, where $\boldsymbol{\nu}^h$ is the in-plane unit vector orthogonal to $\boldsymbol{\nu}^m$ and p^h is the magnitude of $\mathbf{p}^h$. The component associated with the source is defined from $\mathbf{p}^s(\mathbf{x}) = \mathbf{p}^h(\mathbf{x}) + \boldsymbol{\nu}^m(\mathbf{x})(\mathbf{p}^s \cdot \boldsymbol{\nu}^m)(\mathbf{x})$, where $(\mathbf{p}^s \cdot \boldsymbol{\nu}^m)(\mathbf{x})$ is the projection of $\mathbf{p}^s$ onto $\boldsymbol{\nu}^m$ (see Figure 3.1). Also we have $\mathbf{p}^r(\mathbf{x}) = -\mathbf{p}^h(\mathbf{x}) + \boldsymbol{\nu}^m(\mathbf{x})(\mathbf{p}^s \cdot \boldsymbol{\nu}^m)(\mathbf{x})$, by Snell's law. Interchanging the source and the receiver and keeping the wave modes in the different parts of the medium the same, results in the same modeling integral. This gives us the condition for reciprocity (Chapman, 1994). We let R be the reciprocal reflection coefficient normalized by the vertical energy flux at the scattering surface with the horizontal slowness as the argument. The surface modeling formula in 2.5-D is then

$$\begin{aligned} U^{(1)}_{pq}(\mathbf{x}^r, \omega, \mathbf{x}^s) = &-\sqrt{2\pi}|\omega|^{1/2} e^{i(3\pi/4)\operatorname{sgn}\omega} \\ &\cdot \int_\Sigma h_p(\mathbf{x}^r) \frac{A^{||}(\mathbf{x}^r, \mathbf{x}) A^{||}(\mathbf{x}, \mathbf{x}^s)}{\mathcal{L}^\perp_R(\mathbf{x}^r, \mathbf{x}, \mathbf{x}^s)} R(p^h \boldsymbol{\nu}^h(\mathbf{x})) 2\rho^{(0)}(\mathbf{x}) \\ &\quad \cdot [V^r(\mathbf{x}) \cos\alpha^r(\mathbf{x}) V^s(\mathbf{x}) \cos\alpha^s(\mathbf{x})]^{1/2} \\ &\quad\quad \cdot e^{i\omega T(\mathbf{x}^r, \mathbf{x}, \mathbf{x}^s)} (\boldsymbol{\nu}^\phi(\mathbf{x}) \cdot \boldsymbol{\nu}^m(\mathbf{x})) h_q(\mathbf{x}^s) d\sigma. \end{aligned} \tag{3.48}$$

Here, V^s and V^r are the group velocities associated with the rays connecting the scattering point with the source and receiver, respectively, and α^s and α^r are the angles the group velocity vectors of the rays from the source and receiver make with the surface normal at

the reflection point.

By comparing equation (3.48) with the Born-Helmholtz integral (3.38), we proceed as in the last section and multiply by the appropriate factors. The inversion result for band-limited source then becomes

$$\hat{R}(p^h \boldsymbol{\nu}^h(\mathbf{y}))\Big|_{\phi(\mathbf{y})=0} w(|\mathbf{p}^\phi(\mathbf{x}^\phi)|\boldsymbol{\nu}^\phi \cdot (\mathbf{y}-\mathbf{x}^\phi)) = \\ -\int_{E_\nu} \frac{\partial_t \tilde{u}(\mathbf{x}^r, T(\mathbf{x}^r,\mathbf{y},\mathbf{x}^s),\mathbf{x}^s;\mathbf{y})|\mathbf{p}^m(\mathbf{y})|}{2[V^r(\mathbf{y})\cos\alpha^r(\mathbf{y})V^s(\mathbf{y})\cos\alpha^s(\mathbf{y})]^{1/2}} d\nu \quad (3.49)$$

The time derivative of the corrected data (3.29) acts on the phase-corrected data only as in the previous section given explicitly in Appendix 3.B, equation (3.B-12). The factor $|\mathbf{p}^\phi|$ is found from equation (3.44).

3.8 Orthorhombic and TI media

Under the assumptions of 2.5-D (out-of-plane slowness zero and anisotropic symmetry plane) the Christoffel-matrix splits into qP-qSV-waves with polarization vectors h_1 and h_3 ($h_2 = 0$) in the plane and a pure SH-wave, still traveling in the plane but with polarization vector h_2 ($h_1 = h_3 = 0$). The SH-wave cannot be generated by an incoming qP- or qSV-wave, so in effect we are only considering the in-plane qP-qSV-waves for PP, SVSV and PSV scattering (we disregard SVP scattering as it gives the same result as does PSV scattering in the following) and SH-waves for SHSH scattering. In the following, we consider an orthorhombic medium (the (x_1, x_3)-plane is assumed to be one of the symmetry planes) and a transversely isotropic medium with the symmetry axis within the (x_1, x_3)-plane. In the natural coordinate system of the medium (the crystal system) the media share the following Christoffel matrix (Rüger, 1996):

$$\begin{bmatrix} c_{11}p_1^2 + c_{55}p_3^2 - \rho v^2 & 0 & (c_{13}+c_{55})p_1p_3 \\ 0 & c_{66}p_1^2 + c_{44}p_3^2 - \rho v^2 & 0 \\ (c_{13}+c_{55})p_1p_3 & 0 & c_{55}p_1^2 + c_{33}p_3^2 - \rho v^2 \end{bmatrix} \begin{bmatrix} h_1 \\ h_2 \\ h_3 \end{bmatrix} = \mathbf{0}, \quad (3.50)$$

but for TI media, $c_{44} = c_{55}$ (in the Voigt-notation). v is the phase velocity of the corresponding wave mode. It can be shown, using a Bond transformation (Carcione, 2001) projecting the natural coordinate system onto the global one in the plane of consideration, that the matrix (3.50) still splits and has the same parameters ρ, c_{11}, c_{13}, c_{33} and c_{55} governing the qP- and qSV-waves, and ρ, c_{44} and c_{66} governing the pure SH-wave, but with a different mixture than the one above. The following discussion is then directly applicable to tilted symmetries, but we restrict our attention to orthorhombic media where the intersection of the two symmetry-planes is parallel to the x_3-axis, and to TI media with

the x_3-axis as the vertical symmetry axis (TIV). The expressions used in the following calculations are found in Rüger (1996), Carcione (2001), Tsvankin (2001) and Ettrich *et al.* (2002).

3.8.1 The qP- and qSV-wave system

Using ray-tracing equations (3.6) and (3.7) (or matrix (3.50)) we observe that by using either of the two media as a background medium, all in-plane kinematic aspects of qP- and qSV-waves are governed by the same five parameters, $c_{11}^{(0)}$, $c_{13}^{(0)}$, $c_{33}^{(0)}$, $c_{55}^{(0)}$ and $\rho^{(0)}$ (in Voigt notation). This means that velocity analysis in 2.5-D (Brandsberg-Dahl *et al.*, 1999), based on study of common-image gathers of PP, PSV or SVSV scattering created from equation (3.46), can be based only on these parameters in both TIV and orthorhomic media. That the two media are kinematically the same in the symmetry plane was also observed by Rüger (1996). The amplitudes, however, are different for the two media due to the difference in the out-of-plane geometrical spreading in equation (3.24). While for TIV media all parameters needed to calculate the geometrical spreading are the same as those that govern the in-plane kinematics, for qP- and qSV-waves in orthorhombic media one needs information on all independent parameters except $c_{22}^{(0)}$ (see Ettrich *et al* (2002) for expressions). This means that one needs information on more parameters than can be obtained from 2.5-D velocity analysis of PP, PSV and SVSV scattering.

Scattering coefficient (3.16) is a vector product of the radiation patterns (3.18) and the medium perturbations (3.17). Since $p_2 = 0$ and $h_2 = 0$ in the radiation patterns for the qP/qSV-system, the medium perturbation with either $i, j, k, l = 2$ in the $c_{ijkl}^{(1)}$ will not contribute to the scattering coefficient. This means that the only medium perturbations that give any contribution are the five parameters $c_{1111}^{(1)}$, $c_{1133}^{(1)}$, $c_{3333}^{(1)}$, $c_{1313}^{(1)}$ (i.e., $c_{11}^{(1)}$, $c_{13}^{(1)}$, $c_{33}^{(1)}$ and $c_{55}^{(1)}$ in Voigt notation) and $\rho^{(1)}$. These are the same parameters that we need to calculate kinematic aspects in the two background media. This particularity is restricted to the 2.5-D inversion, but is not true for 3-D inversion (Brandsberg-Dahl *et al.*, 2003a). These parameters are the only parameters one can invert for in TIV or orthorhombic medium, e.g., using equations (3.27) or (3.41). Since the out-of-plane geometrical spreading differs for these two types of media, the appropriate background medium has to be used to get the correct amplitude behavior.

For both types of media, we remove the radiation patterns by a pseudo-inverse to get the medium perturbations. Resolution analysis in the sense of De Hoop *et al.* (1999) gives estimates on the ability to recover the parameters by removing the radiation patterns in this way. This is done by studying the so-called *resolution matrix*,

$$\langle \mathbf{\Lambda}(\boldsymbol{\nu}^m; \mathbf{y}) \rangle^{-1} \mathbf{\Lambda}(\boldsymbol{\nu}^m; \mathbf{y}), \tag{3.51}$$

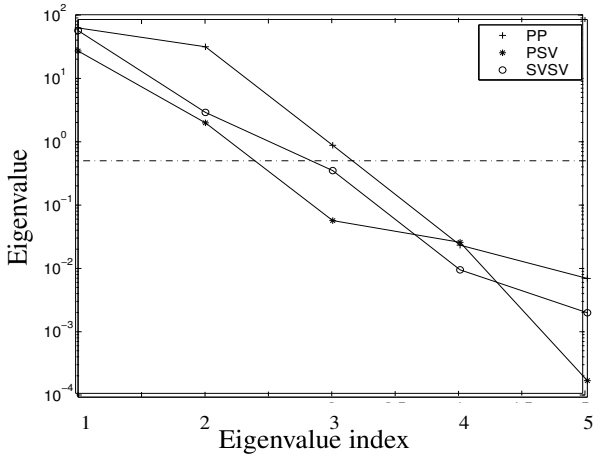

Figure 3.2: The eigenvalues of the $\mathbf{\Lambda}$-matrix (3.28) for PP and PS scattering. Horizontal line indicates 10^{-2} of the largest eigenvalue. The large difference in the eigenvalues indicate an instability in the inversion.

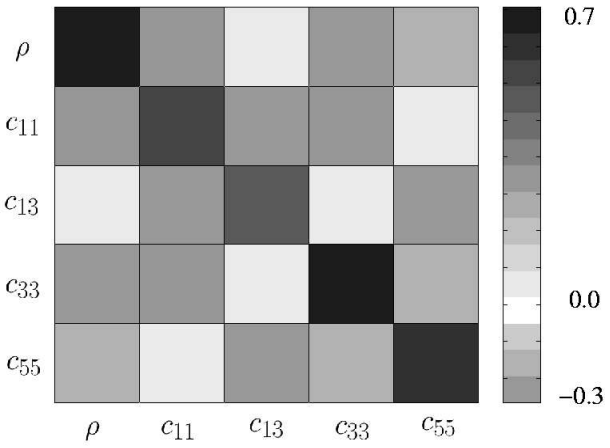

Figure 3.3: The resolution matrix for PP scattering. The non-zero elements off the diagonal indicate the inability to remove the radiation pattterns in direct inversion. The axes indicate the connection to the different parameters through equation (3.16).

ideally considered to be the identity in the derivation of the inversion formulas (see the discussion of equations (3.B-6) to (3.B-7) in Appendix 3.B). Choosing, e.g., an orthorhombic background medium with density-normalized stiffness parameters (in MPa): $a_{11} = 9$, $a_{13} = 2.25$, $a_{33} = 5.9275$ and $a_{55} = 1.6$ (Schoenberg & Helbig, 1997) and letting the range of scattering angles be $E_\theta = \langle 0, \pi/2 \rangle$ for a given migration dip, we construct the $\mathbf{\Lambda}$-matrices for PP, PSV and SVSV scattering. Figure 3.2 shows the five eigenvalues for the three types of scattering, in a singular value decomposition (SVD) (the multiplication of the averaged phase velocities in equation (3.18) is vital in order to stabilize the numerical calculation here). Note that the ratio of the largest to the smallest eigenvalue is large. Thus the inverse by SVD, using all eigenvalues, is unstable in the sense that the small eigenvalues lead to large contributions in the inversion. Indicated in the figure is a suggested threshold for PP, PSV and SVSV at 10^{-2} of the largest eigenvalue for all cases. Eigenvalues below this value are disregarded in order to stabilize the procedure. Figures 3.3, 3.4, and 3.5 shows the resulting matrix (3.51) for PP, PSV and SVSV scattering, respectively. In the figures, we consider only how far from zero (i.e., from white) are the values off the diagonal. Because the matrices are not identity matrices, the radiation patterns are not completely removed as is assumed in the deriviation of the inversion results, equations (3.27) and (3.41), giving poor resolution of the parameters. For PP scattering, the main diagonal contains large values, but also sizable values exists off the diagonal. For PSV and SVSV scattering, only the density and c_{55} have strong values on the diagonal, with some modest amplitudes off the diagonal. In all cases, parameters involved in vertical acoustic impedances are well resolved, i.e., ρ and c_{33} for PP, and ρ and c_{55} for PSV and SVSV, the parameters that we usually observe best (Dębski & Tarantola, 1995). The radiation patterns are not well removed for the other parameters. The results deteriorate further when using a smaller range of scattering angles E_θ.

3.8.2 The SH-wave system

All kinematic aspects of SH-waves in the background medium are governed by $c_{44}^{(0)}$ and $c_{66}^{(0)}$ for both orthorhombic and TIV media, but as remarked earlier, for TIV media $c_{44}^{(0)} = c_{55}^{(0)}$. These parameters are the only ones that can be found from velocity analysis studying SHSH scattering by equation (3.46). They are also the only parameters needed to calculate the out-of-plane geometrical spreading for a TIV medium. For an orthorhombic medium we need information on all independent parameters. Thus, just as in the previous section, information on more parameters are needed than one actually can get from 2.5-D velocity analysis by equation (3.46) using PP, PSV, SVSV and SHSH scattering .

Since the in-plane polarization vectors are zero for SH-waves, the only parameters we can invert for (by the same argument as in the previous section) are ρ, $c_{2323}^{(1)}$ and $c_{1212}^{(1)}$ (or

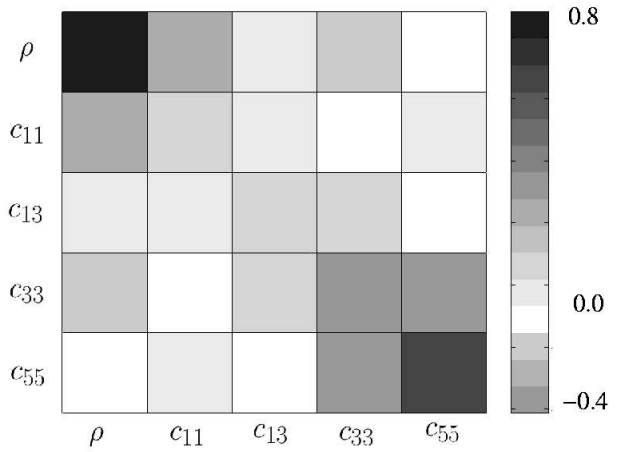

Figure 3.4: The resolution matrix for PSV scattering. Low values on the diagonal indicate low resolution of parameters c_{11} and c_{13}.

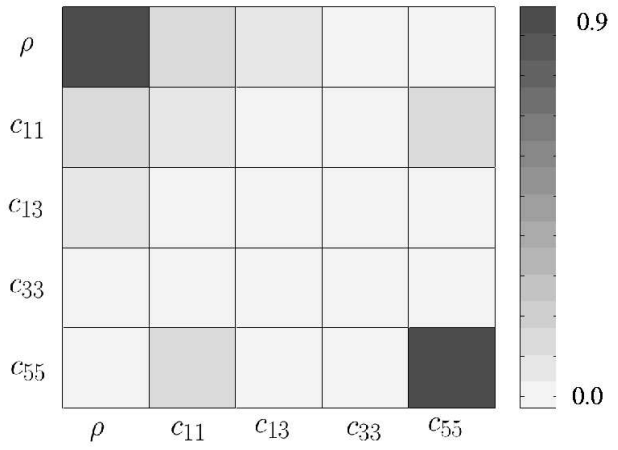

Figure 3.5: The resolution matrix for the SVSV scattering.

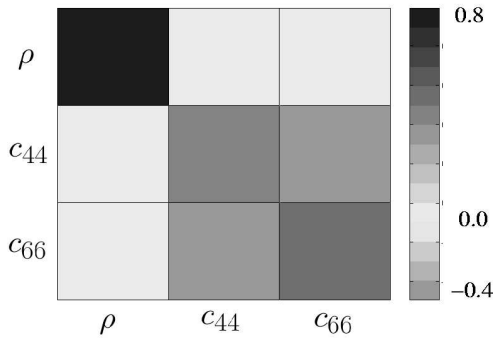

Figure 3.6: The resolution matrix for the SHSH scattering.

ρ, $c_{44}^{(1)}$ and $c_{66}^{(1)}$ in the Voigt notation) for both TIV and orthorhombic media. We calculate the resolution matrix (3.51) in the orthorhombic medium of the previous section for SHSH scattering with additional density-normalized parameters (in MPa): $a_{44} = 2$ and $a_{66} = 2.182$, and we use the same range of scattering angles. Only the eigenvalues of $\mathbf{\Lambda}$ that are larger than 10^{-2} of the largest eigenvalue are used when constructing the inverse by SVD (as in the previous section). The result, given in Figure 3.6, is again far from being an identity matrix.

The above result suggests that direct inversion yields unreliable parameter estimates. A true-amplitude migration, e.g. using equation (3.30) or (3.49), followed by amplitude-versus-angle analysis (Hilterman, 2001) to invert for the parameters, is much better constrained (Sollid, 2000).

3.9 Conclusions

We have reviewed 2.5-D modeling and derived formulas for true-amplitude inversion, and migration and AVA-compensated migration in anisotropic media, using the inverse GRT. The formulas use natural integration variables at the imaging point and require no calculation of a Jacobian.

Analysis of orthorhombic media and tilted TI media have been done based on the formulas derived in this paper. The use of either form of anisotropy for the background medium yields no kinematic distinction. For example, velocity analysis for both types of media is the same. Amplitudes, however, depend on particular parameters, through the out-of-plane geometrical spreading, which are different for the two types. While for a TIV medium the parameters are the same as those involved in the in-plane considerations, in

orthorhombic media the out-of-plane geometrical spreading depend on additional parameters that one cannot find through either velocity analysis, as suggested in this paper, or inversion/migration in 2.5-D.

The inversion formula relies on the ability to separate the radiation patterns from the medium perturbations in the scattering coefficient. This, however, cannot be done sufficiently in an orthorhombic media. Hence the inversion result will be a mixture of the actual medium perturbations and remnants of the radiation patterns.

Acknowledgement

The authors thank Center of Wave Phenomena for the possibility to stay as guests for the fall of 2001 to the summer of 2002 and Ken Larner and Norman Bleistein for giving their comments on the manuscript. We also thank M. V. de Hoop for helpful discussions. S.-K. Foss would also like to thank the URE-project at NTNU, Trondheim, Norway for its financial support.

Appendix 3.A. The 2-D inversion formula

For a real and causal function $f(\mathbf{x},t)$, with $\mathbf{x},\mathbf{k}\in\mathbb{R}^2$, we use the Fourier transform (Aki & Richards, 1980, Box 5.2)

$$F(\mathbf{k},\omega)=\int_0^\infty\int_{\mathbb{R}^2} f(\mathbf{x},t)e^{i(\omega t-\mathbf{k}\cdot\mathbf{x})}d\mathbf{x}dt, \tag{3.A-1}$$

with inverse transform

$$f(\mathbf{x},t)=\frac{1}{\pi}Re\int_0^\infty\frac{1}{4\pi^2}\int_{\mathbb{R}^2}F(\mathbf{k},\omega)e^{-i(\omega t-\mathbf{k}\cdot\mathbf{x})}d\mathbf{k}d\omega. \tag{3.A-2}$$

$\mathbf{k}$ is usually referred to as the wavenumber. The following identity will give the inversion formula

$$\frac{1}{(2\pi)^2}\int_{\mathbb{R}^2}e^{i\mathbf{k}\cdot(\mathbf{x}-\mathbf{y})}d\mathbf{k}=\delta(\mathbf{x}-\mathbf{y}). \tag{3.A-3}$$

We introduce the equivalent of polar coordinates, where we let the radius be $k=\sqrt{k_1^2+k_2^2}$ and the angle ν be such that

$$\begin{aligned}\mathbf{k}&=k(\cos\nu,\sin\nu)=(k_1,k_2)\\&=k\boldsymbol{\nu}^m.\end{aligned} \tag{3.A-4}$$

Using this parametrization in integral (3.A-3) we get

$$\int_0^\infty k\int_0^{2\pi}e^{ik\boldsymbol{\nu}^m\cdot(\mathbf{x}-\mathbf{y})}d\nu dk=4\pi^2\delta(\mathbf{x}-\mathbf{y}). \tag{3.A-5}$$

In the framework of wave propagation, the wavenumber is $\mathbf{k}=\omega\mathbf{p}^m(\mathbf{y})$. We substitute this into equation (3.A-5) and take the real part on both sides to get

$$Re\left\{\int_0^\infty\omega d\omega\int_0^{2\pi}|\mathbf{p}^m(\mathbf{y})|^2d\nu e^{i\omega\mathbf{p}^m(\mathbf{y})\cdot(\mathbf{x}-\mathbf{y})}\right\}=4\pi^2\delta(\mathbf{x}-\mathbf{y}). \tag{3.A-6}$$

After a preconditioning of the data given in the main text, we use Taylor expansions (Beylkin, 1984) of amplitudes, polarization vectors, and phase functions around $\mathbf{x}$ (as done in detail in Appendix 3.B). The first term in the expansion has the form of the inversion formula in equation (3.A-3). The result is the inversion formula

$$\begin{aligned}\frac{1}{\pi}Re\left\{\int_0^\infty\omega d\omega\frac{1}{4\pi}\int_{E_\nu}|\mathbf{p}^m(\mathbf{y})|^2d\nu[1+\mathcal{O}(|\mathbf{x}-\mathbf{y}|)]e^{i\omega[\mathbf{p}^m(\mathbf{y})\cdot(\mathbf{x}-\mathbf{y})+\mathcal{O}(|\mathbf{x}-\mathbf{y}|^2)]}\right\}\\=\delta(\mathbf{x}-\mathbf{y})+\text{smoother terms.}\end{aligned} \tag{3.A-7}$$

Integration of the other terms of the Taylor expansion yields smoother amplitude terms by the Bolker conditions (Guillemin, 1985) or the equivalent traveltime injectivity conditions

(Stolk, 2000). They are discarded in inversion for the most singular term. E_ν is the domain of ν here considered to be $E_\nu = [0, 2\pi\rangle$. In practise one uses a smaller range of migration dip angles, ν, which makes the delta function in equation (3.A-5) a band-limited delta function (Bleistein, 1984). This follows over to the inversion formula (3.A-7).

Appendix 3.B. 2.5-D inversion of the Born modeling equation

By the following inversion we get the most singular part of the medium perturbations $\mathbf{c}^{(1)}$ (de Hoop *et al.*, 1999). This means that we disregard the smoother terms. The inversion makes use of the inversion formula (3.A-7). The imaging point, $\mathbf{y}$, is the spatial point in the subsurface at which we invert for the rock parameters. In order to get our modeling formula into the appropriate form, we precondition our data u_{mn} in equation (3.26) with factors evaluated at the imaging point and the polarization vectors at the source and receiver given in equation (3.29)

$$\tilde{U}(\mathbf{x}^r,\omega,\mathbf{x}^s;\mathbf{y}) = \frac{1}{2\,(2\pi)^{3/2}}\frac{e^{-i\frac{\pi}{4}\mathrm{sgn}\,\omega}}{|\omega|^{1/2}}h_m(\mathbf{x}^r;\mathbf{y})U^{(1)}_{mn}(\mathbf{x}^r,\omega,\mathbf{x}^s)h_n(\mathbf{x}^s;\mathbf{y})\frac{\mathcal{L}^{\perp}_R(\mathbf{x}^r,\mathbf{y},\mathbf{x}^s)}{\rho^{(0)}(\mathbf{y})A^{||}(\mathbf{x}^r,\mathbf{y})A^{||}(\mathbf{y},\mathbf{x}^s)}e^{-i\omega T(\mathbf{x}^r,\mathbf{y},\mathbf{x}^s)}. \tag{3.B-1}$$

After this preconditioning, we perform a Taylor expansion of the resulting amplitude terms, phase function and polarization vectors in the integral around the imaging point $\mathbf{y}$,

$$\begin{aligned}
\omega(T(\mathbf{x}^r,\mathbf{x},\mathbf{x}^s)-T(\mathbf{x}^r,\mathbf{y},\mathbf{x}^s)) &= \omega\nabla T(\mathbf{x}^r,\mathbf{y},\mathbf{x}^s)\cdot(\mathbf{x}-\mathbf{y})+\mathcal{O}(|\mathbf{x}-\mathbf{y}|^2),\\
\frac{A^{||}(\mathbf{x}^r,\mathbf{x})A^{||}(\mathbf{x},\mathbf{x}^s)\mathcal{L}^{\perp}(\mathbf{x}^r,\mathbf{y},\mathbf{x}^s)}{A^{||}(\mathbf{x}^r,\mathbf{y})A^{||}(\mathbf{y},\mathbf{x}^s)\mathcal{L}^{\perp}(\mathbf{x}^r,\mathbf{x},\mathbf{x}^s)} &= 1+\mathcal{O}(|\mathbf{x}-\mathbf{y}|),\\
h_m(\mathbf{x}^r)h_m(\mathbf{x}^r;\mathbf{y}) &= 1+\mathcal{O}(|\mathbf{x}-\mathbf{y}|),\\
h_n(\mathbf{x}^s)h_n(\mathbf{x}^s;\mathbf{y}) &= 1+\mathcal{O}(|\mathbf{x}-\mathbf{y}|),
\end{aligned} \tag{3.B-2}$$

where we have used that the polarization vectors are normalized. This means that, after a multiplication with $|\mathbf{p}^m(\mathbf{y})|^2$ and $1/\pi$ on both sides, equation (3.26) preconditioned using equation (3.B-1), becomes

$$\begin{aligned}
&\frac{1}{\pi}\tilde{U}(\mathbf{x}^r,\omega,\mathbf{x}^s;\mathbf{y})|\mathbf{p}^m(\mathbf{y})|^2\\
&=\frac{\omega|\mathbf{p}^m(\mathbf{y})|^2}{(2\pi)^2}\int_{\mathcal{D}(x_2=0)}[1+\mathcal{O}(|\mathbf{x}-\mathbf{y}|)]\mathbf{r}^T(\mathbf{x}^r,\mathbf{x},\mathbf{x}^s)\mathbf{c}^{(1)}(\mathbf{x})e^{i\omega[\nabla T\cdot(\mathbf{x}-\mathbf{y})+\mathcal{O}(|\mathbf{x}-\mathbf{y}|^2)]}d\mathbf{x}.
\end{aligned} \tag{3.B-3}$$

We wish to remove the amplitude variation of the radiation patterns in order to invert for the medium perturbation only. Multiplying both sides with the radiation patterns (3.18) at the image point, $\mathbf{r}(\mathbf{x}^r,\mathbf{y},\mathbf{x}^s)$, and using the Taylor expansion

$$\mathbf{r}(\mathbf{x}^r,\mathbf{y},\mathbf{x}^s)\mathbf{r}^T(\mathbf{x}^r,\mathbf{x},\mathbf{x}^s)=\mathbf{r}(\mathbf{x}^r,\mathbf{y},\mathbf{x}^s)\mathbf{r}^T(\mathbf{x}^r,\mathbf{y},\mathbf{x}^s)+\mathcal{O}(|\mathbf{x}-\mathbf{y}|), \tag{3.B-4}$$

we can write

$$\frac{1}{\pi}\mathbf{r}(\mathbf{x}^r,\mathbf{y},\mathbf{x}^s)\tilde{U}(\mathbf{x}^r,\omega,\mathbf{x}^s;\mathbf{y})|\mathbf{p}^m(\mathbf{y})|^2$$
$$= \frac{\omega|\mathbf{p}^m(\mathbf{y})|^2}{(2\pi)^2}\int_{\mathcal{D}(x_2=0)}\mathbf{r}(\mathbf{x}^r,\mathbf{y},\mathbf{x}^s)\mathbf{r}^T(\mathbf{x}^r,\mathbf{y},\mathbf{x}^s)[1+\mathcal{O}(|\mathbf{x}-\mathbf{y}|)]$$
$$\cdot\,\mathbf{c}^{(1)}(\mathbf{x})e^{i\omega[\nabla T\cdot(\mathbf{x}-\mathbf{y})+\mathcal{O}(|\mathbf{x}-\mathbf{y}|^2)]}d\mathbf{x}. \quad (3.B\text{-}5)$$

The radiation patterns are dependent on the scattering angle θ (see equation (3.18) and Figure 3.1), so we integrate over θ spanning the domain E_θ (see equation equation (3.19))

$$\frac{1}{\pi}\int_{E_\theta}\mathbf{r}(\mathbf{x}^r,\mathbf{y},\mathbf{x}^s)\tilde{U}(\mathbf{x}^r,\omega,\mathbf{x}^s;\mathbf{y})|\mathbf{p}^m(\mathbf{y})|^2d\theta$$
$$= \frac{\omega|\mathbf{p}^m(\mathbf{y})|^2}{(2\pi)^2}\int_{\mathcal{D}(x_2=0)}\mathbf{\Lambda}(\boldsymbol{\nu}^m;\mathbf{y})[1+\mathcal{O}(|\mathbf{x}-\mathbf{y}|)]\mathbf{c}^{(1)}(\mathbf{x})e^{i\omega[\nabla T\cdot(\mathbf{x}-\mathbf{y})+\mathcal{O}(|\mathbf{x}-\mathbf{y}|^2)]}d\mathbf{x}, \quad (3.B\text{-}6)$$

where the $M\times M$ matrix $\mathbf{\Lambda}$ is defined in equation (3.28) in the main text. Introducing the pseudo-inverse $\langle\mathbf{\Lambda}(\boldsymbol{\nu}^m;\mathbf{y})\rangle^{-1}$ and multiplying by this factor on both sides we in effect remove the radiation patterns. This yields

$$\frac{1}{\pi}\langle\mathbf{\Lambda}(\boldsymbol{\nu}^m;\mathbf{y})\rangle^{-1}\int_{E_\theta}\mathbf{r}(\mathbf{x}^r,\mathbf{y},\mathbf{x}^s)\tilde{U}(\mathbf{x}^r,\omega,\mathbf{x}^s;\mathbf{y})|\mathbf{p}^m(\mathbf{y})|^2d\theta$$
$$\approx \frac{\omega|\mathbf{p}^m(\mathbf{y})|^2}{(2\pi)^2}\int_{\mathcal{D}(x_2=0)}[1+\mathcal{O}(|\mathbf{x}-\mathbf{y}|)]\mathbf{c}^{(1)}(\mathbf{x})e^{i\omega[\nabla T\cdot(\mathbf{x}-\mathbf{y})+\mathcal{O}(|\mathbf{x}-\mathbf{y}|^2)]}d\mathbf{x}. \quad (3.B\text{-}7)$$

Now integrate both sides over the domains of ω and $\nu\in E_\nu$ as indicated in the inversion formula (3.A-7)

$$\frac{1}{\pi}\int_0^\infty d\omega\int_{E_\nu}d\nu\langle\mathbf{\Lambda}(\boldsymbol{\nu}^m;\mathbf{y})\rangle^{-1}\int_{E_\theta}\mathbf{r}(\mathbf{x}^r,\mathbf{y},\mathbf{x}^s)\tilde{U}(\mathbf{x}^r,\omega,\mathbf{x}^s;\mathbf{y})|\mathbf{p}^m(\mathbf{y})|^2d\theta$$
$$= \int_{\mathcal{D}(x_2=0)}\mathbf{c}^{(1)}(\mathbf{x})\frac{1}{\pi}\int_0^\infty\omega d\omega\frac{1}{4\pi}\int_{E_\nu}|\mathbf{p}^m(\mathbf{y})|^2d\nu[1+\mathcal{O}(|\mathbf{x}-\mathbf{y}|)]e^{i\omega[\nabla T\cdot(\mathbf{x}-\mathbf{y})+\mathcal{O}(|\mathbf{x}-\mathbf{y}|^2)]}d\mathbf{x}. \quad (3.B\text{-}8)$$

After taking the real part here, the last part of the integrals on the right hand side now has the form of inversion formula (3.A-7). We can write them this way because of the particular terms we multiplied with in the preconditioning. We disregard the smoother terms because we are interested in the most singular term only. The resulting delta function collapses the integral over $\mathbf{x}$ and leaves the estimate of $\mathbf{c}^{(1)}$ evaluated at the imaging point

$$\hat{\mathbf{c}}^{(1)}(\mathbf{y}) = \frac{1}{\pi}Re\left\{\int_0^\infty\int_{E_\nu}\mathbf{\Lambda}^{-1}(\boldsymbol{\nu}^m;\mathbf{y})\int_{E_\theta}\mathbf{r}(\mathbf{x}^r,\mathbf{y},\mathbf{x}^s)\tilde{U}(\mathbf{x}^r,\omega,\mathbf{x}^s;\mathbf{y})|\mathbf{p}^m(\mathbf{y})|^2d\theta d\nu d\omega\right\}, \quad (3.B\text{-}9)$$

where $\tilde{U}$ is found in equation (3.B-1). This is the inversion result for the 2.5-D Born modeling formula in the Fourier domain. Note that the only factor that depends on the frequency integration is the corrected data $\tilde{U}(\mathbf{x}^r, \omega, \mathbf{x}^s; \mathbf{y})$. Because of the factor $e^{-i\omega T(\mathbf{x}^r, \mathbf{y}, \mathbf{x}^s)}$ in the corrected data (3.B-1), the integration has the form of an inverse Fourier transform

$$\begin{aligned}\tilde{u}(\mathbf{x}^r, T(\mathbf{x}^r, \mathbf{y}, \mathbf{x}^s), \mathbf{x}^s; \mathbf{y}) &= \frac{1}{\pi} Re \left\{ \int_0^\infty \tilde{U}(\mathbf{x}^r, \omega, \mathbf{x}^s; \mathbf{y}) d\omega \right\} \\ &= h_m(\mathbf{x}^r; \mathbf{y}) \tilde{u}^{(1)}_{mn}(\mathbf{x}^r, T(\mathbf{x}^r, \mathbf{y}, \mathbf{x}^s), \mathbf{x}^s) h_n(\mathbf{x}^s; \mathbf{y}) 2\sqrt{2\pi} \mathcal{L}^{\perp}_R(\mathbf{x}^r, \mathbf{y}, \mathbf{x}^s) \\ &\quad \cdot [\rho^{(0)}(\mathbf{x}^r) v(\mathbf{x}^r) v^r(\mathbf{y}) v^s(\mathbf{y}) \rho^{(0)}(\mathbf{x}^s) v(\mathbf{x}^s)]^{1/2} [Q^{||}_2(\mathbf{x}^r, \mathbf{y}) Q^{||}_2(\mathbf{y}, \mathbf{x}^s)]^{1/2}. \quad \text{(3.B-10)}\end{aligned}$$

Here we have written the amplitude factors of the 2.5-D GRA Green's function (3.25) explicitly. Due to the half integration in the corrected data (through the $e^{-i(\pi/4)\mathrm{sgn}\omega}/|\omega|^{1/2}$-factor), in equation (3.B-1), and the possible values of the KMAH-index accounting for caustics, we find the phase-corrected data by computing

$$\begin{aligned}&\tilde{u}^{(1)}_{mn}(\mathbf{x}^r, T(\mathbf{x}^r, \mathbf{y}, \mathbf{x}^s), \mathbf{x}^s) \\ &\quad = \frac{1}{\pi} Re \left\{ \int_0^\infty \frac{1}{\omega^{1/2}} U^{(1)}_{mn}(\mathbf{x}^r, \omega, \mathbf{x}^s) e^{-i\pi/4} e^{[i\pi/2(\kappa(\mathbf{x}^r, \mathbf{y}) + \kappa(\mathbf{y}, \mathbf{x}^s))]} e^{-i\omega T(\mathbf{x}^r, \mathbf{y}, \mathbf{x}^s)} d\omega \right\}. \quad \text{(3.B-11)}\end{aligned}$$

The inversion result in equation (3.B-9), using equation (3.B-11), is then given in equation (3.27) in the main text. When the inversion/migration is done for a surface, equation (3.41), the time derivative of the data is used (which in the Fourier domain is a multiplication by $-i\omega = \omega e^{-i\pi/2}$), which yields

$$\begin{aligned}&\partial_t \tilde{u}^{(1)}_{mn}(\mathbf{x}^r, T(\mathbf{x}^r, \mathbf{y}, \mathbf{x}^s), \mathbf{x}^s) \\ &\quad = \frac{1}{\pi} Re \left\{ \int_0^\infty \omega^{1/2} U^{(1)}_{mn}(\mathbf{x}^r, \omega, \mathbf{x}^s) e^{-i3\pi/4} e^{[i\pi/2(\kappa(\mathbf{x}^r, \mathbf{y}) + \kappa(\mathbf{y}, \mathbf{x}^s))]} e^{-i\omega T(\mathbf{x}^r, \mathbf{y}, \mathbf{x}^s)} d\omega \right\}. \quad \text{(3.B-12)}\end{aligned}$$

All inversion, migration and AVA-compensated migration results in this paper are derived in the same way as above.

Appendix 3.C. 2-D modeling and inversion

2-D modeling is done with a line source in a 2-D model; the response will therefore not vary along a receiver line. We derive the 2-D GRA Green's function from the 3-D GRA Green's function by summing the contributions from all point sources along the source line. This gives the response

$$U_{pq}(\mathbf{x},\omega,\mathbf{x}^s) = \int_{-\infty}^{\infty} G_{pq}(\mathbf{x},\omega,\mathbf{x}^s)dx_2^s, \tag{3.C-1}$$

where $G_{pq}(\mathbf{x},\omega,\mathbf{x}^s)$ is the 3-D GRA Green's function defined in equation (3.3). Using the same arguments as in the main text, the stationary point of the integral is found to be at $x_2^s = x_2$, so

$$\left|\frac{\partial^2 T(\mathbf{x},\mathbf{x}^s)}{\partial x_2^2}\right|_{x_2=0} = \left|\frac{1}{Q_2^{\perp}(\mathbf{x},\mathbf{x}^s)}\right|. \tag{3.C-2}$$

Approximating the integral in equation (3.C-1) by the method of stationary phase then yields the reciprocal 2-D Green's function

$$G_{pq}^{2D}(\mathbf{x},\omega,\mathbf{x}^s) = |\omega|^{-1/2} e^{i\frac{\pi}{4}\mathrm{sgn}\,\omega} h_p^s(\mathbf{x}) A^{2D}(\mathbf{x},\mathbf{x}^s) e^{i\omega T(\mathbf{x},\mathbf{x}^s)} h_q(\mathbf{x}^s), \tag{3.C-3}$$

where the 2-D amplitude function is

$$A^{2D}(\mathbf{x},\mathbf{x}^s) = \frac{e^{-i\frac{\pi}{2}\kappa(\mathbf{x},\mathbf{x}^s)\mathrm{sgn}\,\omega}}{2(2\pi)^{1/2}[\rho(\mathbf{x})v^s(\mathbf{x})\rho(\mathbf{x}^s)v(\mathbf{x}^s)]^{1/2}|Q_2^{||}(\mathbf{x},\mathbf{x}^s)|^{1/2}}, \tag{3.C-4}$$

and $Q_2^{||}$ is defined in equation (3.10). The indices p, q take on values 1 and 3, and all vectors also have components only in the x_1 and x_3 directions.

The 2-D Born single-scattering integral can be derived from the 2-D equations exactly as in the 3-D case. A line source at $\mathbf{x}^s$ will excite a line scatterer at $\mathbf{x}$, which acts as a secondary line source producing the response as $\mathbf{x}^r$. Taking into account the reciprocity of the GRA Green's function, the 2-D Born integral can be written

$$u_{mn}(\mathbf{x}^r,\omega,\mathbf{x}^s) = i\omega \int_{\mathcal{D}(x_2=0)} h_m^r(\mathbf{x}^r) A^{2D}(\mathbf{x}^r,\mathbf{x}) A^{2D}(\mathbf{x},\mathbf{x}^s) \rho^{(0)}(\mathbf{x}) S(\mathbf{x}) e^{i\omega T(\mathbf{x}^r,\mathbf{x},\mathbf{x}^s)} h_n^s(\mathbf{x}^s) d\mathbf{x}. \tag{3.C-5}$$

For inversion and migration, we proceed as in the main text and create data corrected for amplitude, phase and traveltime

$$\begin{aligned}\tilde{u}(\mathbf{x}^r, T(\mathbf{x}^r,\mathbf{y},\mathbf{x}^s),\mathbf{x}^s;\mathbf{y}) = \\ h_m(\mathbf{x}^r;\mathbf{y})\tilde{u}_{mn}^{(1)}(\mathbf{x}^r, T(\mathbf{x}^r,\mathbf{y},\mathbf{x}^s),\mathbf{x}^s) h_n(\mathbf{x}^s;\mathbf{y}) \\ \cdot 2[\rho^{(0)}(\mathbf{x}^r)v(\mathbf{x}^r)v^r(\mathbf{y})v^s(\mathbf{y})\rho^{(0)}(\mathbf{x}^s)v(\mathbf{x}^s)]^{1/2}[Q_2^{||}(\mathbf{x}^r,\mathbf{y})Q_2^{||}(\mathbf{y},\mathbf{x}^s)]^{1/2}.\end{aligned} \tag{3.C-6}$$

Here the phase-corrected data $\tilde{u}_{mn}$ are given by

$$\tilde{u}^{(1)}_{mn}(\mathbf{x}^r,t,\mathbf{x}^s) = \begin{cases} \mathcal{H}\{u^{(1)}_{mn}((\mathbf{x}^r,t,\mathbf{x}^s)\} \\ u^{(1)}_{mn}(\mathbf{x}^r,t,\mathbf{x}^s) \\ -\mathcal{H}\{u^{(1)}_{mn}(\mathbf{x}^r,t,\mathbf{x}^s)\} \\ -u^{(1)}_{mn}(\mathbf{x}^r,t,\mathbf{x}^s) \end{cases} \text{ if } \kappa(\mathbf{x}^r,\mathbf{y})+\kappa(\mathbf{y},\mathbf{x}^s) = \begin{cases} 4n \\ 4n+1 \\ 4n+2 \\ 4n+3 \end{cases} \tag{3.C-7}$$

with n being an integer, and $\mathcal{H}\{\}$ denotes the Hilbert transform (Aki & Richards, 1980, Box 5.6). With this the inversion and migration results are given by inserting the corrected data in equations (3.27) and (3.30) in the main text. The inversion is done equivalently to the derivation in Appendix 3.B using the 2-D inverse GRT in equation (3.A-7).

The derivation of the 2-D Born-Helmholtz surface modeling integral is similar to that in the main text, equation (3.38), and is given by

$$u_{mn}(\mathbf{x}^r,\omega,\mathbf{x}^s) = -\int_{\mathcal{D}(x_2=0)} h_m(\mathbf{x}^r)\rho^{(0)}(\mathbf{x})A^{2D}(\mathbf{x}^r,\mathbf{x})A^{2D}(\mathbf{x},\mathbf{x}^s)$$
$$\cdot\, \mathbf{r}^T(\mathbf{x}^r,\mathbf{x},\mathbf{x}^s)\ \mathbf{c}^{(1)}(\mathbf{x})\big|_{\phi(\mathbf{x})=0}\,\delta(\phi(\mathbf{x}))|\nabla_{\mathbf{x}}\phi(\mathbf{x})|\frac{\boldsymbol{\nu}^{\phi}(\mathbf{x})\cdot\boldsymbol{\nu}^{m}(\mathbf{x})}{|\mathbf{p}^{m}(\mathbf{x})|}e^{i\omega T(\mathbf{x}^r,\mathbf{x},\mathbf{x}^s)}h_n(\mathbf{x}^s)d\mathbf{x}. \tag{3.C-8}$$

The inversion is done by comparing the two 2-D modeling integrals (3.C-5) and (3.C-8) and multiplying with the appropriate factors. The inversions are done assuming a band-limited source wavelet. Using the time derivative of the corrected data (3.C-6) (i.e. of (3.C-7) since this is the only time dependent term), the inversion result is given by equation (3.41) with the factor $|\mathbf{p}^{\phi}|$ calculated from equation (3.42) in the main text. The migration and AVA-compensated migration formulas are given by equations (3.43) and (3.46), respectively with $|\mathbf{p}^{\phi}|$ from equation (3.44).

Part II

Tomography

Chapter 4

Depth consistent PP and PS seismic angle tomography

S.-K. Foss, B. Ursin and M.V de Hoop
In progress

Summary

The velocity-depth ambiguity in depth migration is a well known problem stemming from several factors such as, limited aperture, band-limited source and the interplay between parameters of the background medium contributing to the non-uniqueness of the problem. In addition, the isotropic assumption can cause severe depth errors in the presence of anisotropy. These are severe issues when considering PP and PS images from depth migration where geologically equivalent horizons should be mapped to the same depths. The present method is based upon the differential semblance misfit function in angle to find fitting background models. This requires amplitude-compensated angle-domain common image-point gathers to be uniform. Depth consistency between the PP and PS depth image is enforced through a regularization approach penalizing mistie between key reflectors in addition to the differential semblance misfit function.

By migration / map demigration time information is obtained on the key reflectors of the PP and PS image. This time information, which is independent of any velocity model, can be map migrated to reconstruct the reflectors in depth for a given background model enabling an automatic way to quantify the depth discrepancy in the tomographic approach.

An approximative simplification uses the normal incidence point rays in the map migration. The method is presented in a general 3-D framework allowing for the use of true depth information such as well markers and the inclusion of anisotropy. A strategy is presented to retrieve all parameters of a transversly isotropic medium with a known symmetry axis depending on the available information. This is employed on an ocean bottom seismic field data set from the North Sea.

4.1 Introduction

In this paper we show the use of differential semblance (Symes & Carazzone, 1991) misfit function to perform angle tomography on PP and PS reflection events. The misfit function associated with this approach is unique in that it depends smoothly on the velocity model. As is common in migration velocity analysis (MVA) we model the reflection data in the single scattering approximation, yielding a forward scattering operator that, given a velocity model, maps reflectors to reflections. By a gradient-based search of the model space, the range of the forward scattering operator is adapted to contain the data. Data are in the range if they can be predicted by the operator.

The differential semblance misfit function detect whether the data are in the range of the forward scattering operator (Stolk & de Hoop, 2002). They have their counterpart in the image domain: The data are in the range if the common image-point gathers (cigs) obtained from the data – parametrized by scattering angle and azimuth – are *uniform*, i.e. flat and show angle independent amplitude.

As MVA, typically, is based on a small collection of reflections, one expects an inherent non-uniqueness in the inverse problem of determining the velocity model. We consider a velocity model to be *acceptable* if the reflections are in the range of the forward scattering operator. In this paper, we combine PP and PS reflection data and search in the class of acceptable velocity models for a model that not only predicts the PP and PS reflections in time, but also ties the PP and PS images of corresponding reflectors in depth. In this so-called *co-depthing* process, one needs to ensure that the PP and PS images indeed have these reflectors in common, which requires a degree of seismic interpretation. Co-depthing can also be carried out with well data.

Classical migration velocity analysis exploits the redundancy in the data by studying the residual moveout on common image-point gathers (Al-Yahya, 1989). Flat gathers indicate a model giving sharp images. The differential semblance misfit function is a way to measure this moveout and to quantify the degree of fit by a local derivative in the redundancy parameters. These can e.g. be the offset parameter as done by Plessix *et al.* (2000) and Chauris and Noble (2001) amongst others, or the angle parameter as done by Brandsberg-Dahl *et al* (1999) and Foss *et al.* (2003b). The differential semblance measure is believed to have desirable convexity properties in a large part of the model space (Symes, 1991). This means that we can be far from the true model and still be able to obtain an optimal model. This stems from the fact that it is a local measure. Numerical results by Plessix *et al.* (2000) suggested using differential semblance to ensure global convergence and then to switch optimization procedure, when the model is sufficiently close to the true model, to a

semblance type method (Taner & Koehler, 1969). Close to the true model the semblance type method will have a shaper peak in the topology of the misfit function more apt in locating the optimal estimate.

The common image-point gathers in the angle domain for the purpose of velocity analysis are computed by the restricted GRT (de Hoop *et al.*, 1994; de Hoop *et al.*, 1999; Brandsberg-Dahl *et al.*, 2003b) or amplitude-compensated migration (Ursin, 2003). The local derivative of the differential semblance misfit function is sensitive to amplitude variations. Amplitude-compensated migration uses a point-wise partial compensation of the amplitude-versus-angle (AVA) behavior. This becomes a amplitude-preserving migration scaled by the radiation patterns. The calculation of the radiation patterns is separable from knowledge of the medium perturbations due to the linear relationship between the smooth and perturbed part of the medium in the Born approximation on which the migration procedure is based. Instead of the point-wise removal of the AVA-effects of the amplitude-compensated migration, a removal in the least-squares sense was formulated by de Hoop *et al.* (1994; 1999) in 3-D and in 2.5-D by Foss *et al.* (2003a). The restriction to scattering angle and azimuth creates artifacts (false reflectors) in the common image-point gathers in the angle domain. See (Stolk, 2000) for a thorough analysis of these. Brandsberg-Dahl *et al.* (2003a) suppressed such artifacts by a procedure called *focusing in dip* using only the contributions to the migration integral that are close to the specular reflections.

Several authors have recently approached the problem of joint PP and PS velocity analysis (Sollid, 2000; Stopin & Ehinger, 2001; Alerini *et al.*, 2002; Grechka & Tsvankin, 2002; Broto *et al.*, 2003), see (Herrenschmidt *et al.*, 2001) for a review. The diodic nature of PS reflections (Thomsen, 1999) demands a treatment of MVA different from the one with PP reflections. The diodic nature is a consequence of the fact that PS reflections are non-reciprocal in source and receiver; indeed, the reciprocal of PS is SP. It is also a well-known problem that images of a common geological reflector from PP and PS reflections often do not match in depth. There are several reasons for this. The velocity-depth ambiguity (Stork & Clayton, 1986; Bube, 1995; Bube *et al.*, 2002) is a well known problem intimately connected to ray coverage and acquisition aperture. In addition, anisotropy has to be included in order to compute depth consistent PP and PS images as an isotropic assumption can cause severe depth errors in the presence of anisotropy (Artola *et al.*, 2003). This applies especially to converted waves such as with PS events. With an anisotropic medium there is an added ambiguity in the interplay between the different elastic parameters (Bube & Meadows, 1999). Versteeg (1993) showed how continuously smoothing a correct model would recreate the image kinematically yet blurring it. All this contributes to the size of the range of the forward modeling operator; the space of possible models that recreates

the data intimately connected to the null space. However, the additional demand of tying the PP and PS events in depth constrains the space of possible solution.

PP angle tomography by means of the differential semblance misfit function in angle is here extended to PS reflection events compared to Brandsberg-Dahl *et al.* (2003b). We perform tying of PP and PS in depth between chosen *key reflectors* that geologically are the same reflectors. To perform the tying in depth of the PP and PS event we use time information, or time horizons, obtained from paired and picked events in depth which are map demigrated to time. Using map migration (Kleyn, 1977; Gjøystdal & Ursin, 1981) of the time horizons for every suggested velocity model we are able to quantify the depth mismatch in an automatic way. Notice that the time horizons need only be picked once. Map migration can be used in complex media, see Douma and de Hoop (2003) for details and references. For the converted wave events the ability to perform PS map migration is highly dependent on how close we are to the true model when starting, hence we suggest applying Gretchka and Tsvankin's 'PP+PS=SS'-approach (2002) to compute pure mode SS data for this purpose. However, in this paper we use a zero-offset restriction by map demigrating normal incidence point (NIP) rays (Hubral & Krey, 1980) as suggested by Whitcombe (1994). For the mode converted waves we employ a simplified version of the 'PP+PS=SS'-approach using NIP rays to compute approximate zero-offset SS data.

The outline of the paper is as follows. In section 2, we introduce notation and show how to compute common image-point gathers for the purpose of velocity analysis. The formulation here is in 3-D and follows the presentation of Ursin (2003); the 2.5-D formulation and its subtleties are presented in (Foss & Ursin, 2004; Foss *et al.*, 2003a). In section 3 we give a brief review of PP angle tomography (Brandsberg-Dahl *et al.*, 2003b) and its extension to PS waves. In the next section, we introduce our co-depthing methodology in the framework of the differential semblance in angle optimization by adding a penalizing term to the misfit function. Then we present a step-wise strategy, similar to (Sollid & Ettrich, 1999), using the aforementioned tomography tools to obtain values of a transversely isotropic (TI) medium with a known symmetry axis. Although the strategy is presented for a 3-D medium, we disregard the presence of azimuthal anisotropy. Such a medium is equivalent to a TI medium with a vertical symmetry axis through the Bond transformations (Carcione, 2001). It can be parameterized by v_{P0}, v_{S0}, ε and δ which are the vertical P- and S-wave velocities and the Thomsen (1986) parameters, respectively. The optimization strategy is split into the following steps:

(i) isotropic P-wave velocity analysis on PP cigs using differential semblance in angle;

(ii) isotropic S-wave velocity analysis on PS cigs using differential semblance in angle, making use of the P-wave velocity model obtained in (i);

(iii) seismic interpretation of the PP and PS images for key reflectors; map demigration of these reflectors yielding time horizons;

(iv) co-depthing of PP and PS images of key reflectors to obtain an optimal isotropic S-wave velocity model, using the differential semblance in angle of the PP and PS cigs as regularizer;

(v) differential semblance in angle and semblance optimization of PP and PS cigs jointly admitting the model to become anisotropic, enforcing the depth consistency.

Several authors have discussed that in order to obtain information on the δ parameter one either needs information of the true depth of a reflector through well logs or traveltimes from rays that have traveled at an oblique angle e.g. from strongly dipping reflectors or from large offset data (Audebert *et al.*, 2001; Iversen *et al.*, 2000). We present approaches for these cases. In the absence of such information several approaches have been suggested (Alkhalifah & Tsvankin, 1995; Grechka & Tsvankin, 2002). Here, we make the convenient choice of setting δ equal to zero considering a quasi-VTI medium. The remaining ε parameter is not the true anisotropy parameter but an effective one.

Finally, we employ the above methodology on a North Sea ocean bottom seismic (OBS) field data set to obtain first a quasi-VTI velocity model and then estimates of all parameters of a VTI velocity model.

4.2 Seismic angle migration

We consider migration in a 3-D heterogeneous anisotropic elastic medium. The geometry is shown in Figure 4.1 where the imaging point is denoted $\mathbf{y} = (y_1, y_2, y_3)$. The source is at $\mathbf{x}^s$ and receiver $\mathbf{x}^r$ (bold fonts indicate vectors). The superscripts s and r indicate association with a ray from the source and receiver, respectively. The slowness vector $\mathbf{p}^s(\mathbf{y}) = (p_1^s, p_2^s, p_3^s)$ is thus the slowness of the ray connecting the source point $\mathbf{x}^s$ and the image point $\mathbf{y}$ evaluated at this latter point. $\mathbf{p}(\mathbf{x}^s)$ indicates the slowness of the same ray evaluated at the source. A similar notation is used for the receiver, namely, $\mathbf{p}^r(\mathbf{y}) = (p_1^r, p_2^r, p_3^r)$ and $\mathbf{p}(\mathbf{x}^r)$. The polarization vector $\mathbf{h}$ is defined in the same manner as the slowness vectors at the source, receiver and imaging point. The scattering angle is defined by

$$\cos\theta = \frac{\mathbf{p}^s \cdot \mathbf{p}^r}{|\mathbf{p}^s||\mathbf{p}^r|} \quad \text{at } \mathbf{y}. \tag{4.1}$$

The scattering azimuth ψ is the angle the $(\mathbf{p}^r, \mathbf{p}^s)$-plane makes with a given reference direction around the migration slowness vector $\mathbf{p}^m$, which is defined by $\mathbf{p}^m(\mathbf{y}) = \mathbf{p}^s(\mathbf{y}) + \mathbf{p}^r(\mathbf{y})$. The migration dip $\boldsymbol{\nu}^m(\mathbf{y})$ is the unit vector of the migration slowness vector $\boldsymbol{\nu}^m(\mathbf{y}) =$

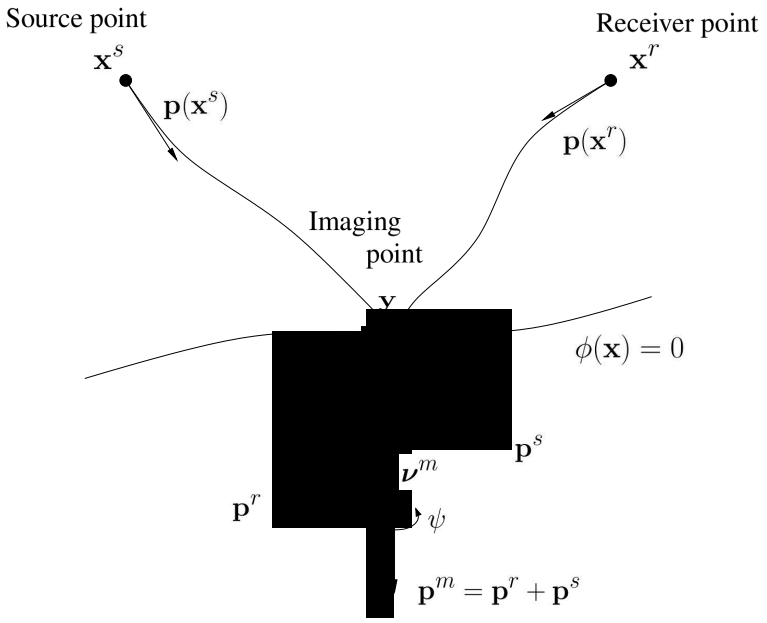

Figure 4.1: Geometry of rays connecting the imaging point with the source and the receiver.

$\mathbf{p}^m(\mathbf{y})/|\mathbf{p}^m(\mathbf{y})|$.

The medium is described by its stiffness tensor c_{ijkl} $(i,j,k,l \in \{1,..,3\})$ and density ρ. These parameters are decomposed as a sum of a smooth part (with superscript (0)) and a perturbation (with superscript (1)):

$$\rho(\mathbf{x}) = \rho^{(0)}(\mathbf{x}) + \rho^{(1)}(\mathbf{x}), \quad c_{ijkl}(\mathbf{x}) = c^{(0)}_{ijkl}(\mathbf{x}) + c^{(1)}_{ijkl}(\mathbf{x}). \tag{4.2}$$

The estimation of the smooth part is the object of velocity analysis while the medium perturbations are found by inversion. We assume that the perturbations are jumps in the parameters along an interface defined by a function $\phi(\mathbf{x}) = 0$ (de Hoop & Bleistein, 1997). Amplitude-preserving migration results in an estimate of the reflectivity at the the interface which, with a band-limited wavelet, $w(t)$, is given by (Ursin, 2003)

$$\begin{aligned}\hat{S}_w(\theta,\psi;\mathbf{y}) = \hat{S}^{(1)}(\theta,\psi;\mathbf{x}^\phi)\Big|_{\phi(\mathbf{y})} & w(p^\phi \boldsymbol{\nu}^\phi \cdot (\mathbf{y}-\mathbf{x}^\phi)) \\ & = \int_{E_{\boldsymbol{\nu}^m}} \partial_t \tilde{u}(\mathbf{x}^r, T(\mathbf{x}^r,\mathbf{y},\mathbf{x}^s),\mathbf{x}^s;\mathbf{y})|\mathbf{p}^m(\mathbf{y})|^3 d\boldsymbol{\nu}^m, \end{aligned} \tag{4.3}$$

in which $\mathbf{x}^s = \mathbf{x}^s(\mathbf{y},\boldsymbol{\nu}^m,\theta,\psi)$ and $\mathbf{x}^r = \mathbf{x}^r(\mathbf{y},\boldsymbol{\nu}^m,\theta,\psi)$ (see Figure 4.1). $\boldsymbol{\nu}^m \in E_{\boldsymbol{\nu}^m} \subset S^2$ is the integration domain of the migration dip (S^2 is the unit sphere). p^ϕ is the stretch factor

(Ursin, 2003; Tygel *et al.*, 1994) which evaluated at the stationary point $\mathbf{x}^\phi$ is given by

$$p^\phi = \left[\frac{1}{(v^s)^2} + \frac{1}{(v^r)^2} + \frac{2\cos\theta}{v^s v^r} \right]^{1/2}, \tag{4.4}$$

with phase velocities, v^s and v^r for the source and receiver ray. $\boldsymbol{\nu}^\phi$ is the surface normal at the point $\mathbf{x}^\phi$ on the interface, projected from the image point $\mathbf{y}$. The data corrected for amplitude, phase and traveltime are

$$\begin{aligned}\tilde{u}(\mathbf{x}^r, T(\mathbf{x}^r, \mathbf{y}, \mathbf{x}^s), \mathbf{x}^s; \mathbf{y}) &= h_p(\mathbf{x}^r)\tilde{u}^{(1)}_{pq}(\mathbf{x}^r, T(\mathbf{x}^r, \mathbf{y}, \mathbf{x}^s), \mathbf{x}^s)h_q(\mathbf{x}^s) \\ &\cdot 2[\rho^{(0)}(\mathbf{x}^r)v(\mathbf{x}^r)v^r(\mathbf{y})v^s(\mathbf{y})\rho^{(0)}(\mathbf{x}^s)v(\mathbf{x}^s)]^{1/2}[\det \mathbf{Q}_2(\mathbf{x}^r, \mathbf{y}) \det \mathbf{Q}_2(\mathbf{y}, \mathbf{x}^s)]^{1/2}, \end{aligned} \tag{4.5}$$

with $\tilde{u}_{pq}$ being the data corrected for a possible phase-shift due to caustics

$$\tilde{u}^{(1)}_{pq}(\mathbf{x}^r, t, \mathbf{x}^s) = \begin{cases} u^{(1)}_{pq}(\mathbf{x}^r, t, \mathbf{x}^s) \\ -\mathcal{H}\{u^{(1)}_{pq}(\mathbf{x}^r, t, \mathbf{x}^s)\} \\ -u^{(1)}_{pq}(\mathbf{x}^r, t, \mathbf{x}^s) \\ \mathcal{H}\{u^{(1)}_{pq}(\mathbf{x}^r, t, \mathbf{x}^s)\} \end{cases} \text{ if } \kappa(\mathbf{x}^r, \mathbf{y}) + \kappa(\mathbf{y}, \mathbf{x}^s) = \begin{cases} 4n \\ 4n+1 \\ 4n+2 \\ 4n+3 \end{cases} \tag{4.6}$$

Here, $\kappa(\mathbf{x}^r, \mathbf{y}) + \kappa(\mathbf{y}, \mathbf{x}^s)$ is the accumulated KMAH-index for the rays between the $\mathbf{x}^r$ and the imaging point and from the imaging point to $\mathbf{x}^s$, respectively, with n being an integer, and $\mathcal{H}\{\}$ denoting the Hilbert transform. $T(\mathbf{x}^r, \mathbf{y}, \mathbf{x}^s)$ is the two-way traveltime from source to receiver via the imaging point $\mathbf{y}$, and $\mathbf{Q}_2(\mathbf{x}^r, \mathbf{y})$ and $\mathbf{Q}_2(\mathbf{y}, \mathbf{x}^s)$ are the relative geometrical spreading for the receiver and source ray, respectively (Červený, 2001). All factors that enter in the amplitude-preserving migration formula (4.3) are calculated by kinematic and dynamic ray tracing (Červený, 2001).

In the migration formula (4.3), $\hat{S}_w(\theta, \psi; \mathbf{y})$ is a band-limited estimate of the linearized scattering coefficient defined by

$$S(\theta, \psi; \mathbf{y}) = \mathbf{r}^T(\mathbf{x}^r, \mathbf{y}, \mathbf{x}^s)\mathbf{c}^{(1)}(\mathbf{y}). \tag{4.7}$$

The relative jumps in the medium parameters are formally defined by the vector

$$\mathbf{c}^{(1)}(\mathbf{y})^T = \left\{ \frac{\rho^{(1)}(\mathbf{y})}{\rho^{(0)}(\mathbf{y})}, \frac{c^{(1)}_{ijkl}(\mathbf{y})}{\rho^{(0)}(\mathbf{y})v^s_\circ(\mathbf{y})v^r_\circ(\mathbf{y})} \right\}. \tag{4.8}$$

Its dimensionality depends on the symmetry of the elastic medium. For the PP and PS reflection problem in a VTI medium, which will be treated in the field data example, it is of dimension 5. The radiation pattern vector is of the same dimension, and it is formally given by

$$\mathbf{r}^T(\mathbf{x}^r, \mathbf{y}, \mathbf{x}^s) = \left\{ h^s_m(\mathbf{y})h^r_m(\mathbf{y}), [h^s_i(\mathbf{y})p^s_j(\mathbf{y})h^r_k(\mathbf{y})p^r_l(\mathbf{y})]v^s_\circ(\mathbf{y})v^r_\circ(\mathbf{y}) \right\}. \tag{4.9}$$

Here, $v_\circ^s$ and $v_\circ^r$ are the averaged phase velocity for the rays connecting the imaging point with the source and receiver, respectively. These are introduced for numerical purposes (Burridge *et al.*, 1998; Foss & Ursin, 2004). The indices of equation (4.9) are defined from the vector product (4.7) using the Einstein summation convention.

For the estimation of the smoothly varying parameters in the background medium (velocity analysis) we use common image-point gathers computed from amplitude-compensated migration (Ursin, 2003) given by

$$\mathcal{I}(\theta, \psi; \mathbf{y}) = \frac{\hat{S}_w(\theta, \psi; \mathbf{y})}{|\mathbf{r}(\theta, \psi; \mathbf{y})|}. \tag{4.10}$$

Here, $|\mathbf{r}(\theta, \psi; \mathbf{y})|$ is the Euclidean norm of the radiation pattern vector computed for specular reflection. The band-limited estimate of the scattering coefficient is given by (4.3). For interpretation and data comparisons we shall use the structural image

$$\mathcal{I}(\mathbf{y}) = \iint \mathcal{I}(\theta, \psi; \mathbf{y}) d\theta d\psi. \tag{4.11}$$

Subscripts are used to indicate if a current common image-point gather (4.10) or structural image (4.11) is computed from a PP- or a PS-event, $\mathcal{I}_{PP}$ and $\mathcal{I}_{PS}$, respectively.

4.3 Angle tomography

Tomography is performed to estimate the parameters describing the smooth part of the medium in equation (4.2) in which kinematic and dynamic ray tracing is performed, to compute the different factors in (4.10). These are the density at the source and receiver and the elastic stiffness tensor. For an isotropic background medium, only the P-wave velocity is required for a P-wave mode and only the S-wave velocity for an S-wave mode. Each parameter is given a parametrization with a finite number of coefficients. We assume that n coefficients, denoted $\mathbf{m} = (m_1, \ldots, m_n)$, are sufficient to describe the background medium. Common image-point angle gathers, computed using a particular set of background model parameters $\mathbf{m}$, are denoted $\mathcal{I}(\theta, \psi; \mathbf{y}, \mathbf{m})$.

The differential semblance misfit function (Symes & Carazzone, 1991; Brandsberg-Dahl *et al.*, 2003b) for PP reflections is given by

$$\mathcal{J}_{PP}(\mathbf{m}) = \frac{1}{2} \iiint |\partial_{\theta,\psi} \mathcal{I}_{PP}(\theta, \psi; \mathbf{y}, \mathbf{m})|^2 \, d\theta d\psi d\mathbf{y}. \tag{4.12}$$

A minimum of this function is found for uniform gathers indicating an optimum model and yielding sharp images. The differential semblance misfit function can be minimized

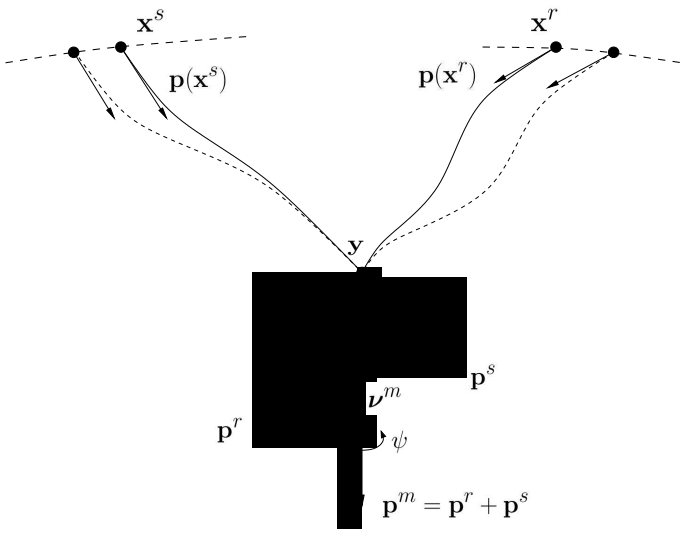

Figure 4.2: The differential semblance misfit function in angle is differentiated keeping the image point, scattering angle, azimuth and migration dip fixed. Dotted lines indicate perturbed rays.

by a gradient-based search of the model space such as a quasi-Newton method (Gill *et al.*, 1981). A component of the gradient of the misfit function (4.12), fixing the scattering angle, migration dip and scattering point, is given by (Brandsberg-Dahl *et al.*, 2003b)

$$\frac{\partial \mathcal{J}_{PP}(\mathbf{m})}{\partial m_i} = \frac{1}{2} \iiint \left(\partial_{\theta,\psi} \mathcal{I}_{PP}(\theta, \psi; \mathbf{y}, \mathbf{m})\right) \frac{\partial \partial_{\theta,\psi} \mathcal{I}_{PP}(\theta, \psi; \mathbf{y}, \mathbf{m})}{\partial m_i} d\theta d\psi d\mathbf{y}. \tag{4.13}$$

This means that, due to a change in the medium we get different source and receiver points, slownesses and two-way traveltime as indicated with dotted line in Figure 4.2. The derivative of the image in the integrand involves a derivative of the phase corrected data (4.5) found in (Brandsberg-Dahl *et al.*, 2003b). All parts of the gradient (4.13) can be calculated from imaging and paraxial ray tracing (Farra & Madariaga, 1987; Červený, 2001). Motivated by a study of Symes (2000) it is conjectured that the minimum of our misfit functions can be obtained by optimization even with poor starting values for the background medium parameters.

4.3.1 PS angle tomography

Due to the diodic nature (Thomsen, 1999) of the PS reflections we split the contributing events to the misfit function into a positive and negative constituent, denoted by $\mathcal{I}_{PS}^{+}$ and $\mathcal{I}_{PS}^{-}$ as an analogy to positive and negative offsets in surface coordinates. We will in the

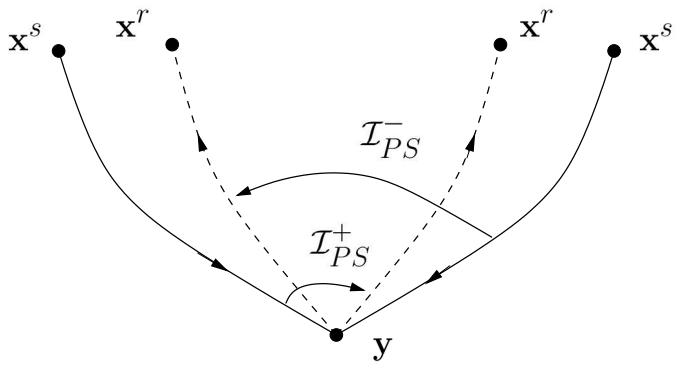

Figure 4.3: Positive and negative PS cigs, $\mathcal{I}^+_{PS}$ and $\mathcal{I}^-_{PS}$. Arrows indicate the wavefield directions in the two reflection events. The solid and dashed curves are the P- and S-wave legs, respectively, of the different events.

following refer to $\mathcal{I}^+_{PS}$ and $\mathcal{I}^-_{PS}$ as the positive and negative common image-point angle gathers, respectively. The $\mathcal{I}^+_{PS}$-cigs are computed with seismic events where the source and receiver rays intersect at the imaging point in the order of Figure 4.3 relative to the scattering angle and vice versa (opposite order of the rays) for $\mathcal{I}^-_{PS}$. This splitting is necessary in a tomographic procedure as the rays, for the two cases, travel in different parts of the background model. This is contrary to the PP reflection events which are symmetric in the sense that the positive and negative PP images are computed from rays that have traveled along the same paths in the medium, but in reverse order. The complete misfit function is given by

$$\mathcal{J}_{PS}(\mathbf{m}) = \frac{1}{2}\iiint \left\{ |\partial_{\theta,\psi}\mathcal{I}^+_{PS}(\theta,\psi;\mathbf{y},\mathbf{m})|^2 + |\partial_{\theta,\psi}\mathcal{I}^-_{PS}(\theta,\psi;\mathbf{y},\mathbf{m})|^2 \right\} d\theta d\psi d\mathbf{y}. \qquad (4.14)$$

4.4 Co-depthing the PP and PS images

Since the GRT approach is based upon a high-frequency approximation and decouples S- from P-wave propagation, we need to consider possible inconsistency in depth of reflectors common in PP and PS images. In reflection tomography we therefore incorporate a term in the misfit function that penalizes mismatch in depth of a small collection of key reflectors. A key reflector in the structural images is chosen on the basis of the following criteria: (i) coherency, and (ii) well-focusing. Then a key reflector is easily picked. We emphasize that finding the key reflectors requires a degree of seismic interpretation.

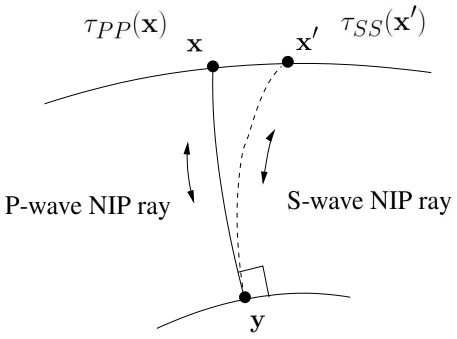

Figure 4.4: Indicated are two normal incidence point (NIP) rays for the P- and S-wave from the subsurface point $\mathbf{y}$.

Let the j'th pair of interpreted key reflectors on depth migrated PP and PS images be given by the graphs

$$\{(y_1, y_2, z^j_{PP}(y_1, y_2; \mathbf{m})), (y_1, y_2, z^j_{PS}(y_1, y_2; \mathbf{m}))\}; \tag{4.15}$$

to obtain the images, the velocity model $\mathbf{m}$ was used. Matching these interfaces in depth can be performed by velocity model updating, each time carrying out the migration on PP and PS data, and performing the interpretation. The key reflectors on the PP and PS images can also be matched to their depths $\{z^j_w(y'_1, y'_2)\}$ derived from well logs at different well locations (y'_1, y'_2).

To include the co-depthing in our MVA procedure without performing full (GRT) migrations repeatedly in the scanning procedure above, we suggest following a map migration approach instead. The small collection of picked key reflectors, yielding position of and normal to each of them, from migrated images (4.15) are map demigrated into PP and PS reflection time surfaces (Kleyn, 1977). This information is now 'data'.

As an approximation, here, we restrict the above mentioned matching procedure to zero scattering angle, i.e. exploding reflector model data; then only normal incidence point (NIP) rays to the surface (Hubral & Krey, 1980) are to be accounted for. The converted wave case with its diodic nature demands special considerations that we expose below.

4.4.1 Pure mode events

Map demigration. Indicated in Figure 4.4 are two NIP rays for the reflector point $\mathbf{y}$ for two different wave modes, namely P waves and S waves. The NIP ray for the PP reflection

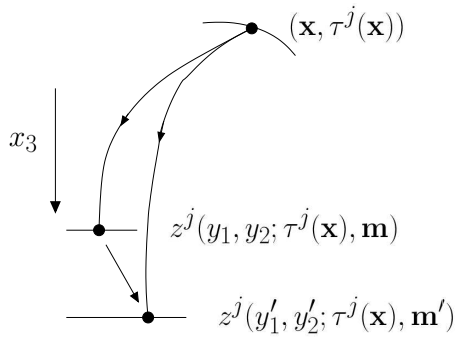

Figure 4.5: Mapping of the NIP reflection traveltime function to reflector depths given a velocity model $\mathbf{m}$ and $\mathbf{m}'$.

connects $\mathbf{x}$ and $\mathbf{y}$, and for the SS reflection $\mathbf{x}'$ and $\mathbf{y}$; the two-way NIP ray traveltimes are $\tau_{PP}(\mathbf{x})$ and $\tau_{SS}(\mathbf{x}')$, respectively. Even though the rays of the two wave modes take off normal to the interface, they usually follow different paths to the surface, as indicated. The PP and SS NIP rays coincide only when the v_P/v_S-ratio is constant throughout the velocity model.

Map migration. Using map migration in a given background medium $\mathbf{m}$, the time horizons are mapped to depth horizons. A particular imaged reflector point is written as $(y_1, y_2, z^j(y_1, y_2; \tau^j(\mathbf{x}), \mathbf{m}))$, see Figure 4.5. Also indicated in the figure is the imaged key reflector point given a different model $\mathbf{m}'$. The arrow indicates the movement of image points along the *velocity ray* (Fomel, 1997). Note that, in principle, the process of repeated map migrations does not require that the images of a key reflector have to be picked again after each velocity model update.

4.4.2 Converted mode events

We shall employ a simplification of and approximation to Grechka and Tsvankin's 'PP+PS=SS' approach (2002). The amplitude of a PS event at zero scattering angle vanishes. However, in the PS angle gathers we can extrapolate the singular supports to zero angle.

In an *acceptable* velocity model, for the PS event, the NIP P ray connects $\mathbf{y}$ to $\mathbf{x}$ and the NIP S-ray connects $\mathbf{y}$ to $\mathbf{x}'$ as in Figure 4.4. The two-way traveltime is then given by,

$$\tau_{PS}(\mathbf{x}, \mathbf{x}') = \tau_{PP}(\mathbf{x})/2 + \tau_{SS}(\mathbf{x}')/2, \tag{4.16}$$

with reflection point $\mathbf{y}$. Notice the use of two arguments in the traveltime function for converted modes as there are two emerging points at the acquisition surface: Zero scattering

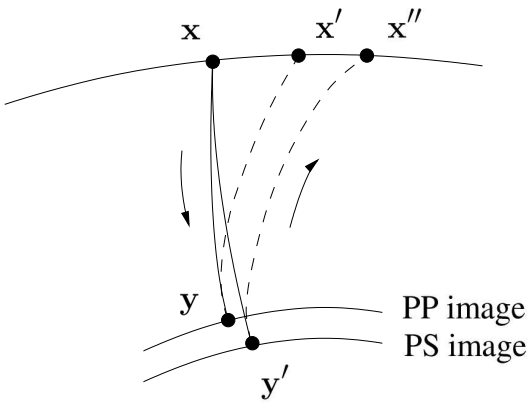

Figure 4.6: The reflector point imaged at $\mathbf{y}$ and $\mathbf{y}'$ from PP and PS reflection data, respectively, due to an inconsistent background model. Indicated are NIP rays from the two reflector points to the acquisition surface.

angle does not necessarily imply zero offset.

In an *unacceptable* velocity model, let us assume that we have successfully identified an interface on both a PP image and a PS image that is geologically the same but is imaged at different depths. This situation is sketched in Figure 4.6, where both the PP and PS images of the key reflector are indicated. The dotted lines indicate the S-wave rays while the solid lines indicate the P-wave rays. In the unacceptable model, the PS event is imaged at $\mathbf{y}'$, while the PP event is imaged at $\mathbf{y}$, assuming the same $\mathbf{x}$ position for the NIP P-ray through map demigration; the PS event tied to the PS image has two-way traveltime $\tau_{PS}(\mathbf{x}, \mathbf{x}'')$ ($\mathbf{x}' \neq \mathbf{x}''$ as the model is unacceptable). The zero scattering angle PP and PS two-way traveltimes are 'data' obtained from map demigration, and are considered to be correct. If we assume that $\mathbf{x}'' \approx \mathbf{x}'$, we can use (4.16) to compute $\tau_{SS}(\mathbf{x}'')$,

$$\tau_{SS}(\mathbf{x}'') \approx 2\tau_{PS}(\mathbf{x}, \mathbf{x}'') - \tau_{PP}(\mathbf{x}). \tag{4.17}$$

We have obtained *pure S-wave* NIP two-way traveltimes that we will exploit as 'data' from now on. The techniques of the previous subsection apply to these data, see Figure 4.5.

4.4.3 Misfit functional for co-depthing

The initial interpretations in (4.15) yield $(\mathbf{x}, \tau^j_{PP}(\mathbf{x}))$ and $(\mathbf{x}, \tau^j_{SS}(\mathbf{x}))$ by map demigration and the 'PP+PS=SS'-approximation (4.17). We are then able to compute the depth of

the key reflectors,

$$(y_1, y_2, z^j_{PP}(y_1, y_2; \tau^j_{PP}, \mathbf{m})), \quad (y_1, y_2, z^j_{SS}(y_1, y_2; \tau^j_{SS}, \mathbf{m})), \tag{4.18}$$

in an automatic way through map migration based on the medium parameters, $\mathbf{m}$, governing the P-wave and the S-wave propagation in a discriminate fashion. For example, we can define a misfit functional for co-depthing penalizing the mistie between the picked PP reflector in depth (4.15) and the map migrated SS reflector based on the medium parameters governing the S-wave propagation, viz.

$$\mathcal{J}_D(\mathbf{m}) = \frac{1}{2} \sum_j \iint \left| z^j_{SS}(y_1, y_2; \tau^j_{SS}, \mathbf{m})) - z^j_{PP}(y_1, y_2) \right|^2 dy_1 dy_2. \tag{4.19}$$

The reason to use the depths of interfaces picked on PP images as a reference is that they are usually much better determined in view of the PP ray coverage versus PS. Poorer ray coverage implies an increased ambiguity in reflector depth (Bube, 1995). The misfit functional can also be formulated to penalize the mistie between PP and SS interfaces and well log markers $(y_1, y_2, z^j_w(y_1, y_2))$ at discrete (y_1, y_2) points.

A misfit functional like (4.19) allows for a gradient based search in model space for an optimum model choice. The gradient of (4.19) involves the derivative of the depth of the reflectors with respect to the medium,

$$\frac{\partial \mathcal{J}_D}{\partial m_i}(\mathbf{m}) = \sum_j \iint \frac{\partial z^j_{SS}}{\partial m_i}(y_1, y_2; \tau^j_{SS}, \mathbf{m})) \\ (z^j_{SS}(y_1, y_2; \tau^j_{SS}, \mathbf{m}) - z^j_{PP}(y_1, y_2)) dy_1 dy_2. \tag{4.20}$$

This derivative is defined in the framework of ray perturbation theory and coincides with a tangent to the velocity ray (Iversen, 2001). It seems, however, that we have introduced an ambiguity: The computation of the gradient of the differential semblance misfit function (4.13) is based upon keeping the imaging point, migration dip, scattering angle and azimuth fixed changing the data, while the gradient of the co-depthing function (4.20) is based on keeping the input variables to map migration, data, fixed. We come back to this in the next section on strategy.

We arrive at a joint angle tomography and co-depthing misfit functional,

$$\mathcal{J}(\mathbf{m}) = \lambda_1 \mathcal{J}_{PP}(\mathbf{m}) + \lambda_2 \mathcal{J}_{PS}(\mathbf{m}) + \mu \mathcal{J}_D(\mathbf{m}), \tag{4.21}$$

where λ_1, λ_2 and μ are regularization parameters governing the trade-off between uniform cigs and depth consistency. By setting $\mu = 0$ the search aims at matching the range of the

PP and PS forward scattering operators to the relevant data constituents. The co-depthing is accomplished by setting $\mu \gg \lambda_1, \lambda_2 > 0$ and aims at a search in model space without changing the range of the forward scattering operators.

4.5 Strategy for depth consistent PP and PS angle tomography in a TI medium

We consider a transversely isotropic (TI) medium with a known direction of the symmetry axis in 3-D, but disregard any azimuthal anisotropy. The medium is equivalent to a TI medium with a vertical symmetry axis (VTI) through the Bond transformation (Carcione, 2001). Thus the medium is described by 4 parameters, for example the vertical P- and S-wave velocities v_{P0}, v_{S0} and Thomsen's (1986) δ and ε. We approach the problem of estimating a velocity model in the framework of TI media by performing the model updates in a step-wise manner, using the following steps reflecting a hierarchy of model complexity; the misfit functional is given in (4.21):

(i) We first carry out isotropic P-wave velocity analysis on PP cigs using differential semblance in angle ($\lambda_1 = 1$, $\lambda_2 = 0$, $\mu = 0$).

(ii) Keeping the P-wave velocity model obtained in (i) fixed, we carry out isotropic S-wave velocity analysis on PS cigs using differential semblance in angle ($\lambda_1 = 0$, $\lambda_2 = 1$, $\mu = 0$).

(iii) We carry out seismic interpretation of the PP and PS images for key reflectors, and pick them. The reflector picked on the PP image will yield the 'reference' in the misfit functional $\mathcal{J}_D$. We map demigrate the results making use of the P- and S-wave velocity models obtained in (i) and (ii) – we derive SS time horizons, which play the role of 'data'.

(iv) We carry out co-depthing keeping the P-wave velocity model from (i) fixed making use of map migration of the data obtained in (iii). The differential semblance in angle contribution to misfit plays the role of regularization ($\lambda_1 = 0$, $\mu \gg \lambda_2 > 0$).

(v) Finally, we carry out differential semblance in angle and semblance optimization of PP and PS cigs jointly admitting the model to become anisotropic (VTI); the co-depthing misfit plays the role of regularization ($\lambda_1 = 0$, $\lambda_2 \gg \mu > 0$).

(i) Isotropic PP angle tomography

The only parameter entering this step, the P-wave velocity, is parameterized following Billette and Lambaré (1998) as

$$v_P(\mathbf{x}) = \sum_k (v_{Pk} + g_k x_3) I_k(\mathbf{x}) + \sum_j a_j B_j(\mathbf{x}). \tag{4.22}$$

Equation (4.22) shows a decomposition of the parametrization into a linear trend within layers and a 3-D B-spline representation. The linear trend is described by a vertical velocity gradient g_k, a constant v_{Pk} and an indicator function I_k which is equal to one in layer k and zero outside. The second summation in equation (4.22) is a 3-D cubic B-spline expansion with 3-D splines, $B_j(\mathbf{x})$, and coefficients a_j (de Boor, 1978). The complete parameter vector is then the collection of coefficients

$$\mathbf{m}_P = \left(\{v_{Pk}, g_k\}_k, \{a_j\}_j\right). \tag{4.23}$$

The interface geometry implied by $\{I_k\}$ is updated automatically in the search procedure (Foss *et al.*, 2003b): From the initial PP image, interfaces/reflectors are picked (in depth) which are then map demigrated along the NIP rays to compute zero-offset time horizons/reflections. For the current velocity model these time horizons are map migrated to generate the new interface geometry. A gradient computation does not account for an update in geometry. As the new interface geometry needs the new model and not the current one, a few iterations are needed to stabilize this procedure.

The P-wave velocity optimization itself follows a step-wise approach: First we optimize with respect to the parameters in the layer-based description of equation (4.22), and then we add the B-splines and optimize with respect to their coefficients to capture features of the velocity function not described by the layer-based model. One iteration, using a quasi-Newton method (Gill *et al.*, 1981), constitutes the calculation of a gradient, equivalent to equation (4.13) and a linesearch in the gradient direction for the minimum of the misfit function (4.12).

(ii) Isotropic PS angle tomography

We keep the P-wave velocity (obtained in the previous step) fixed and parameterize the S-wave velocity in a manner similar to equation (4.22),

$$v_S(\mathbf{x}) = \sum_k (v_{Sk} + h_k x_3) I_k(\mathbf{x}) + \sum_j b_j B_j(\mathbf{x}), \tag{4.24}$$

which yields

$$\mathbf{m}_S = \left(\{v_{Sk}, h_k\}_k, \{b_j\}_j\right). \tag{4.25}$$

The interface geometry $\{I_k\}$ is kept fixed and is given by the P-wave velocity model representation. We carry out differential semblance in angle optimization of PS data and obtain an isotropic S-wave velocity model.

(iii) Generating the data for co-depthing

We generate a PS image using the isotropic P- and S-wave velocity models obtained in the previous two steps. On this image we find and trace key reflectors that we are able to recognize in and pair with the PP image. In practice, these form a subset of the interfaces already found in the estimation of the PP layer geometry. The paired key reflectors are map demigrated and SS traveltimes are computed using equation (4.17).

(iv) Co-depthing PP and PS images

We use the picked PP reflectors in depth from the isotropic processing and update the isotropic S-wave velocity to obtain depth consistent PP and PS key reflectors by (4.19). This is done with a gradient-based optimization where the data are the SS traveltimes obtained in the previous step. The search is constrained to the range of the forward scattering operators in *isotropic* velocity models. In the presence of *anisotropy* the PS cigs will now exhibit residual moveout again as prior to step (ii).

(v) Anisotropic PP and PS angle tomography

The ε and δ parameters are represented in a similar manner to the P- and S-wave velocities within the interface geometry of the P-wave velocity model, viz.

$$\varepsilon(\mathbf{x}) = \sum_k \varepsilon_k I_k(\mathbf{x}) + \sum_j c_j B_j(\mathbf{x}), \quad \delta(\mathbf{x}) = \sum_k \delta_k I_k(\mathbf{x}) + \sum_j d_j B_j(\mathbf{x}), \tag{4.26}$$

which yields

$$\mathbf{m}_{\varepsilon,\delta} = \left(\{\varepsilon_k, \delta_k\}_k, \{c_j, d_j\}_j\right). \tag{4.27}$$

In seismic velocity models, the anisotropy parameters typically vary slowly over large regions. We hence use constant values within layers, but with a B-splines contribution we capture other spatial variations.

We assume weak anisotropy. The P- and S-wave (interval) NMO velocities (Thomsen, 1986) are then given by

$$v_{PNMO} = v_{P0}\sqrt{1+2\delta} \tag{4.28}$$

and

$$v_{SNMO} = v_{S0}\sqrt{1+2\sigma}, \quad \sigma = \left(\frac{v_{P0}}{v_{S0}}\right)^2 (\varepsilon - \delta). \tag{4.29}$$

The S-wave NMO velocity depends on the relationship $(\varepsilon - \delta)$ which is scaled by the squared v_{P0}/v_{S0} ratio through the σ parameter. It is well known that due to this, the processing of PS events is much more sensitive to the presence of anisotropy than that of PP events. Estimating the δ parameter requires well logs, large offset PP data or other information concerning depths of reflectors, as discussed by Audebert *et al.* (2001). If well log information is present the true depth of the reflectors can be obtained where the wells

penetrate them. The true depth of a reflector – in the absence of too strong lateral heterogeneity – is governed by the v_{P0} parameter, the vertical P-wave velocity, which can be obtained by matching the PP reflectors to well markers by map migration, similar to (4.19).

We denote the estimate for the P-wave velocity function obtained in (i) by $\hat{v}_P$ and the estimate for the S-wave velocity function obtained in (iv) (after (ii)) by $\hat{v}_S$. In the absence of too strong lateral heterogeneity, the P-wave velocity obtained in (i) is approximately an interval NMO velocity,

$$\hat{v}_P \approx v_{PNMO}. \tag{4.30}$$

The δ parameter can readily be identified as a parameter causing the ambiguity between v_{PNMO} and v_{P0} through equation (4.28). In order to maintain the depth consistency while admitting anisotropy, the ratio of the vertical interval P- and S-wave velocities need to be fixed,

$$\frac{\hat{v}_P}{\hat{v}_S} = \frac{\hat{v}_{P0}\sqrt{1+2\delta}}{\hat{v}_S} = \text{constant}, \tag{4.31}$$

which motivates the introduction of a scaled S-wave velocity,

$$\hat{v}_{S0} = \frac{\hat{v}_S}{\sqrt{1+2\delta}} \quad \text{subject to } \frac{\hat{v}_{P0}}{\hat{v}_{S0}} = \text{constant}. \tag{4.32}$$

The ε-parameter can subsequently be found from anisotropic PS angle tomography using (4.14).

If large offset PP data are available a joint PP and PS angle tomography can be performed by (4.21) ($\lambda = 1$ and $\mu = 0$). The same considerations pertaining to the depth consistency given a δ value applies here as well. Due to (4.30), given a δ-value the vertical P-wave velocity becomes

$$\hat{v}_{P0}(\mathbf{x}) = \frac{\hat{v}_P(\mathbf{x})}{\sqrt{1+2\delta(\mathbf{x})}}, \tag{4.33}$$

and by equation (4.31) the vertical S-wave velocity is given by (4.32).

In the absence of information needed to resolve the δ-parameter we make the convenient choice of setting it to zero, $\delta = 0$, considering a quasi-VTI medium. Then an update is performed to compute uniform PS cigs from the previous section by updating the ε-parameter. The parameter is not the true ε-parameter, but an effective anisotropy parameter. This yields focused depth consistent PP and PS images yet at unphysical depths (due to $\delta = 0$). It can also be used to estimate an initial starting model in the aforementioned approaches including δ.

4.6 Field data example

Our procedure has been tested on an OBS line from the North Sea. This assumes the use of a 2.5-D formalism found in Foss and Ursin (2004) considering 3-D wave propagation in a 2-D model where all calculations are done in the plane. The data have been subjected to standard processing such as static corrections, designatur and multiple removal (Yilmaz, 1987).

(i) For isotropic PP angle tomography we use the P-wave parametrization in (4.22), but in 2-D. Thus the B-spline is 2-D and $\mathbf{x} = (x_1, x_3)$ in the following. The 2-D B-spline nodes are sampled every 250 m in the horizontal direction and every 100 m in depth. The relatively dense sampling in depth was deemed necessary due to the sharp velocity increases observed during the optimization. The image resulting from a simple 1-D optimization is used to identify the layering of the velocity model. The time horizons of the interface geometry in (4.22) are found from map demigration as described in previous sections. These time horizons, a total of 13 of them, are used in the subsequent velocity estimation steps to control the interface geometry in (4.22). The starting values of the constant velocity and velocity gradient within each layer are taken from well information from close to the 2-D slice in the medium under consideration here. The initial model and the corresponding PP image are given in Figures 4.7 (top left) and 4.9.

To construct a 'well-behaved' misfit function (4.13) and guarantee a numerically stable computation of the gradient (4.13), we bandpass filter the data between 3 and 15 Hz. The derivatives in angle inside the misfit function are tapered at small and large angles to remove truncation effects. We normalize the misfit function (4.13) following Chauris and Noble (2001) to reduce the influence of erroneous amplitude calculations and noise in the data (this could have been circumvented by making the GRT of the data to cigs unitary). The gradient contributions are tapered as we approach the boundaries of the model or in places with low ray coverage. Before calculating both the gradient and the misfit function, the cigs are smoothed by a simple $\{1/4, 1/2, 1/4\}$-convolution filter in angle and depth; in addition, a 2-D Fourier 'dip' filter (in depth and angle) is applied to suppress imaging artifacts and noise (Yilmaz, 1987). The filter is applied adaptively, allowing for less 'dipping' events as we approach uniform gathers. This is done in a conservative manner to avoid destroying the moveout behavior of the primary events. These considerations are taken into account in all subsequent calculations.

The 14 cigs are sampled every 250 m from 1250 m onwards. They are sampled every 0.5 degrees up to 45 degrees in incoming P-wave reflection angle. Figure 4.8 shows the a) starting, b) after 4 iterations and c) after 7 iterations (final) collection of cigs in the

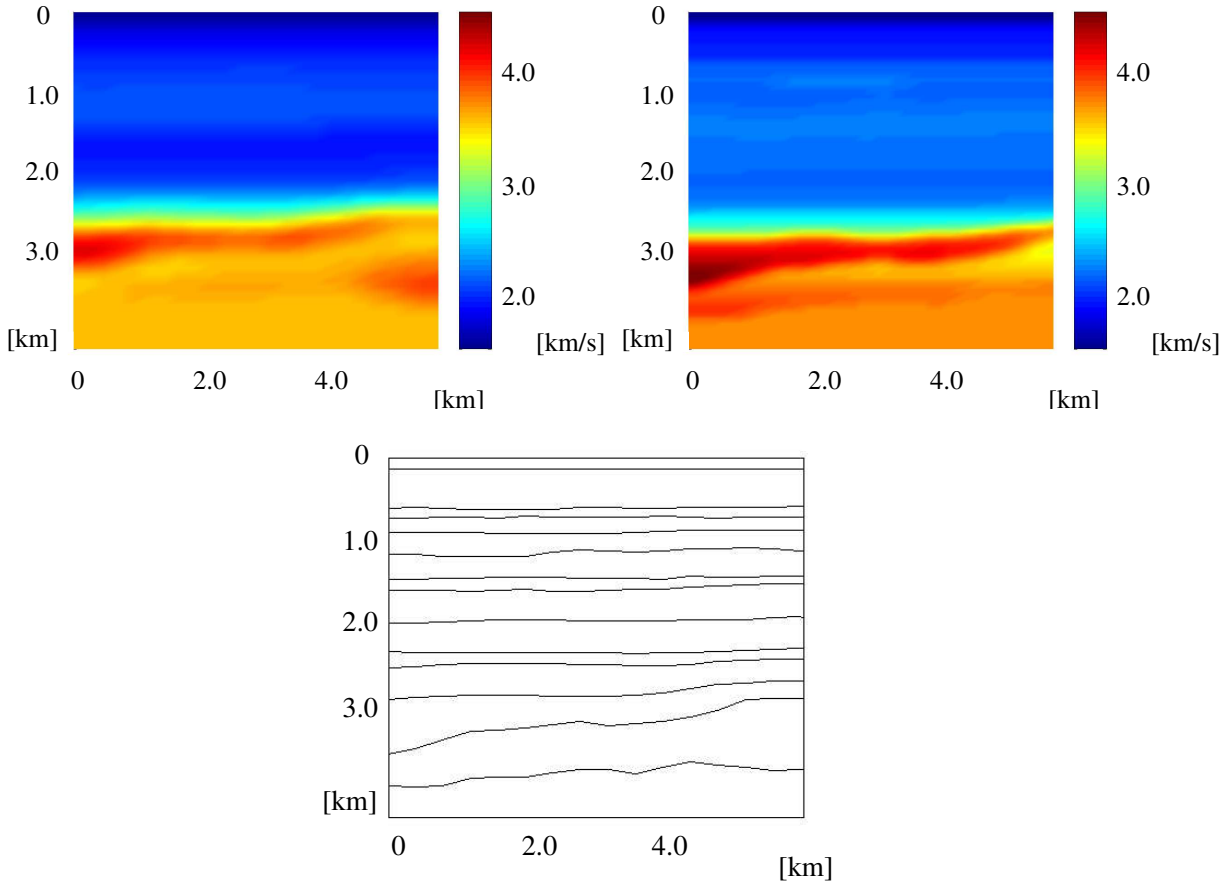

Figure 4.7: Initial (top left) and final (top right) P-wave velocity model from isotropic angle tomography with the final interface geometry (bottom).

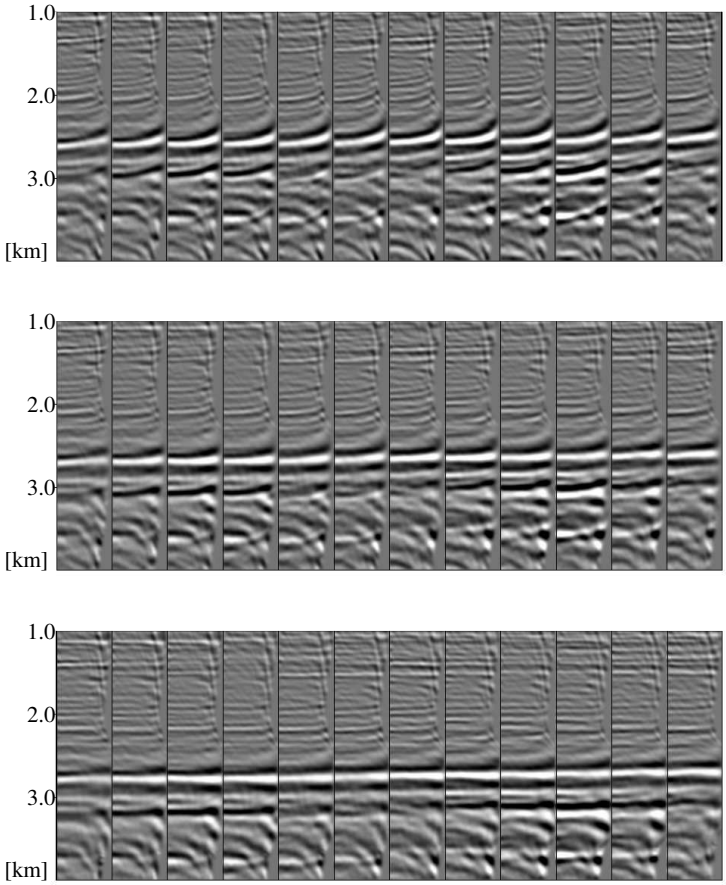

Figure 4.8: The common-image point gathers of the isotropic P-wave velocity optimization after 0, 4 and 7 iterations.

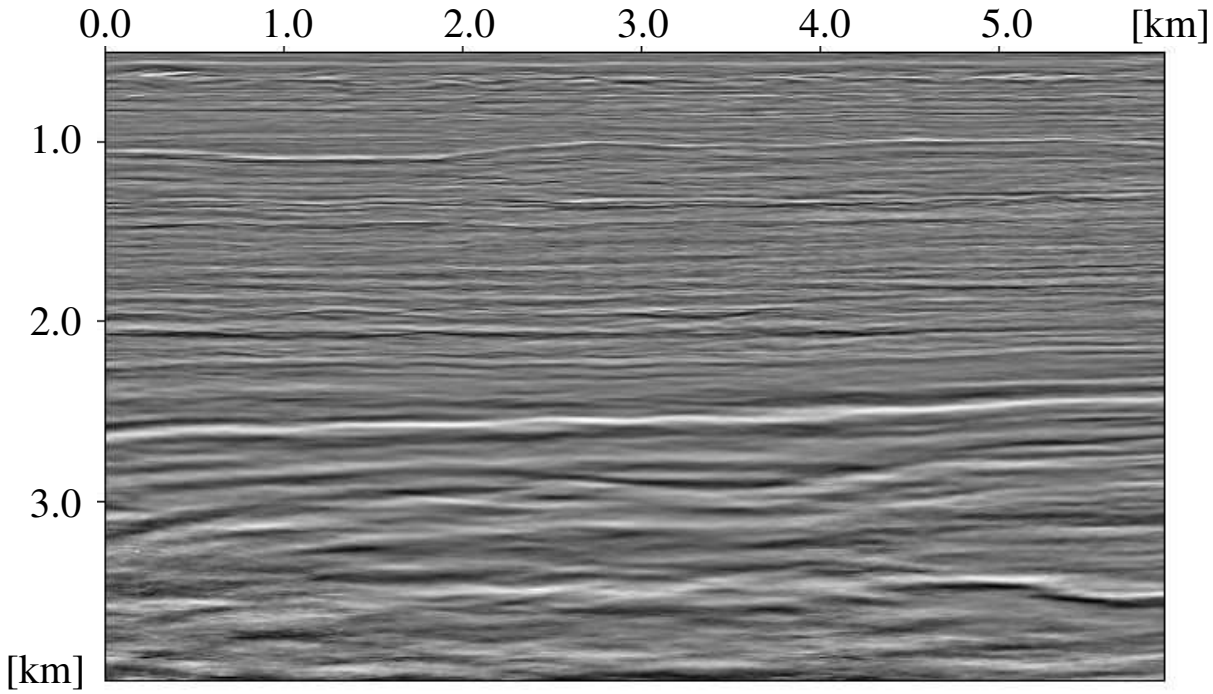

Figure 4.9: The PP image using the initial isotropic P-wave velocity model in Figure 4.7 (top left).

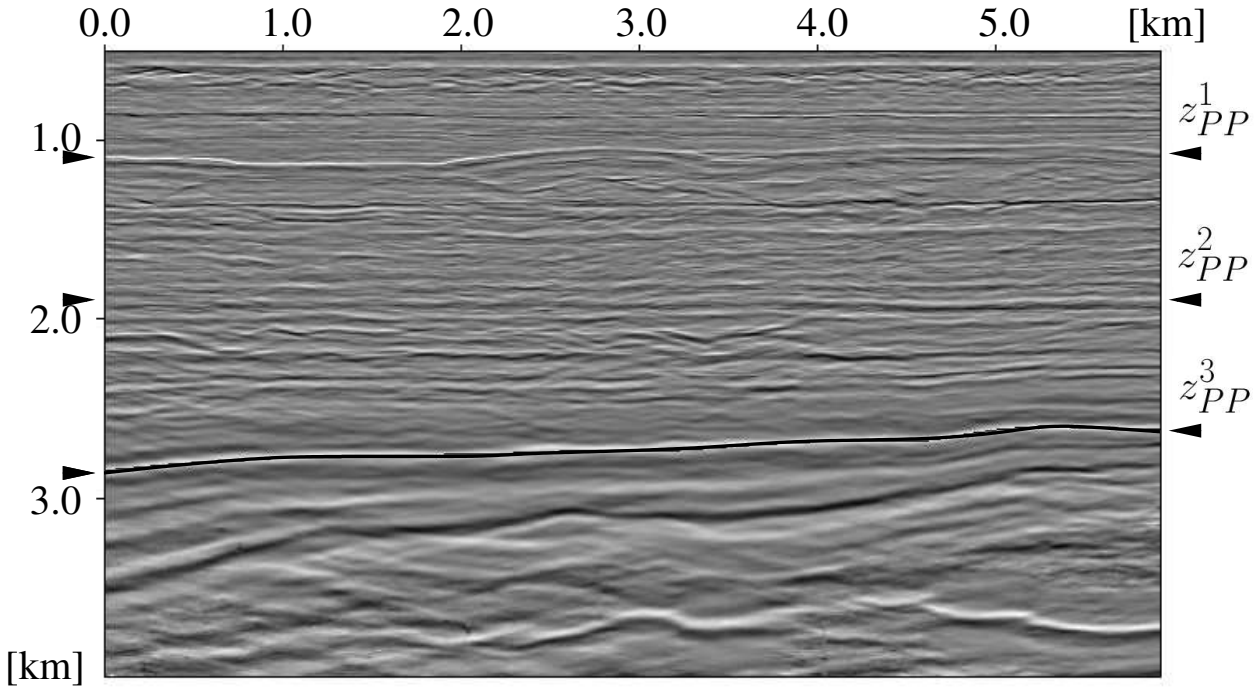

Figure 4.10: The PP image using the final isotropic P-wave velocity model in Figure 4.7 (top right). Indicated with arrows are a selection of interfaces of particular interest denoted by z^1_{PP}, z^2_{PP} and z^3_{PP}.

optimization. The resulting velocity model and corresponding PP image are given in Figures 4.7 (top right) and 4.10, respectively. The optimization for the B-spline coefficients was carried out in the final couple of iterations, but this showed little improvement in the misfit function. Notice in particular the movement of the interface geometry in the final velocity model Figure 4.7 (top right) as compared with the initial one (top left).

(ii) The initial S-wave velocity model is chosen naively by a fixed v_S/v_P ratio in the entire model based on the final P-wave velocity, and is given in Figure 4.11 (left). The corresponding PS image is given in Figure 4.13. The P-wave velocity model is considered reliable up to 45 degrees incoming P-wave angle (which was the range of angles used in the isotropic P-wave velocity analysis). We apply a tapered mute on the outgoing S-wave angles that through Snell's law are tied to incoming P-wave angles larger than 45 degrees. We use 8 positive and negative cigs, $\mathcal{I}^+_{PS}$ and $\mathcal{I}^-_{PS}$, from surface position 1750 m onwards with a 300 m horizontal spacing. The initial cigs and the ones after the third and fifth iteration are shown in Figure 4.12 a), b) and c), respectively. The cigs are displayed pairwise for the same horizontal position with the positive image on the left and the negative image on the right, as explained in Figure 4.3. They are plotted as functions of out-going S-wave angle (contrary to convention) running from the indicated axis separating them, in the positive and negative directions. The S-wave angle ranges from 0.4 to 25 degrees.

(iii) The PS image resulting from the isotropic velocity analysis is given in Figure 4.14. Superimposed are the arrows and tracing of the main reflector (z^3_{PP}) as found on the PP image, Figure 4.10. In the shallow part we see that equivalent reflector z^1_{PP} of the PP image occurs slightly deeper in the PS image. The depth discrepancy cannot be explained by the cigs in Figure 4.12c), which are uniform and indicate a fitting model according to our differential semblance in angle misfit measure. In the deeper parts the superimposed PP reflector z^3_{PP} seems to match a PS reflector. However, the geologically equivalent reflector on the PS image is indicated with the dotted line z^3_{PS}. We observe that under the isotropic assumption the migrated, equivalent reflectors are *several hundred meters* apart by comparing the PP and PS images.

To compute pure mode SS traveltimes we identify and pair several interfaces on both the PP and the PS images, which are then map demigrated along the NIP rays to obtain the approximative SS traveltimes from equation (4.17). The key interfaces used are z^1_{PP}, z^2_{PP} and z^3_{PP} in the PP image, see Figure 4.14.

(iv) In the process of co-depthing, the S-wave velocity is parameterized as in (4.24). The resulting depth consistent PS image is given in Figure 4.17 and is computed with the velocity model given in Figure 4.11 (right). The key reflectors in the PP and PS images are

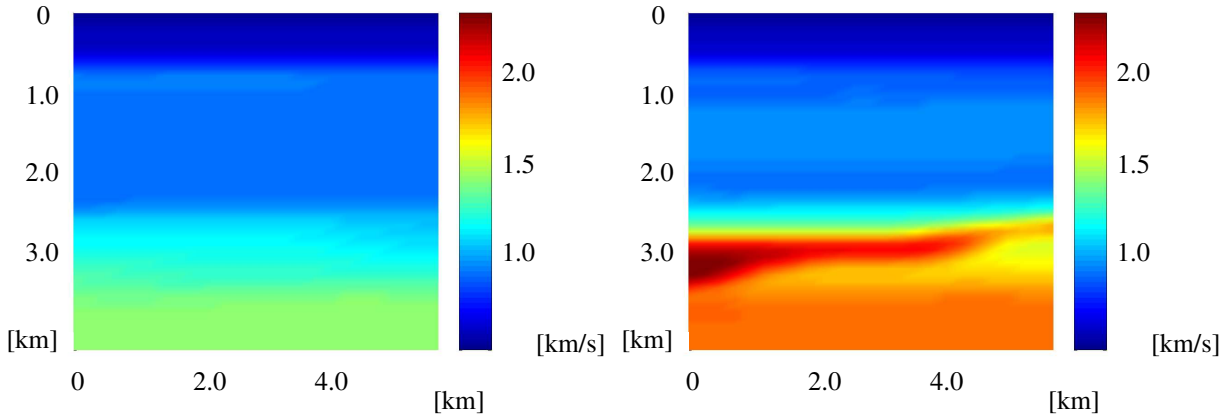

Figure 4.11: Initial (left) and final (right) S-wave velocity model obtained with isotropic angle tomography.

now at matching depths, but due to the isotropic assumption the PS cigs show residual moveout behavior, again, as illustrated in Figure 4.16a). This concludes the isotropic processing procedure.

(v) For the anisotropic processing we parameterize ε as (4.26) assuming the medium is VTI. There is no well log information from wells intersecting our plane of consideration. In addition, the data has to be muted so that there are no large offset data for PP reflections from the shallow part of the model. Hence, we set $\delta = 0$, as mentioned before. The starting value for the optimization is $\varepsilon \equiv 0$ in the entire model. The cigs are now sampled every 550 m in the horizontal direction starting at 1750 m; there are still 8 pairs of positive and negative cigs.

The gradient in the optimization is tapered at 700 m (and above) and 2700 m (and below) because of ray coverage. All parameters except ε are kept fixed at their values obtained from isotropic velocity analysis. Figure 4.16 shows two sets of cigs. The first set, a), is the outcome of co-depthing (iv). We observe that the shallow reflecting events are still quite uniform in these cigs. We observe in Figure 4.17 that they have, in fact, moved in the co-depthing step. This means that the velocity update in (iv) was not detectable by the differential semblance in angle misfit function, as we have stayed in the range of the forward scattering operator. The final set of cigs, Figure 4.16b), are optimized gathers after 2 iterations with ε. We observe that most of the change applies to the middle depth interval between 1500 m and 2500 m. The resulting ε function and the corresponding image are given in Figure 4.15 (left) and 4.18, respectively, where the indicators from the PP image

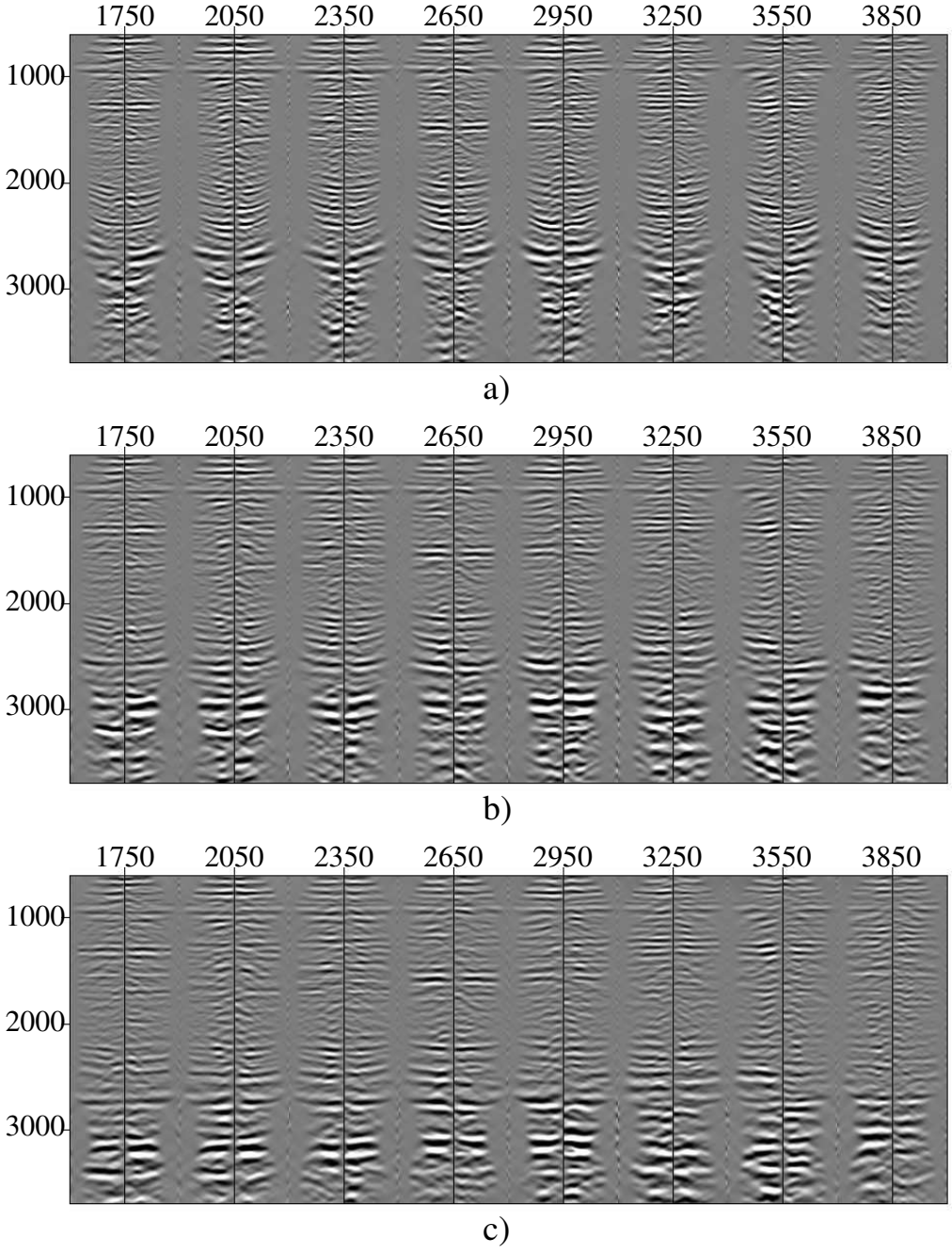

Figure 4.12: The common-image point gathers of the isotropic S-wave velocity optimization after 0, 2 and 5 iterations.

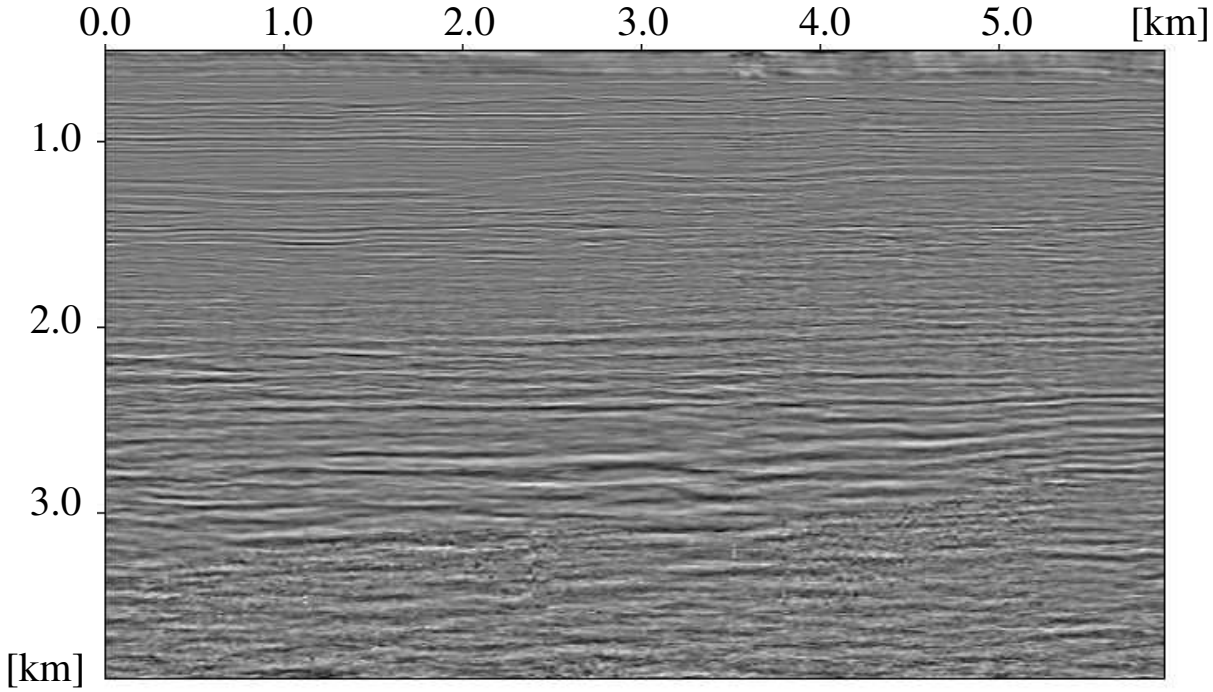

Figure 4.13: PS image using the initial S-wave velocity model in Figure 4.11 (left) and using the P-wave velocity model from the isotropic P-wave angle tomography.

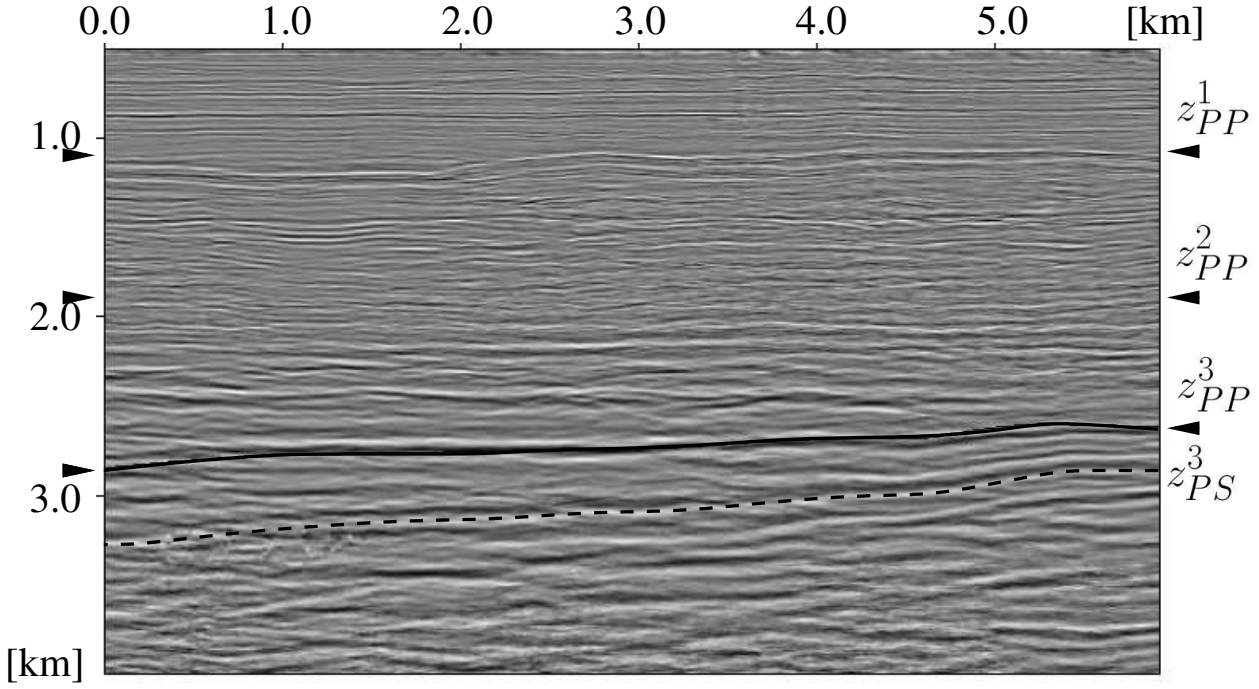

Figure 4.14: PS image after isotropic S-wave angle tomography on PS cigs.

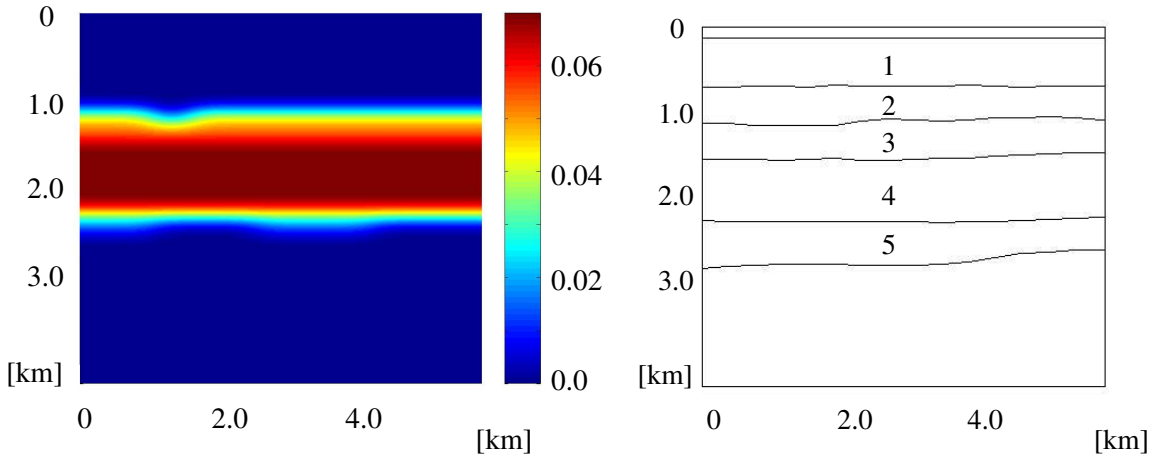

Figure 4.15: The ε model after the final anisotropic update ($\delta = 0$) (left) and the 5 anisotropic layers used in the layer stripping approach (right).

(Figure 4.10) are superimposed. The geologically equivalent reflectors on the PP and PS images appear to match in depth. However, below the reflector equivalent to z^3_{PP}, the PS image misses some of the structure observable in the PP image. By investigating the set of cigs in Figure 4.16b) in this region, we observe misalignment or alignment along lines with steep angles. Since the formation of caustics is unlikely here, we attribute these to wave constituents not modeled by our 2.5D scattering operator, such as multiples.

In Figure 4.19 we summarize the results by extracting a single trace, at 3200 m horizontal distance, from the images in Figures 4.10 (step (i)), 4.14 (step (ii)), 4.17 (step (iv)) and 4.18 (step (v)). One can clearly observe the mistie in depth between the first two traces, the shift in depth from the second to the third trace, and the improved focusing from the third trace to the fourth trace.

Depth fidelity. In order to examine how the δ-parameter function affects the analysis proposed and carried out above, we perform a joint PP and PS angle tomography, in a layer stripping manner. We use the layering structure only, in the parametrization of δ and ε, and omit the contribution from the splines. In addition, we limit the number of layers used to 5 as indicated in Figure 4.15 (right). Note that the interfaces in this geometry form a subset of the set of interfaces in the geometry in Figure 4.7 (bottom). The top layer (water) and the bottom layer below approximately 2700 m are assumed isotropic. Isotropic parameters are taken from (i)-(ii)-(iv); the sampling of cigs is the same as in step (v).

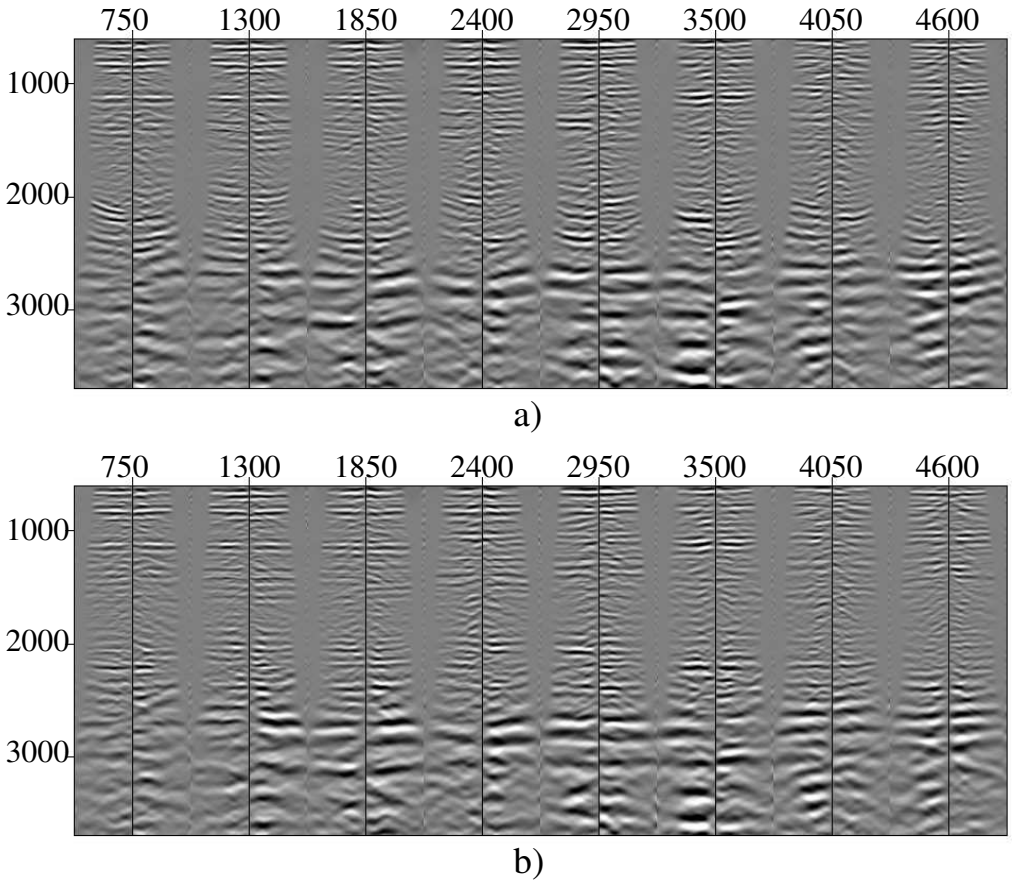

Figure 4.16: The common-image point gathers of the angle tomography in ε after a) 0 and b) 2 iterations.

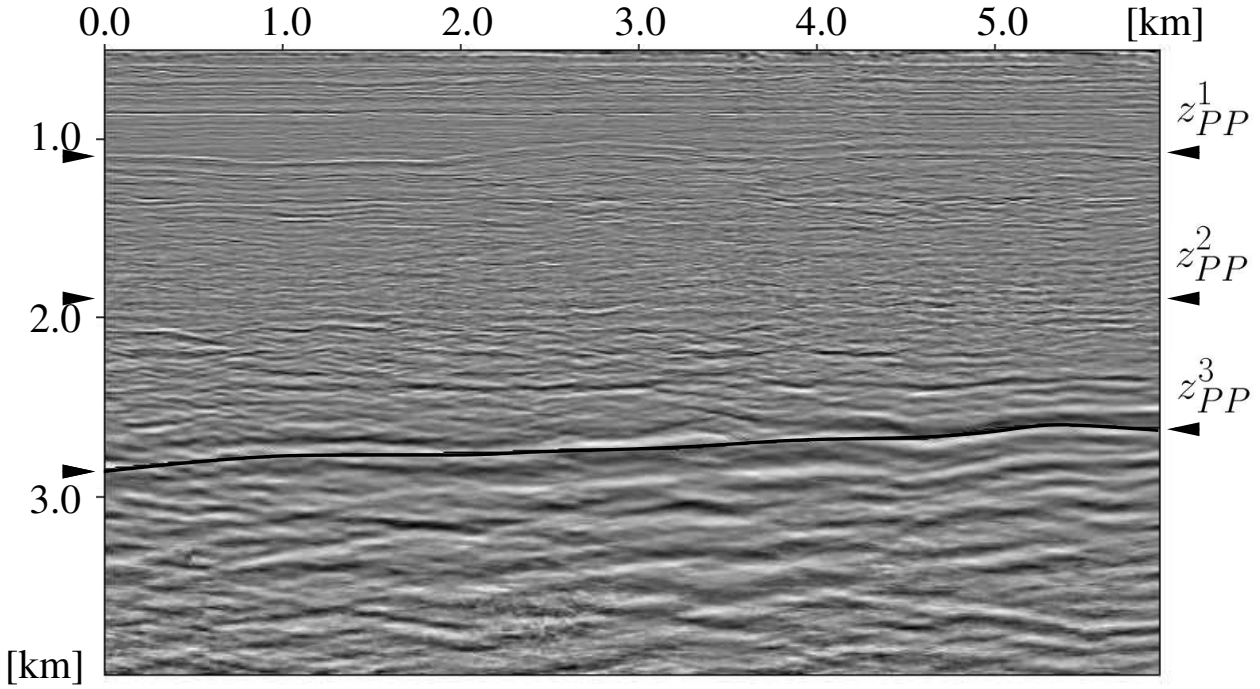

Figure 4.17: PS image after isotropic co-depthing.

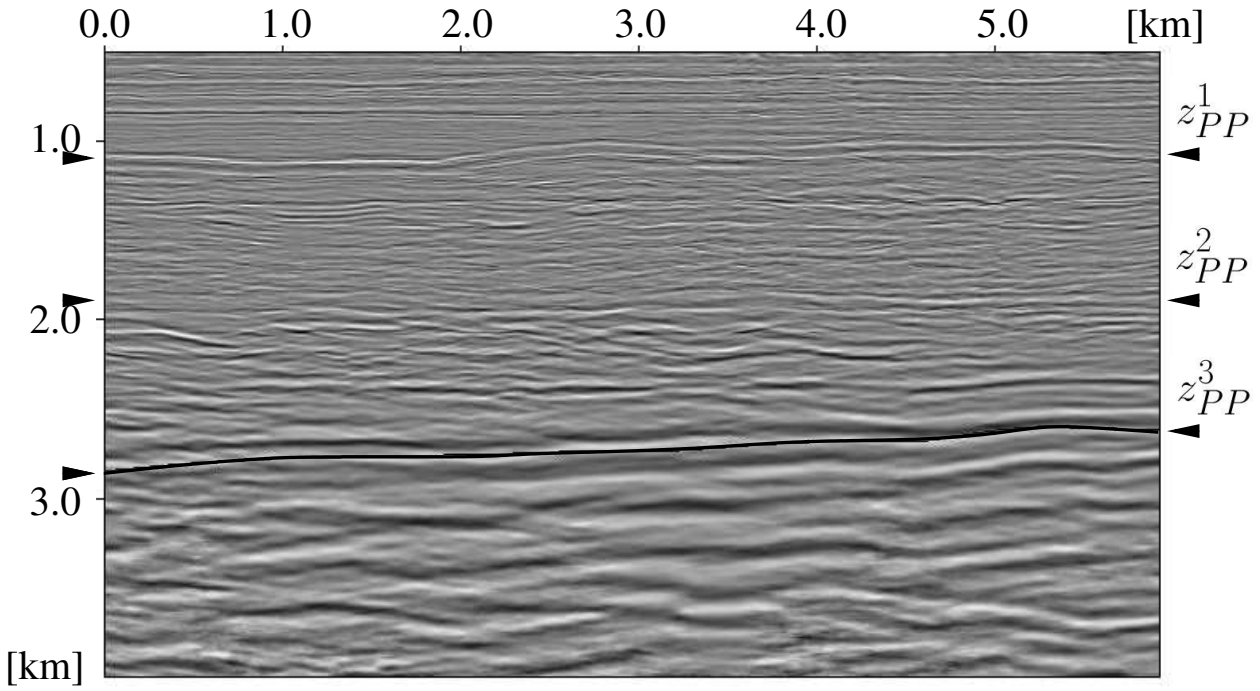

Figure 4.18: PS image after quasi-VTI parameter update ($\delta = 0$).

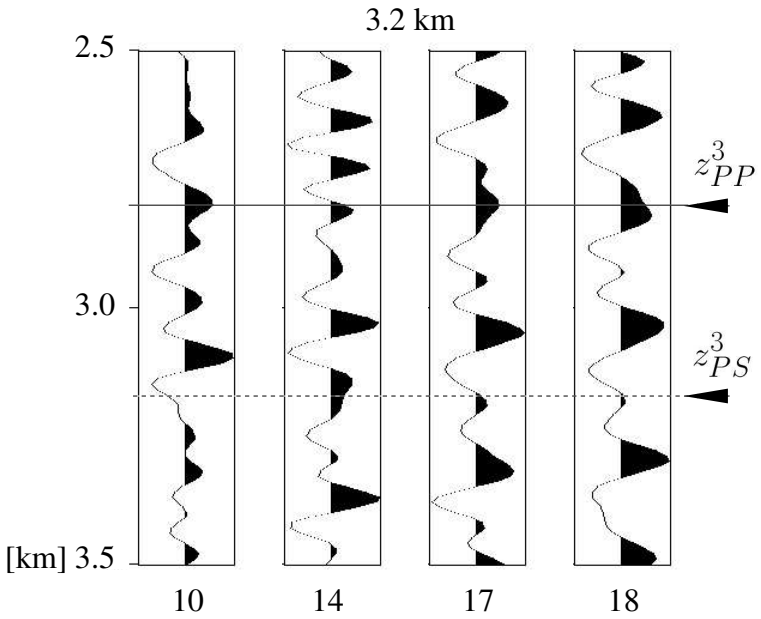

Figure 4.19: A single trace, at 3200 m horizontal distance, from the images in Figures 4.10 (step (i)), 4.14 (step (ii)), 4.17 (step (iv)) and 4.18 (step (v)).

In addition to the differential semblance in angle misfit function we also include the sensitive semblance measure. We introduce the PP semblance-based misfit as

$$\mathcal{S}_{PP}(\mathbf{m}) = 1 - \frac{1}{N_{\theta,\psi} N_{y_1,y_2}} \iint \frac{\int \left| \iint \mathcal{I}_{PP}(\mathbf{y},\mathbf{m};\theta,\psi) d\theta d\psi \right|^2 dy_3}{\iiint \left| \mathcal{I}_{PP}(\mathbf{y},\mathbf{m};\theta,\psi) \right|^2 d\theta d\psi dy_3} dy_1 dy_2, \tag{4.34}$$

where the division in the integrand is a normalization of each cig with its 'energy' (Chauris & Noble, 2001). Upon discretizing the integrals, $N_{\theta,\psi}$ becomes the number of θ and ψ values used, and N_{y_1,y_2} becomes the total number of cigs used. Semblance optimization is here formulated as a minimization problem. We introduce in a similar manner the PS semblance-based misfit,

$$\begin{aligned} \mathcal{S}_{PS}(\mathbf{m}) = 1 - \frac{1}{2} \Bigg(& \frac{1}{N^+_{\theta,\psi} N^+_{y_1,y_2}} \iint \frac{\int \left| \iint \mathcal{I}^+_{PS}(\mathbf{y},\mathbf{m};\theta,\psi) d\theta d\psi \right|^2 dy_3}{\iiint \left| \mathcal{I}^+_{PS}(\mathbf{y},\mathbf{m};\theta,\psi) \right|^2 d\theta d\psi dy_3} dy_1 dy_2 \\ & + \frac{1}{N^-_{\theta,\psi} N^-_{y_1,y_2}} \iint \frac{\int \left| \iint \mathcal{I}^-_{PS}(\mathbf{y},\mathbf{m}\theta,\psi) d\theta d\psi \right|^2 dy_3}{\iiint \left| \mathcal{I}^-_{PS}(\mathbf{y},\mathbf{m};\theta,\psi) \right|^2 d\theta d\psi dy_3} dy_1 dy_2 \Bigg), \end{aligned} \tag{4.35}$$

where $N^+_{\theta,\psi}$ and $N^+_{y_1,y_2}$ are defined as in (4.34) for the positive cigs and $N^-_{\theta,\psi}$ and $N^-_{y_1,y_2}$ for the negative cigs.

Figure 4.20 illustrates the shapes of the misfit for the five different layers in a layer stripping approach as function of ε and δ. In the layer stripping approach, we use the optimal (ε, δ) values obtained in the layers above the layer in which the parameters are under investigation. The illustrations in a row are the semblance misfits for PS, PP (equations (4.35) and (4.34)), their normalized sum, and our joint PP, PS differential semblance in angle misfit ($\lambda_1 = \lambda_2 = 1$, $\mu = 0$). The PP and PS semblance functions are plotted on the same scale. We observe that in the PS semblance plot the apparent valley at a 45 degree angle is governed by $(\varepsilon - \delta)$ as in equation (4.29). This indicates the feasibility of detecting anisotropy in the PS cigs, without discriminating between the two parameters. In the PP semblance plot we are unable to observe significant change in the value of the misfit function with changing anisotropy. This is expected as the data offsets are not sufficiently large for the shallow part of the model due to the aforementioned mute.

In the joint PP, PS semblance and joint PP, PS differential semblance in angle misfit plots, the lines $\delta = 0$ and

$$\varepsilon - \hat{\varepsilon} = \delta - \hat{\delta}, \tag{4.36}$$

are drawn, where $\hat{\varepsilon}$ and $\hat{\delta}$ are optimal values for ϵ and δ in each layer, and can be found in Table 4.1. In the first three layers the values are chosen using the PS semblance plot only, with $\delta = 0$, since there is not enough resolution in δ. In layers 4 and 5 we use the joint PP, PS semblance plots. In these layers values for ε and δ can be resolved by locating the semblance misfit minimum after analyzing the joint PP, PS differential semblance in angle misfit function first. In the deepest layer, the differential semblance in angle misfit function limits the region where the semblance misfit minimum is to be found, and thus enables us to discriminate between the two apparent minima in the semblance misfit function.

In the calculations we use a fixed depth window of the cigs. This implies, for example, that if δ becomes too negative, an event can move out of this depth window and hence no longer contributes to the misfit.

The final PP and PS cigs for the $\hat{\varepsilon}$ and $\hat{\delta}$ values in Table 4.1 are shown in Figure 4.21. The corresponding images are given in Figures 4.22 and 4.23 in *depth* and in *two-way* PP *time* (obtained by depth-to-time conversion using the P-wave velocities from (i)) in Figures 4.24 and 4.25. For comparison, the initial PP image obtained in (i) is also converted to two-way PP time in Figure 4.26.

4.7 Discussion and conclusion

layer	$\hat{\varepsilon}$	$\hat{\delta}$
1	0.035	0.0
2	0.0	0.0
3	0.02	0.0
4	0.09	-0.04
5	-0.02	-0.02

Table 4.1: Anisotropic parameter values resulting from layer stripping.

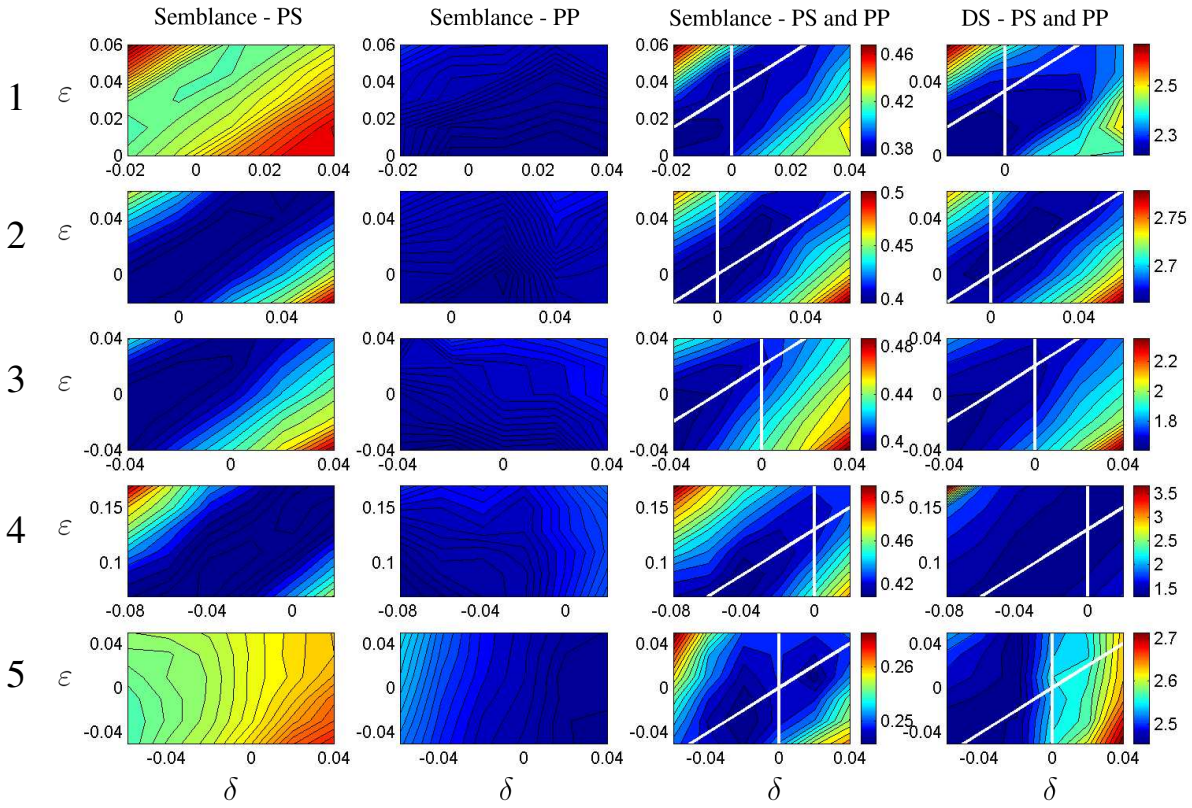

Figure 4.20: Contour plots for anisotropic layers 1-5 (vertical direction) and misfit plots for PS, PP and PP+PS semblance, and differential semblance in angle for PP+PS. Notice that the semblance plots are given by equations (4.34) and (4.35) formulated as minimization problems for comparison with the differential semblance misfit function.

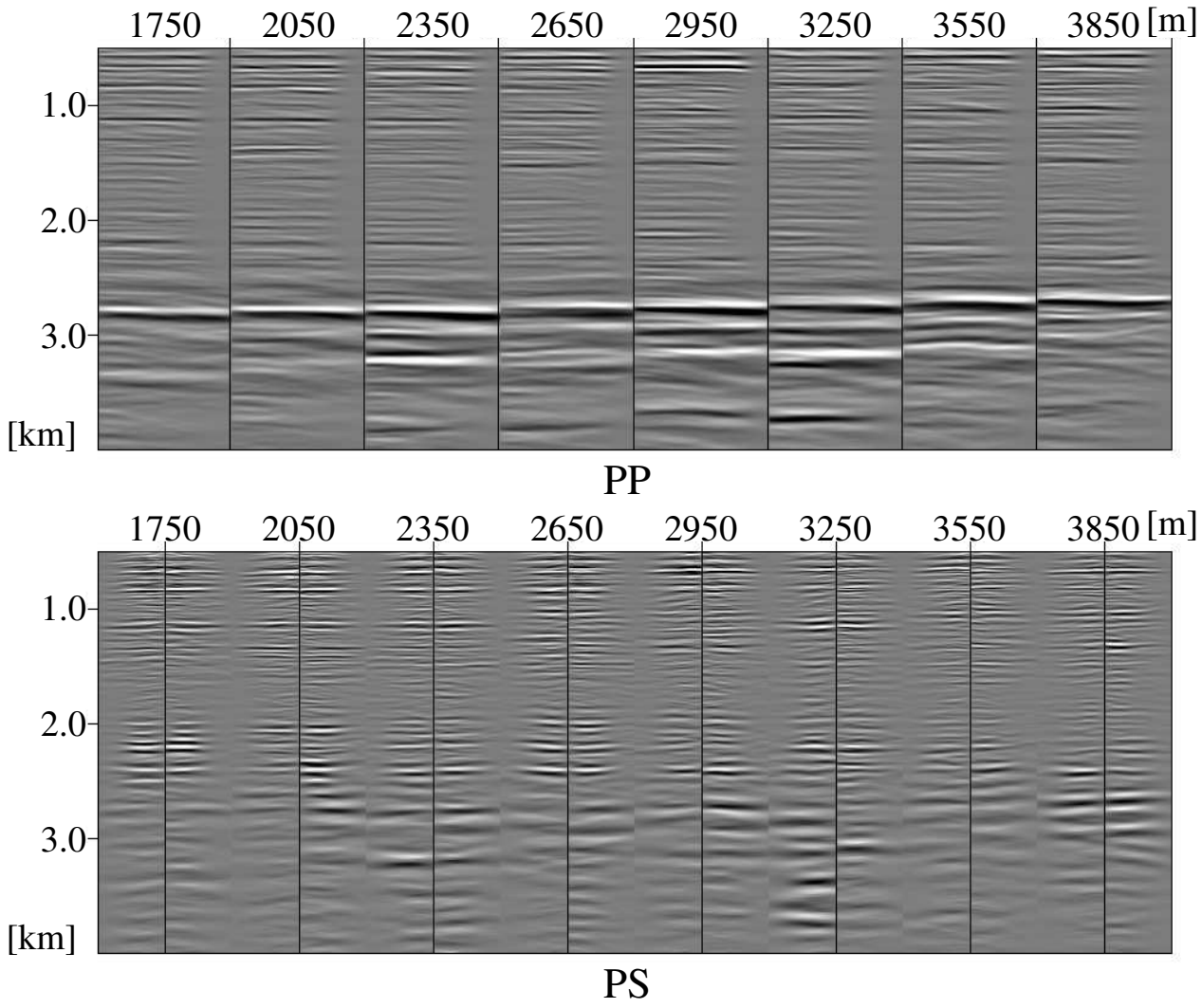

Figure 4.21: Final PP and PS cigs after anisotropic model update obtained following a layer stripping approach.

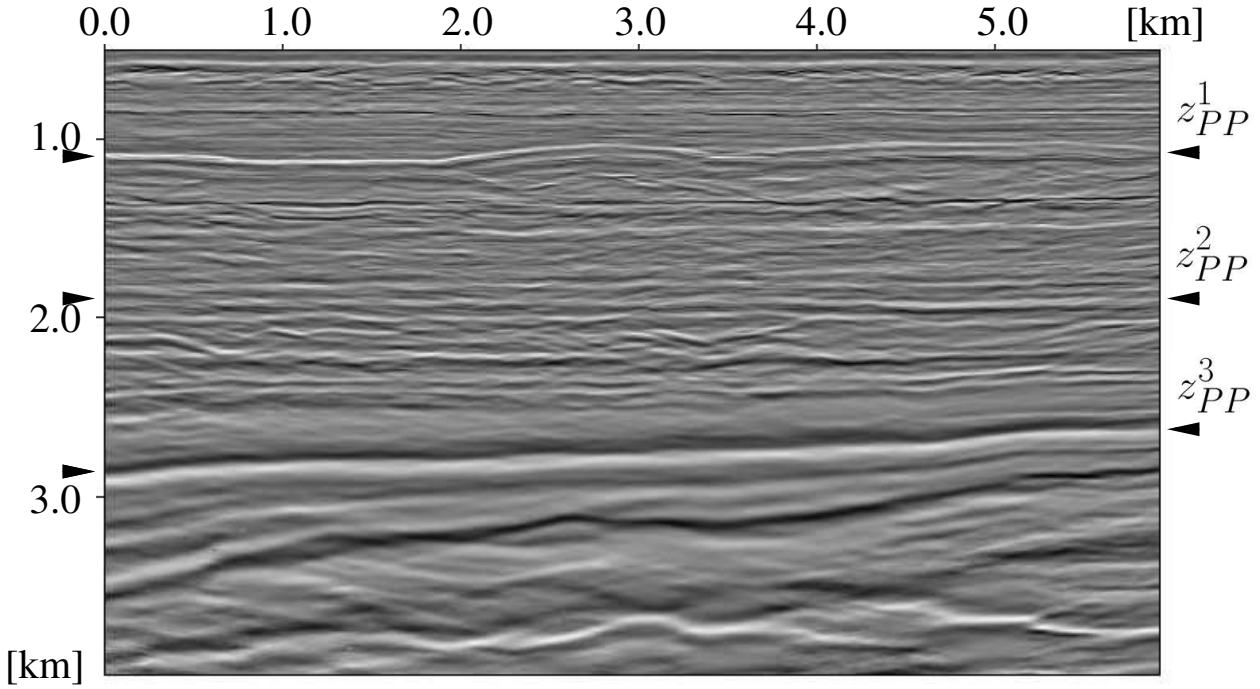

Figure 4.22: PP image using the anisotropic parameters obtained from the layer stripping.

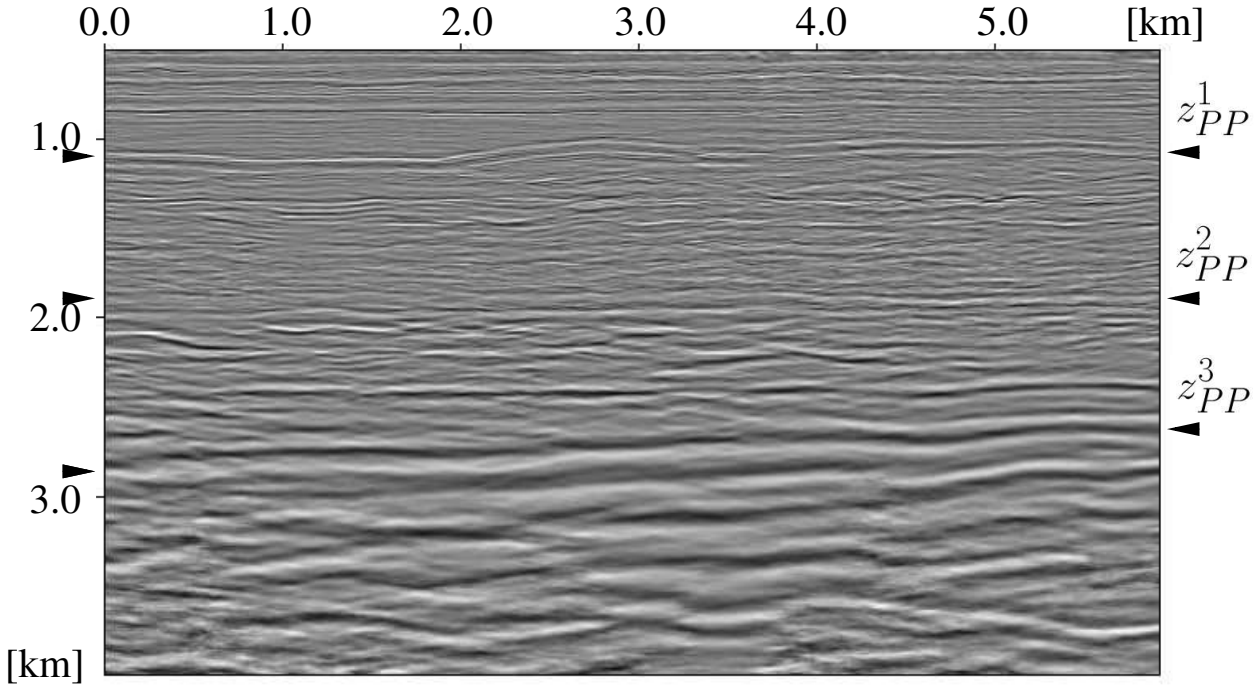

Figure 4.23: PS image using the anisotropic parameters obtained from the layer stripping.

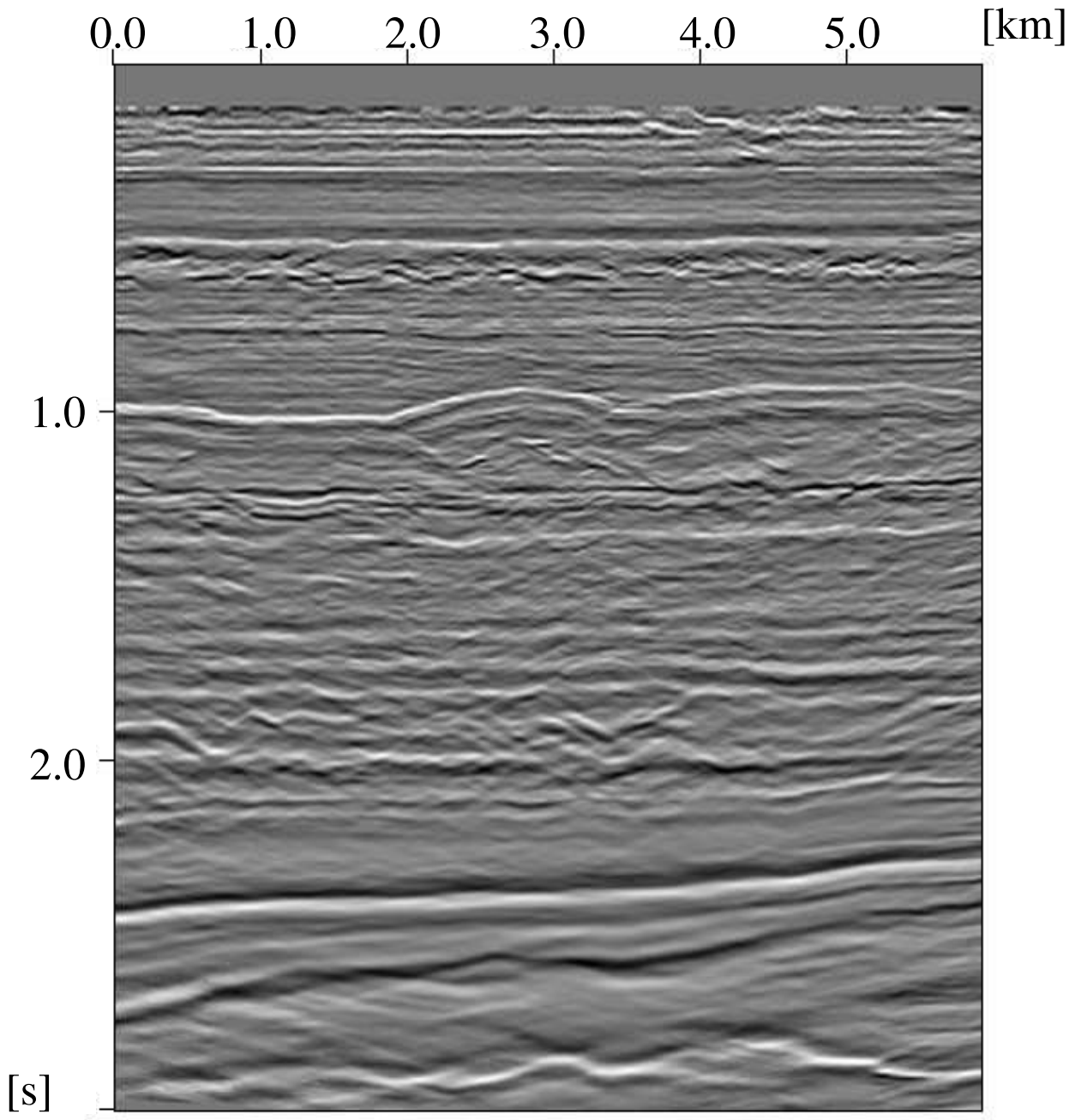

Figure 4.24: PP image using the anisotropic parameters obtained from the layer stripping, in two-way PP time.

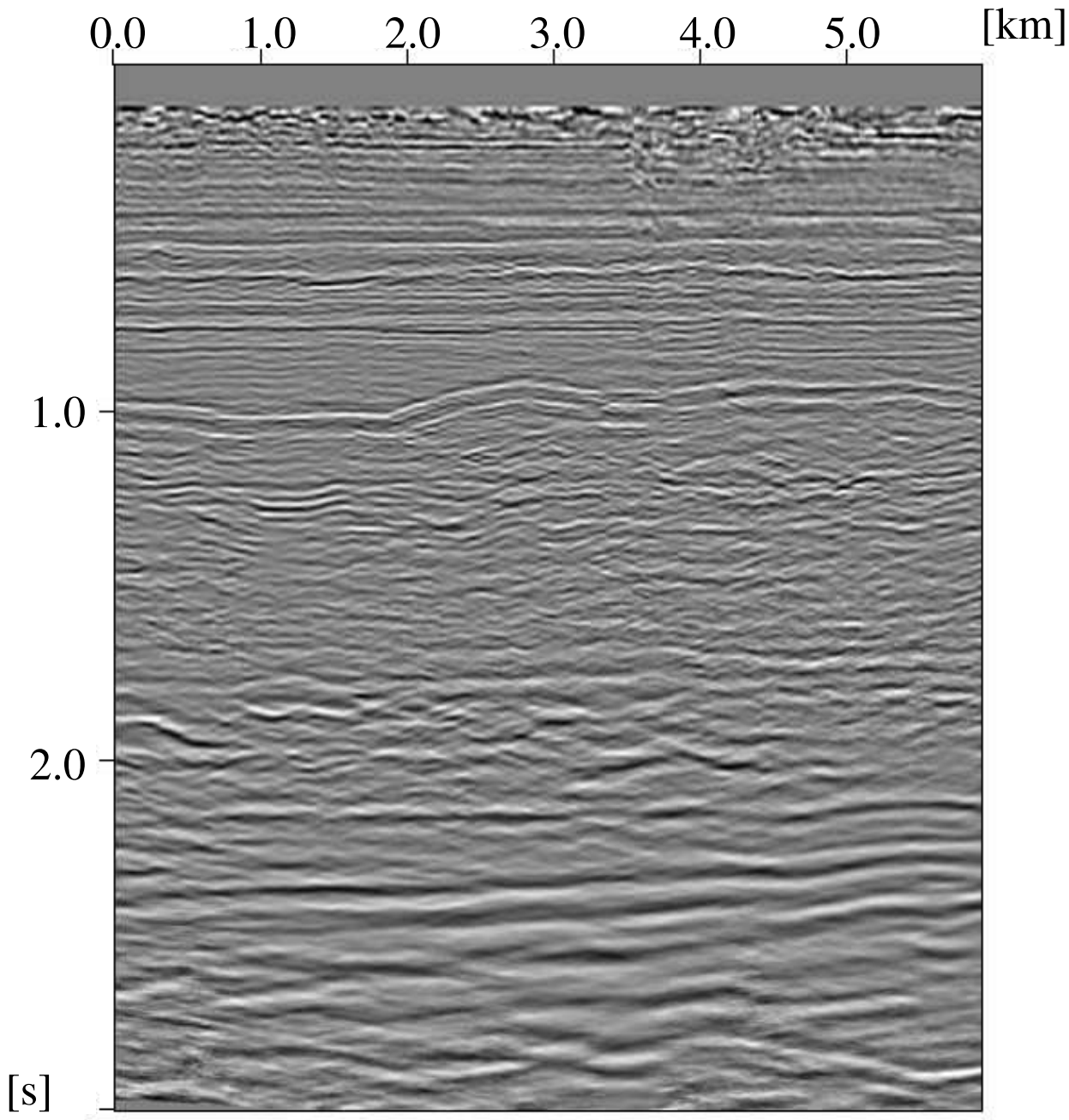

Figure 4.25: PS image using the anisotropic parameters obtained from the layer stripping, in two-way PP time.

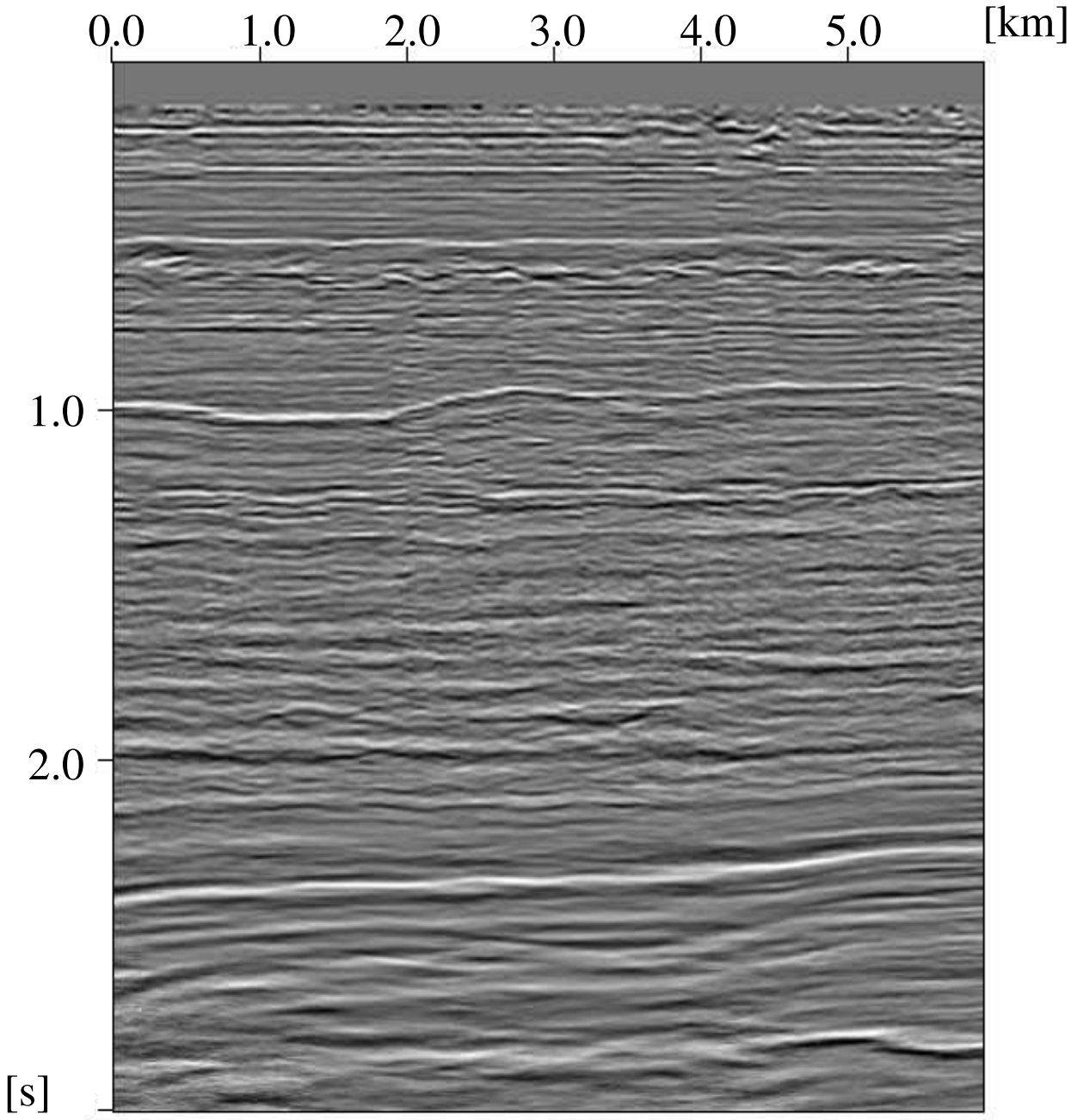

Figure 4.26: The initial PP image obtained in (i) (same as in Figure 4.9), in two-way PP time.

We have presented a tomographic approach to obtain depth consistent PP and PS images by a combination of differential semblance in angle and map migration enabling automatic measurement of the mistie in depth. This involves an extension of differential semblance in angle to converted waves. In addition, a way has been presented to perform PS map migration by approximatively resolving the S-wave leg of the PS event. The approximation uses NIP rays from the scattering surfaces and removes the P-wave leg of the PS event by using the PP traveltimes. This is similar to a zero scattering angle case of Gretchka and Tsvankin's 'PP + PS = SS'-concept (2002). When the suggested medium is far from the true model, or there is a huge inconsistency between the models governing the P-wave leg and the S-wave leg of the PS scattering event, the approximation deteriorates accordingly. For these cases and very complex media, the method can be extended by using the aforementioned 'PP + PS = SS'-approach by Grechka and Tsvankin (2002) to compute prestack SS traveltimes and not only the NIP rays of our approximation. Also, the uniqueness of the map demigration / migration does not apply even for simple caustics in the zero-offset case. However, in practice the map migration of the NIP ray traveltime information can be regularized into a surface smoothing smaller errors of the approximation. In addition, the approximative SS traveltimes can be updated during the optimization.

Perhaps one would expect that by first estimating a P-wave velocity model from PP reflections and then an S-wave velocity model from PS reflections would guarantee consistency in depth between PP and PS images, since the mode converted wave is tied to the P wave. The field data example illustrates that this is not the case: The difference in depths can be several hundred meters even if the differential semblance in angle measure, through uniform cigs, indicate a model fitting both the PP and PS scattering events.

The tying of the PP and PS events forces us to take anisotropy into account – this has been observed by several authors, see for example (Artola *et al.*, 2003). We developed an approach derived from joint PP and PS angle tomography, consisting of 5 steps, for carrying out MVA. We estimated a compressional and shear wave velocity model based on a quasi-VTI medium (Thomsen's $\delta = 0$ (1986)) assumption. We also succeeded in estimating δ separately from ε, with a degree of uncertainty, in part of the model; in this estimation we made additional use of a semblance measure applied to the PP and PS cigs. As to be expected, the best resolved parameter combination from PS angle tomography is $\varepsilon - \delta$.

The ε, δ parameter estimation was carried out in a layer stripping manner. The estimates for ε are significantly different from the ones obtained by the automatic global search for a quasi-VTI medium. This shows that our procedure and strategy cannot lead to uniqueness of the reflection tomography problem.

Our method shows the potential to achieve depth consistency and uniform cigs at the same time. It relies heavily on the ability to identify, interpret, and pair interfaces on the PP and PS images. The success of this depends on whether PS images of sufficient quality can be generated to begin with. It can be argued that the current field data example could have been solved by a less sophisticated method such as one based on the generalized Dix approach. However, our method extends far beyond the cases where the generalized Dix equation applies.

One of the potential applications of reflection tomography is pore pressure prediction (Sayers *et al.*, 2004). Our method will not only provide P-wave velocity models at a higher spatial resolution than can be obtained by hyperbolic moveout or other conventional velocity analyses, but will also yield an improved estimate of the local 'v_P/v_S' ratio.

Acknowledgement

The authors thank Statoil for the North Sea data set and Børge Arntsen for data handling. In addition we thank Anders Sollid, Statoil for helpful discussions. S.-K. Foss would like to thank the URE-project at NTNU, Norway for financial support.

References

Aki, K., & Richards, P. G. 1980. *Quantitative seismology. Theory and methods.* Vol. 1. W.H. Freeman, New York.

Al-Yahya, K. 1989. Velocity analysis by iterative profile migration. *Geophysics*, **54**, 718–729.

Alerini, M., Le Bégat, S., Lambaré, G., & Baina, R. 2002. 2D PP- and PS-stereotomography for a multicomponent dataset. *Proceedings 72th Ann. Internat. Mtg., Soc. Explor. Geophys.*, 838–841.

Alkhalifah, T., & Tsvankin, I. 1995. Velocity analysis for transversely isotropic media. *Geophysics*, **60**, 1550–1566.

Amundsen, L. 1999. Elimination of free surface-related multiples without the of the source wavelet. *Proceedings 69th Ann. Internat. Mtg., Soc. Explor. Geophys.*

Artola, F.A.V., Da Fontoura, S.A.B., Leiderman, R., & Silva, M.B.C. 2003. P-S conversion point in anisotropic media - errors due to isotropic considerations. *Proceedings 64th Mtg. Eur. Assn. Geosci. Eng.*, D–12.

Audebert, F., Granger, P.-Y., Gerea, C., & Herrenschmidt, A. 2001. Can joint PP and PS velocity analysis manage to corner δ, the anisotropic depthing parameter? *Proceedings 69th Ann. Internat. Mtg., Soc. Explor. Geophys.*, 145–148.

Berg, E., Svenning, B., & Martin, J. 1994. A new strategic tool for exploration and reservoir mapping. *Proceedings 56th Ann. Mtg. Eur. Assn. Geoscient. Eng.*

Beydoun, W. B., & Mendes, M. 1989. Elastic ray-Born l_2-migration/inversion. *Geophysical Journal.*

Beylkin, G. 1984. The inversion problem and applications of the generalized Radon Transform. *Communications in Pure and Applied Mathematics*, **XXXVII**, 579–599.

Beylkin, G. 1985. Imaging of discontinuities in the inverse scattering problem by inversion of a causal generalized Radon transform. *J. of Math. Phys.*, **26**, 99–108.

Beylkin, G., & Burridge, R. 1990. Linearized inverse scattering problems in acoustics and elasticity. *Wave Motion*, **12**, 15–52.

Billette, F., & Lambaré, G. 1998. Velocity macro-model estimation from seismic reflection data by stereotomography. *Geophys. J. Int.*, **135**, 671–690.

Biondi, B., & Palacharla, G. 1996. 3-D prestack migration of common-azimuth data. *Geophysics*, **61**, 1822–1832.

Bleistein, N. 1984. *Mathematics of wave phenomena.* Academic Press Inc.

Bleistein, N. 1986. Two-and-one-half dimensional in-plane wave propagation. *Geophysical Prospecting*, **34**, 686–703.

Bleistein, N. 1987. On imaging of reflectors in the earth. *Geophysics*, **52**, 931–942.

Bostock, M. G., Rondenay, S., & Shragge, J. 2001. Multiparameter two-dimensional inversion of scattered teleseismic body waves: 1. Theory for oblique incidence. *J. Geophys. Res.*, **106**, 30771–30782.

Brandsberg-Dahl, S., de Hoop, M. V., & Ursin, B. 1999. Velocity analysis in the common scattering-angle/azimuth domain. *Proceedings 69th Ann. Internat. Mtg., Soc. Explor. Geophys.*, 1222–1223.

Brandsberg-Dahl, S., de Hoop, M. V., & Ursin, B. 2003a. Focusing in dip and AVA compensation on scattering-angle/azimuth gathers. *Geophysics*, **68**, 232–254.

Brandsberg-Dahl, S., Ursin, B., & de Hoop, M. V. 2003b. Seismic velocity analysis in the scattering angle/azimuth domain. *Geophysical Prospecting*, **51**, 295–314.

Broto, K., Ehinger, A., Kommedal, J. H., & Folstad, P. G. 2003. Anisotropic traveltime tomography for depth consistent imaging of PP and PS data. *The Leading Edge*, **22**, 114–119.

Bube, K. P. 1995. Uniqueness of reflector depths and characterization of the slowness null space in linearized seismic reflection tomography. *SIAM Journal on Applied Mathematics*, **55**, 255–266.

Bube, K. P., & Meadows, M. A. 1999. The null space of a generally anisotropic medium in linearized surface reflection tomography. *Geophys, J. Int.*, **139**, 9–50.

Bube, K. P., Langan, R. T., & Nemeth, T. 2002. On the velocity vs. depth ambiguity in limited-aperture reflection tomography. *Proceedings 72th Ann. Internat. Mtg., Soc. Explor. Geophys.*, 834–837.

Burridge, R., de Hoop, M. V., Miller, D., & Spencer, C. 1998. Multiparameter inversion in anisotropic media. *Geophysical Journal International*, **134**, 757–777.

Carcione, J. M. 2001. *Wave fields in real media: Wave propagation in anisotropic, anelastic and porous media.* Pergamon.

Červený, V. 1972. Seismic rays and rays intensities in inhomogeneous anisotropic media. *Geophysical Journal of the Royal Astronomocal Society*, **29**, 1–13.

Červený, V. 1981. Computation of geometrical spreading by dynamic ray tracing. *Stanford University: SEP-28*, 61–73.

Červený, V. 2001. *Seismic Ray Theory*. Cambridge University Press.

Chapman, C. H. 1994. Reflection/transmission coefficients reciprocities in anisotropic media. *Geophysical Journal International*, **116**, 498–501.

Chapman, C. H., & Pratt, R. G. 1992. Traveltime tomography in anisotropic media-I. Theory. *Geophys. J. Int.*, **109**, 1–19.

Chauris, H., & Noble, M. 2001. Two-dimensional velocity macro model estimation from seismic reflection data by local differential semblance optimization: application to synthetic and real data sets. *Geophys. J. Int.*, **144**, 14–26.

Claerbout, J. F. 1971. Towards a unified theory of reflector mapping. *Geophysics*, **36**, 467–481.

Dębski, W., & Tarantola, A. 1995. Information on elastic parameters obtained from the amplitudes of reflected waves. *Geophysics*, **60**, 1426–1436.

de Boor, C. 1978. *A practical guide to splines*. New York: Springer.

de Hoop, M. V., & Bleistein, N. 1997. Generalized Radon transform inversions for reflectivity in anisotropic elastic media. *Inverse Problems*, **13**, 669–690.

de Hoop, M. V., & Brandsberg-Dahl, S. 2000. Maslov extension of generalized Radon transform inversion in anisotropic elastic media:A least-squares approach. *Inverse Problems*, **16**, 519–562.

de Hoop, M. V., & de Hoop, A. T. 1997 (May). Wavefield reciprocity and local optimization in remote sensing. *Pages 7–42 of: CWP Project Review.*

de Hoop, M. V., Burridge, R., Spencer, C., & Miller, D. 1994. Generalized Radon transform amplitude versus angle (GRT/AVA) migration/inversion in anisotropic media. *Proceedings SPIE 2301*, 15–27.

de Hoop, M. V., Spencer, C., & Burridge, R. 1999. The resolving power of seismic amplitude data: An anisotropic inversion/migration approach. *Geophysics*, **64**, 852–873.

de Hoop, M.V., Le Rousseau, J. H., & Biondi, B. 2003a. Seismic wavefield continuation in the single scattering approximation: A framework for dip and azimuth moveout. *Can. Appl. Math. Q.* in print.

de Hoop, M.V., Le Rousseau, J. H., & Biondi, B. 2003b. Symplectic structure of wave-equation imaging: A path-integral approach based on the double-square-root equation. *Geophys. J. Int.* in print.

Dellinger, J. A., Gray, S. H., Murphy, G. E., & Etgen, J. T. 2000. Efficient 2.5-D true-amplitude migration. *Geophysics*, **65**, 943–950.

Douma, H., & de Hoop, M.V. 2003. Closed-form expressions for map time-migration in VTI media and applicability of map depth-migration in the presence of caustics. *Geophysics, submitted.*

Dragoset, W. H., & Jeričević, Ž. 1998. Some remarks on surface multiple attenuation. *Geophysics*, 772–789.

Duistermaat, J. J. 1996. *Fourier integral operators.* Boston: Birkhäuser.

Ettrich, N., Sollid, A., & Ursin, B. 2002. Out-of-plane geometrical spreading in anisotropic media. *Geophysical Prospecting*, **50**, 383–392.

Farra, V., & Madariaga, R. 1987. Seismic waveform modeling in heterogeneous media by ray perturbation theory. *Journal of Geophysical Research*, **92**, 2697–2712.

Fomel, S. 1997. Velocity continuation and the anatomy of residual prestack migration. *Proceedings 67th Ann. Internat. Mtg. Soc. of Expl. Geophys.*, 1762–1765.

Foss, S. K., & Ursin, B. 2004. 2.5-D modeling, inversion and angle migration in anisotropic elastic media. *Geophysical Prospecting, Accepted.*

Foss, S. K., de Hoop, M.V., & Ursin, B. 2003a. Linearized 2.5-D parameter imaging-inversion in anisotropic elasic media. *Geophys. J. Int., submitted.*

Foss, S. K., Ursin, B., & Sollid, A. 2003b. A practical approach to automated PP angle tomography. *EAGE / SEG summer research workshop in Trieste.*

Gazdag, J., & Sguazzero, P. 1984. Migration of seismic data. *Pages 1302–1315 of: Proceedings of IEEE*, vol. 72.

Geoltrain, S. 1989. *Asymptotic solutions to direct and inverse scattering in anisotropic media.* Ph.D. thesis, Colorado School of Mines.

Gill, P. E., Murray, W., & H., Wright M. 1981. *Practical optimization.* Academic Press.

Gjøystdal, H., & Ursin, B. 1981. Inversion of reflection times in three-dimensions. *Geophysics*, **46**, 972–983.

Goldin, S. V. 1986. *Seismic traveltime inversion.* SEG: Investigations in Geophysics No. 1.

Grechka, V., & Tsvankin, I. 2002. PP + PS = SS. *Geophysics*, **67**, 1961–1971.

Guillemin, V. 1985. On some results of Gelfand in integral geometry. *Proceedings of Symposia in Pure Mathematics, American Mathematical Society*, **43**, 149–155.

Hansen, S. 1991. Solution of a hyberbolic inverse problem by linearization. *Comm. Partial Differential Equations*, **16**, 291–309.

Herrenschmidt, A., Granger, P.-Y., Audebert, F., Gerea, C., Etienne, G., Stopin, A., Alerini, M., Le Bégat, S., Lambaré, G., Berthet, P., Nebieridze, S., & Boelle, J-L. 2001. Comparison of different strategies for velocity model building and imaging of PP and PS real data. *The Leading Edge*, **20**, 984–995.

Hilterman, F. J. 2001. *Seismic Amplitude Interpretation.* SEG: Distinguished Instructor Series, No. 4.

Hörmander, L. 1983. *The analysis of linear partial differential operators.* Vol. III. Berlin: Springer-Verlag.

Hubral, P., & Krey, T. 1980. *Interval velocities from seismic reflection time measurements.* Soc. of Expl. Geophys.

Iversen, E. 2001. First-order perturbation theory for seismic isochrones. *Studia geophysica et geodaetica*, **45**, 394–444.

Iversen, E., Gjøystdal, H., & Hansen, J. O. 2000. Prestack map migration an engine for parameter estimation in TI media. *Proceedings 70th Ann. Internat. Mtg., Soc. Explor. Geophys.*, 1004–1007.

Jaramillo, H. H., & Bleistein, N. 1999. The link of Kirchhoff migration and demigration to Kirchhoff and Born modeling. *Geophysics*, **64**, 1793–1805.

Kleyn, A. H. 1977. On the migration of reflection-time contour maps. *Geophys. Prosp.*, **25**, 125–140.

Klimeš, L. 1997. Phase shift of the Green function due to caustics in anisotropic media. *Expanded Abstracts: 68th Ann. Internat. Mtg. ,Soc. Explor. Geophys.*, 1834–1837.

Miller, D., Oristaglio, M., & Beylkin, G. 1987. A new slant on seismic imaging: migration and integral geometry. *Geophysics*, **52**, 943–964.

Musgrave, M.J.P. 1970. *Crystal Acoustics*. San Francisco: Holden-Day.

Nolan, C. J., & Symes. 1997. Global solution of a linearized inverse problem for the wave equation. *Comm. Partial Differential Equations*, **22**, 919–952.

Plessix, R.-E., ten Kroode, F., & Mulder, W. 2000. Automatic crosswell tomography by differential semblance optimization: theory and gradient computation. *Geophysical Prospecting*, **48**, 913–935.

Rakesh. 1988. A linearised inverse problem for the wave equation. *Comm. in Part. Diff. Eqs.*, **13**, 573–601.

Rüger, A. 1996. *Reflection coefficients and azimuthal AVO analysis in anisotropic media*. Ph.D. thesis, Center for wave phenomenon, Colorado School of Mines.

Sayers, C. M., Smit, T. J. H., van Eden, C., Wervelman, R., Bachmann, B., Fitts, T., Bingham, J., McLachlan, K., Hooyman, P., Noeth, S., & Mandhiri, D. 2004. Use of reflection tomography to predict pore pressure in overpressured reservoir sands. *Proceedings 74th Ann. Internat. Mtg., Soc. Explor. Geophys.*, 1362–1365.

Schoenberg, M., & Helbig, K. 1997. Orthorhombic media: Modeling elastic wave behavior in a vertically fractured earth. *Geophysics*, **62**, 1954–1974.

Sollid, A. 2000. *Imaging of ocean bottom seismic data*. Ph.D. thesis, Norwegian University of Science and Technology, Trondheim.

Sollid, A., & Ettrich, N. 1999. Coherency optimiation of transversely isotropic velocity models via PP/PS prestack migration. *Proceedings 69th Ann. Internat. Mtg., Soc. Explor. Geophys.*, 1707–1710.

Sollid, A., & Ursin, B. 2003. Scattering-angle migration of OBS data in weakly anisotropic media. *Geophysics*, **68**, 641–655.

Stockwell, Jr., J. W. 1995. 2.5-D wave equations and high-frequency asymptotics. *Geophysics*, **60**, 556–562.

Stolk, C. C. 2000. Microlocal analysis of a seismic linearized inverse problem. *Wave Motion*, **32**, 267–290.

Stolk, C. C., & de Hoop, M. V. 2002. Microlocal analysis of seismic inverse scattering in anisotropic elastic media. *Communications in Pure and Applied Mathematics*, **55**, 261–301.

Stopin, A., & Ehinger, A. 2001. Joint PP PS tomographic inversion of the Mahogany 2-D-4-C OBC seismic data. *Proceedings 71th Ann. Internat. Mtg., Soc. Explor. Geophys.*, 837–840.

Stork, C., & Clayton, R. W. 1986. Analysis of the resolution between ambiguous velocity and reflector position for traveltime tomography. *Proceedings 56th Ann. Internat. Mtg., Soc. Explor. Geophys.*, 545–550.

Symes, W. 1991. A differential semblance algorithm for the inverse problem of reflection seismology. *Computers Math. Applic.*, **22**, 147–178.

Symes, W. 2000. *All stationary points of differential semblance are asymptotic global minimizers: layered acoustics.* Rice Inversion Project, Annual report.

Symes, W., & Carazzone, J. 1991. Velocity inversion by differential semblance optimization. *Geophysics*, **56**, 654–663.

Taner, M. T., & Koehler, F. 1969. Velocity spectra - Digital computer derivation and applications of velocity functions. *Geophysics*, **34**, 859–881.

Tarantola, A. 1987. *Inverse Problem Theory*. 3 edn. Elsevier.

ten Kroode, A. P. E., Smit, D. J., & Verdel, A. R. 1998. A microlocal analysis of migration. *Wave Motion*, **28**, 149–172.

Tenorio, L. 2001. Statistical regularization of inverse problems. *SIAM Review*, **43**, 347–366.

Thomsen, L. 1986. Weak elastic anisotropy. *Geophysics*, **51**, 1954–1966.

Thomsen, L. 1999. Converted-wave reflection seismology over inhomogeneous, anisotropic media. *Geophysics*, **64**, 678–690.

Treves, F. 1980. *Introduction to pseudodifferential and Fourier integral operators*. Vol. 1. New York: Plenum Press.

Tsvankin, I. 2001. *Seismic signatures and analysis of reflection data in anisotropic media*. Elsevier.

Tygel, M., Schleicher, J., & Hubral, P. 1994. Pulse distortion in depth migration. *Geophysics*, **59**, 1561–1569.

Tygel, M., Schleicher, J., Hubral, P., & Santos, L.T. 1998. 2.5-D true-amplitude Kirchhoff migration to zero offset in laterally inhomogeneous media. *Geophysics*, **63**, 557–573.

Ursin, B. 2003. Parameter inversion and angle migration in anisotropic elastic media. *Geophysics, Accepted*.

Ursin, B., & Tygel, M. 1997. Reciprocal volume and surface scattering integrals for anisotropic elastic media. *Wave Motion*, **26**, 31–42.

Versteeg, R. J. 1993. Sensitivity of prestack depth migration to the velocity model. *Geophysics*, **58**, 873–882.

Wang, Y. 2003. *Seismic amplitude inversion in reflection tomography.* Pergamon/Elsevier Science.

Wang, Y., & Houseman, G. A. 1994. Inversion of reflection seismic amplitude data for interface geometry. *Geophysical Journal International*, **117**, 92–110.

Wapenaar, C. P. A. 1996. Inversion versus migration: A new perspective to an old discussion. *Geophysics*, **61**, 804–814.

Whitcombe, D. N. 1994. Fast model building using demigration and single-step ray migration. *Geophysics*, **59**, 439–449.

Yilmaz, O. 1987. *Seismic data processing.* Investigations in Geophysics, vol. 2. Tulsa: Society of Exploration Geophysicists.

Chapter 5

Appendix: A practical approach to PP seismic angle tomography

S.-K. Foss, B. Ursin and A. Sollid

Submitted, Geophysical Prospecting 2004

Summary

The use of the differential semblance misfit function on common image-point gathers in the angle domain, lends itself to an automated tomographic approach through a gradient based search of the model space. The common image-point gathers are created by the AVA-compensated or restricted generalized Radon transform. We present the complete description of all 2.5-D formulas for the purpose of isotropic velocity analysis of PP scattering events on a field ocean bottom seismic data example. In addition an approach is presented to regularize the optimization by only considering velocity models that respect geological features obtained from time information.

5.1 Introduction

Migration velocity analysis exploits the redundancy in the data to estimate a smooth velocity model. This is done by studying the residual moveout on migrated gathers (Al-Yahya, 1989). Symes and Carazzone (1991) proposed to measure this moveout by means of the differential semblance (DS) misfit functional. The DS misfit functional has been successfully applied to a number of problems using offset as the redundancy parameter (Plessix *et al.*, 2000; Chauris & Noble, 2001). Brandsberg-Dahl *et al.* (2003b) derived the framework for DS to work in a more natural coordinate system, namely scattering angle and azimuth at the imaging point. The misfit functional measures the residual moveout and amplitude behavior on common image-point gathers computed by a restricted inverse generalized Radon transform (GRT) (de Hoop *et al.*, 1999; Brandsberg-Dahl *et al.*, 1999; Brandsberg-Dahl *et al.*, 2003b) or amplitude-compensated migration (Ursin, 2003). The local derivative of the DS misfit functional makes it sensitive to amplitude variations. Amplitude-compensated migration uses a point-wise partial compensation of the amplitude-versus-angle (AVA) behavior. The minimum of the misfit functional is obtained for so-called *uniform* angle gathers where the amplitude and depth is constant for every angle in the common image-point gather. Brandsberg-Dahl *et al.* (2003b) showed the feasibility of PP angle tomography on a synthetic data example.

We present a practical approach by regularizing the optimization procedure with time information of the interface geometry of a layer-based velocity model. The method is a generalization of Gjøystdal and Ursin's (1981) scheme for building velocity models that are consistent with the zero-offset traveltimes. The zero-offset traveltime horizons enable the interface geometry to be updated in an automatic fashion through map migration (Kleyn, 1977). The interfaces are recognized on initial PP depth images and map demigrated along

normal incidence point (NIP) rays (Hubral & Krey, 1980) into time horizons which are unrelated to any velocity model. For every velocity parameter set in the optimization, the interface geometry of the velocity model is map migrated to depth. In this way we only search amongst velocity models that are consistent with the zero-offset time information of the seismic data.

We proceed considering a 2.5-D formalism, that is 3-D wave propagation in a 2-D model where all calculations are done in a plane (Bleistein, 1986). However, the methods presented are fully applicable to 3-D data, but for clarity and adaption to the single line of the ocean bottom seismic (OBS) field data example, we limit ourself to 2.5-D. Formulas for the 3-D case are found in the review by Ursin (2003). Here, we present the expressions for the creation of PP common image-point gathers assuming an isotropic medium. Complete description of the 2.5-D formulas for anisotropic media is given by Foss *et al.* (2004).

The outline of the paper is as follows. The first section introduces notation and gives a complete description of how to create isotropic PP amplitude-compensated common image-point gathers for the purpose of velocity analysis for OBS data in a 2.5-D formalism. The next section introduces the DS misfit functional and explains how time information on the interface geometry is incorporated in the tomographic optimization. Then we present a field data example from the North Sea to illustrate our procedure.

5.2 Isotropic PP common image-point gathers

We consider a heterogeneous isotropic elastic medium. The procedure is presented in a 2-D model with the (x_1, x_3)-plane as the plane of consideration. The geometry is given in Figure 5.1 where the imaging point is denoted $\mathbf{y} = (y_1, y_3)$. The source is at $\mathbf{x}^s$ and the receiver is at $\mathbf{x}^r$ (boldfonts indicate vectors). The superscripts s and r indicate association with a

ray from the source and receiver, respectively. The slowness vector $\mathbf{p}^s(\mathbf{y}) = (p_1^s, p_3^s)$ is thus the slowness of the ray connecting the source point $\mathbf{x}^s$ and the image point $\mathbf{y}$ evaluated at this latter point. $\mathbf{p}(\mathbf{x}^s)$ indicates the slowness of the same ray evaluated at the source. A similar notation is used for the receiver, namely, $\mathbf{p}^r(\mathbf{y}) = (p_1^r, p_3^r)$ and $\mathbf{p}(\mathbf{x}^r)$. Observe that the out-of-plane slowness p_2 is zero in 2.5-D (Bleistein, 1986; Foss & Ursin, 2004). In an isotropic medium, the P-wave polarization vectors are the unit vectors of the slowness vectors, denoted $\mathbf{h}(\mathbf{x}^s) = (h_1(\mathbf{x}^s), h_3(\mathbf{x}^s))$ and $\mathbf{h}(\mathbf{x}^r) = (h_1(\mathbf{x}^r), h_3(\mathbf{x}^r))$ for the polarization vectors at the source and receiver, respectively. The scattering angle θ is define by the angle between the slowness vectors of the rays from the source and receiver at the imaging point

$$\cos\theta = \frac{\mathbf{p}^s \cdot \mathbf{p}^r}{|\mathbf{p}^s||\mathbf{p}^r|} \quad \text{at } \mathbf{y}. \tag{5.1}$$

The migration slowness vector is defined by $\mathbf{p}^m(\mathbf{y}) = \mathbf{p}^s(\mathbf{y}) + \mathbf{p}^r(\mathbf{y})$ with unit vector

$$\boldsymbol{\nu}^m(\mathbf{y}) = \frac{\mathbf{p}^m(\mathbf{y})}{|\mathbf{p}^m(\mathbf{y})|}, \tag{5.2}$$

which is the migration dip.

Elastic, isotropic media can be described by the Lamé parameters $\lambda(\mathbf{x})$ and $\mu(\mathbf{x})$, and density $\rho(\mathbf{x})$. These parameters are given as a sum of a smooth part (with superscript (0)) and a perturbation (with superscript (1)):

$$\begin{aligned} \rho(\mathbf{x}) &= \rho^{(0)}(\mathbf{x}) + \rho^{(1)}(\mathbf{x}) \\ \lambda(\mathbf{x}) &= \lambda^{(0)}(\mathbf{x}) + \lambda^{(1)}(\mathbf{x}). \\ \mu(\mathbf{x}) &= \mu^{(0)}(\mathbf{x}) + \mu^{(1)}(\mathbf{x}) \end{aligned} \tag{5.3}$$

The estimation of the smooth part is the object of velocity analysis, while the medium perturbations are found by inversion. We assume that the perturbations are jumps in the parameters along an interface defined by a function $\phi(\mathbf{x}) = 0$ (de Hoop & Bleistein, 1997).

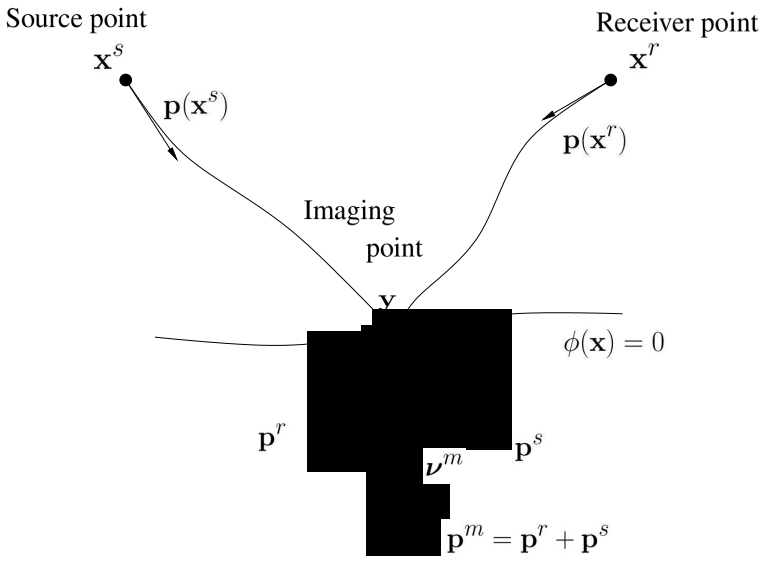

Figure 5.1: Geometry of rays connecting the imaging point with the source and the receiver.

Amplitude-preserving migration results in an estimate of the reflectivity at the interface which, with a band-limited wavelet $w(t)$, is given by (Ursin, 2003)

$$\begin{aligned}\hat{S}_w(\theta;\mathbf{y}) &= \hat{S}(\theta;\mathbf{x}^\phi)\Big|_{\phi(\mathbf{y})} w(p^\phi \boldsymbol{\nu}^\phi \cdot (\mathbf{y}-\mathbf{x}^\phi)),\\ &\approx \int_{E_\nu} \partial_t \tilde{u}(\mathbf{x}^r, T(\mathbf{x}^r,\mathbf{y},\mathbf{x}^s),\mathbf{x}^s;\mathbf{y})|\mathbf{p}^m(\mathbf{y})|^2 d\nu,\end{aligned} \tag{5.4}$$

where $\mathbf{x}^s = \mathbf{x}^s(\mathbf{y},\nu,\theta)$ and $\mathbf{x}^r = \mathbf{x}^r(\mathbf{y},\nu,\theta)$ (see Figure 5.1). The migration dip $\boldsymbol{\nu}^m(\mathbf{y})$ is parameterized by the migration dip angle ν such that $\boldsymbol{\nu}^m(\mathbf{y}) = (\cos\nu, \sin\nu)$ where $\nu \in E_\nu \subset [0, 2\pi\rangle$ is the integration domain. $\boldsymbol{\nu}^\phi$ is the surface normal at the point $\mathbf{x}^\phi$ on the interface, projected from the image point $\mathbf{y}$. The stretch factor p^ϕ (Ursin, 2003; Tygel *et al.*, 1994) is equal to the length of the migration slowness vector evaluated at the stationary point $\mathbf{x}^\phi$. For PP scattering in an isotropic medium the length of the migration slowness vector is given by

$$|\mathbf{p}^m(\mathbf{y})| = \frac{2\cos(\theta/2)}{v(\mathbf{y})}, \tag{5.5}$$

where $v(\mathbf{y})$ is the P-wave velocity. The data corrected for amplitude, phase and traveltime

are

$$\partial_t \tilde{u}(\mathbf{x}^r, T(\mathbf{x}^r, \mathbf{y}, \mathbf{x}^s), \mathbf{x}^s; \mathbf{y}) =$$
$$h_m(\mathbf{x}^r)\, \partial_t \tilde{u}_m^{(1)}(\mathbf{x}^r, T(\mathbf{x}^r, \mathbf{y}, \mathbf{x}^s), \mathbf{x}^s)\, 2\sqrt{2\pi}\, \mathcal{L}_R^{\perp}(\mathbf{x}^r, \mathbf{y}, \mathbf{x}^s)$$
$$\cdot\, v(\mathbf{y}) \left[\frac{\rho^{(0)}(\mathbf{x}^r) v(\mathbf{x}^r)}{\rho^{(0)}(\mathbf{x}^s) v(\mathbf{x}^s)}\right]^{1/2} |Q_2^{||}(\mathbf{x}^r, \mathbf{y}) Q_2^{||}(\mathbf{y}, \mathbf{x}^s)|^{1/2}. \quad (5.6)$$

where $Q_2^{||}$ is the in-plane relative geometrical spreading calculated from dynamical ray tracing (Červený, 2001). The total out-of-plane relative geometrical spreading is given by

$$\mathcal{L}_R^{\perp}(\mathbf{x}^r, \mathbf{y}, \mathbf{x}^s) = \left[\int_{source\ ray} v(\mathbf{x}(t))^2 dt + \int_{receiver\ ray} v(\mathbf{x}(t))^2 dt\right]^{1/2}, \quad (5.7)$$

where both integrals are path integrals of the squared P-wave velocity using time t as the ray parameter along the indicated rays. $\mathbf{x}(t)$ is the spatial position of the ray at time t. The differentiated data corrected for a possible phase-shift due to caustics are given by

$$\partial_t \tilde{u}_m^{(1)}(\mathbf{x}^r, T(\mathbf{x}^r, \mathbf{y}, \mathbf{x}^s), \mathbf{x}^s)$$
$$= \frac{1}{\pi} Re \left\{ \int_0^{\infty} \omega^{1/2} U_m^{(1)}(\mathbf{x}^r, \omega, \mathbf{x}^s) e^{-i3\pi/4} e^{[i\pi/2(\kappa(\mathbf{x}^r, \mathbf{y}) + \kappa(\mathbf{y}, \mathbf{x}^s))]} e^{-i\omega T(\mathbf{x}^r, \mathbf{y}, \mathbf{x}^s)} d\omega \right\}. \quad (5.8)$$

Here, $T(\mathbf{x}^r, \mathbf{y}, \mathbf{x}^s)$ is the two-way traveltime from source to receiver via the imaging point $\mathbf{y}$. $\kappa(\mathbf{x}^r, \mathbf{y}) + \kappa(\mathbf{y}, \mathbf{x}^s)$ is the accumulated KMAH-index for the rays connecting the scattering point and receiver and source, respectively. $U_m^{(1)}(\mathbf{x}^r, \omega, \mathbf{x}^s)$ is the m-component of the Fourier transformed data received at $\mathbf{x}^r$ due to a source at $\mathbf{x}^s$. OBS data are usually created by means of a pressure source, hence there is no directivity of the source.

In the migration formula (5.4), $\hat{S}_w(\theta; \mathbf{y})$ is a band-limited estimate of the isotropic linearized PP scattering coefficient defined by

$$S(\theta; \mathbf{y}) = \mathbf{r}(\theta)^T \mathbf{c}^{(1)}(\mathbf{y}), \quad (5.9)$$

where the medium parameter vector is given by (Beylkin & Burridge, 1990)

$$\mathbf{c}^{(1)}(\mathbf{y})^T = \left\{ \frac{\lambda^{(1)}}{\lambda^{(0)} + 2\mu^{(0)}}, \frac{\rho^{(1)}}{\rho^{(0)}}, \frac{2\mu^{(1)}}{\lambda^{(0)} + 2\mu^{(0)}} \right\} \tag{5.10}$$

and the radiation pattern vector by

$$\mathbf{r}(\theta) = \left\{ 1, \cos\theta, \cos^2\theta \right\}^T. \tag{5.11}$$

Note that θ is the scattering angle (see Figure 5.1) which is twice the angle of incidence. For the estimation of the smoothly varying parameters in the background medium (velocity analysis) we use common image-point gathers computed from amplitude-compensated migration

$$\mathcal{I}(\theta; \mathbf{y}) = \frac{\hat{S}_w(\theta; \mathbf{y})}{|\mathbf{r}(\theta)|}. \tag{5.12}$$

Using equations (5.4) and (5.11) this equation gives the formula for a common image-point gather

$$\mathcal{I}(\theta; \mathbf{y}) = \frac{4\cos^2(\theta/2)}{v^2(\mathbf{y})(1 + \cos^2\theta + \cos^4\theta)^{1/2}} \int_{E_\nu} \partial_t \tilde{u}(\mathbf{x}^r, T(\mathbf{x}^r, \mathbf{y}, \mathbf{x}^s), \mathbf{x}^s; \mathbf{y}) d\nu. \tag{5.13}$$

A structural image is computed by (Ursin, 2003)

$$\mathcal{I}(\mathbf{y}) = \int \mathcal{I}(\theta; \mathbf{y}) d\theta. \tag{5.14}$$

5.3 Angle tomographic procedure

The differential semblance misfit functional (Symes & Carazzone, 1991) measures the residual moveout on common image-point gathers indicating the fit of a given velocity model used to migrate the current gathers. In the scattering angle domain this is given by (Brandsberg-Dahl *et al.*, 2003b)

$$\mathcal{J}(\mathbf{m}) \;=\; \frac{1}{2} \int \int |\partial_\theta \mathcal{I}(\theta, \mathbf{y}; \mathbf{m})|^2 d\theta d\mathbf{y}. \tag{5.15}$$

Here, $\mathbf{m} = (m_1, \ldots, m_n)$ is the current value of n model parameters needed for a finite dimensional description of the smooth background medium (i.e. some P-wave velocity parametrization), $\mathbf{y} = (y_1, y_3)$ is the image point in spatial coordinates and θ is the scattering angle at the image point. $\mathcal{I}(\theta, \mathbf{y}; \mathbf{m})$ is the common image-point gather at position $\mathbf{y}$, with angle θ and computed with the current model $\mathbf{m}$ using equation (5.13). ∂_θ is the partial derivative with respect to the scattering angle. Equation (5.15) should in addition be normalized with the energy of each common image-point gather making the misfit function less sensitive to noise in the data and erroneous amplitude calculations (Chauris & Noble, 2001).

The DS misfit functional lends itself to an automated tomographic approach through a gradient-based search in the model parameter space. Numerical evidence (Plessix *et al.*, 2000; Chauris & Noble, 2001) suggests that the misfit function has, for a large region in the model space, desirable convexity properties for an automated search procedure. We use a quasi-Newton method in search of the minimum taking the gradient of equation (5.15) with respect to the model parameters $\mathbf{m}$. The i-th component of the gradient is given by

$$\partial_{m_i} \mathcal{J}(\mathbf{m}) = \int \int \left[\partial_\theta \mathcal{I}(\theta, \mathbf{y}; \mathbf{m})\right] \partial_\theta \partial_{m_i} \mathcal{I}(\theta, \mathbf{y}; \mathbf{m}) d\theta d\mathbf{y}. \tag{5.16}$$

To calculate this gradient it is necessary to compute the gradient of the image with respect to the model parameters. All expressions for this gradient are given by Brandsberg-Dahl *et al.* (2003b). The calculations are based on imaging and paraxial ray theory (Farra & Madariaga, 1987).

Following Billette and Lambaré (1998), we let the complete velocity field be described by the superposition of a layered model with linear velocity profiles in each layer and a sparsely sampled 2-D B-spline function. The P-wave velocity at a given point $\mathbf{x} = (x_1, x_3)$

given by

$$v(\mathbf{x}) \;=\; \sum_k (a_k + b_k x_3) I_k(\mathbf{x}) + \delta v(\mathbf{x}). \tag{5.17}$$

Here, $(a_k + b_k x_3)$ is the linear velocity profile in layer k, with a constant a_k in each layer with velocity gradient b_k. I_k is an indicator function which is equal to one in layer k and zero outside. For a given velocity model, the interface geometry is found by map migration of the zero-offset two-way traveltimes for the different interfaces, as done in the inverse scheme of Gjøystdal and Ursin (1981). As the interface geometry of the new model needs the new model itself, a few iterations is needed to stabilize the velocity field and interface geometry. The zero-offset two-way traveltimes for the key reflectors may be obtained from a stacked section or by map demigration of an initial migrated section. This procedure ensures that the interfaces between the layers always give the correct zero-offset traveltimes. $\delta v(\mathbf{x})$ is a 2-D B-spline function with coefficients δv_j. The complete finite dimensional parameter model vector is then the collection of the velocity parameters of the layers and coefficients of the 2-D B-spline, given by

$$\mathbf{m} = \{a_k, b_k, \delta v_j\}\,. \tag{5.18}$$

The velocity estimation procedure starts by finding an optimal solution using only the first part of the model description. In order to avoid parts of the problem of the velocity-depth ambiguity, we may fix the velocity gradients, b_k, using information from well logs. After finding reasonable estimates of the parameters a_k, we proceed by optimizing with respect to the coefficients of the 2-D B-spline representation, using δv_j as our model parameters. This last step is designed to capture inhomogeneities not explained by the simple layered model.

5.4 Field data example

Our procedure has been tested on an OBS line taken from the North Sea. Prior to the

tomographic procedure (and not for the subsequent imaging shown below) the data have been passed through a bandpass filter between 3 and 15 Hz. The common image-point gathers are calculated sparsely; every 250 meters with a total of 12 gathers starting at 1250 meters. The gathers are sampled at every 10 meters in depth and a 0.5 degree sampling in angle up to 45 degrees incoming P-wave reflection angle. Both the gradients and the common image-point gathers are smoothed by a simple $\{1/4, 1/2, 1/4\}$-convolution filter in angle and depth, and, in addition, a 2-D Fourier dip filter in angle and depth is applied as suggested by Chauris and Noble (2001). The B-spline nodes are placed with 250 meter intervals in the horizontal direction and 100 meter intervals in the depth direction. This relatively fine sampling in the depth domain is necessary due to a sharp velocity increase over a very small region in the velocity model (at 2500-3000 meters in depth). In order to avoid oscillatory behavior of the optimization due to this oversampling, we employ a Tikhonov regularizer in depth of the medium parameters (Tenorio, 2001; Brandsberg-Dahl *et al.*, 2003b).

An initial image was created using a model from a simple 1-D optimization. From this image the time horizons were constructed by map demigration along the NIP rays from chosen key reflectors as described above with a total of 14 interfaces. These time horizons were used in the consecutive velocity estimation steps to govern the interface geometry in equation (5.17). The velocity gradients and starting constant velocities within each layer were chosen from a well log close by. The velocity gradients were kept fixed in all subsequent velocity updates. This initial velocity model and the corresponding image are shown in Figure 5.2 (top left) and 5.4. Figure 5.3 a) shows the common image-point gathers using the starting model in Figure 5.2 (top left). The common image-point gathers shown in Figure 5.3 b) are after 4 iterations. The two last iterations (of 7 in total) were done with respect to the 2-D B-spline parameters given in equation (5.17). This gave little im-

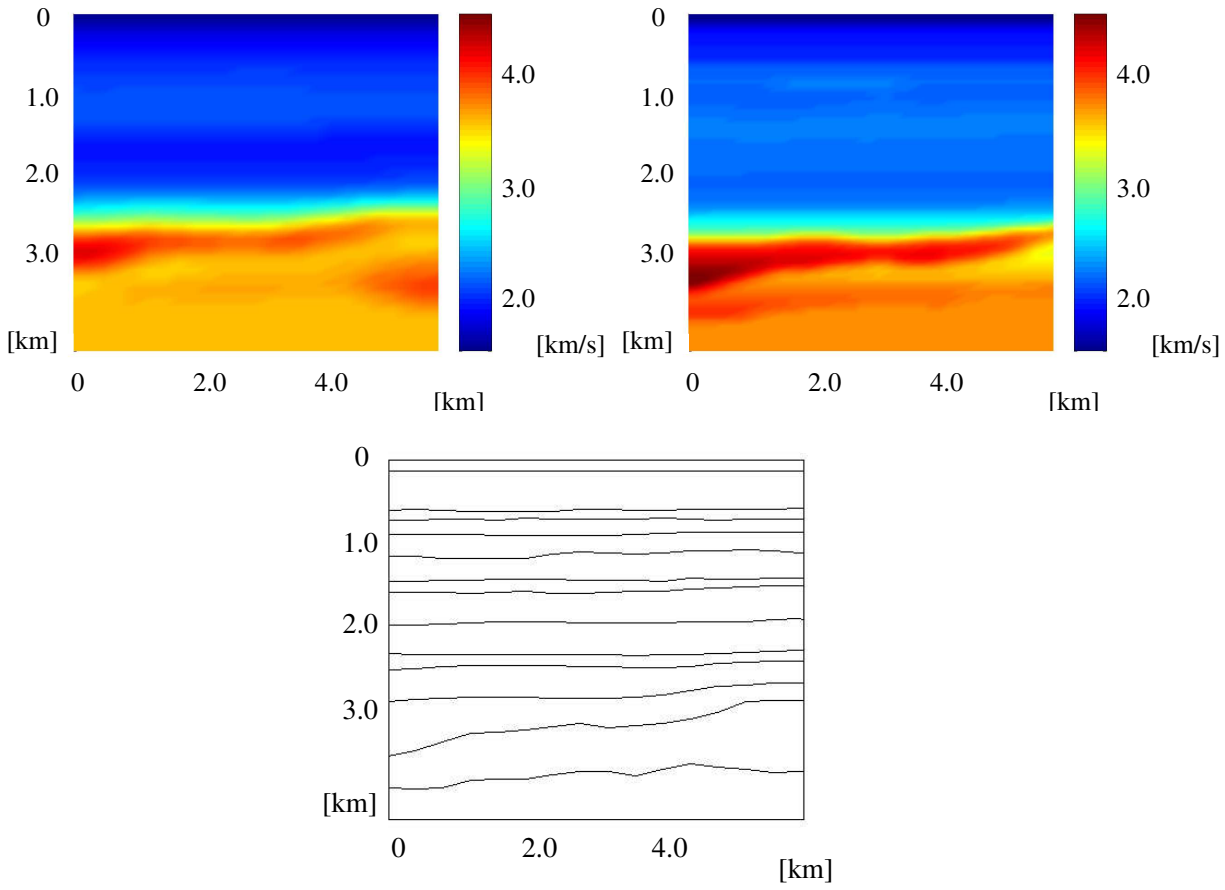

Figure 5.2: Initial (top left) and final (top right) P-wave velocity with the final interface geometry in depth (bottom).

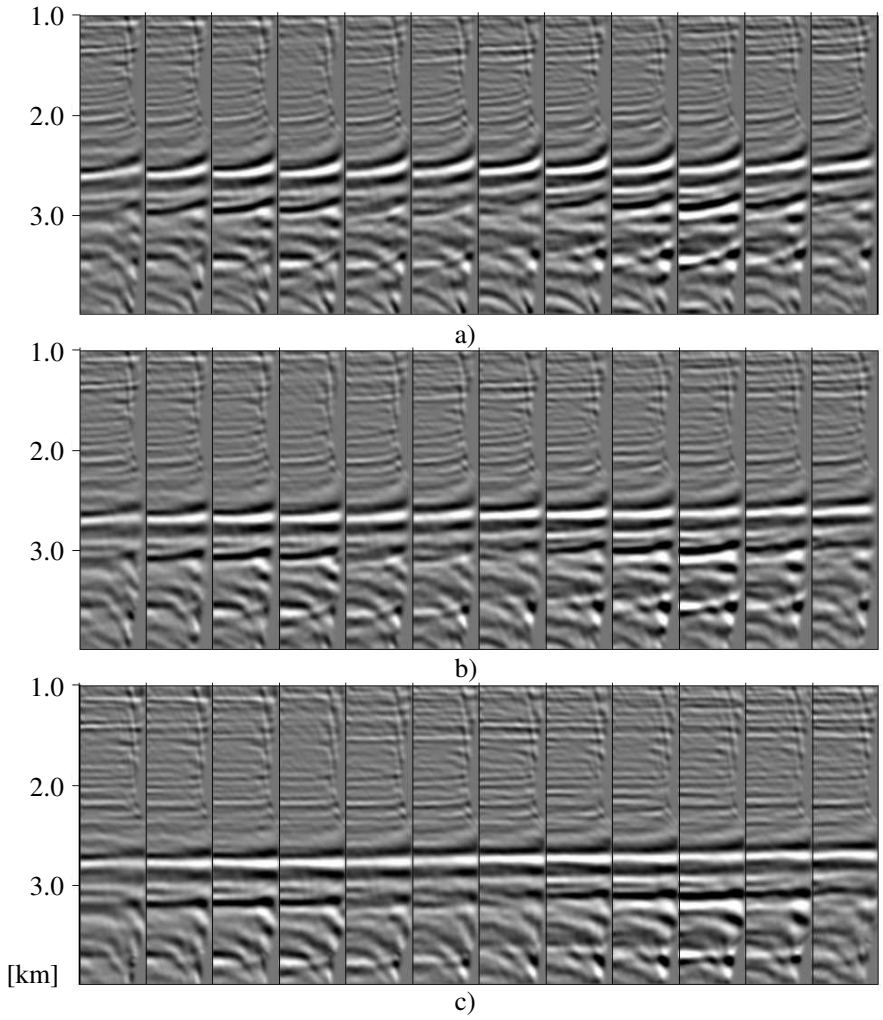

Figure 5.3: The common image-point gathers in the optimization after 0 iterations a), 4 iterations b) and after 7 iterations c).

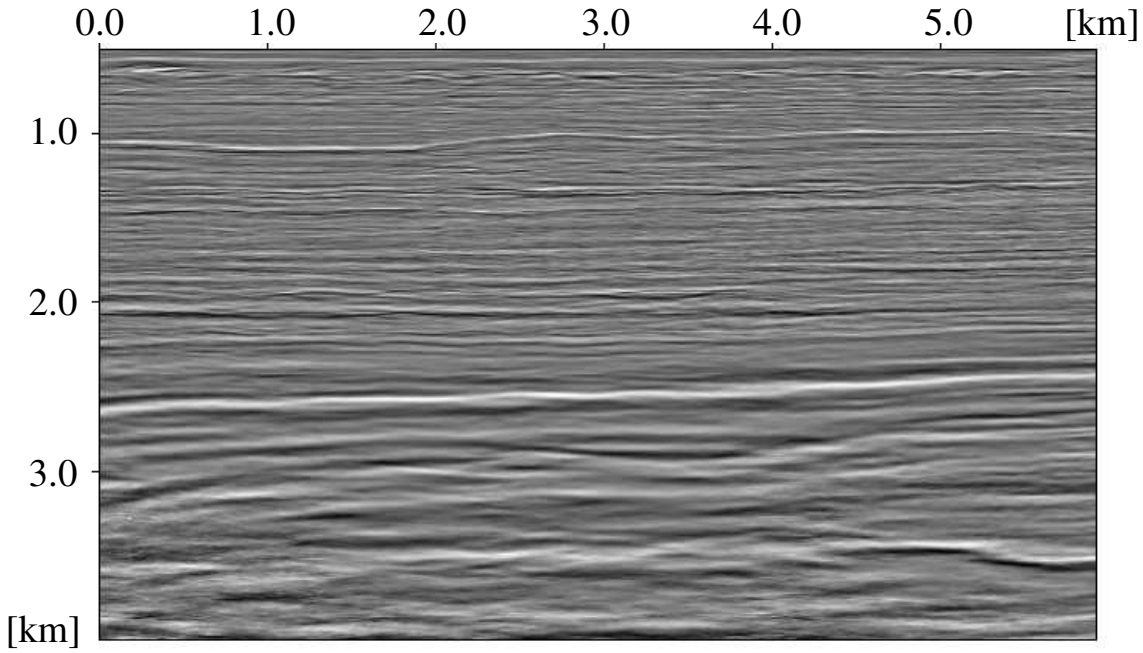

Figure 5.4: Starting PP image computed with the initial velocity model in Figure 5.2 (top left).

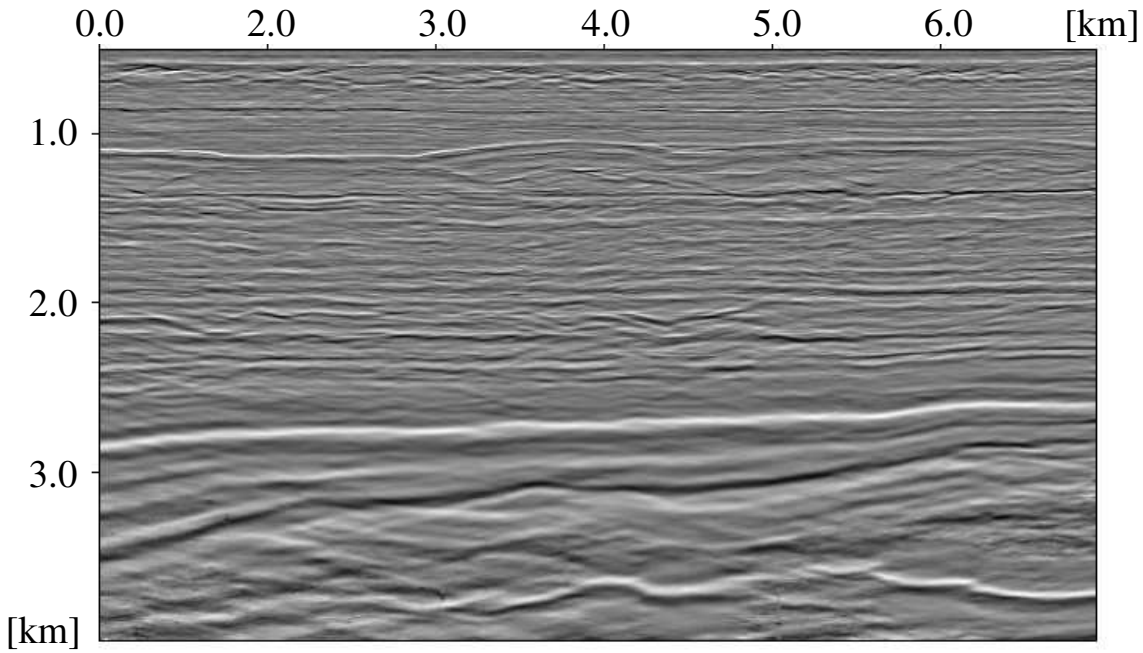

Figure 5.5: Final PP image after 7 iterations corresponding to the final velocity model in Figure 5.2 (top right).

provement in the value of the misfit functional. The common image-point gathers shown in Figure 5.3 c) are after 7 iterations and show reasonable convergence. Notice the apparent internal multiples below main reflector at 2700 meters with strongly overmigrated moveout behavior. These multiples made it very difficult to estimate a correct velocity model as the method tends to flatten primaries and multiples which have conflicting moveout behavior.

The final velocity model from the optimization is found in Figure 5.2 (top right) with the final interface geometry in depth (bottom). Notice the change in the interface geometry between the starting and the final velocity model in the figure. From starting model to final model the misfit functional dropped by 14%. The focused image created by the optimized model is given in Figure 5.5. Notice the deeper interface (at roughly 3700 meters) becoming more focused compared to the starting image Figure 5.4.

5.5 Conclusion

We have presented an approach to PP seismic angle tomography based on an iterative differential semblance optimization scheme. The P-wave velocity model consists of a number of layers with constant velocity gradients plus a 2-D bicubic spline function to take into account lateral velocity changes. For each iteration the layer boundaries were constructed by map migration of the zero-offset traveltime maps. In this way, the zero-offset traveltimes from the main reflectors in the model are always correct. The OBS data example indicates that the sensitivity to multiple reflections is the main problem in migration velocity analysis.

Acknowledgment

S.-K. Foss thanks the URE-project for financial support. We thank Statoil for the use of

the North Sea data set and Børge Arntsen for help with data handling.

Stig-Kyrre Foss

Department of Mathematical Sciences,

Norwegian University of Science and Technology,

Norway